CERN-THESIS-2013-385

Search for physics beyond the Standard Model in events with a Z boson and large missing transverse momentum with the ATLAS detector

by

Devin Randall Harper

A dissertation submitted in partial fulfillment
of the requirements for the degree of
Doctor of Philosophy
(Physics)
in the University of Michigan
2013

Doctoral Committee:
Professor Homer A. Neal, Chair
Professor Lennard A. Fisk
Professor Jianming Qian
Professor Gregory Tarlé
Professor James Daniel Wells

Acknowledgments

The road to a doctoral degree is a very personal experience for any candidate. As for most graduate students, the list of those whom I owe a debt of gratitude is far too long (indeed, I could make this list its own 200 page tome) to give here. However, I would like to thank several people who have helped in innumerable ways to get me to this point in my career.

During my time as an undergraduate at the University of Oklahoma, Professors Michael Strauss, Eric Abraham, and Matthew Johnson provided guidance in all aspects of my academic training, from research discussions to in-depth conversations about course work and outreach activities. You all were important voices in my choir of early academic advisors. To my fellow OU physics students Ethan Brown and Jerod Parrent: you guys were the most important driving force in my achieving any measure of excellence as a young physicist. Thank you for challenging me to continue on this difficult path, and for countless nights of rambling over difficult problem sets and the woes of rigorous research. The future holds massive potential for us all.

Moving to the University of Michigan, my foothold on the ways of a department (and the comfort of a familiar town) were gone. Brian Nord and Ross O'Connell provided invaluable advice and mentorship during my first months as a graduate student in Ann Arbor. The lessons learned over many a happy hour regarding educational practices and the proper work-life balance for a budding scientist have stuck with me to this day. Brian: you have always kept me grounded and passionate about even the most menial tasks, and your enthusiasm for learning and truth are contagious. Ross: under your guidance, I learned all there is to know about the undergraduate physics laboratories here at U-M, and our close work together when I was a young Lead GSI helped me to chisel my leadership skills in the classroom for the first time. For the many late nights finishing problem sets and wondering what exactly we had gotten ourselves into as young Ph.D. students, I should certainly thank Brandon Erickson and Tomasz Biesiadzinski.

As a member of the U-M ATLAS group, I had the pleasure to spend a significant

portion of my time as a student at CERN, in Geneva, Switzerland. To Jianming Qian, Bing Zhou, Junjie Zhu, and Tiesheng Dai, as well as all the other members of U-M ATLAS: I will be forever grateful for all the fruitful scientific and technical conversations we had while I was performing my research. My fellow "CERNois" helped me to acclimate to life in Europe, and played pivotal roles in my development as a particle physicist. To Ryan Reece, Josh Kunkle, Liz Hines, and the rest of the UPenn army; to Zach Marshall; to Emma Kuwertz; to Laura Jeanty; to Alan Wilson and Jeremy Herr; to Aaron Armbruster and Jonathan Long; and to countless others: the good times, scientific discourse, and unforgettable experiences abroad have shaped me in ways I find difficult to articulate. Thank you.

Two U-M postdoctoral fellows closely guided me through my transition to CERN and through my tenure as a graduate student. To Jonas Strandberg, who provided many important insights and discussions about code, physics, and life in Geneva, I deeply appreciate your wisdom, and truly value your instruction and vision. Natalia Panikashvili, with whom I worked very closely over the last three years, has had perhaps the deepest impact on my development as a student. Natalia, your collaboration has been an invaluable resource for me. Thank you for the late nights finalizing plots and numbers, for the challenging and insightful questions, and for the confidence you instilled in me. By extension, I would like to thank my advisor, Homer Neal, for graciously encouraging and enabling mine and Natalia's research visions.

As a student returning to Ann Arbor after three years of work at CERN, many things were different the second time around. I would like to thank Tomasz Biesiadzinski, Jake Ketchum, Ryo Saotome, and Alex Burgers for quickly filling the void left behind as I lost my CERN support structure. For the long lunches, the procrastination (via gratuitous coffee breaks), and for tolerating my complaining about thesis-writing, I owe you guys.

Finally, I want to thank my family. The support and love given to me by my mother, father, and two siblings have always proven to be a sturdy anchor in helping me reach my academic goals. To Samanthe and Grant: watching both of you thrive in your own paths has inspired me throughout my student career, and I am extremely excited to watch our stories continue. Mom, your voice has never failed to help me keep my eye on the prize, and my work ethic is largely a result of your example. Dad, you have continually helped me to prioritize my endeavors, and you (with mom) have helped me through many trying times. I will never be able to thank you all enough.

To the many other individuals not mentioned here who have helped me in this journey, please know that my gratitude is enormous.

Table of Contents

Acknowledgments ii

List of Tables vii

List of Figures ix

Abstract xiii

Chapter 1 Introduction 1

Chapter 2 The Standard Model and Supersymmetry 6
2.1 History and introduction 6
2.2 The Standard Model 8
2.2.1 Gauge invariance 8
2.2.2 Electroweak sector 10
2.2.3 QCD 12
2.2.4 Electroweak symmetry breaking 12
2.3 Supersymmetry 14
2.3.1 Introduction 14
2.3.2 Gauge mediated supersymmetry breaking 16
2.3.3 General Gauge Mediation 19

Chapter 3 The Large Hadron Collider 20
3.1 Luminosity goals 20
3.2 Design 21
3.3 Injection chain 24
3.4 Beam dump system 27
3.5 2011 operation 27
3.6 2012 operation 28

Chapter 4 The ATLAS detector 30
4.1 Magnet system 32
4.1.1 Solenoid 33
4.1.2 Toroids 33

4.2 Inner Detector . . . 34
4.2.1 Silicon pixel detector . . . 35
4.2.2 Semiconductor Tracker . . . 36
4.2.3 Transition Radiation Tracker . . . 37
4.3 Calorimetry . . . 41
4.3.1 Electromagnetic calorimetry . . . 42
4.3.2 Hadronic calorimetry . . . 45
4.4 Muon spectrometer . . . 48
4.4.1 Monitored Drift Tubes . . . 49
4.4.2 Cathode Strip Chambers . . . 52
4.4.3 Resistive Plate Chambers . . . 53
4.4.4 Thin Gap Chambers . . . 56
4.5 Forward Detectors . . . 58
4.6 Trigger and DAQ . . . 59
4.6.1 Level-1 Trigger . . . 60
4.6.2 DAQ and HLT . . . 61

Chapter 5 Reconstruction and particle identification . . . 63
5.1 Electrons . . . 63
5.2 Photons . . . 67
5.3 Muons . . . 70
5.4 Jets . . . 72
5.5 Missing transverse energy . . . 74
5.5.1 Cell-based $E_{\mathrm{T}}^{\mathrm{miss}}$ . . . 76
5.5.2 Object-based $E_{\mathrm{T}}^{\mathrm{miss}}$ . . . 77

Chapter 6 Searches for SUSY in the $Z + E_T^{\mathrm{miss}}$ final state with 2011 data . . . 79
6.1 Introduction . . . 79
6.2 Data and Monte Carlo samples . . . 79
6.2.1 Dataset and Trigger Selection . . . 79
6.2.2 Monte Carlo simulation . . . 80
6.3 Object definitions . . . 84
6.4 Event selection . . . 87
6.4.1 Z preselection . . . 87
6.4.2 Signal regions . . . 89
6.5 Backgrounds . . . 97
6.5.1 Non-Z background estimation . . . 97
6.5.2 $Z/\gamma^* +$ jets background estimation . . . 97
6.5.3 Summary of SM backgrounds . . . 120
6.6 Systematic uncertainties for MC . . . 122
6.6.1 Systematic uncertainties for $t\bar{t}$ MC . . . 126
6.6.2 Systematic uncertainties for signal MC . . . 129
6.7 Interpretation in the Context of SUSY . . . 131
6.7.1 The likelihood function . . . 134

6.7.2 The test statistic . . . 134
6.7.3 Pseudo-experiments . . . 135
6.7.4 Interpretation in higgsino-like NLSP GGM . . . 136
6.7.5 Exclusion limits . . . 136

Chapter 7 Searches for SUSY in the $Z + E_T^{\text{miss}}$ final state with 2012 data . . . 137
7.1 Introduction . . . 137
7.2 Simulation . . . 137
7.2.1 Signal MC . . . 137
7.2.2 Background MC . . . 144
7.3 Object and Event Selection . . . 144
7.4 Background Evaluation . . . 149
7.4.1 WW, $t\bar{t}$, Wt, $\tau\tau$ background estimation . . . 149
7.4.2 WZ and ZZ backgrounds . . . 163
7.4.3 $Z/\gamma^* +$ jets background estimation . . . 163
7.5 Systematic Uncertainties . . . 177
7.6 Results and Interpretation . . . 180
7.6.1 GGM $\tan\beta = 1.5$ grid interpretation . . . 180
7.6.2 GGM $\tan\beta = 30$ grid interpretation . . . 181

Chapter 8 Summary and concluding remarks . . . 184

Appendix . . . 187

Bibliography . . . 191

List of Tables

Table

1.1 The four forces. 2

2.1 The particle content of the MSSM. 16

3.1 Summary of details for the LHC runs in 2011-2012. 29

6.1 GGM parameters for 7 TeV models. 80
6.2 Sparticle masses for a sample GGM model. 82
6.3 GGM cross sections at 7 TeV. 83
6.4 GGM cross sections at 7 TeV. 85
6.5 The NLO cross sections for $\tilde{g}\tilde{g}$ production only. 85
6.6 The NLO cross sections for the electroweak processes. 86
6.7 SM background estimations using MC in SR1. 95
6.8 SM background estimations using MC in SR2. 96
6.9 SM background estimations using MC in SR3. 96
6.10 Fraction of non-photon backgrounds in photon sample. 99
6.11 Data-driven $Z/\gamma^* + \text{jets}$ estimations. 112
6.12 Relative systematic uncertainties for $Z/\gamma^* + \text{jets}$ results. 122
6.13 Final SR1 results for 7 TeV. 123
6.14 Final SR2 results for 7 TeV. 123
6.15 Final SR3 results for 7 TeV. 123
6.16 Summary of non-Z systematic uncertainties. 130
6.17 GGM signal systematic uncertainties, scale and PDF. 130
6.18 Total systematic uncertainties for GGM signal. 132
6.19 Total systematic uncertainties for GGM signal (cont). 133

7.1 GGM parameters for 8 TeV models. 138
7.2 GGM model details for $\tan\beta = 1.5$. 139
7.3 GGM model details for $\tan\beta = 1.5$ (cont). 140
7.4 GGM model details for $\tan\beta = 30$. 141
7.5 GGM model details for $\tan\beta = 30$ (cont). 142
7.6 The NLO+NLL cross sections for $\tilde{g}\tilde{g}$ production only. 142

7.7 Sample GGM sparticle mass spectrum. 143
7.8 MC sample details. 144
7.9 Signal region definitions for the 2012 analysis. 149
7.10 ee and $\mu\mu$ results in the control regions (data). 156
7.11 ee and $\mu\mu$ results in the control regions (MC). 156
7.12 Subtracted MC for the $e\mu$ estimation. 156
7.13 Results of data-driven WW, $t\bar{t}$, Wt, $\tau\tau$ estimation. 161
7.14 Closure test for WW, $t\bar{t}$, Wt, $\tau\tau$ estimation. 162
7.15 MC predictions for WW, $t\bar{t}$, Wt, $\tau\tau$ in SR1. 162
7.16 MC predictions for WW, $t\bar{t}$, Wt, $\tau\tau$ in SR2. 162
7.17 WZ MC predictions. 163
7.18 ZZ MC predictions. 163
7.19 Cuts for signal, seed, and control regions for the $Z/\gamma^* + \text{jets}$ method. 169
7.20 $Z/\gamma^* + \text{jets}$ predictions in the signal regions. 173
7.21 Systematic uncertainties on SM backgrounds. 177
7.22 Theoretical GGM uncertainties. 178
7.23 Theoretical GGM uncertainties (cont). 179
7.24 SM backgrounds, GGM signal, and observed data results for SR1. . . 180
7.25 SM backgrounds, GGM signal, and observed data results for SR2. . . 181

List of Figures

Figure

1.1 The unification of coupling constants. 3

2.1 First order corrections to the mass of the Higgs field. 14
2.2 A sample GMSB event at the LHC. 17

3.1 The lattice layout of the LHC. 22
3.2 LHC dipole and its cold mass. 23
3.3 LHC quadrupole and its cold mass. 24
3.4 The LHC accelerator complex. 25
3.5 LHC injection scheme. 26
3.6 2011 luminosity summary. 28
3.7 2012 luminosity summary. 29

4.1 The ATLAS detector. 31
4.2 An overview of the ATLAS magnet system. 33
4.3 A cutaway view of the ATLAS inner detector. 35
4.4 A cutaway view of the ATLAS silicon pixel detector. 36
4.5 An exploded cutaway view of the ATLAS inner detector. 38
4.6 Illustration of drift tube ionization and electron drift. 39
4.7 TRT $R-T$ relations. 40
4.8 A module of the electromagnetic calorimeter. 43
4.9 A module of the tile calorimeter. 45
4.10 Module and electronics for the hadronic endcap calorimeter. 47
4.11 Muon spectrometer layout. 50
4.12 MDT chamber illustration. 51
4.13 CSC module illustration. 53
4.14 Schematic of the muon trigger system. 54
4.15 Placement of the RPC chambers relative to MDT chambers. 55
4.16 RPC chamber structure. 55
4.17 TGC chamber structure. 57
4.18 Level-1 trigger schematic 60

5.1 Electron identification performance. 66
5.2 Electron identification performance as a function of pileup. 67
5.3 Photon identification performance. 70
5.4 Muon identification performance. 72
5.5 A schematic of jet reconstruction. 75

6.1 Example gluino production Feynman diagrams. 81
6.2 Example electroweak production Feynman diagrams. 84
6.3 $E_{\mathrm{T}}^{\mathrm{miss}}$ distributions after dilepton and Z preselections. 88
6.4 GGM $E_{\mathrm{T}}^{\mathrm{miss}}$ dependence on $m(\tilde{h})$. 89
6.5 Jet multiplicity distributions after Z preselection. 90
6.6 Leading jet p_{T} distributions after Z preselection. 90
6.7 H_{T} distributions after Z preselection. 91
6.8 Distributions of ΔR between leading leptons after Z preselection. . . 91
6.9 Distributions of leading lepton p_{T} after Z preselection. 92
6.10 Distributions of dilepton p_{T} after Z preselection. 92
6.11 $E_{\mathrm{T}}^{\mathrm{miss}}$ values for signal region optimization. 93
6.12 H_{T} and ΔR values for signal region optimization. 94
6.13 $E_{\mathrm{T}}^{\mathrm{miss}}$ distributions after cutting $p_{\mathrm{T}}(Z) > 45$GeV. 94
6.14 $E_{\mathrm{T}}^{\mathrm{miss}}$ distributions for $\gamma +$ jets and $\gamma\gamma +$ jets events (data). 99
6.15 Data/MC comparisons of $E_{\mathrm{T}}^{\mathrm{miss}}$ in $\gamma +$ jets events. 100
6.16 $E_{\mathrm{T}}^{\mathrm{miss}}$ in $\gamma +$ jets from data compared with scaled single electron events from MC. 101
6.17 $E_{\mathrm{T}}^{\mathrm{miss}}$ in $\gamma +$ jets data after background subtraction. 102
6.18 Comparison of $E_{\mathrm{T}}^{\mathrm{miss}}$ in $Z/\gamma^* +$ jets data with that of $\gamma +$ jets data. . 103
6.19 The scalar sum of the p_T of jets in Z and γ data samples. 103
6.20 The p_T of the Z or γ in Z and γ data samples. 104
6.21 H_T distributions for Z and γ data samples. 105
6.22 H_T distributions as function of $E_{\mathrm{T}}^{\mathrm{miss}}$ for Z data samples. 105
6.23 $E_{\mathrm{T}}^{\mathrm{miss}}$ and H_{T} profile distributions. 105
6.24 Reweighting function used for the $\gamma +$ jets method for $Z/\gamma^* +$ jets estimation. 106
6.25 H_{T} distributions for Z and reweighted γ samples. 107
6.26 $E_{\mathrm{T}}^{\mathrm{miss}}$ distributions for Z and reweighted γ samples. 107
6.27 $E_{\mathrm{T}}^{\mathrm{miss}}$ distributions for $Z(\mu\mu)$ and reweighted γ samples, with additional smearing. 108
6.28 Scalar sum of jet p_T of Z and reweighted γ samples. 108
6.29 Z p_{T} of Z events, compared to γ p_{T} in reweighted γ events. 109
6.30 $E_{\mathrm{T}}^{\mathrm{miss}}$ of Z events, compared to p_{T}-reweighted γ events. 110
6.31 $E_{\mathrm{T}}^{\mathrm{miss}}$ fits in SR1 using $\gamma +$ jets events to model $Z/\gamma^* +$ jets. 111
6.32 $E_{\mathrm{T}}^{\mathrm{miss}}$ fits in SR2 using $\gamma +$ jets events to model $Z/\gamma^* +$ jets. 112
6.33 $E_{\mathrm{T}}^{\mathrm{miss}}$ fit results using alternate binning. 114
6.34 $E_{\mathrm{T}}^{\mathrm{miss}}$ fit results using alternate CR definitions. 116
6.35 $E_{\mathrm{T}}^{\mathrm{miss}}$ fits using alternate subtraction schemes for the $\gamma +$ jets sample. 117

6.36 $E_{\mathrm{T}}^{\mathrm{miss}}$ fits using alternate subtraction schemes for the γ + jets sample (cont). . . . 118
6.37 $t\bar{t}$ $E_{\mathrm{T}}^{\mathrm{miss}}$ distributions for MC generator uncertainties. . . . 119
6.38 $t\bar{t}$ $E_{\mathrm{T}}^{\mathrm{miss}}$ distributions for ISR/FSR uncertainties (SR1). . . . 119
6.39 $t\bar{t}$ single electron events $E_{\mathrm{T}}^{\mathrm{miss}}$ distributions for ISR/FSR uncertainties (SR2). . . . 120
6.40 $E_{\mathrm{T}}^{\mathrm{miss}}$ fits for systematic uncertainties in the $Z(\mu\mu)$ event sample. . . . 121
6.41 $E_{\mathrm{T}}^{\mathrm{miss}}$ fits for systematic uncertainties in the $Z(\mu\mu)$ event sample (cont). 121
6.42 $E_{\mathrm{T}}^{\mathrm{miss}}$ in the signal regions. . . . 124
6.43 $E_{\mathrm{T}}^{\mathrm{miss}}$ in $t\bar{t}$ events in SR2, with ISR/FSR fluctuations. . . . 127
6.44 $E_{\mathrm{T}}^{\mathrm{miss}}$ in $t\bar{t}$ events generated with alternate MC generators. . . . 127
6.45 $E_{\mathrm{T}}^{\mathrm{miss}}$ in $t\bar{t}$ events with SR-like cuts, with systematic variations. . . . 128
6.46 Relative uncertainties on $t\bar{t}$ estimation as a function of $E_{\mathrm{T}}^{\mathrm{miss}}$ cut value for ISR/FSR variations. . . . 128
6.47 Relative uncertainties on $t\bar{t}$ estimation as a function of $E_{\mathrm{T}}^{\mathrm{miss}}$ cut value for alternate generators. . . . 129
6.48 95% CL mass limit contours for the combination of SR1 and SR2. . . . 136

7.1 $BR(\tilde{\chi}_1^0 \to Z\tilde{G})$ and $BR(\tilde{\chi}_1^0 \to h\tilde{G})$ for GGM grid points 138
7.2 $m_{\ell\ell}$ distributions after dilepton selection 146
7.3 $E_{\mathrm{T}}^{\mathrm{miss}}$ distributions after dilepton selection 147
7.4 $E_{\mathrm{T}}^{\mathrm{miss}}$ distributions after Z preselection 148
7.5 H_{T} distributions after Z preselection 150
7.6 N_{jets} distributions after Z preselection 151
7.7 leading jet p_{T} distributions after Z preselection 152
7.8 sub-leading jet p_{T} distributions after Z preselection 153
7.9 third jet p_{T} distributions after Z preselection 154
7.10 leading lepton p_{T} distributions after Z preselection 155
7.11 sub-leading lepton p_{T} distributions after Z preselection 155
7.12 $E_{\mathrm{T}}^{\mathrm{miss}}$ distributions in ZCR1 and ZCR2 157
7.13 H_{T} distributions in ZCR1 and ZCR2 158
7.14 $E_{\mathrm{T}}^{\mathrm{miss}}$ distributions for $e\mu$ events in SR1 and SR2 159
7.15 H_{T} distributions for $e\mu$ events in SR1 and SR2 160
7.16 leading jet p_{T} distributions for $e\mu$ events in SR1 and SR2 160
7.17 $E_{\mathrm{T}}^{\mathrm{miss}}$ significance distributions after Z preselection 165
7.18 $E_{\mathrm{T}}^{\mathrm{miss}}$ significance vs. $E_{\mathrm{T}}^{\mathrm{miss}}$ after Z preselection with $E_{\mathrm{T}}^{\mathrm{miss}} < 140$ GeV 166
7.19 sum of jet p_{T} in control and seed regions 167
7.20 $E_{\mathrm{T}}^{\mathrm{miss}}$ vs. $f_{\texttt{CellOut}}$ in the seed regions (data) 168
7.21 $E_{\mathrm{T}}^{\mathrm{miss}}$ vs. $f_{\texttt{CellOut}}$ in the seed regions (GGM signal MC) 169
7.22 Jet response distributions 170
7.23 jet smearing results for Z/γ^* + jets 173
7.24 $E_{\mathrm{T}}^{\mathrm{miss}}$ distributions in ZCR1, ZCR2 with data-driven backgrounds 174
7.25 MC closure test for the jet smearing method 175
7.26 Jet smearing results in SR1 and SR2 176
7.27 95% CL exclusion limits, GGM with $\tan\beta = 1.5$, SR1 182

7.28 95% CL exclusion limits, GGM with $\tan\beta = 30$, SR1 183

8.1 Mass reach of ATLAS searches for Supersymmetry. 186

Abstract

This dissertation summarizes two searches for new physics in LHC proton collision data collected by the ATLAS detector at CERN. In particular, these searches were designed to optimize the chances of discovery of supersymmetric particles, assuming a supersymmetry breaking scheme known as General Gauge Mediation (GGM). The final state considered in these analyses consists of a Z boson, where the Z decays to an electron or muon pair, in association with large missing transverse momentum and jets. The first of the two analyses is based on data collected in 2011, when the LHC delivered collisions at a center of mass energy $\sqrt{s} = 7$ TeV. Using 1.04 fb^{-1} of good quality ATLAS data, signal region optimization and quantification of backgrounds using data-driven methods were carried out. No excess above the Standard Model expectation was observed, and these results were interpreted in a GGM context in which the lightest neutralino (the NLSP) is higgsino-like. A follow-up to this search was also performed using 5.84 fb^{-1} of $\sqrt{s} = 8$ TeV ATLAS data recorded in 2012. Overall, this analysis is similar to the 2011 work, with some changes in the data-driven background methods and signal models used for interpretation. Again, no excess was observed in relation to the expectation from the Standard Model processes. In addition to the GGM models used in 2011, which are characterized with a low value of $\tan\beta$, a high $\tan\beta$ interpretation was considered for the 2012 analysis. 95% CL limits on the gluino and higgsino mass $(m(\tilde{g}), m(\tilde{h}))$have been set. For the low $\tan\beta$ scenario, gluino masses in the range $680 < m(\tilde{g}) < 880$ GeV have been excluded for higgsino masses between 180 and 800 GeV. Assuming high $\tan\beta$, gluino masses between 680 and 820 GeV were excluded for $180 < m(\tilde{h}) < 740$ GeV.

Chapter 1

Introduction

Mankind has always strived for progress by questioning the nature of the universe. A cornerstone of the development of understanding has been the attempt to explain the state of the universe at its most fundamental level. Efforts to answer the question, "what is the universe made of?" date back to the atomic hypothesis of Democritus and Leucippus, which states that matter is composed of *atoms*, indivisible components that bond together in some way so as to give rise to macroscopic objects. Since these days of antiquity, our descriptions of the universe have iteratively become much more sophisticated and rigorous. The field of high energy physics (HEP) seeks to answer these questions in light of the rapid developments in both experiment and theory over the 20th century.

Since Röntgen and Thomson's work with x-rays and electrons in the late 1800s, the modern understanding of atoms, their constituents, and particle interactions has progressed very quickly. The advent of Einstein's special relativity and insight into the constant nature of the speed of light, c, helped to shape the interpretation of experimental findings. With quantum mechanics, developed in the 1920s, we were catapulted to a new (and, indeed, disorienting) method of understanding microscopic processes as statistical processes. Combining relativity with quantum mechanics, Dirac's theory of quantum electrodynamics (QED) was another pivotal step in the path to a complete description of the fundamental makeup of nature. The decades following this development proved very fruitful, and a coherent description of fundamental particles and forces began to emerge. This quantum field theory, described naturally in the beautiful language of groups, became known as the Standard Model of particle physics [1] (SM).

The SM describes a set of spin-1/2 matter particles, known as fermions, and a set of force-mediating spin-1 particles, called bosons. Together, along with a special spin-0 boson associated with the field responsible for bestowing mass on these fundamental particles, we have an incredibly successful framework to explain the universe at its

Interaction	Theory	Mediator	Strength	Range (m)
Gravity	General relativity	Graviton(?)	1	∞
Strong	QCD	Gluon	10^{38}	10^{-15}
Weak	Electroweak theory	W and Z bosons	10^{25}	10^{-18}
Electromagnetism	QED	Photon	10^{36}	∞

Table 1.1: The four fundamental forces, along with the theory that describes each, the associated mediating boson, the relative strength (using gravity as the reference), and the effective range. Note that the graviton is still a theoretical particle that has not been experimentally observed.

most basic level. The matter particles are grouped into two categories: quarks and leptons. Quarks are the fundamental particles making up protons and neutrons, and leptons include the familiar electron, as well as heavier versions and very light particles known as neutrinos. There are four known forces in nature: gravitational, electromagnetic, weak, and strong. Table 1.1 gives a summary of these interactions. Although gravity, described mathematically by general relativity, is the most familiar force in the macroscopic world, there is yet to be a consistent quantum framework into which it fits. The theoretical particle associated with the mediation of gravity has not been confirmed. The strong and weak forces describe the interactions between constituents of the nucleus, as well as processes like beta decay (or anything involving neutrinos). The gluon is responsible for mediating strong interactions between quarks. The W and Z bosons are present in weak interactions between quarks as well, but also provide for weak interactions amongst the leptons. Finally, the electromagnetic interactions between charged fermions is mediated by the photon (*i.e.*, light particles).

An interesting principle behind the fundamental interactions is the idea of unification. As it turns out, the coupling constant of a given interaction (which determines its strength) is not constant at all, but instead varies with the energy of the particles involved. See Figure 1.1 for an illustration of the evolution of coupling constants from low to high energies. Thus far, the SM has successfully described one unification: the electromagnetic and weak interactions unify into one force, known as the electroweak force. The true nature of these interactions lies in the symmetries respected by transformations under the gauge group that describes them. In the case of electromagnetism, the relevant group is known as $U(1)$. For the strong and weak forces, the groups are $SU(3)$ and $SU(2)$, respectively. As shown in Figure 1.1, the $U(1)$ and $SU(2)$ symmetries appear to be connected, and indeed the larger group $SU(2) \times U(1)$ is found to describe the physics well. However, at lower energies, this

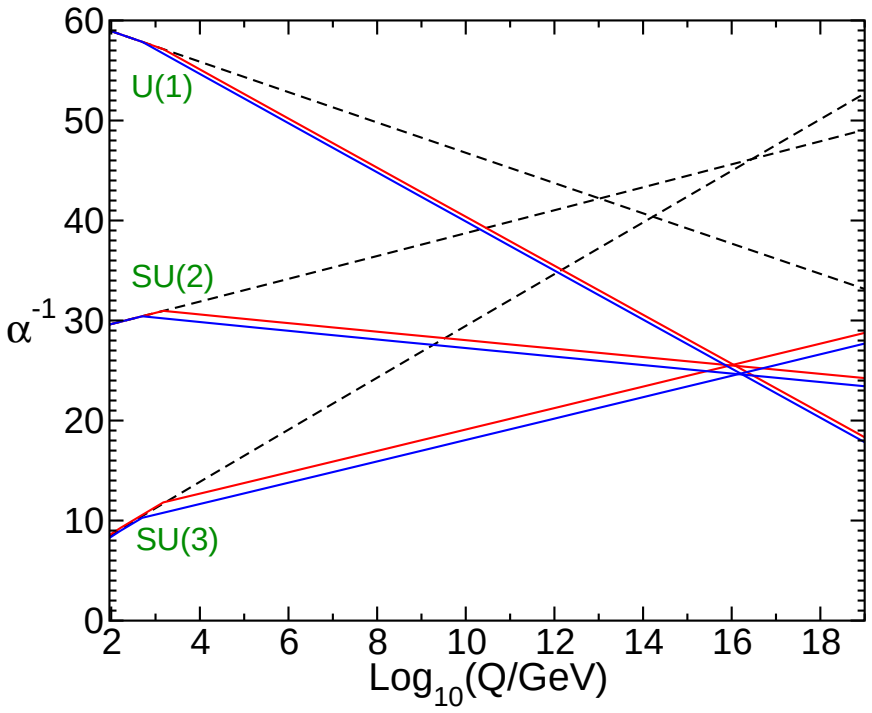

Figure 1.1: The running of coupling constants in the SM (dashed lines) and in the MSSM (solid lines) [2]. The unification of forces is a motivation for a theory such as SUSY. The difference between red and blue lines in the MSSM case is related to the values of MSSM particles, which are varied between 500 GeV and 1.5 TeV.

symmetry is broken, and the two forces manifest separately. Therefore, each generation of experiments is designed to probe higher and higher energy interactions, with the hope of discovering new force unifications. Many physicists hold to the idea of a Grand Unified Theory (GUT) that successfully describes all of physics with one symmetry at some unification scale, usually the Planck scale.

The SM has proved itself to be a magnificently successful description of the natural phenomena observable at energies probed thus far. Indeed, given the 2012 discovery of a SM Higgs-like boson [3, 4], the SM continues its winning streak. Despite its overwhelming success, however, the SM has yet to provide adequate solutions to several burning questions about the universe and its fundamental state. For example, what is the source of dark matter? And how is gravity incorporated into the framework as a quantum theory? Are the various couplings of the SM unified at higher energies; if so, how? Slightly more subtle is the question of the Higgs mass stability, an issue often referred to as the *hierarchy problem*: how is the mass of the Higgs kept so low, considering its virtual corrections due to couplings with the fermions of the SM?

Supersymmetry [5–13] (SUSY) is a framework constructed to answer many of these

questions, and is the topic of many searches for physics beyond the SM in ongoing experiments. The minimal supersymmetric extension to the SM is called the MSSM, and it predicts a new spectrum of particles that mirror the already known SM particles. SUSY can provide viable candidates for dark matter, and its particle content provides the possibility for a striking unification of the electromagnetic, weak, and strong forces. The solid lines in Figure 1.1 demonstrate this idea. Also, by introducing a scalar (spin-0) particle for each fermion, SUSY can stabilize the Higgs mass, solving the hierarchy problem. Thus, it is a well-motivated extension to the SM. Given there has been no scalar partner for the electron observed, we know that the partners for the SM particles must be quite massive; otherwise, we would have produced them in large numbers by now in particle colliders. Therefore, we can safely say that SUSY is a broken symmetry, and this SUSY breaking is responsible for increasing the masses of the SUSY particles. Discovery of massive particles like this provide another motivation for constructing particle colliders capable of studying larger and larger energy interactions.

To this end, the Large Hadron Collider (LHC) was constructed outside Geneva, Switzerland, and began its physics program in 2010. The LHC collides two beams of protons moving at nearly the speed of light, striving to recreate conditions of the very early universe, when particles moved freely and were subject to very high energy collisions. The LHC was built with two primary goals in mind: to understand the phenomenon of electroweak symmetry breaking, which gives masses to the W and Z bosons; and, to probe physics beyond the SM. The Higgs boson discovered in 2012 provides a nice conclusion to the search for the mechanism of electroweak symmetry breaking, although the true nature of this boson are still being studied (and will continue to be for some time). Searches for new physics have so far come up with no striking signals, but the SUSY parameter space is being combed quite thoroughly. Additionally, LHC experiments have a diverse search program exploring the possibilities of large extra dimensions, heavy gauge bosons, and gravitons. The work presented herein uses data collected by the ATLAS detector, one of two general-purpose detectors along the LHC

SUSY is a challenging framework, because it requires a large number of parameters to completely define a theory. Most theoretical progressions in SUSY have focused on a few mechanisms for SUSY breaking, which help to reduce the parameter set to a manageable size. As examples of these mechanisms, minimal supergravity (mSUGRA) and gauge mediated SUSY breaking (GMSB) are very heavily studied. The work presented in this dissertation summarizes two searches for SUSY signal described by

a flavor of GMSB known as general gauge mediation, or GGM. In GGM, signatures involving Z bosons along with significant missing transverse energy are possible, which give good handles on event selection and reduction of SM backgrounds. In particular, two searches have been performed, both looking in the $Z + \text{jets} + E_{\text{T}}^{\text{miss}}$ final state, where the Z boson decays to two leptons ($Z \to \ell\ell$, where $\ell = e, \mu$). One analysis uses a fraction of the 2011 LHC dataset (approximately 1 fb^{-1}), delivered with a center-of-mass energy $\sqrt{s} = 7$ TeV. The other uses a larger dataset (about 6 fb^{-1}), collected at $\sqrt{s} = 8$ TeV in 2012. These analyses feature in depth studies of the distribution of missing energy, and present multiple methods for estimating SM backgrounds using data-driven techniques. Given no excess in data in the signal regions designed for these analyses, exclusion limits are placed on the rate of new physics, and are interpreted in a GGM framework such that a range of masses of heavy SUSY particles are excluded.

First, a brief overview of the theory of the SM and SUSY is presented in Chapter 2. Next, the LHC and ATLAS are described in Chapters 3 and 4. The details on reconstruction of particles with ATLAS is given in Chapter 5. Finally, the analysis details will be discussed in Chapters 6 and 7, and conclusions can be found in Chapter 8.

Chapter 2

The Standard Model and Supersymmetry

2.1 History and introduction

The beginning of the study of elementary particles is a somewhat tricky concept, due to the fact that musing about the fundamental units of matter and nature has been a theme since days of antiquity, with *e.g.*, the works of Democritus and other Greek atomists. However, the study of modern particle physics can be considered to have started near the end of the 19th century. As a by-product of his research with vacuum tubes in 1895, Wilhelm Röntgen discovered the phenomenon of x-rays. Not long after this, in 1897, a physicist named Joseph John Thomson was investigating cathode rays and their interaction with E and B-fields. Thomson devised an experiment that allowed for the measurement of the charge-to-mass ratio of the cathode ray particles. This signified the discovery of the electron. In 1911, Ernest Rutherford's experiments with α-particles and gold foil provided an avenue for the discovery of the proton, as the nucleus of the hydrogen atom. Niels Bohr (1914) surmised that the electrons must be held in orbits around these proton nuclei, and the Bohr model is a canonical system in quantum mechanics. As the study of nuclei progressed, Wolfgang Pauli proposed the existence of another type of elementary particle, the neutrino, to explain mysterious missing energy in beta decay observations (although this particle would not be observed experimentally until the 1950s). In 1932, James Chadwick's discovery of the neutron provided an explanation for the mass of nuclei having more mass than expected when considering only proton nuclei, and advances of particle physics were moving quickly.

Paul Dirac was a pioneer in the field of quantum field theory, fusing Einstein's special relativity with quantum mechanics into a new theory called quantum electrodynamics (QED). QED called for a new spectrum of particles, identical to the normal

positive energy states, that provided negative energy solutions to Dirac's relativistic wave equation. Alternatively, these particles could be positive energy solutions, but with the opposite charge to the particle: these new solutions became known as antiparticles. Carl Anderson discovery of the positron (*i.e.*, the positively-charged partner for the electron) in 1932 was a spectacular confirmation of the theory.

The following decades proved to be very fruitful for the development of the field. Heavier partners of the electron (e), known as the muon (μ) and tau (τ) leptons, were discovered, as was the π meson, or pion. In addition, many heavier particles were discovered that decayed into pions (*e.g.*, K^0, K^+, Λ, Σ^+, Ξ^-). Indeed, a zoo of particles was forming.

As of 1964, it was clear that these new particles could be described with patterns involving their quantum numbers, known as The Eightfold Way. However, this arrangement could be further explained with the idea that protons, neutrons, and many of these heavier particles (known as hadrons) were, in fact, *not* fundamental. Instead, these hadrons are now known to be composed of constituents, called quarks. The quark model was confirmed experimentally by the 1960s experiments in deep inelastic scattering of electrons on protons and neutrons. It was soon discovered that quarks are subject to a confinement principle, and thus are not observable as free particles. Quarks are subject to strong interactions, and can be found in bound states with (a) a $q\overline{q}$ pair (meson), or (b) a qqq triplet (baryon).

As the theory of particle physics continued to develop and the electroweak force was proposed, the searches for massive vector bosons accelerated. In 1983, the discovery of the $W^{\pm}$ and Z^0 bosons were announced by the UA1 and UA2 experiments at CERN. The W and Z have been produced in abundance in collider experiments since their discovery, and serve as standard candles for early detector calibration. In addition, they are of crucial importance to many searches. The discovery of the Higgs boson in 2012, which triumphantly confirmed the theory of electroweak symmetry breaking, hinged upon analyses involving the $H \to ZZ$ decay mode.

The spectrum of elementary particles discovered in the 20th century is described fundamentally by a theory of matter and interactions known as the Standard Model [1] (SM). The SM interactions are described by a non-Abelian Yang-Mills type gauge theory, and symmetries in this theory provide crucial insight into nature. The matter content of the SM is made of quarks and leptons. There are 6 of each type of particle. The so-called "up-type" quarks (u, c, t) carry a fractional electric charge, $+2/3$. The "down-type" quarks (d, s, b) have electric charge $-1/3$. Quarks are subject to electromagnetic, weak, and strong forces, and are fermions having $S = 1/2$. The

leptons also come in three families, corresponding to the electron, muon, and τ. Each of these charged leptons ($Q = -1$) is paired with a corresponding neutrino, $\nu_{e,\mu,\tau}$. There are four known fundamental forces: gravity[1], electromagnetism, the weak force, and the strong force. The force-carriers in the SM are known as gauge bosons, and are all spin-1 bosons. The photon (γ) is the familiar mediator of the electromagnetic interaction. The $W^{\pm}$ and Z^0 bosons facilitate weak interactions. Finally, the gluon (g) is responsible for mediating strong interactions between quarks. The neutral Higgs (h) boson is the only scalar (*i.e.*, spin-0) particle in the theory. The h is the quantum of the Higgs field, which is responsible for giving mass to the fundamental particles.

Despite its somewhat complicated organization, the SM is a very elegant and powerful description of nature. However, most physicists feel that the SM is not a complete theory of physics. Some notable shortcomings include the lack of a consistent quantum theory of gravity, as well as the instabilities in radiative corrections to the Higgs mass (known as the hierarchy problem). Additionally, there is motivation to understand the possible unification of all the gauge forces at higher energies. The unification of the weak and electromagnetic force into the so-called electroweak interaction is an example of this type of unification. Supersymmetric extensions to the SM provide solutions to these problems, and are the subject of a great deal of study in phenomenology and modern experimental particle physics. Supersymmetry is a symmetry that relates fermions to bosons, which in fact unifies forces and matter, and it predicts a new spectrum of partners to the SM particles.

2.2 The Standard Model

2.2.1 Gauge invariance

As a relativistic quantum gauge theory, the SM is expressed most concisely through its Lagrangian. The Lagrangian for the SM describes all the matter and interactions present in the theory. The dynamics of the fields in the SM arise from symmetry principles. For example, consider the Lagrangian of a free electron, a fermion:

$$\mathcal{L} = \mathrm{i}\overline{\psi}\gamma^{\mu}\partial_{\mu}\psi - m\overline{\psi}\psi. \tag{2.1}$$

[1]Although gravity is probably the most familiar force, there is no successful quantum theory for this interaction. Hereafter, gravity will be discussed minimally.

Now, this Lagrangian, which contains the kinetic and the mass term of the fermion field, is clearly invariant under a global phase transformation of the field:

$$\psi(x) \to e^{\mathrm{i}e\alpha}\psi(x). \tag{2.2}$$

However, if this transformation is not global, but instead local, so that the phase is allowed to vary with spacetime (*i.e.*, $\alpha = \alpha(x)$), then the invariance no longer holds. While the mass term is still clearly unchanged by a local gauge transformation, the kinetic term is different:

$$\mathrm{i}\overline{\psi}\gamma^\mu\partial_\mu\psi \to \mathrm{i}\overline{\psi}\gamma^\mu\left(\partial_\mu + \mathrm{i}e\partial_\mu\alpha(x)\right)\psi. \tag{2.3}$$

This problem can be remedied by introducing a new operator, known as the covariant derivative, that contains a vector potential $A_\mu(x)$. This $A_\mu(x)$ represents the electromagnetic field.

$$D_\mu = \partial_\mu + \mathrm{i}eA_\mu(x). \tag{2.4}$$

Now if, in addition to the local transformation on ψ, the vector potential transforms as

$$A_\mu(x) \to A_\mu(x) - \partial_\mu\alpha(x), \tag{2.5}$$

then the kinetic term will be invariant, as well as the mass term. To see this, replace ∂_μ with D_μ, and use the local field transformations for the fermion and vector fields, $\psi \to \psi'$ and $A \to A'$:

$$\begin{aligned}
\mathrm{i}\overline{\psi}\gamma^\mu D_\mu\psi &\to \mathrm{i}\overline{\psi}'\gamma^\mu\left(\partial_\mu + \mathrm{i}eA'_\mu(x)\right)\psi' && (2.6)\\
&= \mathrm{i}e^{-\mathrm{i}e\alpha(x)}\overline{\psi}\gamma^\mu\left(\partial_\mu\psi + \mathrm{i}e\partial_\mu\alpha(x)\psi + \mathrm{i}eA_\mu\psi - \mathrm{i}e\partial_\mu\alpha(x)\psi\right)e^{\mathrm{i}e\alpha(x)} && (2.7)\\
&= \mathrm{i}\overline{\psi}\gamma^\mu\left(\partial_\mu\psi + \mathrm{i}eA_\mu\psi\right) && (2.8)\\
&= \mathrm{i}\overline{\psi}\gamma^\mu D_\mu\psi. && (2.9)
\end{aligned}$$

Finally, in order to recover Maxwell's equations of electromagnetism, a kinetic term for the vector field must be introduced: $-\frac{1}{4}F_{\mu\nu}F^{\mu\nu}$, where $F_{\mu\nu} = \partial_\mu A_\nu - \partial_\nu A_\mu$. The complete QED Lagrangian can then be written:

$$\mathcal{L} = \mathrm{i}\overline{\psi}\gamma^\mu D_\mu\psi - m\overline{\psi}\psi - \frac{1}{4}F_{\mu\nu}F^{\mu\nu}. \tag{2.10}$$

This example demonstrates the power behind using gauge invariance as a way to derive the dynamics of the system. Indeed, imposing gauge invariance necessitates

the presence of the vector potential. When introducing the covariant derivative, the minimal coupling between the matter and vector fields became evident, via the term $-e\overline{\psi}\gamma^{\mu}A_{\mu}\psi$ in Equation 2.8. This approach is a common theme when discussing the various interactions in the SM.

In the language of group theory, the set of all phase transformations like the one in Equation 2.2 form the group $U(1)$. The SM is a non-Abelian Yang-Mills type gauge theory [14] based on the group $SU(3)_{\mathrm{C}} \times SU(2)_{\mathrm{L}} \times U(1)_{\mathrm{Y}}$. Due to electroweak symmetry breaking (EWSB), $SU(2)_{\mathrm{L}} \times U(1)_{\mathrm{Y}}$ is spontaneously broken to become $U(1)_{\mathrm{em}}$, whereas $SU(3)_{\mathrm{C}}$ is unbroken. The Lagrangian for the SM can be written as

$$\mathcal{L}_{\mathrm{SM}} = \mathcal{L}_{\mathrm{EW}} + \mathcal{L}_{\mathrm{QCD}}, \tag{2.11}$$

where the electroweak components, represented in the $SU(2)_{\mathrm{L}} \times U(1)_{\mathrm{Y}}$ gauge group, are found in $\mathcal{L}_{\mathrm{EW}}$, and the terms for $SU(3)_{\mathrm{C}}$ are found in $\mathcal{L}_{\mathrm{QCD}}$. These Lagrangian terms involve matter fields, like the electron field used above, as well as more general versions of the covariant derivative. Sections 2.2.2 and 2.2.3 will go into some more detail on these two terms, giving the relevant interactions and principles behind each.

2.2.2 Electroweak sector

The electroweak sector of the SM is described by the $SU(2)_{\mathrm{L}} \times U(1)_{\mathrm{Y}}$ symmetries [14]. All matter particles in the SM have both $U(1)$ and $SU(2)$ symmetries. The gauge invarianace of the theory under $U(1)$, as seen above, will necessitate the presence of a vector potential, denoted as B^{μ}. The non-Abelian $SU(2)$ case requires the existence of three vector fields, labeled W_i^{μ} $(i = 1, 2, 3)$, one for each generator of the $SU(2)$ transformation. In the mass basis, these three fields represent two charged and one neutral gauge boson state:

$$W^{+} = \frac{-W_1 + \mathrm{i}W_2}{\sqrt{2}} \tag{2.12}$$

$$W^{-} = \frac{-W_1 - \mathrm{i}W_2}{\sqrt{2}} \tag{2.13}$$

$$W^{0} = W_3 \tag{2.14}$$

Left- and right-handed fermion states transform differently under $SU(2)$ rotations, giving rise to multiple representations for leptons and quarks. For example, left-handed electron neutrinos and left-handed electrons are grouped together in a $SU(2)$

doublet, but right-handed electrons form singlets in $SU(2)$ space (due to there being no right-handed neutrinos). In general, left-handed (right-handed) states will form doublets (singlets) in $SU(2)$.

The charged W bosons are linear combinations of the W_1 and W_2 gauge fields, as seen in Equations 2.12 and 2.13. The B and $W_3(= W^0)$ states also combine, giving rise to the observable photon and Z boson states:

$$A_\mu = \frac{g_2 B_\mu - g_1 Y_L W_\mu^0}{\sqrt{g_2^2 + g_1^2 Y_L^2}} \tag{2.15}$$

and

$$Z_\mu = \frac{g_1 Y_L B_\mu + g_2 W_\mu^0}{\sqrt{g_2^2 + g_1^2 Y_L^2}}. \tag{2.16}$$

Here, $g_{1,2}$ are the coupling strengths for Lagrangian terms involving the $U(1)$ and $SU(2)$ gauge bosons, and Y_L is the generator for the $U(1)$ transformations (a constant).

The electroweak sector of the SM Lagrangian can be expressed as the sum of four terms,

$$\mathcal{L}_{\text{EW}} = \mathcal{L}_{\text{gauge}} + \mathcal{L}_{\text{matter}} + \mathcal{L}_{\text{Higgs}} + \mathcal{L}_{\text{Yukawa}}. \tag{2.17}$$

The latter two terms, describing the phenomenon of EWSB and mass terms for the SM fermions, will be discussed in Section 2.2.4. The first term represents kinetic terms for the gauge bosons, like $-\frac{1}{4}F_{\mu\nu}F^{\mu\nu}$ in the case of A_μ:

$$\mathcal{L}_{\text{gauge}} = -\frac{1}{4}W_{i\mu\nu}W_i^{\mu\nu} - \frac{1}{4}B_{\mu\nu}B^{\mu\nu}. \tag{2.18}$$

The second Lagrangian term contains all descriptions for fermions, including kinetic terms and interactions between the fermions and the gauge bosons. Terms like these give rise to all the known SM interactions, like Z boson decays ($Z \to e^+e^-$, $Z \to \nu\overline{\nu}$, $Z \to b\bar{b}$, for example), QED interactions like Bremsstrahlung ($e \to e\gamma$), and W decays ($W \to e^\pm\nu_e$, $W \to ud$). The matter term can be expressed with terms for the different particles in their various $SU(2)$ representations. As an example, consider the first family (also referred to as flavors, or generations):

$$\mathcal{L}_{\text{matter}} = \mathrm{i}\overline{L}\gamma^\mu D_\mu L + \mathrm{i}\overline{Q}\gamma^\mu D_\mu Q + \mathrm{i}\overline{u}_R\gamma^\mu D_\mu u_R + \mathrm{i}\overline{d}_R\gamma^\mu D_\mu d_R + \mathrm{i}\overline{e}_R\gamma^\mu D_\mu e_R, \tag{2.19}$$

where L (Q) is the doublet containing the left-handed leptons (quarks), and each covariant derivative is defined according to the matter multiplet on which it operates, with the general form $D_\mu = \partial_\mu - \mathrm{i}g_1\frac{Y_L}{2}B_\mu - \mathrm{i}g_2\frac{\tau_i}{2}W_{i\mu}$. The τ_i are the generators

associated with $SU(2)$ transformations.

2.2.3 QCD

The SM particles also have a third invariance, in addition to their properties under $U(1)$ and $SU(2)$ transformations. This third type of transformation falls under the non-Abelian $SU(3)$ group. Invariance under $SU(3)$ implies the existence of eight gauge bosons, called gluons, represented by G_a^μ, where $a = 1, 2, \ldots, 8$. The dynamics of particles with these gluons is known as quantum chromodynamics, or QCD. As the name implies, the internal charge associated with rotations in $SU(3)$ is known as a color charge. The fermions associated with QCD are the quarks, and each quark carries a certain color charge. This color charge is the strength of coupling under the color force, also known as the strong force. As discussed above, quarks are not observable as free particles, but instead combine to form mesons and baryons. These mesons and baryons are color-neutral.

The QCD terms in the SM Lagrangian are of the form [14]

$$\mathcal{L}_{\text{QCD}} = -\frac{1}{4} G_{a\mu\nu} G_a^{\mu\nu} + \sum_{i=\text{flavors}} \overline{q}_i (\mathrm{i}\gamma^\mu D_\mu - m_i) q_i, \tag{2.20}$$

where

$$G_{\mu\nu a} = \partial_\mu G_{a\nu} - \partial_\nu G_{a\mu} - g_3 f_{abc} G_{b\mu} G_{c\nu} \quad \text{and} \quad D_\mu = \partial_\mu + \mathrm{i} g_3 \frac{\lambda_a}{2} G_{a\mu},$$

and the q_i is a $SU(3)_{\text{C}}$ triplet of quarks of flavor i. The field strength, $G_{\mu\nu a}$, is constructed similarly to the field strength in the $U(1)$ case, with the additional term required for the non-Abelian nature of the $SU(3)$ group[2]. The strong force coupling, g_3, and the generators of $SU(3)$ transformations, λ_a, are clearly present in the covariant derivative. This Lagrangian provides description of the quark-gluon interactions, of the form $gq\overline{q}$, as well as the self-couplings of the gluons themselves.

2.2.4 Electroweak symmetry breaking

An unbroken symmetry in the electroweak sector predicts massless W and Z gauge bosons. However, it is well known that these particles are massive, and thus the

[2]Note that the gauge fields used in $SU(2)$ have a similar construction for the field strength used in Equation 2.18.

symmetry is broken. To account for this spontaneous symmetry breaking, theorists in the 1960s proposed an idea, known as the Higgs mechanism, based on the assumption that the universe is filled with a scalar field [15–20]. This Higgs field, ϕ, is a complex doublet in $SU(2)$ space, and carries non-zero $U(1)$ charge and zero $SU(3)$ charge. The electroweak gauge bosons and fermions can interact with this field, and it is this interaction that is responsible for their masses. An important feature of this field is that it is not orthogonal to the vacuum, giving rise to non-zero expectation values for the $SU(2)$ and $U(1)$ quantum numbers, *i.e.*, these symmetries are broken. The Lagrangian for the scalar field is written with a kinetic term and two potential terms, one quadratic and one quartic in ϕ:

$$\mathcal{L}_{\text{Higgs}} = |D_\mu \phi|^2 + \mu^2 \phi^\dagger \phi - \lambda \left(\phi^\dagger \phi\right)^2 . \tag{2.21}$$

To consider the vacuum, the potential energy should be taken at its minimum. Minimizing the potential terms in $\mathcal{L}_{\text{Higgs}}$, taking $\mu^2 < 0$, a set of solutions presents itself. By choosing the "direction" of the Higgs field arbitrarily, the field acquires a vacuum expectation value, or VEV. This maneuver breaks the $SU(2) \times U(1)$ symmetry, and expanding the Higgs field around its VEV in fact gives rise to terms in the Lagrangian representing the masses of the W and Z bosons. In addition, coupling terms between the Higgs and gauge bosons, hWW, hZZ, $hhWW$, and $hhZZ$, are produced in the process.

Also, introducing Yukawa couplings between the scalar Higgs field and the spin-1/2 matter fields,

$$\mathcal{L}_{\text{Yukawa}} = \sum_{\text{generations}} \left[-\lambda_e \overline{L} \phi e_R - \lambda_d \overline{Q} \phi d_R - \lambda_u \epsilon^{ab} \overline{Q}_a \phi_b^\dagger u_R + \text{h.c.} \right], \tag{2.22}$$

and then expanding around the VEV of the Higgs, mass terms for the fermions can be seen, along with $hf\overline{f}$ interactions. The masses of the particles can be deduced from these terms, and are dependent upon the VEV itself.

(a) Fermionic correction (b) Scalar correction

Figure 2.1: First order corrections to the mass of the Higgs field.

2.3 Supersymmetry

2.3.1 Introduction

Given that the Higgs field couples to massive fermions in such a way as to add a term $-\lambda_f h\bar{f}f$ to the Lagrangian, one can expect Higgs mass corrections due to this coupling of the form [2]

$$\Delta m_h^2 = -\frac{|\lambda_f|^2}{8\pi^2}\Lambda_{\mathrm{UV}}^2 + \cdots , \tag{2.23}$$

where Λ_{UV} is an ultraviolet momentum cutoff imposed to regulate the loop integral. Figure 2.1a shows a Feynman diagram illustrating this correction, to first order. If $\Lambda_{\mathrm{UV}} \sim M_{\mathrm{Pl}}$ (*i.e.*, the Planck scale, where gravitational effects become important), this correction presents a serious problem to the stability of the Higgs mass [2]. Namely, this correction will be tens of orders of magnitude larger than the known mass, which is $m_h \approx 125$ GeV.

However, suppose there exists a heavy complex scalar, S, that also couples to the Higgs with a Lagrangian term $-\lambda_S |H|^2 |S|^2$. Then, the correction due to this particle (see Figure 2.1b) looks like

$$\Delta m_h^2 = \frac{|\lambda_S|}{16\pi^2}\left[\Lambda_{\mathrm{UV}}^2 - 2m_S^2 \ln\left(\frac{\Lambda_{\mathrm{UV}}^2}{m_S}\right)\cdots\right]. \tag{2.24}$$

Noting the differences in sign between the two corrections in Equations 2.23 and 2.24, it seems clear that this "hierarchy problem" can be mediated by the introduction of this new heavy scalar, and reduce the divergence from a quadratic one to a logarithmic one. This extension to the SM apparently motivates some sort of symmetry between fermions and bosons, called a supersymmetry (SUSY).

Supersymmetric transformation turn fermion states into boson states, and vice versa. Since the SUSY operator Q is fermionic, it must be spin-1/2, and as such SUSY is a spacetime symmetry. The single-particle states of a SUSY theory are represented

in chiral or gauge supermultiplets. A chiral supermultiplet contains both a SM fermion and a scalar superpartner. A gauge supermultiplet is made of a spin-1 gauge boson and a spin-1/2 superpartner. If SUSY is an unbroken symmetry, then these superpartners must have the same mass as their SM counterparts. Experimentally, we know this is not the case, otherwise the bosonic partner of the electron would have been discovered long ago. Therefore, since superpartners apparently have large masses, SUSY is a broken symmetry.

The superpartner of a given SM particle is "stepped down" in spin by 1/2. That is to say, leptons and quarks have spin-0 superpartners, and gauge bosons have spin-1/2 superpartners. The scalar partners of the quarks and leptons are known as squarks and sleptons. All the quantum numbers, like the various charges under the SM group transformations, remain the same after SUSY operations. Therefore, squarks still couple strongly, and the selectron is still negatively charged in electromagnetism. The fermionic partners of the gauge bosons are known as gauginos. There are partners for all the gauge eigenstates, with names such as gluinos, winos, and binos. Additionally, the scalar Higgs theory can be extended into a supersymmetric scenario. However, only one supermultiplet is not sufficient for the Higgs sector in SUSY, due to details with gauge anomalies. Thus, there are two supermultiplets, separating the Higgs into components for coupling up-type quarks and down-type quarks. The scalar Higgs fields are known as H_u and H_d, and each has a superpartner known as a higgsino. This particle content is sufficient to define the minimal supersymmetric extension to the SM, or MSSM [21–25]. Due to effects of EWSB, electroweak gauginos mix with higgsinos. The combinations of these gauge eigenstates in the mass basis are known as neutralinos and charginos. At the LHC, searches for strongly-produced superpartners (gluinos, squarks) and these weakly coupled neutralinos and charginos are a major analysis theme.

A new discrete symmetry that is introduced in SUSY is known as R-parity [2]. The value of R-parity for a particle depends on its baryon number (B), lepton number (L), and its spin (s):

$$P_R = (-1)^{3(B-L)+2s} \tag{2.25}$$

R-parity odd particles are known as supersymmetric particles, or sparticles, and are denoted with a tilde ($\tilde{}$). In theories with R-parity conservation, then no particles with different values of P_R can mix, and every interaction must involve an even number of sparticles. This gives rise to two important experimental features:

- The lightest $P_R = -1$ particle is known as the lightest supersymmetric particle,

Names	Spin	P_R	Gauge Eigenstates	Mass Eigenstates
Higgs bosons	0	$+1$	$H_u^0\ H_d^0\ H_u^+\ H_d^-$	$h^0\ H^0\ A^0\ H^\pm$
squarks	0	-1	$\widetilde{u}_L\ \widetilde{u}_R\ \widetilde{d}_L\ \widetilde{d}_R$ $\widetilde{s}_L\ \widetilde{s}_R\ \widetilde{c}_L\ \widetilde{c}_R$ $\widetilde{t}_L\ \widetilde{t}_R\ \widetilde{b}_L\ \widetilde{b}_R$	(same) (same) $\widetilde{t}_1\ \widetilde{t}_2\ \widetilde{b}_1\ \widetilde{b}_2$
sleptons	0	-1	$\widetilde{e}_L\ \widetilde{e}_R\ \widetilde{\nu}_e$ $\widetilde{\mu}_L\ \widetilde{\mu}_R\ \widetilde{\nu}_\mu$ $\widetilde{\tau}_L\ \widetilde{\tau}_R\ \widetilde{\nu}_\tau$	(same) (same) $\widetilde{\tau}_1\ \widetilde{\tau}_2\ \widetilde{\nu}_\tau$
neutralinos	1/2	-1	$\widetilde{B}^0\ \widetilde{W}^0\ \widetilde{H}_u^0\ \widetilde{H}_d^0$	$\widetilde{\chi}_1^0\ \widetilde{\chi}_2^0\ \widetilde{\chi}_3^0\ \widetilde{\chi}_4^0$
charginos	1/2	-1	$\widetilde{W}^\pm\ \widetilde{H}_u^+\ \widetilde{H}_d^-$	$\widetilde{\chi}_1^\pm\ \widetilde{\chi}_2^\pm$
gluino	1/2	-1	$\widetilde{g}$	(same)

Table 2.1: The particle content of the MSSM.

or LSP. The heavier sparticles must decay eventually into an odd number of LSPs (usually one). If the LSP is electrically neutral, then it only interacts weakly and can escape conventional methods of detection. Thus, the LSP in SUSY theories provides a viable candidate for cold dark matter [26, 27].

- Sparticles produced in collisions of SM particles are made in pairs. In collisions at a hadron collider like the LHC, strongly-produced sparticles are expected to be produced at a much higher rate than electroweak sparticles.

Table 2.1 shows the particle content of the MSSM, along with the spin and R-parity properties of these states. The discussion of SUSY breaking, which provides insight into the phenomenology of various models of the theory, is contained in the next section.

2.3.2 Gauge mediated supersymmetry breaking

In gauge mediated SUSY breaking (GMSB) models [28] SUSY is broken in a hidden sector and the effects of SUSY breaking are propagated to the visible sector via the $SU(3)_C \times SU(2)_L \times U(1)_Y$ gauge boson and gaugino interactions of some new chiral supermultiplets, called messengers, and the MSSM particles. The main advantage of GMSB models relative to minimal supergravity (mSUGRA) and anomaly mediated SUSY breaking (AMSB) models is the automatic feature that scalars with the same gauge quantum numbers, but different flavors, have identical soft SUSY breaking

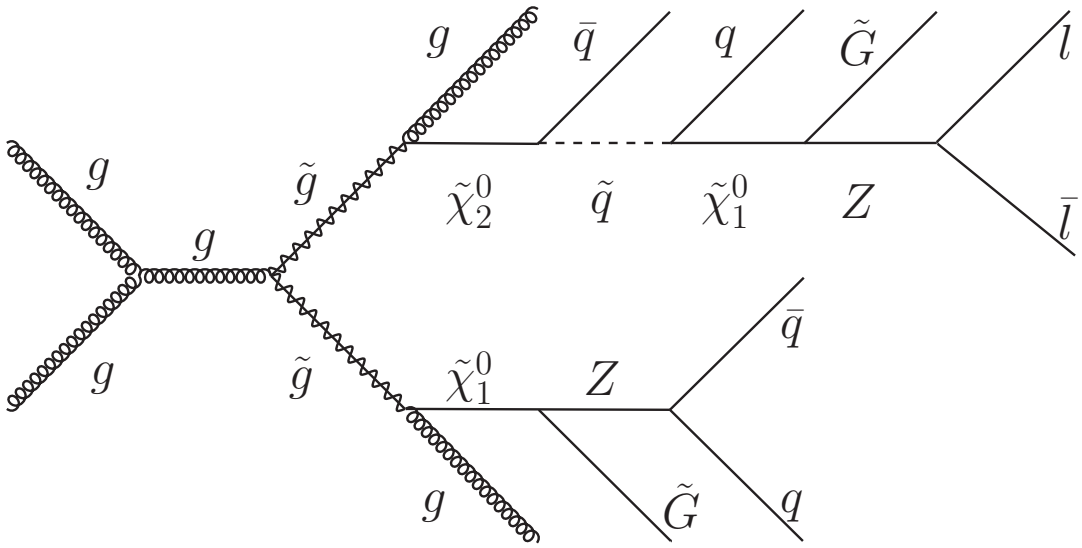

Figure 2.2: One example process with production of higgsino NLSP's. Here, two gluinos are pair produced, and each one decays to higgsino-like neutralinos directly or in cascade. The gravitinos carry missing energy, so that the signature is $Z(\ell\ell)$ + jets + $E_{\mathrm{T}}^{\mathrm{miss}}$.

masses; therefore, there is no problem with flavor changing neutral currents (FCNC) or CP violation constraints.

In GMSB the gravitino ($\tilde{G}$) is the LSP (in general $\mathrm{M}(\tilde{G}) \ll 1\,\mathrm{keV}$). The $\tilde{G}$ has a coupling to each particle and its superpartner with an interaction strength inversely proportional to $\sqrt{F}$, where F is a vacuum expectation value of an auxiliary field which determines the magnitude of SUSY breaking in the vacuum state. Because of this coupling, the next-to-lightest supersymmetric particle (NLSP) is unstable and decays to its lighter partner through gravitino emission. As a result, the nature of the NLSP defines the phenomenology of the GMSB model. Depending on the region in parameter space, either the lightest neutralino, $\tilde{\chi}_1^0$, or the lightest stau, $\tilde{\tau}$, arises as the NLSP. Its decay length, which depends on $\sqrt{F}$, can be divided into three ranges. The NLSP can decay (1) promptly, (2) inside the detector away from the collision point ($\sqrt{F} \lesssim 10^6\,\mathrm{GeV}$), or (3) outside the detector ($\sqrt{F} > 10^6\,\mathrm{GeV}$). In the analyses presented in later chapters, only promptly decaying ($c\tau < 0.1\,\mathrm{mm}$) $\tilde{\chi}_1^0$ NLSP models are considered.

Neutralinos are mixtures of gaugino ($\tilde{B}$, $\tilde{W}^0$) and higgsino ($\tilde{H}_u^0$, $\tilde{H}_d^0$) eigenstates, and therefore the lightest neutralino decays to either a γ, Z or Higgs boson, h. If the $\tilde{\chi}_1^0$ is bino-like, it mainly decays as $\tilde{\chi}_1^0 \to \gamma\tilde{G}$, leading to the signature of $\gamma\gamma + E_{\mathrm{T}}^{\mathrm{miss}}$.

If the $\tilde{\chi}_1^0$ is higgsino-like, it decays as $\tilde{\chi}_1^0 \to h\tilde{G}$. In addition, since the longitudinal component of the Z boson mixes with the Goldstone mode of the Higgs field, a higgsino-like neutralino also can decay as $\tilde{\chi}_1^0 \to Z\tilde{G}$. Due to a strong phase-space suppression of the h and Z final states, decays to photons can also be important for higgsino-like neutralinos, which are not expected to be very much heavier than the Z boson. Consequently, a pair of higgsino-like neutralinos produced in a collider can give rise to the di-boson final states $(hh, h\gamma, hZ, Z\gamma, ZZ) + E_{\mathrm{T}}^{\mathrm{miss}}$. Two scenarios are considered in this work. The Z-rich case of higgsino-like neutralino NLSPs, where $BR(\tilde{\chi}_1^0 \to H\tilde{G})$ is negligible, is the first. In this scenario both neutralinos decay as $\tilde{\chi}_1^0 \to Z\tilde{G}$, leading to the final state $ZZ + E_{\mathrm{T}}^{\mathrm{miss}}$ (see Figure 2.2). Due to the low branching ratio of Z to leptons, the four lepton final state has a low acceptance times branching ratio. Therefore, the final state that includes at least one Z boson which decays to a pair of electrons or muons is considered here. The same final state is expected in the other considered scenario, when the $BR(\tilde{\chi}_1^0 \to h\tilde{G})$ is not negligible. This leads to the $Zh + E_{\mathrm{T}}^{\mathrm{miss}}$ final state and can be observed with a $Z(\ell\ell) + E_{\mathrm{T}}^{\mathrm{miss}}$ search.

The simplified GMSB scenario considered most in the literature is known as minimal GMSB. The couplings and masses of the sparticles in the observable sector are determined by the following parameters:

$$\Lambda, M, N_5, \tan\beta, \mathrm{sign}(\mu), C_{\mathrm{grav}}. \tag{2.26}$$

Here, $\Lambda = F/M$ is the SUSY breaking energy scale, and M is the size of the messenger mass scale, $M > \Lambda$. For electroweak scale superpartners, Λ is ~ 100 TeV$/\sqrt{N_5}$. N_5 is the number of generations of the messenger fields. $\tan\beta$ is the ratio of the MSSM Higgs vacuum expectation values ($\langle H_u^0 \rangle / \langle H_d^0 \rangle$). sign($\mu$) is the sign of the higgsino mass parameter, the absolute value of which is set by electroweak symmetry breaking (EWSB) radiative corrections:

$$\mu^2 = -\frac{M_Z^2}{2} + \frac{M_{H_u}^2 - M_{H_d}^2 \tan^2(\beta)}{\tan^2(\beta) - 1} \tag{2.27}$$

Finally, C_{grav} is the ratio of the messenger sector SUSY breaking order parameter to the intrinsic SUSY breaking order parameter, which controls the coupling of the gravitino.

2.3.3 General Gauge Mediation

In recent years, the effort to formulate GMSB in a model-independent way has led to the development of General Gauge Mediation (GGM) [29, 30]. GGM includes an observable sector with all the MSSM fields, a hidden sector which contains the source of SUSY breaking at a scale M, and messengers (if there are any). In GGM the gauge fields of the MSSM can couple to the hidden sector and communicate SUSY breaking directly. Furthermore, there is no hierarchy between colored and uncolored states and thus there is no theoretical constraint on how light the colored states can be. Removing this constraint raises the possibility of GGM discovery even with early LHC data.

The GGM benchmark parameter space is described by the higgsino mass parameter (μ), the gluino mass ($m_{\tilde{g}}$), the $U(1)$ and $SU(2)$ gaugino mass parameters (M_1 and M_2), the NLSP decay length ($c\tau_{\mathrm{NLSP}}$), and $\tan\beta$.

Searches for the higgsino–like $\tilde{\chi}_1^0$ GGM SUSY models, suggested in [31, 32], were performed for this work. In these models, the gluino mass ($m(\tilde{g})$) and the higgsino mass parameter (μ) are treated as free parameters. The higgsino mass parameter was chosen to be positive to ensure $\tilde{\chi}_1^0 \to Z\tilde{G}$ is the dominant NLSP decay. The $U(1)$ and $SU(2)$ gaugino mass parameters (M_1 and M_2) are fixed to 1 TeV. All other sparticle masses are fixed at ∼1.5 TeV, which leads to gluino pair production via strong interactions being the dominant production mode. The gluinos then cascade-decay into final states involving the NLSP $\tilde{\chi}_1^0$ and jets. In this particular region of parameter space, the two lightest neutralinos ($\tilde{\chi}_1^0$ and $\tilde{\chi}_2^0$) and lightest chargino ($\tilde{\chi}_1^\pm$) become higgsino-like. In the limit $(M_1,\ M_2) \to \infty$, the exact relations $m(\tilde{\chi}_1^0) = m(\tilde{\chi}_2^0) = m(\tilde{\chi}_1^\pm) = \mu$ hold true. In practice, M_1 and M_2 are never infinite, and therefore the effect of neutralino and chargino mixing will push the masses of $\tilde{\chi}_1^0$, $\tilde{\chi}_2^0$ and $\tilde{\chi}_1^\pm$ away from μ. Two different values of $\tan\beta$ were selected in this analysis. A $\tan\beta$ value of 1.5 was chosen to ensure $\tilde{\chi}_1^0 \to Z\tilde{G}$ is the dominant NLSP decay ($BR(\tilde{\chi}_1^0 \to Z\tilde{G}) \sim 97\%$) [31]. Since larger values of $\tan\beta$ increase the $BR(\tilde{\chi}_1^0 \to h\tilde{G})$ up to 40%, a $\tan\beta$ value of 30 was chosen to investigate models with mixture of $\tilde{\chi}_1^0 \to Z\tilde{G}$ and $\tilde{\chi}_1^0 \to h\tilde{G}$ final states. Finally, the NLSP decay length is fixed to be $c\tau_{\mathrm{NLSP}} < 0.1\,\mathrm{mm}$.

Chapter 3

The Large Hadron Collider

The Large Hadron Collider (LHC) [33] is a circular accelerator constructed in the tunnel that used to house the CERN Large Electron-Positron (LEP) accelerator. At a depth of 100 meters, the tunnel has a circumference of 26.7 kilometers, and runs under both France and Switzerland, just west of Geneva. The LHC consists of two particle beams moving in opposite directions, each beam containing some bunches of protons arranged in "buckets." At several points along the ring, by steering these beams such that they are nearly head-on, the LHC delivers pp collision data at the highest luminosities yet achieved in a hadron collider. The LHC was designed to accelerate each proton beam to an energy of 7 TeV, resulting in a center-of-mass (CM) energy of 14 TeV. Since the beginning of data taking in 2009, however, CM energies of only 7-8 TeV have been achieved, due to limitations in the apparatus. Energies this high require large magnetic fields in order to bend the protons, and thus the LHC makes extensive use of superconducting magnets in order to accomplish its goals. Construction of the accelerator commenced in 2000 and was finalized in 2009 [1].

3.1 Luminosity goals

The principal goal of the LHC is to provide an avenue for discovery of physics beyond the SM. The relationship that describes the number of events expected for a given physics process at the LHC is

$$N_{\text{event}} = \sigma_{\text{process}} \times \int \mathcal{L}_{\text{inst}}(t)dt = \sigma_{\text{process}} \times \mathcal{L}_{\text{int}}, \tag{3.1}$$

where N_{event} is the expected number of events, σ_{event} is the total theoretical cross

[1] In spite of completing construction and beginning beam commissioning in 2008, extensive damage to the LHC due to an unexpected magnet quench in September 2008 [34] delayed further commissioning for a year, and thus no stable data-taking occured until March 2010.

section for the process corresponding to these events, and $\mathcal{L}_{\text{int}}$ is the total integrated machine luminosity of the incoming proton beams. Given that most new physics is characterized by small cross sections in comparison to SM processes, it is paramount that the LHC maximize its delivered luminosity. The integrated luminosity is computed by integrating with respect to time the instantaneous LHC luminosity, which is a function solely of machine parameters. The instantaneous luminosity is given by

$$\mathcal{L}_{\text{inst}} = \frac{N_{b,1} N_{b,2} n_b f_{\text{rev}} \gamma_r}{4\pi \varepsilon_n \beta^*} \left(1 + \left(\frac{\theta_c \sigma_z}{2\sigma^*}\right)^2\right)^{-1/2}, \tag{3.2}$$

where $N_{b,1}$ ($N_{b,2}$) is the number of protons per bunch in beam 1 (beam 2), n_b is the number of colliding bunches at the interaction point, f_{rev} is the revolution frequency of the beams, and γ_r is the relativistic gamma factor. ε_n is the normalized beam emittance in the transverse plane, and β^* is the beta factor at the interaction point; these quantities describe how confined, or "squeezed," the beams are in both distance and momentum space. Smaller values of emittance and and β^* lead to larger values of luminosity. The final factor in Equation 3.2 represents a geometric effect introduced by the fact that the beams are not strictly anti-parallel at the moment of collision. θ_c is the crossing angle of the beams at the interaction point, σ_z is the RMS bunch length in the longitudinal direction, and σ^* is the transverse RMS beam width at the interaction point.

The LHC was designed to provide pp collisions at luminosities as high as 10^{34} cm^{-2} s^{-1}. Nominally, the LHC is designed to collide beams with 2,808 bunches, having $N_b = 10^{11}$ protons per bunch, with a 25 ns spacing between each. In 2011, the maximum achieved luminosity was 3.65×10^{33} cm^{-2} s^{-1} as measured by the ATLAS experiment. In 2012, it was 7.73×10^{33} cm^{-2} s^{-1}. For the majority of data taking in these two years, a bunch spacing of 50 ns was used.

3.2 Design

To save costs on construction, the LHC was decided to be built in the same tunnel as LEP. As such, given the space constraints in the tunnel, the LHC uses a twin-bore magnet design first proposed by Blewett in 1971 at Brookhaven [35]. Thus, the LHC follows the LEP tunnel geometry, with eight arcs and eight straight sections; see Figure 3.1. The straight sections correspond with insertions – either for experimental or utility purposes – and are approximately 528 m long. The experimental insertions

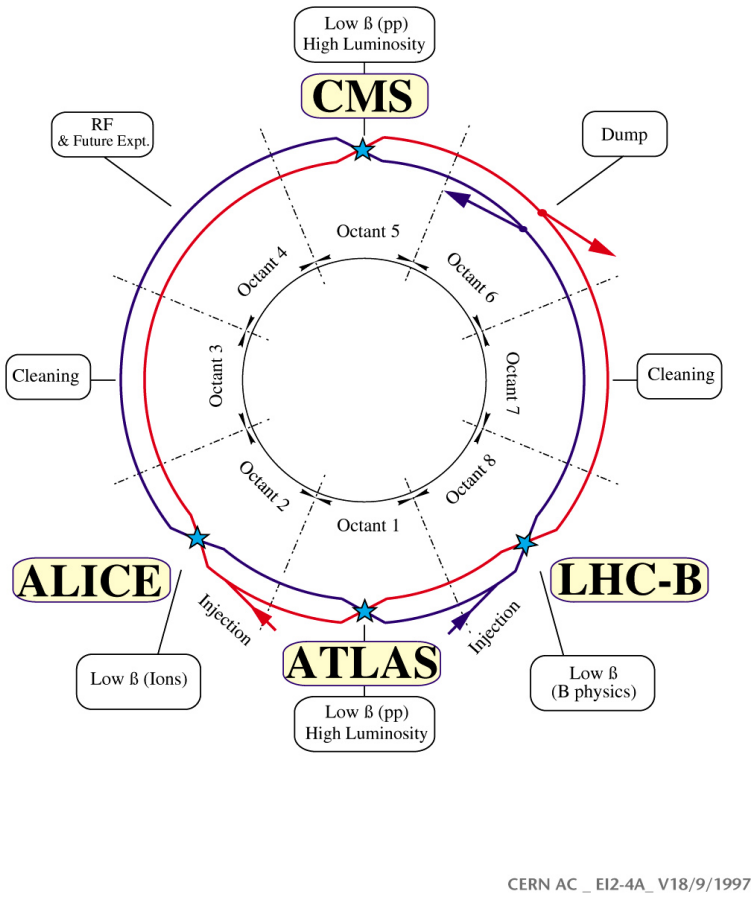

Figure 3.1: The lattice layout of the LHC. Image source: CERN.

are found at Points 1 & 5 (the ATLAS and CMS experiments, respectively), and at Points 2 & 8 (the ALICE and LHCb experiments, respectively). In addition, Points 2 & 8 include the injection systems for the LHC beams. Point 4 is home to the RF systems for each of the LHC beams, and the beam dumping machinery is located at Point 6. Arcs are composed of 23 "arc cells," which are approximately 107 m in length. Each half cell is made up of a long cold mass, a short straight section assembly, and three long dipole magnets. The LHC design was optimized in order to minimize the number of interconnections between magnets, and to provide the smallest possible beam envelope.

The LHC makes use of NbTi Rutherford superconducting cable technology to reach currents large enough to generate ~ 8 T magnetic fields. Previous accelerators also made use of superconducting magnets (FNAL's Tevatron [36], DESY's HERA [37],

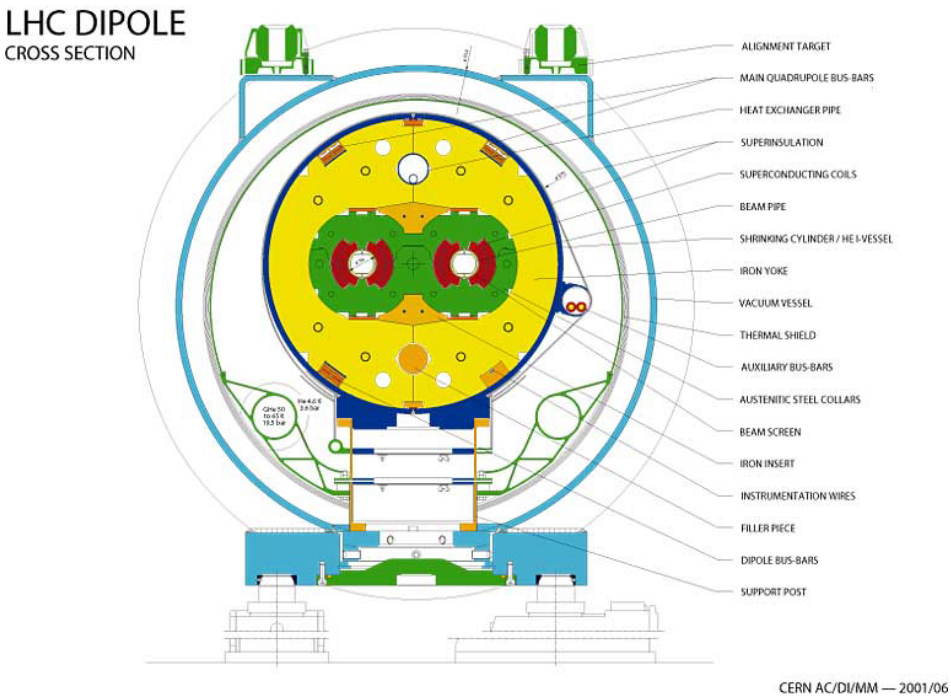

Figure 3.2: A cross section of a LHC dipole and its cold mass [33].

and BNL's RHIC [38]), with fields of about 5 T. Using superfluid helium, the LHC cools its magnet system to temperatures below 2 K. More details about the cables used in the LHC magnets can be found in Ref. [33].

The LHC employs 1,232 dipole magnets to bend the trajectories of the proton beams. Figure 3.2 shows a cross sectional view of an LHC dipole and its cryostat. The core of this apparatus, known as a *cryodipole*, is the "dipole cold mass," containing all components that are cooled by the superfluid He. There are two 56 mm apertures in the dipole cold mass for the bore tubes, where the proton beams travel. Each cryodipole has an overall length of 16.5 m, and is curved horizontally with an angle of 5.1 mrad, which corresponds to a radius of curvature of 2,812 m at room temperature. When the proton beam is injected to the LHC, corresponding to 450 GeV energies, the cryodipole's cables are operating with currents of 763 A, producing a 0.54 T field. At nominal (7 TeV) energies, the magnets reach 11,850 A currents and 8.33 T magnetic fields.

In addition to the large number of dipole magnets, the LHC utlizes more complex field shapes in its straight sections to constrain and focus the proton beams. This is a crucial component in delivering high-luminosity pp collision data. Figure 3.3 shows a cross sectional view of an LHC quadrupole. In addition to these, sextupole and octupole magnets are used for focusing and correcting beam trajectories. The

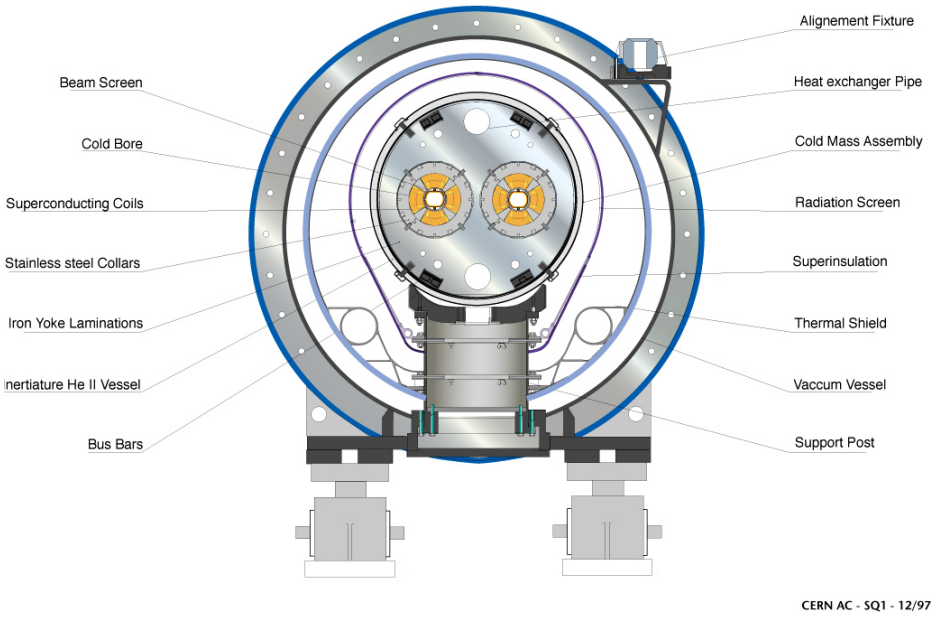

Figure 3.3: A cross section of a LHC quadrupole and its cold mass [33].

aperture size for the quadrupoles is identical to that of the dipole magnets (56 mm). At nominal LHC energies, the quadrupoles operate with currents of 11,870 A and a field gradient of 223 T/m.

3.3 Injection chain

Before injection into the main LHC tunnel, the proton beam undergoes several stages of energy and intensity changes. Figure 3.4 shows the complete LHC accelerator complex. The LHC protons are supplied by the following injection chain:

Linac2 → Proton Synchrotron Booster (PSB) → Proton Synchrotron (PS) → Super Proton Synchrotron (SPS).

Though these accelerators were already in place for previous experiments, the increased demands due to the LHC conditions (many high intensity bunches with small transverse emittances) necessitated upgrades to these components. Throughout the beam's progression up the chain, the small emittances required by the LHC must

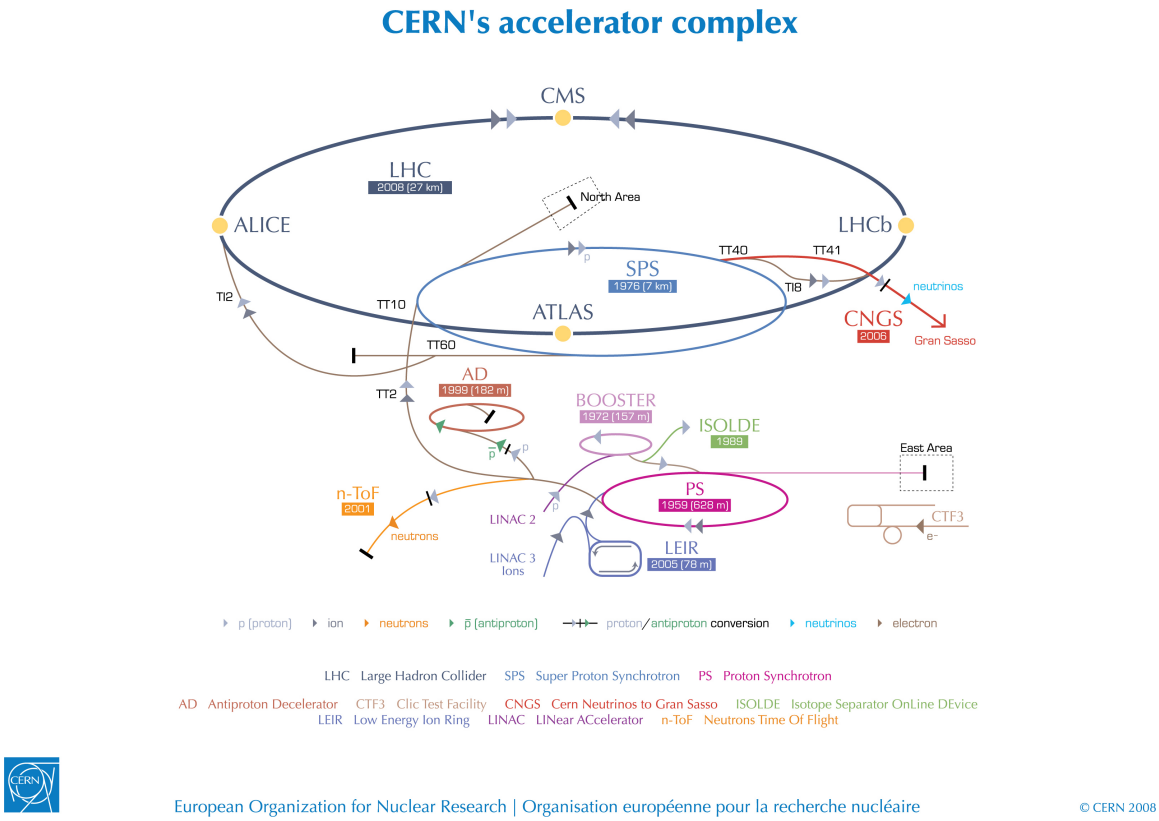

Figure 3.4: The LHC accelerator complex. Image source: CERN.

be maintained. Any small variations in the beam's steering and mismatches between the accelerators must be closely measured, and therefore the LHC complex is equipped with sophisticated high-resolution beam profile monitors.

The Linac2 has been the primary source of protons for the CERN accelerator complex for over 30 years [39, 40], and it is the only non-circular component of the LHC system (except for transfer lines). Using a Duoplasmotron and a radio-frequency quadrupole (RFQ) as a proton source, Linac2 accelerates the beam to energies of 50 MeV, and injects into the PSB. The PSB, comprised of four separate rings, acclerates the protons to energies of 1.4 GeV and ejects its bunches sequentially, providing the groundwork for bunch train generation in the PS. Here, the bunches are accelerated further, to an energy of 26 GeV, and then sent to the penultimate injection stage in the SPS. The SPS prepares the beam for final injection into the LHC beam pipe, which corresponds to a 450 GeV proton energy. At this stage, a septum dipole magnet is used to bring the injected beam closer to the circulating beam, and a fast pulsating dipole magnet, known as a *kicker* magnet, fires synchronously with the arrival of the injected bunches. This deflects the injected beam such that its trajectory matches that of the circulating beam.

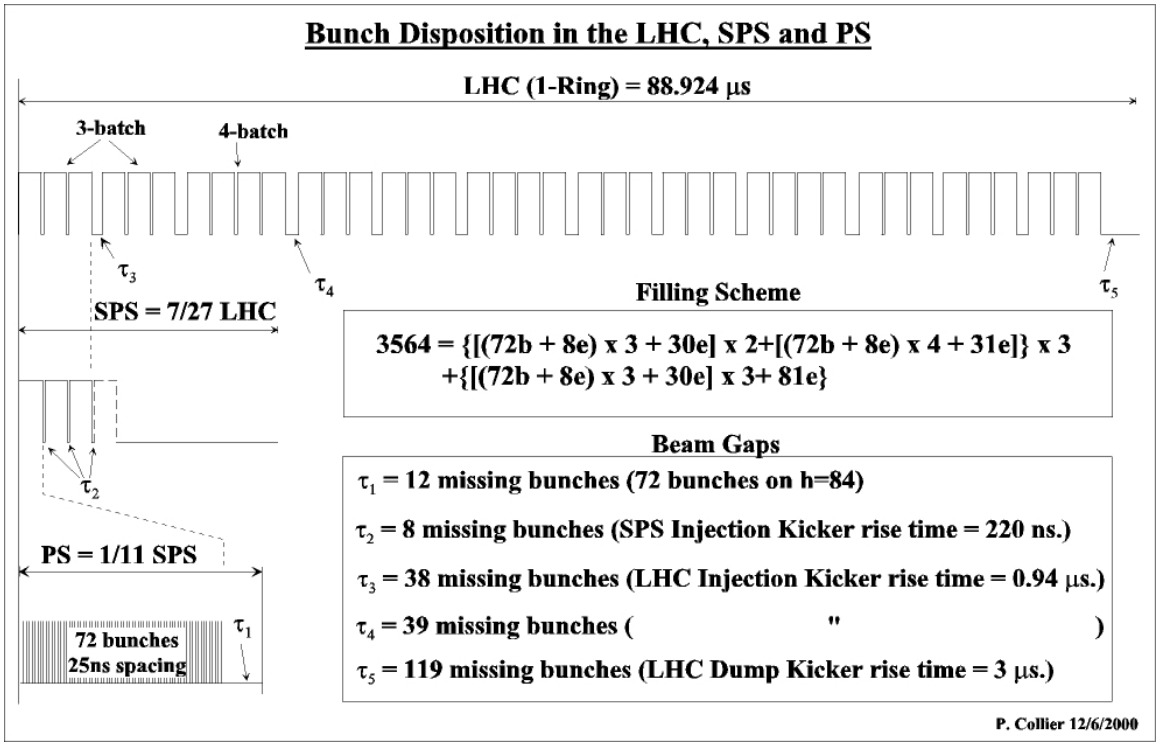

Figure 3.5: Bunch scheme for the PS-SPS-LHC injection system for a 25 ns bunch separation [41].

When transferring from the PS to the LHC, the bunch filling pattern is a crucial facet in achieving specific beam configurations. The LHC operates nominally with 2,808 circulating bunches per beam, which equates to a 25 ns gap between each. In 2011 and 2012, the LHC operated primarily with 50 ns bunch spacings, and sometimes with 75 ns separation. See Figure 3.5 for a schematic view of the bunch injection scheme for the PS-SPS-LHC chain under nominal (25 ns) beam conditions. The LHC is filled with 12 injections from the SPS [41]. The bunch train pattern in this case is written as 333 334 334 334, indicating that the SPS injects 3 batches for most of its injection cycles, but 4 batches for the 6th, 9th, and 12th cycle, totalling in 39 batches. Each batch in the SPS is comprised of 72 proton bunches from the PS. Along with the bunches are gaps, or empty bunches, that allow for the SPS and LHC kicker rise times. For 50 ns and 75 ns running, this scheme is altered to optimize the beam, yielding the highest possible number of collisions in IP1 and IP5 while accounting for the necessary changes to maintain interactions in IP2 and IP8.

3.4 Beam dump system

Having a system to extract the beam from the LHC is important for many reasons. As a physics run progresses, beam intensity drops substantially such that it is more advantageous to stop collisions in order to re-inject with new proton bunches. Also, given the destructive nature of the LHC beam, any spurious trajectories that may lead to the beam damaging detector or magnet components justify the need to have a highly reliable beam dumping system, one that is able to handle beams not characterized by normal parameters. This can result from equipment failure or incorrect optics settings in the rings.

The beam dump machinery is installed at Point 6 (see Figure 3.1). The system is composed of multiple magnet types for extraction and beam dilution, as well as absorber material for the actual dump. For each ring in the LHC, the beam dump system is comprised of: 15 extraction kicker magnets, to deflect the whole beam horizontally; 15 steel septum magnets, which provide vertical deflection to steer the beam away from the LHC cryostat; 10 dilution kicker magnets, used to sweep the beam in an 'e' motion to the absorbers; the beam dump cavern, which contains the carbon used for beam absorption and sits approximately 750 m from the septum magnets.

Given the importance of the beam extraction technology for safe and extended LHC operation, magnet redundancy and extensive post-mortem analysis are employed for the beam dump system. The beam can be safely extracted even if only 14 of the total 15 kicker magnets are operating correctly, and injection into the LHC is only possible if the previous beam dump status is satisfactory.

3.5 2011 operation

In 2011, the LHC produced pp physics collisions at $\sqrt{s} = 7$ TeV, reaching a maximum instantaneous luminosity of 3.6×10^{33} cm^{-2}s^{-1}, and delivered more integrated luminosity than expected: ~ 5.7 fb^{-1} in IP 1&5. Operation of the LHC in 2011 began 21 February and concluded 7 December. The run proceeded in several phases, separated by 5 technical stops (TS):

- **Phase I**: With intensities of ~ 200 bunches, with $N_b = 10^{11}$ p, and energies of 3.5 TeV per beam, collision data were delivered with a 75 ns bunch spacing and optics $\beta^* = 1.5$ m in IP1&5.

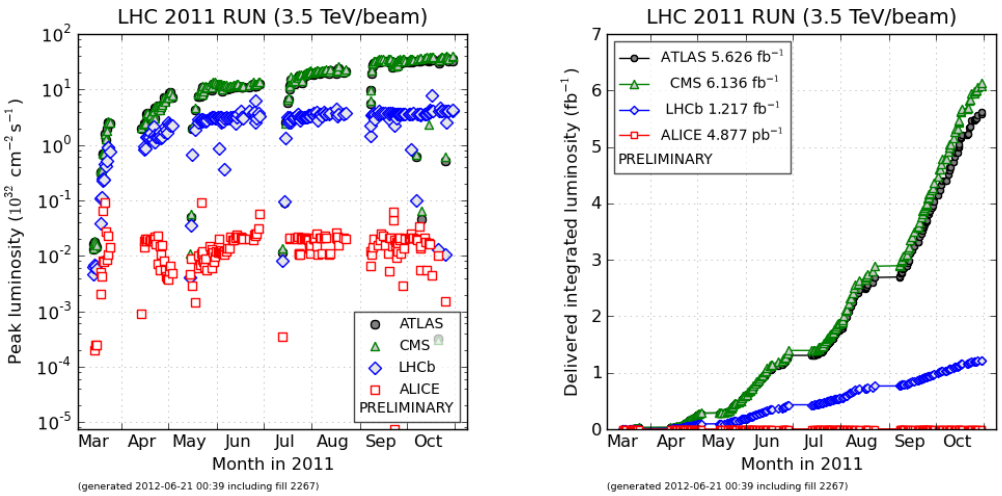

Figure 3.6: Summary of the LHC delivered luminosity for the 2011 *pp* physics run. The left (right) distribution shows delivered peak instantaneous (integrated) luminosity as a function of time.

- **Phase II**: After Technical Stop 1 (TS1), 50 ns spacing was initiated, with intensities up to $\sim$ 800 bunches per beam.
- **Phase III**: Continuation of ramping intensities, reaching 1380 bunches by TS3.
- **Phase IV**: Extended data-taking with 1380 bunches, and additional reduction of the transverse emittance from $\sim$ 2.5 to $\sim$ 2 μm.
- **Phase V**: Reduced β^* to 1 m in IP1&5, more data-taking with 1380 bunches.
- **Phase VI**: Lead ion run (Pb-Pb) from TS5 until the end of operation.

3.6 2012 operation

Before the start of the 2012 LHC run, it was clear to the community of experiments that there were a few principal goals for the year: it was imperative that the LHC deliver enough data to both ATLAS and CMS, independently, to discover or exclude the Higgs boson; preparations for the higher-energy running after the long shutdown in 2013-2014 would be crucial, in terms of machine development exercises for studying conditions related to effective high-luminosity running. To this end, the LHC initiated a four phase plan for 2012, separated by 3 technical stops:

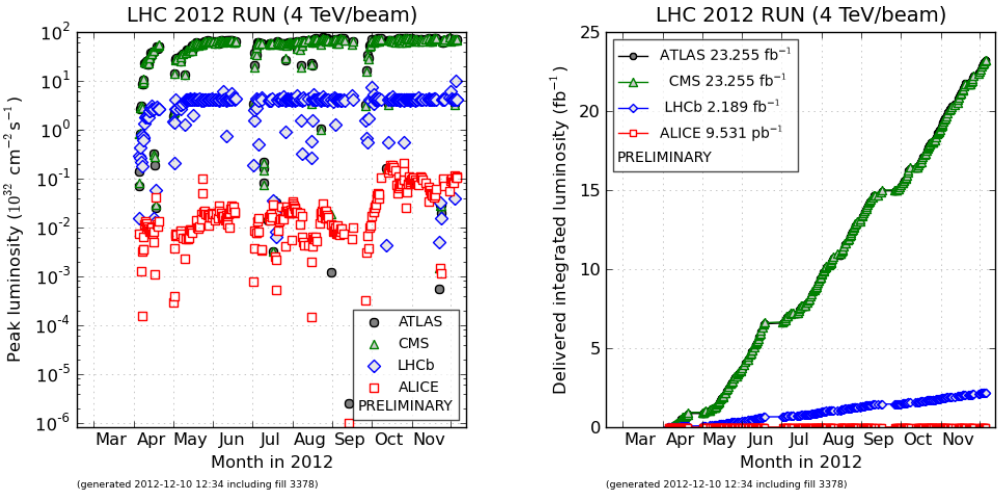

Figure 3.7: Summary of the LHC delivered luminosity for the 2012 *pp* physics run. The left (right) distribution shows delivered peak instantaneous (integrated) luminosity as a function of time.

- **Phase I**: Following the winter shutdown, small bunch numbers were injected for initial beam commissioning for 2012 running. This allowed for commissioning of a smaller $\beta^*(= 0.6$ m), after which larger bunch numbers were injected over several days, until 1380 bunches were colliding with 50 ns spacing, as in 2011.

- **Phase II-IV**: Amongst periods of machine development and technical stops, stable data-taking with 1380 bunches proceeded for much of the year.

	2011	2012
CM energy [TeV]	7	8
Peak $\mathcal{L}_{\text{inst}}$ [cm^{-2}s^{-1}]	3.6×10^{33}	7.7×10^{33}
Total $\mathcal{L}_{\text{int}}$ (ATLAS) [fb^{-1}]	5.7	21.7

Table 3.1: Summary of details for the LHC runs in 2011-2012.

Chapter 4

The ATLAS detector

The ATLAS detector [42] is one of two general purpose particle detectors along the LHC. ATLAS (A Toroidal LHC ApparatuS) is located at IP1 (see Figure 3.1), 100 m below the surface. Several subsystems comprise the detector, ranging from precision tracking in the inner detector (ID) to calorimetry and muon spectrometry, along with a solenoid magnet and a toroid system to assist with tracking charged particles. A three-level trigger system is employed.

ATLAS is constructed with a cylindrical geometry. The coordinate system used for the detector is summarized as follows:

- The nominal interaction point is defined as the origin $(x, y, z) = (0, 0, 0)$.
- The beam direction corresponds with the z axis, and thus the $x - y$ plane is transverse to the beam direction.
- Positive x is defined as pointing from the interaction point to the center of the LHC ring, and positive y is defined as the vertical direction.
- Given the symmetry in z about the origin, it is useful to define the "A side" ("C side") of the ATLAS detector as the positive (negative) z side.
- The ϕ coordinate is defined as the azimuthal angle, as is usual in cylindrical coordinates.
- The polar angle θ is defined off the z axis, with 0° corresponding to the positive z direction.

The "pseudorapidity," η, is commonly used as a proxy for θ, with the definition:

$$\eta \equiv -\ln(\tan(\theta/2)) \tag{4.1}$$

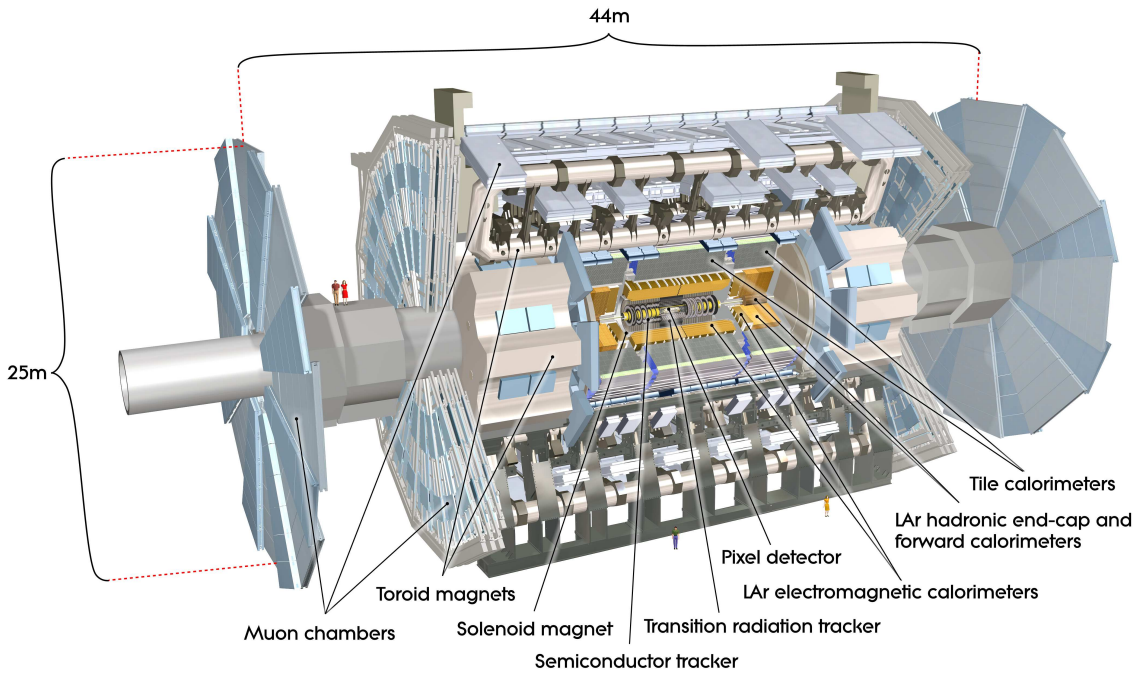

Figure 4.1: The ATLAS detector [42].

Pseudorapidity is equivalent to "rapidity" in the limit of massless particles. Rapidity, y is defined as

$$y \equiv \frac{1}{2} \ln \left(\frac{E + p_z}{E - p_z} \right), \tag{4.2}$$

and will sometimes be discussed, *e.g.*, in the case of massive objects like hadronic jets.

Transverse quantities, such as transverse energy (E_T) and transverse momentum (p_T), are used ubiquitously, as is the separation in the pseudorapidity-azimuthal space, defined as $\Delta R = \sqrt{\Delta\eta^2 + \Delta\phi^2}$.

As a general purpose detector, ATLAS was constructed to maximize its ability to detect and identify particles for a range of purposes, including precision measurements of SM processes, discovery and measurement of the Higgs boson, and discovery of new phenomena, *e.g.*, supersymmetry, large extra dimensions, or exotic gauge bosons. Given the broad physics agenda of the ATLAS detector and its analysis program, the design and construction of the various components is such that detection and identification is robust for all relevant physics objects and quantities. The innermost detector system is the high precision tracking system, surrounded by a 2 T solenoidal magnetic field. The ID is designed to have good momentum resolution and reconstruction efficiency for charged particles, and uses a combination of silicon sensor and drift tube technology based detection. A high granularity electromagnetic calorimeter system is immediately

outside of the tracking system. Liquid argon (LAr) sampling calorimetry is utilized for this system, which is responsible for good electron and photon identification and measurement. The hadronic calorimeter, which provides full-coverage detection of hadronic jets, uses a combination of scintillator tile and LAr sampling calorimetry, and is found immediately outside the EM calorimeter. The outermost system is the muon spectrometer, which defines the overall dimensions of the ATLAS detector. Good muon identification and momentum resolution (independent of the ID) over the full detector range is crucial for the ATLAS physics goals. An air-core toroid system generates strong bending power in a large volume, but provides for an open structure, to help reduce effects of multiple-scattering.

With the experimental conditions at the LHC, the proton-proton interaction rate can be as high as 1 GHz. However, due to resource and technology constraints, ATLAS can only record data at a rate of about 200 Hz. The trigger system is responsible for providing the necessary rejection of minimum-bias processes in favor of interesting events, and is comprised of three levels. The Level-1 (L1) trigger system reduces the rate to 75 kHz, and is limited by the overall readout system bandwidth. The Level-2 (L2) trigger and event filter (EF) make up what is known as the high-level trigger system, which reduces the rate to approximately 200 Hz.

The following sections will describe the various elements of the ATLAS detector in greater detail.

4.1 Magnet system

The ATLAS magnet system is a complex configuration of four superconducting magnets: one solenoid encloses the inner detector, providing bending power for charged particles coming from the interaction point (IP), and three toroids (one barrel, two endcaps) to provide bending for muons reaching the outer muon detectors. ATLAS derives its name from the unique toroidal design, which is a prominent feature of the detector. In total, the magnet system is 22 m in diameter, 26 m in length, and stores 1.6 gigajoules of energy. See Figure 4.2 for an illustration of the ATLAS magnet system. The solenoid, which is arranged concentrically to the beam, provides an axial field with 2 T strength. The toroids produce a field of 0.5 T (1 T) in the barrel (endcap) region.

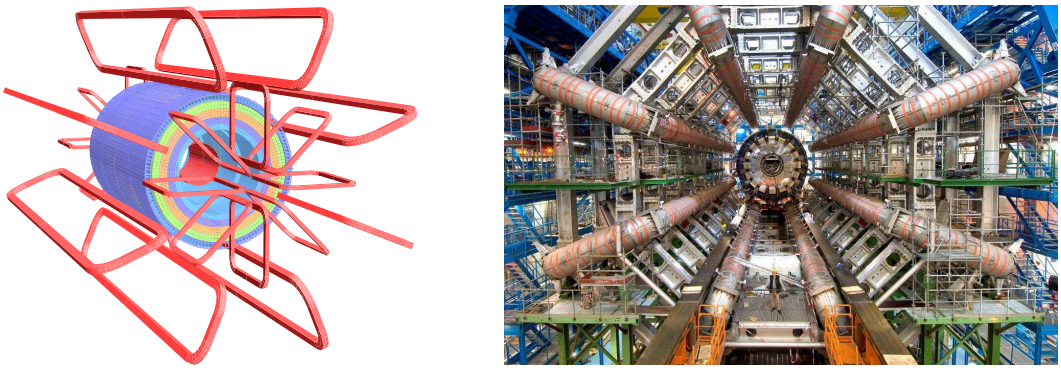

Figure 4.2: An overview of the ATLAS magnet system. Left: a schematic illustration of the ATLAS magnet system, showing the interleaved barrel and endcap toroid coils as well as the solenoid windings found inside the tile calorimeter volume, which provides a return yoke for the solenoid field. Right: The barrel toroid as installed in the ATLAS cavern. The symmetry of the coils and support structure can be clearly seen [42].

4.1.1 Solenoid

The central solenoid is constructed immediately outside the inner detector system, and uses a nominal current of 7.730 kA to produce its nearly 2 T field for bending charged particles arising from LHC collisions. To maintain calorimeter performance, the configuration of the solenoid is optimized in order to minimize the thickness of material in front of the calorimeters. The solenoid contributes approximately 0.66 radiation lengths for particles at normal incidence. A single layer of coils is used, wound with a high strength NbTi wire, stabilized by aluminum. The superconducting coil is cooled to a temperature of 4.5 K, and is housed in an aluminum support cylinder of 12 mm thickness. The inner (outer) diameter of the solenoid is 2.46 m (2.56 m), and the length of the solenoid is 5.8 m. The magnetic flux of the solenoid is returned by the steel structure in the ATLAS hadronic calorimeter (see Section 4.3.2). Under normal charging and discharging conditions, the solenoid can go from zero field to nominal in about 30 minutes. The solenoid system is housed within the same cryostat as the barrel liquid argon calorimeter.

4.1.2 Toroids

The field from the barrel toroid permeates the cylindrical volume outside the calorimeter system and the endcap toroid magnets. The barrel system is made of eight

superconducting coils that are enclosed in oblong vacuum vessels (see Figure **??**), and is 25.3 m in length. The inner diameter of the coils is 9.4 m, and the outer diameter is 20.1 m. The endcap toroids are responsible for generating the bending power for muons traversing the forward regions of the muon spectrometer, and are made of eight flat square coil units. The coils are made of aluminum-stabilized Nb/Ti/Cu conducting wire, and are cooled to 4.6 K for operation. In both the barrel and endcap toroids, the Lorentz forces on the coil present a challenge for the structure and support systems. The barrel coils are subject to approximately 1,400 tonnes (directed inwards), and each endcap unit is subject to 240 tonnes from the Lorentz force. For this reason, robust support structures are crucial to the construction of the magnet systems, and detailed studies were performed to understand the potential deformations associated with cooldown and warmup procedures.

4.2 Inner Detector

The ATLAS inner detector (ID) provides high precision tracking of charged particles with fine detector granularity. The ID was designed to provide robust pattern recognition, excellent momentum resolution, and precise primary and secondary vertex measurements out to $|\eta| < 2.5$. The ID is composed of three independent but complementary subsystems. The innermost layer is the pixel detector. The semiconductor tracker (SCT), composed of silicon strips, is the next layer. The outermost component of the ID is a drift tube detector that utilizes transition radiation to provide particle identification, known as the transition radiation detector (TRT). The entire ID system is immersed in a 2 T field provided by the ATLAS solenoid.

As the innermost detector components are subject to the most extreme radiation of any of the ATLAS subsystems, serious considerations had to be made for the design and implementation of the ID. After three years of running at the design LHC luminosity, the inner vertexing layer of the pixel detector will be replaced. Furthermore, to reduce the effects of noise after radiation damage, all the silicon sensors used must be kept at very low temperatures: -5 to -10° C. This necessitates a cooling system that must be held at approximately -25° C. The TRT, however, is designed to operate at room temperature.

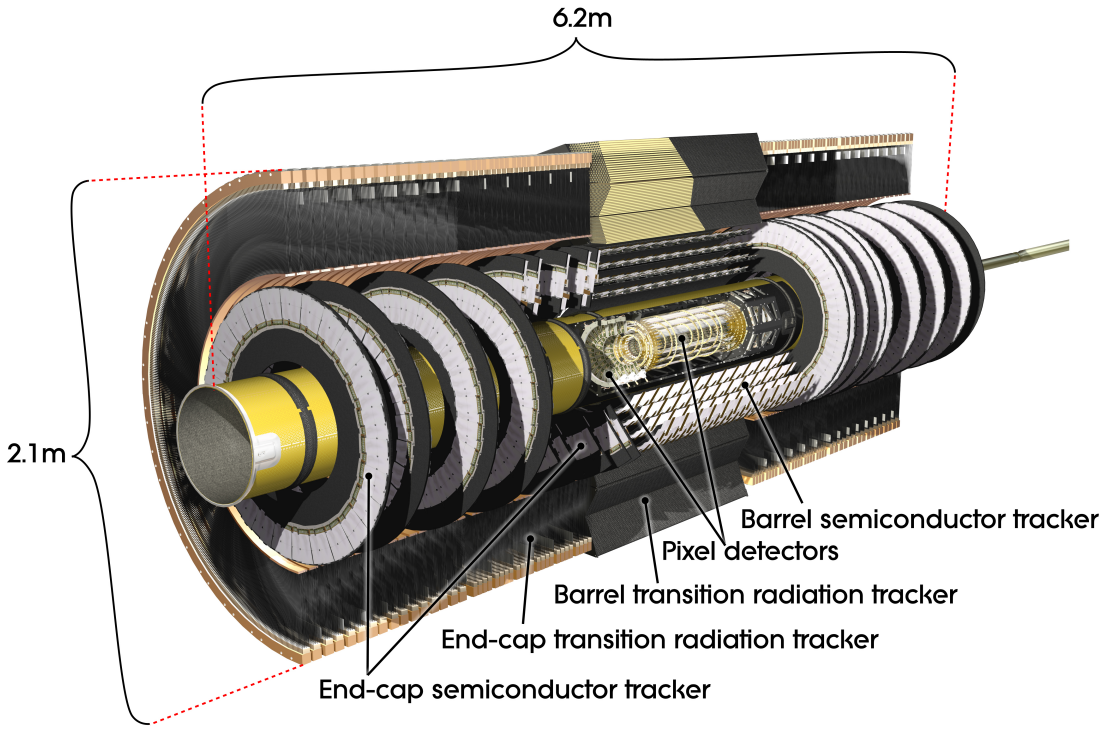

Figure 4.3: A cutaway view of the ATLAS inner detector [42].

4.2.1 Silicon pixel detector

The closest detector to the interaction point is the silicon pixel detector. Comprised of approximately 80.4 million readout channels, the pixel system provides the highest granularity of any system in ATLAS. The pixel detector is segmented in both $(R-\phi)$ and in z. The sensors used are all of the same size: $(R-\phi) \times z = 50 \times 400\ \mu\text{m}^2$. The pixels are split into two main regions: the barrel and the endcap. The pixels in the barrel are arranged in concentric cylinders around the beam axis, and in the endcap are formed into disks perpendicular to the beam axis. The intrinsic accuracies for the pixel detector in the barrel are 10 μm $(R-\phi)$ and 115 μm (z). For the endcap, the accuracies are 10 μm $(R-\phi)$ and 115 μm (R).

As a charged particle passes through a silicon detector, many electron-hole pairs are created in the depletion region as a result of ionization [43]. The depletion region is formed by creating a $p-n$ junction (*i.e.* the basic component of a semiconductor diode), and a reverse bias voltage is applied to provide an extended volume over which ionization can occur. The current caused by the electric field of the reverse bias semiconductor junction is collected by the front end electronics and processed for readout.

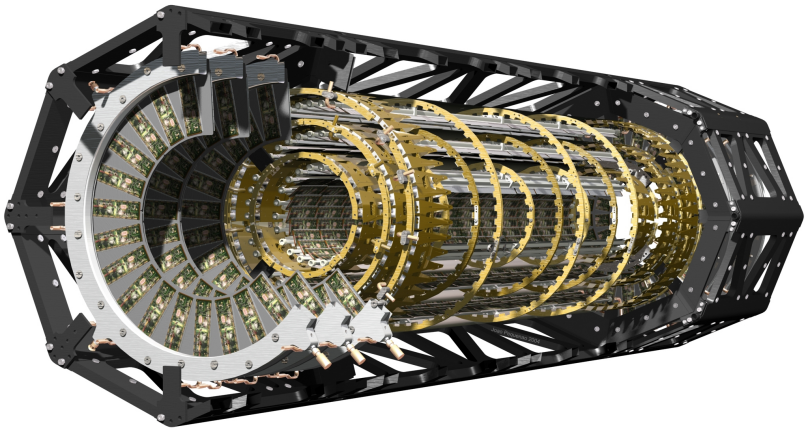

Figure 4.4: A cutaway view of the ATLAS silicon pixel detector [42].

The pixel sensors used [44] required the most leading-edge and novel technology available at the time of construction, due to the very stringent requirements for radiation hardness and resolution in the innermost layers. The silicon sensors have a thickness of 250 μm, and use a double-sided processing: oxygenated n-type wafers are combined with readout components on the n^+-implanted side of the detector modules.

In total, there are 1,744 pixel modules. The modules are arranged in a hermetic cylinder: the barrel is composed of three layers of pixel modules, and each endcap consists of three disk layers. A typical track will thus cross three layers of pixels. The length of active barrel is 801 mm, and the endcap disks have inner (outer) radii of 88.8 (149.6) mm. The total active area of silicon is approximately 1.7 m^2, with 112 barrel staves and 48 endcap sectors (eight sectors per disk).

4.2.2 Semiconductor Tracker

The semiconductor tracker, or SCT, provides a second level of silicon detection, with eight silicon microstrip layers (yielding at least four space points) crossed by a typical charged particle. The total number of readout channels is about 6.3 million. The barrel region is comprised of 40 milliradian stereo strips, which allow for measurement of both coordinates, $R-\phi$ and z. One set of strips in each layer is parallel to the beam direction. In the endcap, the SCT has one set of strips that run radially, and another set of strips at a 40 mrad angle to these. Intrinsic accuracies in the barrel are 17 μm in $R-\phi$ and 580 μm in z, and for the endcap disks 17 μm in $R-\phi$ and 580 μm in R.

The SCT is made up of a total of 15,912 silicon sensors, arranged into 4,088

modules [45]. The sensors are configured as single-sided "p-in-n" with AC-coupled readout strips. For both the barrel and the endcap, an inter-strip distance, or "pitch," of 80 μm was chosen. Each sensor is 6 cm long, and strips are formed by daisy-chaining two sensors together using a polyimide hybrid with a carbon fiber substrate [46]. Each module thus contains 4 sensors, two each on the top and bottom side. One set of sensors is rotated with respect to their hybrids, by $\pm$20 mrad about the geometrical center of the sensors. The two sensors on each side are composed of 770 microstrips of silicon, and high voltage is applied to them via a conducting base.

The 2,112 barrel modules are arranged in four coaxial cylindrical layers. These cylinders must be very stable under variations in both temperature and humidity. They are made from carbon fiber skins with $\sim$ 200 μm thickness over carbon fiber and cyanate ester honeycomb cores. The barrel modules are arranged in rows of 12, and each layer is rotated by $\pm$20 mrad, always ensuring that strips of one side are along the cylinder axis. The 1,976 endcap modules are arranged into two endcaps, each having nine disk layers. The 8.7 mm thick disks are made of carbon fiber skins (200 μm thick) with an aramid/phenolic honeycomb core, and the endcamp modules are also rotated at $\pm$20 μrad with respect to one another.

Precise aligment of the layers of SCT modules was paramount during construction at Point 1, and during operation. The SCT is thus equipped with an array of 842 interferometers to monitor real-time deformations at the few μm level. This provides access to short time scale and high spatial resolution detector deformations.

4.2.3 Transition Radiation Tracker

The third component of the ID, at larger radii, is the transition radiation tracker, or TRT. The TRT employs a combination of drift tube technology and transition radiation detection to provide high-precision momentum measurements of charged tracks in addition to allowing for robust particle identification, complementary to that of the electromagnetic calorimeter. With an average of 36 hits per track with $p_{\mathrm{T}} > 0.5$ GeV (see Figure 4.5, the TRT gives continuous tracking, which enhances the pattern recognition of the ID, and improves the momentum resolution for pseudorapidities within $|\eta| < 2.0$.

The TRT employs drift tube (or straw) detection [47] for tracking charged particles. A drift tube consists of a cylindrical cathode, with a taut anode wire in the center. The tube is filled with high-pressure gas that is ionized as a charged particle passes through. The ionizing particle creates electron-ion pairs in the gas, that drift toward

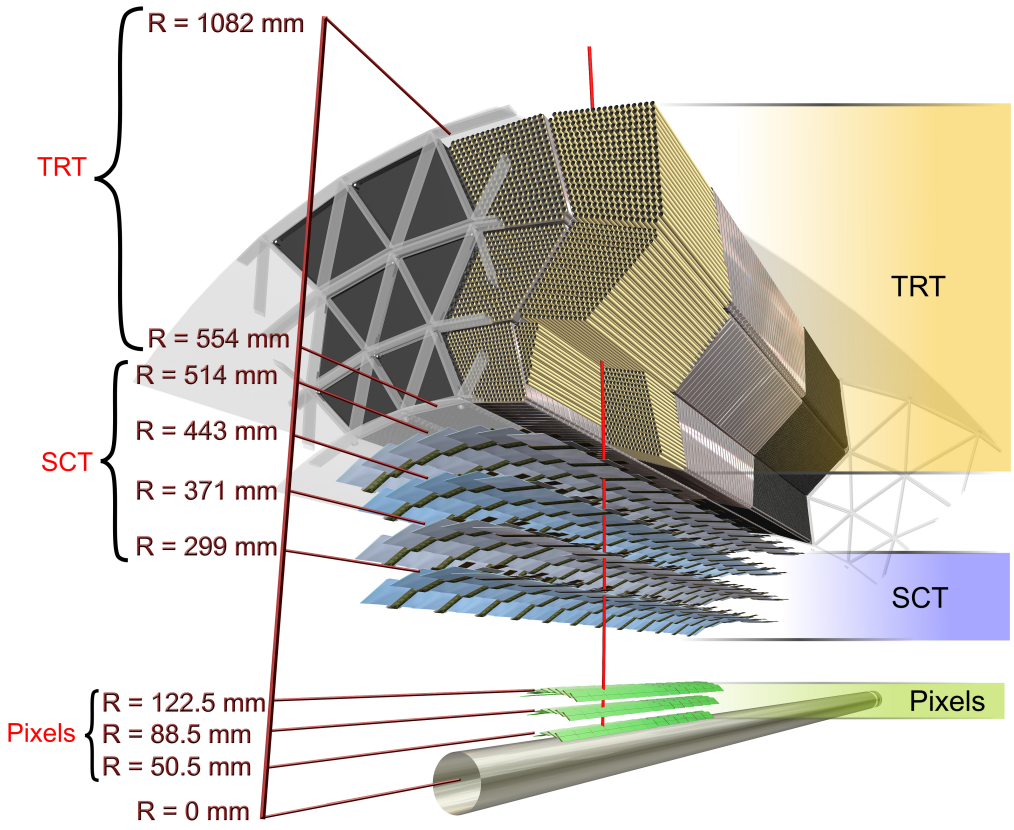

Figure 4.5: A cutaway view of the various layers of the ATLAS inner detector [42], traversed by a charged track with 10 GeV p_{T}. The track traverses the beryllium beam pipe, three cylindrical silcon pixel layers, four cylindrical double layers of silicon microstrip sensors (SCT), and about 36 straws in the TRT modules.

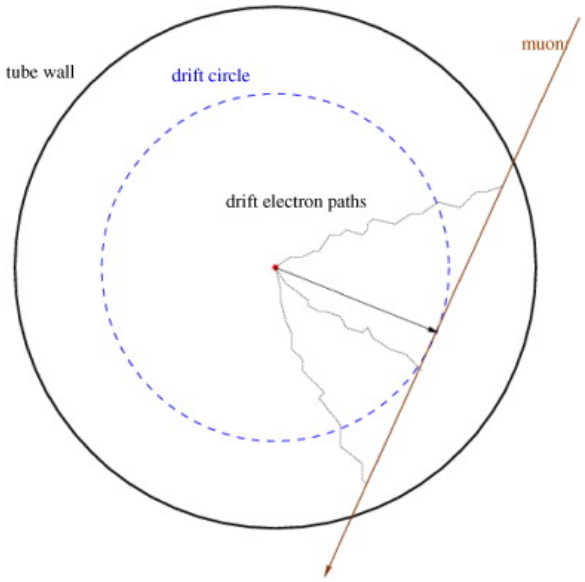

Figure 4.6: Illustration of drift tube ionization and electron drift.

the anode and cathode, respectively, due to the influence of the electric field between them. In the absence of a magnetic field, these electrons drift radially toward the anode. As they approach the anode, where the E-field is of higher magnitude, the drift electrons initiate an avalanche of more electrons, multiplying the initial charge by a large factor. This factor is known as the *gas gain*, and is dependent upon the gas composition. The electrons collected by the anode provide a signal that can be read-out by electronics for further processing.

The drift time of the primary electrons from ionization is measured by the drift tube system, and depends on many factors: the geometry of the tube, the drift gas temperature and pressure, the voltage difference between the cathode and anode, and magnetic field. To measure the drift time, Δt, the initial time and the time corresponding to the arrival of the primary electrons at the anode must be known. The initial time is measured by an external source (the trigger). The electrons that reach the anode first originate from the coordinate corresponding to the radius of closest approach between the ionizing particle and the anode wire. The distribution of all drift times will thus have a characteristic spread, with the later-arriving electrons originating from closer to the cathode (*i.e.*, the tube wall). See Figure 4.6. After measuring the electron drift times, the distance can be found knowing the drift velocity of the ionization electrons along the drift trajectory, using the so-called $R-T$ relation. Figre 4.7 shows the measured $R-T$ relation for both the TRT barrel and endcaps.

The TRT straw tubes are 4 mm in diameter, and are made of polyimide. The tube wall is of minimal thickness, made of two 35 μm thick multi-layer films that are

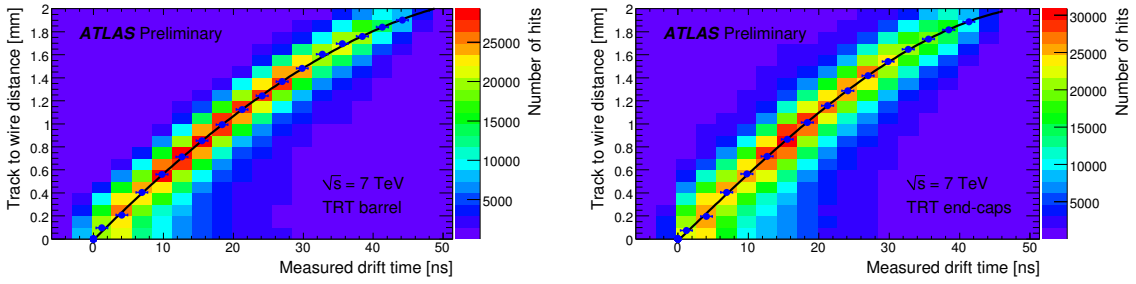

(a) (b)

Figure 4.7: These plots show the TRT *RT* dependency for the TRT (a) barrel and (b) end-caps. This relation is used to infer track to wire distance, i.e., drift radius, based on measured drift time.

bonded. The straws are stablized using carbon fibers, and are 144 cm (37 cm) in length for the barrel (endcap). The straw tubes, which serve as the cathodes, were constructed such that their resistance is $< 300\ \Omega/\text{m}$. The anode wires are made of 31 μm diameter tungsten, plated with $\sim 0.5\ \mu$m gold, and are held to a nominal tension of 70 g. These anodes are connected directly to the front-end electronics, and are kept at ground potential. The resistance of the wires is approximately 60 Ω/m. The cathodes are typically kept at a voltage of -1530 V, which gives rise to a gain factor of 2.5×10^4 for the gas mixture chosen: 70% Xe, 27% CO_2 and 3% O_2, kept at an overpressure (*i.e.,* a pressure larger than one atmosphere) of $5 - 10$ mbar. To ensure stable operation of the TRT, the gas mixture must be re-circulated regularly, and the gas quality measured continuously. To avoid contamination from leaks and other backgrounds, the straws operate in a bath of CO_2.

In the barrel, the anode wires are read out from each end, and are supported mechanically by a plastic insert glued to the inner wall of the straw, and are divided electrically by a glass capillary of 6 mm, which reduces the occupancy of the straws. As a result, however, each barrel straw is inefficient near its center, over a length of about 2 cm.

A key feature of the TRT is its strength in particle identification, due to the use of transition radiation (TR) detection [48]. TR is produced when a charged particle moves between two homogenous media having different dielectric constants. The low-energy TR photons are absorbed by the Xe-based gas mixture of the TRT, and they produce signal amplitudes that are much larger than charged particles that ionize. TR is distinguished from these ionizing particles using separate low and high thresholds in the front-end electronics.

In the barrel region, the TRT is composed of three layers of 32 modules each.

Barrel modules are composed of carbon fiber laminate shells, with an internal array of tubes which are interleaved with polypropyline fibers that serve as TR material. The tubes, oriented axially, are arranged in a uniform array with a mean spacing of approximately 7 mm. In total, there are 52,544 straw tubes (144 cm in length) in the barrel. Each layer is characterized with an increased number of tubes, moving from the inner to outer rings. The end of the barrel modules are home to the electrical connections for the TRT. Each module is equipped with a HV plate and circuitry for readout purposes.

The TRT endcaps each have two sets of disks (or "wheels"): the set closer to the interaction point has 12 wheels with eight layers of tubes, with a spacing of 8 mm between each wheel, and the outer set has eight wheels with eight layers of tubes, with a 15 mm spacing. Each layer has 768 straw tubes, oriented radially, 37 cm in length. In between each layer, 15 μm thick polypropylene foils are installed to allow for TR. Each wheel is made of two four-plane assembly units, into which the tubes are inserted and precisely glued using inner and outer carbon fiber rings. Similarly to the barrel modules, each wheel in the enccap has circuit boards for HV and signal connections are installed on the end of the straw tubes.

4.3 Calorimetry

The ATLAS calorimetry system covers the pseudorapidity range $|\eta| < 4.9$, and is made of multiple types of detectors in order to fulfill the diverse requirements of detection of a broad spectrum of physics objects. Covering a similar region in η as the ID, the electromagnetic (EM) calorimeter provides robust and precise measurements of electrons and photons. With coarser granularity, the rest of the calorimetry is geared toward measurements for hadronic jet reconstruction and for $E_{\mathrm{T}}^{\mathrm{miss}}$.

Since the primary objectives of a calorimeter include full containment of the EM and hadronic showers, and to prevent punch-through of these kinds of particles into the outermost muon system, the depth of the calorimeters is paramount. The total thickness of the barrel (endcap) EM calorimeter is > 22 (> 24) radiation lengths[1], or X_0. For hadronic measurements, approximately 9.7 interaction lengths[2] (λ) in the barrel, and 10 λ in the endcap, are adequate for the desired resolution for high energy

[1] A radiation length is the distance traveled by a particle while its energy decreases to $1/e$ of its original value [49].

[2] Similar to X_0, the interaction length is defined for nuclear particles. In addition to being the distance at which a hadronic particle has $1/e$ of its original energy, it is the mean distance traveled by such a particle before undergoing an inelastic nuclear interaction.

jets. The total thickness, 11 λ, is sufficient to reduce punch-through to levels below that of prompt or decay muons.

The calorimeters used in the ATLAS detector are sampling calorimeters. A sampling calorimeter is one that uses different materials for the creation of particle showers and for energy measurement. This type of calorimetry can be very beneficial, in that each material can be uniquely suited for its purpose, providing for greater detection power. The ATLAS calorimeters have full azimuthal symmetry and coverage about the beam axis. The inner calorimeters are housed in cryostats, and rely on the usage of liquid argon (LAr) as the active medium, due to its linear behavior and radiation hardness. The barrel cryostat contains the EM calorimeter, and each endcap cryostat is home to an EM endcap calorimeter (EMEC), a hadronic endcap calorimeter (HEC), and a forward calorimeter (FCal) that covers the region closest to the beam.

4.3.1 Electromagnetic calorimetry

Precision EM measurements are made with the ATLAS LAr calorimetry system [50] over the pseudorapidity range $|\eta| < 4.9$. These EM calorimeters employ an accordion geometry, making use of lead as the absorber medium and LAr as the sampling medium. There are three active layers in the precision measurement region, $0 < |\eta| < 2.5$, and two in the high-η region, $(2.5 < |\eta| < 3.2)$ as well as in the overlap region, covering the transition from the barrel to the EMEC. In the precision measurement region, the first layer is finely segmented along η (see Figure 4.8). In the central region $(0 < |\eta| < 1.8)$, complementary presamplers are constructed, providing a measurement for the energy lost before reaching the calorimeter. The second calorimetry layer collects the largest fraction of energy from the EM shower, thus justifying the finer η-segmentation than the third layer, which collects the tail of the shower.

The accordian geometry allows for complete azimuthal coverage without cracks as well as fast signal retrieval from the electrodes. In the barrel, the waves of the accordion are axial, and run in ϕ. In the endcap, the waves are radial, and run axially. In both the barrel and endcap, the angles of the folds of the waves vary with radius such that the LAr gap remains constant.

The lead absorbers used in the EM calorimeters are combined with 0.2 mm thick stainless sheets. In the barrel, the absorbers have a thickness of 1.53 mm (1.13 mm) for $|\eta| < 0.8$ ($|\eta| > 0.8$), while the endcap absorbers are 1.7 mm (2.2 mm) thick for $|\eta| < 2.5$ ($|\eta| > 2.5$). Readout electrodes are placed in the gaps between absorbers, and consist of three conductive copper layers separated by insulating polyimide sheets.

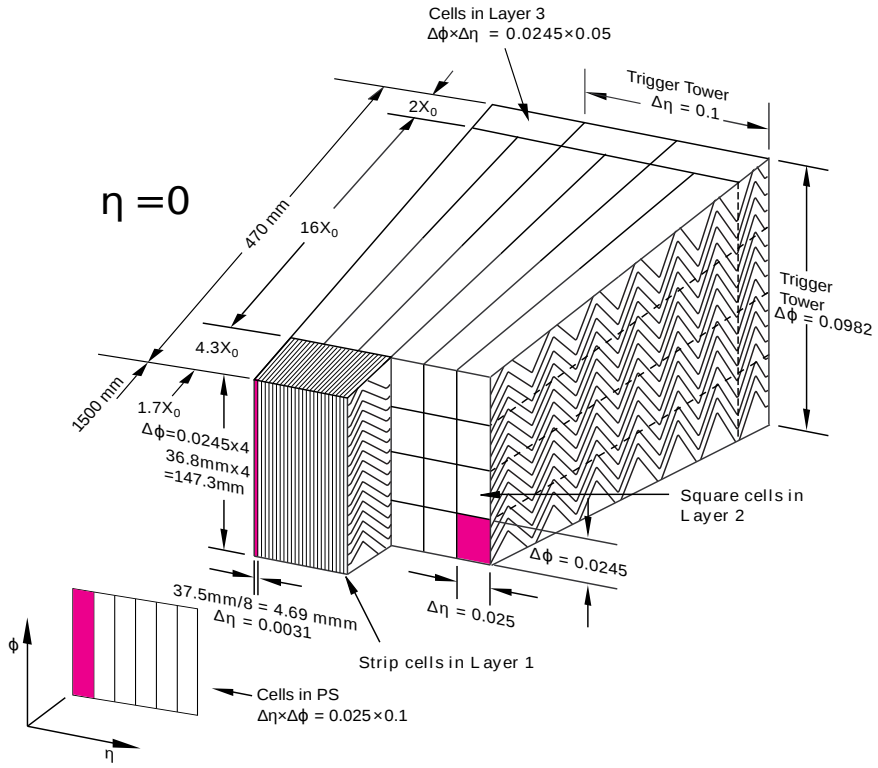

Figure 4.8: A module of the barrel electromagnetic calorimeter [42], showing the different layers and the granularity in η and ϕ.

The two outer layers are kept at a high voltage potential and the middle layer is used for signal readout via capacitive coupling.

The barrel of the EM calorimeter consists of two half-barrels, one for $z > 0$ and one for $z < 0$. Each half has a length of 3.2 m, and an inner (outer) radius of 2.8 m (4 m). Divided into 16 ϕ modules for construction purposes, each half-barrel consists of 1,024 accordion style absorbers interleaved with readout electrodes. Each module is at least 22 X_0 thick, ranging from 22 X_0 to 33 X_0 in the range $0 < |\eta| < 1.3$.

The EMEC is made of two wheels, one being on each side of the barrel calorimeter. One EMEC wheel is 63 cm thick, and is composed of two coaxial wheels, referred to as the inner and outer wheels. At room temperature, the overall inner (outer) radius of the EMEC wheels is 330 mm (2098 mm), spanning $1.375 < |\eta| < 3.2$. Due to an abundance (several X_0) of dead material in the transition region from the barrel to the endcap calorimeter ($1.5 < |\eta| < 1.8$), a LAr presampler has been implemented to improve the energy resolution in this region. Full azimuthal coverage is achieved in the EMEC by using eight wedge-shaped modules characterized by the accordion geometry described above. In the inner wheel ($2.5 < |\eta| < 3.2$), 256 absorbers (and the associated read out electrodes) are used, and in the outer wheel ($1.475 < |\eta| < 2.5$),

there are 768 absorbers. Due to high radiation levels for the inner wheel, all electrodes have their signals read out from the back side, whereas the outer wheel electrodes are read out from both the front and the back side.

As in the barrel region, the endcap has a precision measurement region, $1.5 < |\eta| < 2.5$, that is made of three longitudinal layers. The innermost layer is finely segmented with strips in η. The middle layer has the same segmentation as in the barrel, $\Delta\eta \times \Delta\phi = 0.025 \times 0.025$. The outermost layer has a granularity that is twice as coarse in η. The other regions (the outermost region of the outer wheel, $|\eta| < 1.5$, and the entirety of the inner wheel, $2.5 < |\eta| < 3.2$) are segmented in two longitudinal layers, with overall coarser transverse granularity. In total, the EMEC operates with thicknesses at least as large as 22 X_0. In the outer wheel, as $|\eta|$ goes from 1.475 to 2.5, the thickness ranges from 24 to 38 X_0. In the inner wheel, from $|\eta| = 2.5$ to $|\eta| = 3.2$, the thickness ranges from 26 to 36 X_0.

Due to the material in front of the calorimeter, moving radially out from the interaction point, and because of the presence of the strong magnetic field inside the calorimeter, a presampler is necessary to correct for the energy lost by particles before they reach the calorimetry system. In both the barrel and endcap, the presampler is made of a separate thin LAr layer to provide shower sampling for this purpose.

The barrel presampler is comprised of 64 identical azimuthal sectors (32 per half-barrel), yielding dimensions in $\Delta\eta \times \Delta\phi$ of 1.52×0.2. Each sector is composed of eight modules of varying sizes. As $|\eta|$ increases, the length of the module increases such that there is constant granularity in η ($\Delta\eta = 0.2$) for all modules except for those at the very end of the barrel, where the segmentation is reduced to $\Delta\eta = 0.12$. Readout for the presampler is handled through the use of interleaved cathodes and anodes, glued between fiberglass plates. The cathodes are double-sided printed circuit boards, and the anodes are made of three conductive layers held at different potentials: the outer two layers are held at 2 kV high voltage, and the signals are read via capacitive coupling from the middle layer, held at ground potential. To obtain the required segmentation, $\Delta\eta \times \Delta\phi = 0.025 \times 0.1$, anodes are ganged together in η, and are etched into halves in ϕ.

Each endcap presampler (one per endcap) is composed of 32 identical azimuthal sectors, or modules, with a segmentation in $\Delta\eta \times \Delta\phi$ of 0.025×0.1. Each module is formed of two 2 mm thick active LAr layers, formed by three electrodes held parallel to the front face of the EMEC. Negative HV is applied to the external electrodes, and the signals are read out from the middle electrodes. Two HV cables separately feed each side of a presampler module in the endcap.

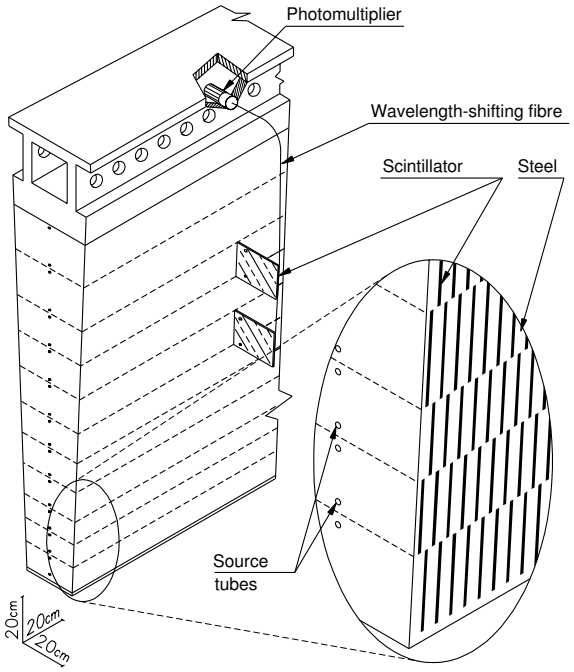

Figure 4.9: A module of the tile calorimeter [42].

All LAr calorimeters in ATLAS process the analog signals from the electrodes in the same way. Front-end electronics, mounted directly on the detector in the ATLAS cavern, receive the raw calorimeter signals. After amplification of the raw readout, integrated circuits shape the signal, and then switched-capacitor arrays provide storage during the latency of the L1 trigger decision. If an event is accepted by L1, analog-to-digital converters (ADC) are used to digitize the analog signals before transmission to the back-end electronics for further processing.

4.3.2 Hadronic calorimetry

The ATLAS hadronic calorimeter is comprised of three subsystems: the tile calorimeter [51], the LAr hadronic endcap, and the LAr forward calorimeter.

Tile calorimeter

The tile calorimeter is a sampling calorimeter that uses steel and scintillating tiles as absorbers and active material, respectively. The tile system is located immediately outside the EM calorimetry system, and is comprised of a barrel (covering $|\eta| < 1.0$) and two extended barrels (covering $0.8 < |\eta| < 1.7$). Divided into 64 azimuthal

modules, and having an inner (outer) radius of 2.28 m (4.25 m), the tile calorimeter is segmented into three layers in depth. The layers have varying thicknesses: in the barrel, the layers are 1.5 λ, 4.1 λ, and 1.8 λ with increasing r, and in the extended barrel, they are 1.5 λ, 2.6 λ, and 3.3 λ.

The detector modules are constructed with steel absorbers to slow the hadrons and scintillating tiles that are read out by wavelength-shifting fibers and sent to photomultiplier tubes (PMT) to provide the energy measurements needed for reconstruction. The electronics for readout are integrated with the mechanical structure, with the PMTs and front-end electronics mounted in 1.4 m "drawers" at the rear of each module. The front-end electronics also provide analog sums over subsets of the tile calorimeter channels, which provide so-called towers used in the L1 trigger. See Figure 4.9 for an illustration of a tile module. The steel girder, which establishes the separation between modules, contains the readout electronics and provides a flux return for the solenoidal magnetic field outside the ID. The steel absorbers are composed of 5 mm thick master plates, onto which 4 mm spacer plates are glued. These absorbers are staggered in order to provide pockets for the scintillator tiles, installed adjacent to the plates. The tiles used vary in size, with their azimuthal sides having lengths of $200 - 400$ mm and their radial sides having lengths of $97 - 187$ mm. These tiles generate UV light when an ionizing particle traverses them, which is then converted to visible light via wavelength-shifting fibers that are connected directly to the edge of the tiles. These fibers are 1 mm in diameter, and aluminized at the ends opposite to the PMT and electronics in order to improve the intensity of their light output.

The fibers transmit the tile signal to the so-called "PMT block." The PMT block consists of a light mixer, the actual PMT, a voltage divider, and what is known as a 3-in-1 card. The light mixer is responsible for mixing light from multiple readout fibers, providing uniform illumination for the photocathode in the PMT. After the PMT detects and measures the light from the mixer, signal shaping and production of analog signals for the L1 trigger are handled by the 3-in-1 card. Every 25 ns, ADCs sample incoming data from the 3-in-1 cards. One ADC receives input from up to six PMT channels. An interface board per pair of tile drawers is used for synchronization with the trigger timing system, as well as transmitting the digital signals from the ADCs via optical links. An adder board is used to perform analog sums of input signals from up to six PMT blocks, and then transmits these towers to the L1 trigger system.

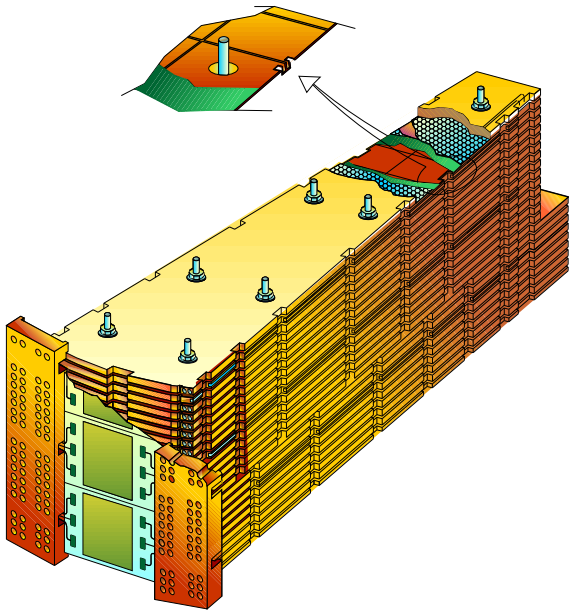

(a) A schematic of a module in the hadronic endcap.

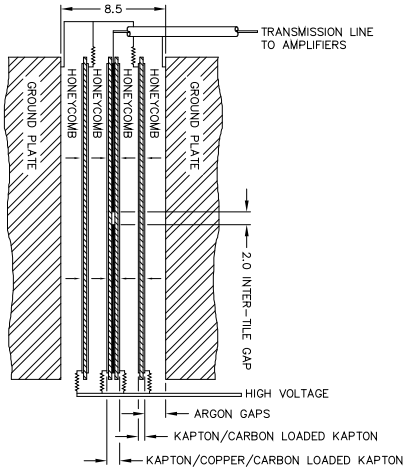

(b) An illustration of the readout electronics for the modules in the hadronic endcap.

Figure 4.10: Module and electronics for the hadronic endcap calorimeter.

Hadronic endcap

The hadronic endcap calorimeter (HEC) is made of two independent wheels per endcap, known as HEC1 and HEC2, which are located directly behind the EMEC. These systems, along with the forward calorimeter, make use of the same cryostat. The HEC is meant to help provide more complete calorimetric coverage, compensating for a drop in material density at the transition between the endcap and forward calorimeters by extending out to $|\eta| = 3.2$, and overlapping with the tile calorimeter starting at $|\eta| = 1.5$. Using copper as the absorber medium and LAr gaps as the active medium, the HEC wheels are each composed of 32 identical wedge-shaped modules, each segmented into two sections in depth (*i.e.*, four layers in each endcap).

The modules used in HEC1 and HEC2 are designed with slightly different granularities, with the HEC2 modules providing coarser measurements farther from the interaction point. Modules in HEC1 are made of 24 copper plates, 25 mm thick, along with a 12.5 mm front plate. HEC2 modules have 16 copper plates of 50 mm thickness, and a 25 mm front plate. Both wheels have an outer radius of 2,030 mm. The inner radius varies, with the first nine plates of HEC1 having an inner radius of 372 mm, and the remaining plates of HEC1 and all of HEC2 having an inner radius of 475 mm. For both HEC1 and HEC2, the LAr gaps are 8.5 mm thick, and are segmented using

three electrodes into four LAr drift zones of 1.8 mm. See Figure 4.10 for illustrations of the HEC modules and the LAr gap structure. The middle electrode is constructed with a pad structure, providing readout in $\Delta\eta \times \Delta\phi$ cells of 0.1×0.1 (0.2×0.2) for $|\eta| < 2.5$ ($|\eta| > 2.5$). The outer electrodes are covered with a highly resistive covering. This arrangement creates an electrostatic transformer. The nominal HV applied to each drift zone is 1800 V, providing a drift time for electrons in these zones of 430 ns.

Forward calorimeter

The ATLAS forward calorimeter (FCal), integrated into the endcap cryostats, provides the most forward coverage of all the calorimeters (covering $3.1 < |\eta| < 4.9$), allowing for more uniform and hermetic detection. Furthermore, it reduces the amount of radiation that reaches the muon spectrometer. The FCal is built with three modules per endcap, providing a depth of 10 λ. With respect to the face of the EMEC, the FCal is recessed by approximately 1.2 m. Thus, given the reduced depth, high-density materials are required for robust energy measurements. Very small LAr gaps are used due to the high particle flux associated with this pseudorapidity range, and the electrodes used are small rods with concentric tubes, oriented parallel to the beam direction.

The three modules are known as FCal1/2/3, and are all 45 cm deep. Each module employs copper plates as absorbers, and FCal1 (FCal2/3) uses copper (tungsten) tubes and rods for the electrodes. The innermost module, FCal1, provides EM measurement, whereas FCal2 and FCal3 provide hadronic energy measurement.

4.4 Muon spectrometer

The ATLAS muon spectrometer (MS) is the outermost component of the detector. Its primary objective is to detect charged particles exiting the calorimeters, and to measure track momentum within $|\eta| < 2.7$. Overall, the design goals of the muon system are to provide robust muon triggering within $|\eta| < 2.4$ and to measure track p_{T} with a resolution of 10% at 1 TeV. A minimum energy of approximately 3 GeV is required for a muon to successfully pass through the calorimeters, thus providing a typical lower limit to the measurements made by the MS.

The tracking and triggering in the MS is handled by chambers that are located between and on top of the coils of the barrel toroid and by chambers in front of and

behind the end cap toroids. To reflect the ϕ-symmetry of the toroids, the MS is divided into octants, which are further divided into two sectors each. The chambers within a given sector have varying lateral extensions, providing overlap in ϕ, which minimizes gaps in coverage and helps with alignment. The barrel system is comprised of three concentric cylindrical shells, with approximate radii $r \approx 5,\ 7.5,\ 10$ m. In the endcaps, the muon system is built as large wheels, at distances $z \approx 7.4,\ 10.8,\ 14,\ 21.5$ m. Precision tracking in the barrel is handled by the monitored drift tube (MDT) system, and the barrel trigger system is composed of resistive plate chambers (RPC). Endcap momentum measurements are made by MDTs in the outer two layers. However, due to the increase in particle flux in the forward-most regions, cathode strip chambers (CSC) are used in the innermost layer. Finally, thin gap chambers (TGC) are responsible for triggering muons in the endcap.

4.4.1 Monitored Drift Tubes

The monitored drift tubes, or MDTs, are constructed as a system of more than 1,000 chambers employing drift tube detection technology. As mentioned in Section 4.2.3, drift tubes rely on highly pressurized gas, coupled with a system of electrodes in a cylindrical geometry, to provide precision measurements in space and time that can be used to reconstruct the momentum of a charged particle traveling through a magnetic field. In the case of the ID, the field was solenoidal, whereas for the muon system, the field is toroidal.

The tubes used in the MDT system are constructed with aluminum, and have a diameter $d = 29.97$ mm. The gas mixture chosen for the tube interior is 93% argon and 7% CO_2, kept at a pressure of 3 bar. Small quantities of H_2O are added to the mixture in order to improve stability of the HV system. The wires at the center of the drift tubes are tungsten-rhenium wires with a diameter $d = 50$ μm. To provide the electric field needed for electron drift in the tube, the wires are held to a potential of 3,080 V. For robust measurements, the wires are kept concentric to within $\sigma < 10$ μm through the use of cylindrical end-plugs at the end of the drift tubes. The geometrical arrangement provides for a radial electric field, which is advantageous for understanding the drift dynamics. However, the MDT tubes are characterized by a long pulse train, due to the fact that electrons from the wall of the tube can take as long as 700 ns to reach the central wire. Since only the distance of closest approach, known as r_{min} or the radius of the drift circle, is needed for a position measurement (see Figure 4.6), this is somewhat of a drawback for readout purposes.

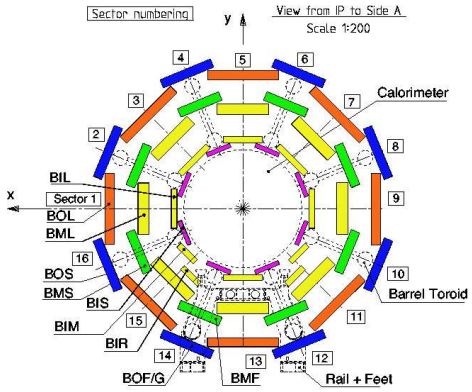

(a) A cross sectional view of the muon system in the barrel region, showing the $r-\phi$ plane. The three concentric layers, as well as the variable size of the chambers, can be seen. The outer diameter is approximately 20 m.

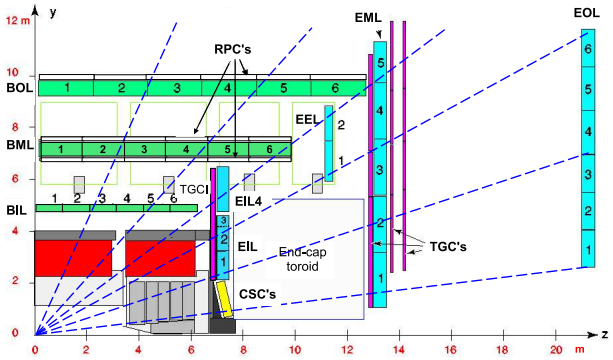

(b) An $r-z$ view of the muon system in the barrel and endcap regions. This shows the three concentric layers of the MS, as well as the breakdown of the various detector technologies used in the endcap out to $|\eta| < 2.7$.

Figure 4.11: Detailed views of the MS in the barrel and endcap regions [42].

MDT chambers are found in both the barrel and in the endcap of the MS. Barrel chambers are rectangular, while endcap chambers have a trapezoidal geometry to optimze coverage over solid angle as well as to respect the geometry and structure of the toroidal magnet coils. In all MDT chambers, the tubes are oriented such that they are tangential to circles concentric to the beam axis at their centers. In barrel chambers, the tubes are all of the same length. In the endcap, the tube length varies in r in 24 steps.

Most MDT chambers are built with two tube layers, known as "multilayers." The two multilayers are separated mechanically by a spacer, which is a support beam having a thickness between 6.5 and 317 mm. In the innermost MDT layer, each multilayer is comprised of 4 layers of tubes. In the middle and outer MDT layers, each multilayer has 3 layers of tubes. The tubes in a multilayer are glued together with epoxy. See Figure 4.12 for a schematic illustration of the MDT multilayer construction.

The MDT chambers are characterized by very robust construction and quality. At the time of installation, tubes used in the chambers were required to be straight to within 100 μm. Nonetheless, deformations in the chambers are expected due to gravitational forces and thermal gradients. For example, chambers in the outer layer of the barrel region my have a wire sag of up to 800 μm when supported at the two ends. To compensate for the sag due to gravity, a sag-adjustment system applies a force to the central cross-plate (see Figure 4.12). An optical aligment system is employed

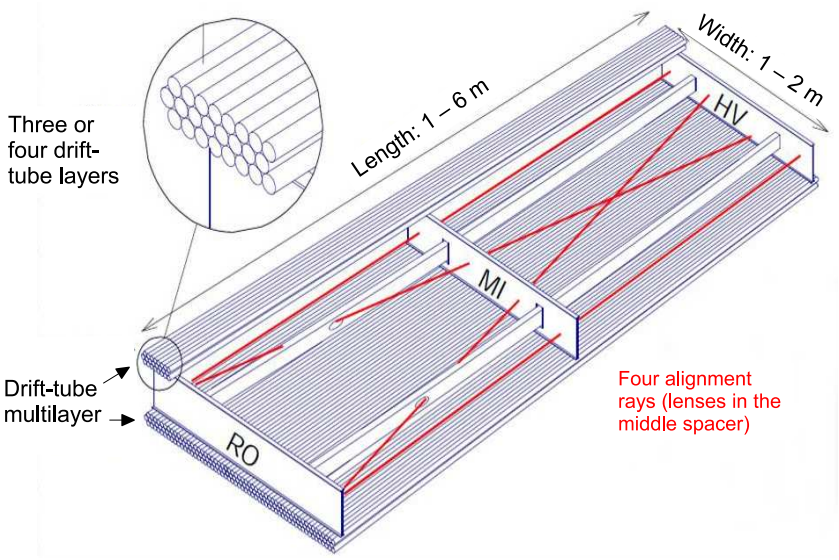

Figure 4.12: An illustration of a typical MDT chamber [42] with two multilayers.

for all MDT chambers as a way to monitor deformations, and uses four rays for each chamber. Deformations of a few microns can be detected, and are recorded in order to adjust precision space-time measurements. In addition, thermal deformations and magnetic field conditions are closely monitored by temperature and B-field sensors mounted directly on the detectors.

The analog signals from the drift electrons in the tubes are amplified, shaped, and discriminated by aptly-named amplifier/shaper/discriminater (ASD) chips, which are each responsible for signals from eight tubes. Binary signal is output by the ASD, and is then sent to the time-to-digital converter (TDC). The TDC stores the arrival times of the leading and trailing edges of tube signals, along with a tube identifier and a flag denoting whether the time is for a leading or trailing edge. One TDC and three ASD cards are implemented on a printed circuit board card, known as a mezzanine card. A given MDT chamber can have up to 18 mezzanine cards, which are in turn controlled by a local processor known as the chamber service module (CSM). The CSM is responsible for collecting the TDC signal for transmission to the RODs. In addition, the CSM provides timing information from the TTC for the on-chamber electronics.

MDT Configuration Database

As an aside, it is worth mentioning that a portion of the author's work on ATLAS involved the MDT configuration database, which is an Oracle 11 database, written

in PL/SQL, that is responsible for the storage and delivery of many different flavors of data regarding the MDTs. In particular, the initialization of the detectors relies on information from the database about thresholds for ASDs and other mezzanine card settings. The database is home to a wealth of bookkeeping information about the detectors, including serial numbers for different hardware, mapping information for high and low voltage systems, and various configurations for the chambers. To complete his service task, which is required for ATLAS authorship, the author was one of the main responsibles for this database. His work included porting code that interfaced users with the database from their original language (C++) to Python. In addition, requests from muon experts and run coordinators often had to be filled, and new chambers installed over the winter break in 2012 had to be fully implemented in the database.

4.4.2 Cathode Strip Chambers

The MDT system is limited by flux per area, to approximately 150 Hz/cm^2. This rate is exceeded in the first layer of the MS endcap for $|\eta| > 2$. Therefore, the MDTs are replaced by cathode strip chambers (CSCs) in this region. CSCs are characterized by high spatial and time resolution with high rate capability. The CSC system is segmented into 16 sectors in azimuth, and alternates between large and small chambers. Each CSC endcap is composed of eight large and eight small chambers. One chamber represents four planes of CSC layers, which in turn provides four independent (η, ϕ) measurements per muon track.

The design of the CSCs is based around multiwire proportional chamber technology [52]. The CSC wires are oriented such that the central wire in each chamber is radial, and the cathodes are all segmented into strips. Radial coordinates are measured by strips that are perpendicular to the wires, and transverse coordinates by strips that are parallel to the wires. Unlike in the TRT and MDT systems, the wires in the CSCs are not read out. Instead, the position is measured by interpolating between charges induced on neighboring cathode strips. Since this measurement is dependent on the relative charge measurements on neighboring strips, the resolution of this detector is limited by the signal-to-noise ratio and the readout pitch. Also, multiwire chambers perform optimally if the incoming tracks are not inclined. For this reason, the CSCs are tilted toward the IP such that tracks with infinite momentum are normal at the center of a CSC chamber.

The CSCs are mounted approximately 7 m from the IP, with MDTs and TGCs

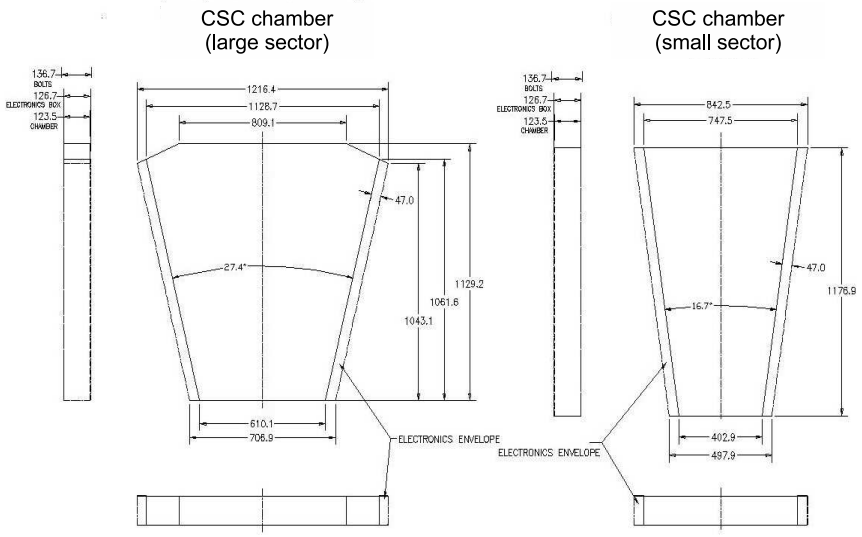

Figure 4.13: Shapes of large and small CSCs [42]. Dimensions are given in mm.

in the so-called small wheel of the endcap. Covering $2 < |\eta| < 2.7$, the inner (outer) radius of the CSC system is 881 mm (2,081 mm). The small (large) chambers have 250 (402) wires per CSC plane. The wires are made of gold-plated tungsten, with 37% rhenium, and have a diameter $d = 30$ μm. With two arrays of cathode strips, the are 192 readout channels per plane. The first cathode plane has strips perpendicular to the wires, providing a position measurement in η. With a larger spacing, the second cathode plane provides a ϕ measurement with strips parallel to the wires.

4.4.3 Resistive Plate Chambers

The trigger system in the barrel consists of three layers of resistive plate chambers (RPC), each layer being referred to as a "trigger station." Figure 4.15 shows an example of the geometry of these chambers. The RPCs in this illustration are colored, and the MDTs to which the RPCs are matched are also shown. A large separation between the inner and outer RPC layers (RPC2 and RPC3, respectively) allow for triggering on high momentum muon tracks in the range $9 < p_{\mathrm{T}} < 35$ GeV. The inner two trigger stations provide the low-p_{T} trigger in the $6 - 9$ GeV range (see Figure 4.14).

In total, there are 260 RPC chambers. Each trigger station has two independent detector layers, as shown in Figure 4.15, and each detector layer provides (η, ϕ) measurements. Thus, for a track traveling through all three RPC stations, six measurements in η and ϕ are available. This configuration provides redundant trac

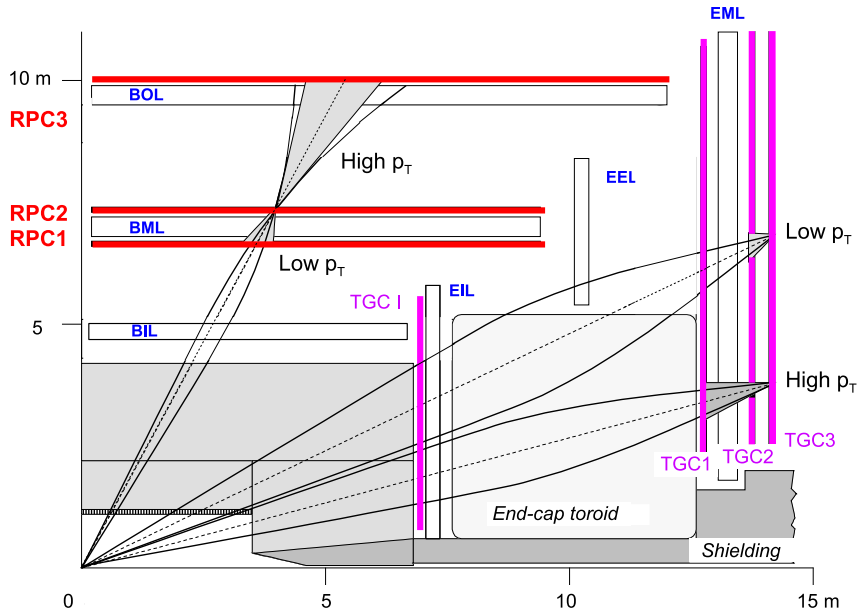

Figure 4.14: Schematic of the muon trigger system [42].

measurements, which are instrumental in rejecting fake signals and maintaining high trigger efficiency even with small chamber inefficiencies.

A RPC detector is a gaseous detector with parallel plate electrodes; no wires are used. Two resistive plates, made of phenolic-melaminic plastic laminate, are kept parallel to each other using 2 mm spacers. An electric field is applied between the plates, with a strength of 4.9 kV/mm. This field allows for ionizing tracks to induce an avalanche of electrons (analogous to the avalanche in a drift tube) that can be read out via metallic strips that are coupled capacitatively. The gas in between the electrodes is a mixture of $C_2H_2F_4$ (94.7%), Iso-C_4H_{10} (5%), and SF_6 (0.3%). This gas mixture was chosen because of the relatively low voltage requirement, its non-flammable nature, and low cost. Each RPC chamber is made up of two detector regions (also known as "units") that are contiguous to one another. In each unit, there are two independent gas layers, each having two orthogonal sets of pickup strips. Thus, each unit provides four independent levels of readout. The total thickness of an RPC chamber is 96 mm (or 106 mm for the large outer layer chambers). Standard RPC chambers are assembled together with an MDT chamber of equal dimensions. Special small RPCs are used around the feet of the ATLAS detector, and in some regions that are too small for MDTs, in order to minimize the losses in trigger acceptance.

The gas volume in each RPC unit is surrounded by two resistive plates of 2 mm thickness, leaving a gas gap of the same depth; see Figure 4.16. The pickup strips

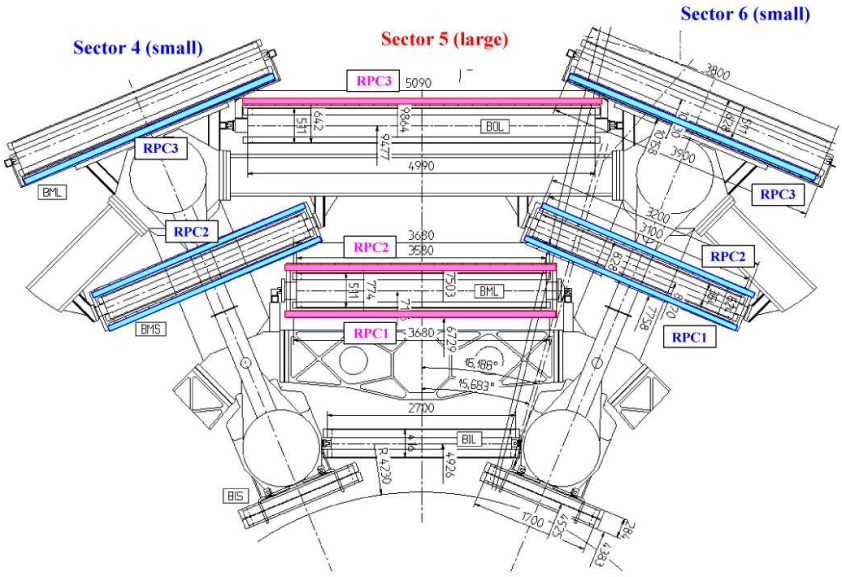

Figure 4.15: Transverse view of the upper part of the MS barrel, showing all three RPC layers and their respective MDT components [42]. Dimensions are in mm.

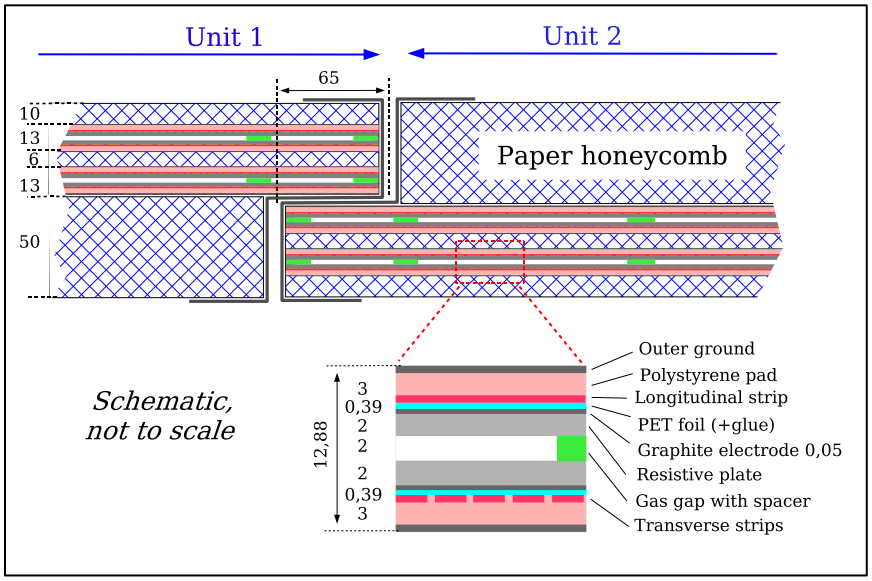

Figure 4.16: An illustration showing the structure of an RPC chamber [42] and its constituent gas volumes. Dimensions are in mm.

are bonded on polystyrene plates, and also are layered with a copper sheet used for grounding. The readout signal is induced on these pickup strips by the drift motion of electrons in the resulting avalanche of an ionizing particle traversing the volume. The copper pickup strips are robust transmission lines with low attenuation that are $25 - 35$ mm wide and 17 μm thick. Each strip is separated from its neighbor by 2 mm. To successfully process the signal from avalanches, the two sets of strips on either side of the gas gap are configured to read out signal of opposite polarity.

The front end boards for the RPC readout are mounted directly on each chamber, and are soldered directly to the pickup strips to minimize losses. Each front end circuit is made of a three-stage shaping amplifier, followed by a comparator. This circuit is implemented in a GaAs die with eight channels, bonded on a board that serves eight strips. For a track to be used, the RPC system must have signal detected in coincidence across different layers of the detectors. For the low-p_{T} trigger, three of the four active detection layers in the inner two stations must have coincidences between strips. For the high-p_{T} trigger, the conditions for the low-p_{T} trigger must be satisfied, and a confirming hit in one of the two outer station layers is further required.

4.4.4 Thin Gap Chambers

The thin gap chambers (TGC) in the endcap of the MS serve two purposes:

1. Robust triggering of muons in $1.05 \leq |\eta| \leq 2.4$
2. Complementary ϕ measurement to MDT measurement in bending (*i.e.*, radial) direction

The TGCs are constructed alongside MDTs in the inner and middle layers. The middle layer of MDTs (EM wheel) has seven associated TGC layers, and the inner layer has two TGC layers. The inner layers of TGCs are radially segmented into two regions, known as EI and FI. The EI, or "endcap," layers are mounted on the endcap toroid support structures. The FI segment is the most forward region, and is also known as the "small wheel" TGC segment.

The azimuthal measurement provided by the TGCs are important for robust momentum measurements for muons traversing the endcap detectors. To determine these values, the TGC uses a system of strips oriented radially in both the EI and FI. Since the MDTs in the EO wheel do not have TGCs paired with them, an extrapolation from the middle layer is required for the outer ϕ measurement. In addition to the

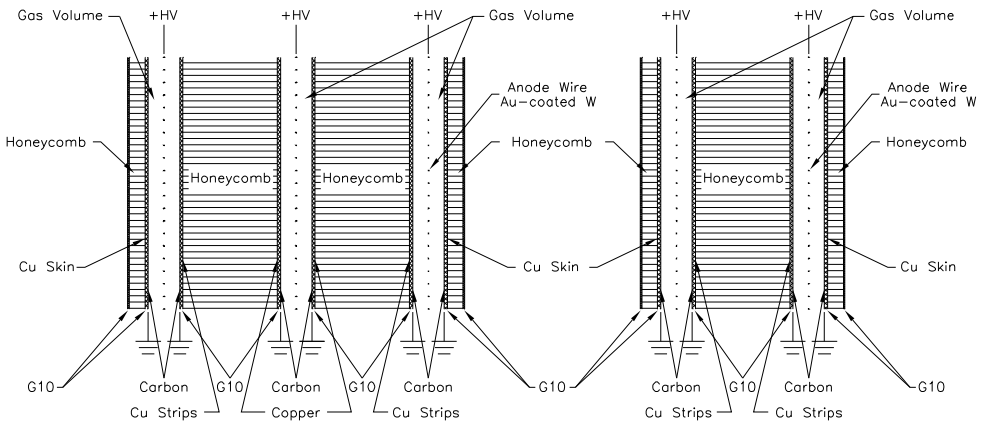

Figure 4.17: Cross sectional views of a TGC triplet and a TGC doublet [42], showing the mechanical structure of the wires, gas gaps, and copper pick up strips.

azimuthal coordinate determination, the TGCs measure radial positions using wires, employing the principles of a multiwire proportional chamber. The time resolution and fine spatial granularity required for the TGC system are rooted in the need for a sharp cut-off in the measured momentum for triggering of muons. To achieve such granularity, wires are grouped into varying sizes – 6 to 31 as a function of *eta* – and these groups staggered. The staggering optimizes position resolution for a given number of electronics channels. The radial strips used for the ϕ measurement are also staggered in order to achieve a $2-3$ mrad granularity, from the perspective of the IP.

The TGC chambers operate as multiwire proportional chambers, characterized by having a smaller separation between the wires and cathodes than between different wires. The wire-to-cathode distance is 1.4 mm, while the wire-to-wire distance is 1.8 mm. The gas mixture is composed of CO_2 and n-C_5H_{12} (or n-pentane), which is advantageous for its highly quenching nature (*i.e.*, low rate of secondary pulses in electron avalanches). The high electric field near the wires, combined with the small inter-wire separation, allows for very good time resolution in the TGCs.

The seven layers of the TGCs in the middle MDT layer are composed of one chamber triplet along with two doublets. See Figure 4.17 are grouped into circular disks, made of two concentric rings. The outer ring, or "endcap" ring, provides coverage over $1.05 \leq |\eta| \leq 1.92$, and the inner (or "forward") ring covers $1.92 \leq |\eta| \leq 2.4$. The TGCs are segmented in ϕ into 12 sectors, thus covering 30° each. In the outer ring, the sectors are further divided into four modules of 7.5° each. The inner ring has half as many modules, each covering 15°.

The signals from the TGC wires and strips are amplified on the front end circuitry, after which they are time aligned and synchronized to the LHC beam crossing. For

any signal to be further processed in the L1 trigger, certain coincidence criteria must be met. In the EM wheel, the triplet must have two out of three hits in coincidence, while the two doublets must have three out of four hits. If a muon track passes this check, it is then sent to the coincidence matrix and then processed by the trigger.

4.5 Forward Detectors

ATLAS has three detector systems for special purposes constructed in regions with very high η, known as LUCID, ALFA, and the ZDC. LUCID (LUminosity measurement using Cerenkov Integrating Detector) measures the relative luminosity[3] delivered to ATLAS, and is located at a distance of ± 17 m from the IP. ALFA (Absolute Luminosity For ATLAS) is another luminosity detector that utilizes Roman pot technology to measure absolute luminosity, and is located approximately ± 240 m from the IP. The Zero-Degree Calorimeter, or ZDC, is housed ± 140 m from the IP, and is designed to detect forward neutrons in collisions involving heavy ions.

LUCID is the only system in ATLAS specifically designed for online luminosity monitoring, which it does through detection of inelastic $p-p$ scattering in the forward direction. At nominal LHC luminosity, multiple $p-p$ interactions per bunch crossing are expected. Since the number of interactions is required in any calculation of luminosity, it is important to have robust measurements of this quantity. LUCID works on the princpiple that the number of particles detected is proportional to the number of interactions in a given bunch crossing. The detector consists of 20 aluminum tubes surrounding the beam that point toward the IP. Each tube is 1.5 m in length and has a diameter of 15 mm. The tubes are filled with C_4F_{10} at a pressure of approximately 1.3 bar, which means that Cerenkov radiation will be produced if a pion (electron) traverses the tube with a minimum energy of 2.8 GeV (10 MeV). Both LUCID endcaps are constructed at a radial distance of approximately 10 cm from the beam, corresponding to $|\eta| \approx 5.8$. PMTs are installed to collect the Cerenkov light, whose signal can be used to deduce the number of particles per tube. LUCID is characterized by fast timing response which allows for unambiguous measurements of individual bunch crossings. The PMT signals are transmitted to a front end card that amplifies and shapes the pulses, after which further electronics refine them. Field programmable gate arrays use the signal to calculate luminosity for each bunch

[3]Relative luminosity is a measure of absolutely luminosity, but multiplied by some time-independent factor.

crossing, and serves as a buffer for these scalar values. Once a L1 trigger accept signal is received, the values are sent for more processing in the readout system.

ALFA is designed to measure absolute luminosity via elastic scattering measurements at small angles. The detector makes use of a Roman pot configuration [53], placing scintillating fiber trackers in volumes that are mechanically separate from the beam vacuum but arranged very close (approximately 1 mm) to the beam. As mentioned earlier, the ALFA Roman pots are situated ± 240 m from the IP so as to measure scattering at very small angles (3 μrad). The detector has 10 two-sided modules, eaching having 64 fibers arranged in a stereo geometry on both sides. The scintillators transfer their output light to phototubes, which are then processed further by the front end boards and readout chips.

The ZDCs are designed for detection of forward neutrons ($|\eta| > 8.3$) in collisions of heavy ions. These detectors thus are used for measurement of centrality in these collisions. Additionally, the ZDCs helped improve the acceptance of ATLAS in early LHC running, and provided a triggering mechanism for minimum-bias processes. There are two ZDC arms, one on each side of ATLAS. Each ZDC arm has one EM module (approximately 29 X_0 deep) and three hadronic modules (about 1.14 λ deep). The modules are made of tungsten plates, oriented vertically, and quartz rods, oriented longitudinally. Particles incident on the detectors shower, and emit Cerenkov radiation, which is viewed by phototubes mounted on the edge of the modules. The EM modules map individual rods' signals, whereas the hadronic module groups four tubes into one phototube, corresponding with the difference in shower shapes for EM and hadronic signals.

4.6 Trigger and DAQ

As mentioned in the introduction, ATLAS has a three-level triggering system. The L1 trigger is implemented using electronics and is based strictly on detector readout patterns. Together, the L2 and EF make up what is known as the High-Level Trigger, or HLT. The HLT is software and firmware based, and is responsible for filtering events such that the rate written to disk is approximately 200 Hz.

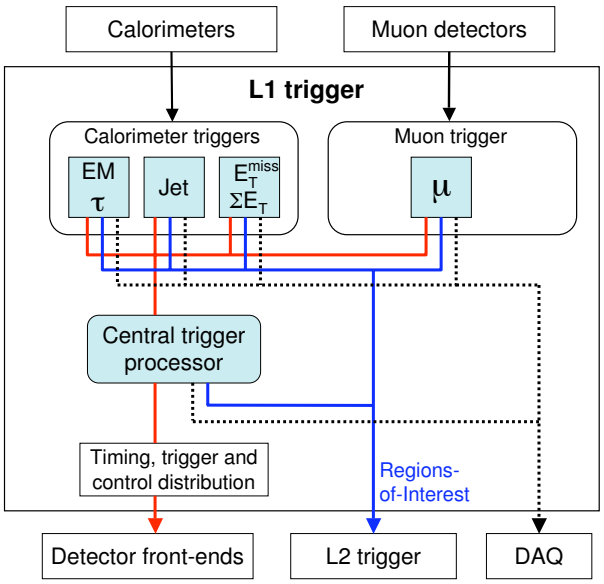

Figure 4.18: A schematic illustration of the data flow for the L1 trigger [42].

4.6.1 Level-1 Trigger

The L1 trigger takes information from the calorimeters and muon detectors to make an initial selection on interesting physics events. See Figure 4.18 for a schematic illustration of the L1 trigger flow. The calorimeter selection is formed using information from all calorimetry subsystems, both EM and hadronic, from the barrel, endcap, and forward detectors. The stream of events selected by this L1 calorimeter trigger is known as "L1Calo," and its aim is to select events having high-E_{T} electrons, photons, hadronic jets, hadronically decaying τ leptons, or events having significant amounts of missing transverse energy ($E_{\mathrm{T}}^{\mathrm{miss}}$). Additionally, events can pass the L1 trigger if enough hadronic energy is present via the trigger on the total scalar sum of hadronic energy, known as "SumET" or $\sum E_{\mathrm{T}}$. To reduce the rate of events with high-E_{T}EM and τ objects, requirements on isolation[4] can be added. Several E_{T} thresholds (between 4 and 16) are defined for each type of L1 trigger. The muon trigger makes decisions based on hits recorded in the MS, using information from the RPCs in the barrel and TGCs in the endcap region. Searches for patterns of high-p_{T} muons originating at the IP result in six p_{T} thresholds, and muons are not double counted across the thresholds.

The decision to accept an event in the L1 trigger is handled by the Central Trigger Processor, or CTP. The CTP merges information from different objects, and can

[4]Isolation is defined as the requirement that the energetic particle have a minimum angular separation from any significant energy deposit in the same trigger.

coordinate trigger menus with up to 256 distinct combinations of requirements (*e.g.*, requiring one muon and one electron, each with p_{T} greater than 10 GeV). Once the L1 accept decision has been made, the CTP transmits this, along with the 40 MHz clock, to the detector front end systems via the Timing, Trigger, and Control (TTC) system. The multiplicty of trigger objects is all that is required for the L1 decision, but the HLT requires geometric information for these objects, as well. For this reason, the locations of hits from the muon and L1Calo processors are sent as so-called regions of interest (RoI) to the L2 trigger if an event passes L1. One of the principle goals of the L1 trigger is to associate without ambiguity the detector signals to the correct bunch-corssing. This is a challenge, in particular because of the width of signals in the calorimeter, which can span up to four bunch-crossings, and because of the time-of-flight of the muons reaching the MS. While the L1 decision is being made, the detector channels' information must be stored in memory pipelines. This is accomplished via front end electronics. To keep these pipelines as short as possible, the L1 latency is kept to 2.5 μs.

4.6.2 DAQ and HLT

The data acquisition system (DAQ) and high-level trigger are made of several components, including detector readout, the L2 trigger, event builder, and event filter (EF). This series of logic systems is responsible for taking the L1 accepted events, performing further selection, and piping the event information to the data recording stage if certain conditions are met.

For the HLT to consider an event, the L1 decision must happen first. During the 2.5 μs latency of the L1 trigger, independent pipeline memories on the front end of the detectors store the event data awaiting the decision. If L1 accepts the event, the event data are further transmitted via 1,574 Readout Links, or ROLs, to the Readout Buffers (ROBs). The ROBs, which are part of the overall Readout Systems (ROS), are responsible for temporarily storing the event fragments and providing them, upon request, to later stages of the DAQ/HLT chain.

Information about RoIs are sent via eight dedicated ROLs to a RoI builder. After the RoI is assembled, it is forwarded to a L2 supervisor, or L2SV. The L2SV serves to escort the event as it proceeds through the L2 trigger. Once the L2SV receives RoIs, it assigns the event to one L2 processing unit (L2PU). The L2PU makes the second decision (after L1), requesting event data from the ROSs. The L2SV receives the decision to accept or reject the event from the L2PU, and forwards the decision to

the DataFlow Manager (DFM). At the same time, the L2PU also sends a summary of its analysis to the ROSs.

The DFM serves as a marshal for the event during the event building phase. If the event was rejected at L2, the DFM tells the ROSs to remove event fragment data from ROBs. However, if the event was accepted, the DFM assigns it to a node that will build the event, known as a sub-farm input (SFI). The SFI builds the event using information from the ROSs, and sends the event structure to the EF. Upon completion of the event build, the SFI tells the DFM, which then informs the ROSs to remove the event data from the ROBs.

Finally, the EF performs the final trigger selection of each event and also classifies the events into streams, depending on the event content. Examples of trigger streams include `JetEtMiss`, `Egamma`, and `Muons`. Information about the streams relevant for each event is added to the event structure. Selected events are next sent to the sub-farm outputs (SFOs), which are responsible for ultimately sending the event to the CERN data recording facility for storage and reconstruction.

Chapter 5

Reconstruction and particle identification

Excellent particle identification capability is required at the LHC for most physics studies. The ATLAS detector provides fast and robust tracking and energy measurements. From these signatures, relevant physics objects such as electrons, photons, τ leptons, hadronic jets, muons, and missing transverse energy are built. Various schemes of reconstruction and identification have been derived for these objects, as explained in the following sections. For brevity, τ lepton reconstruction and identification will not be discussed, as these objects are not used in the analyses presented later.

5.1 Electrons

Electrons play a hugely important role in many physics analyses for the ATLAS program. Many models describing potential new physics processes, a multitude of well-known SM processes, and Higgs boson decays all involve electrons. As many of these processes are characterized by small cross sections and simultaneously are plagued by large backgrounds from QCD, powerful and efficient electron reconstruction and identification are required to observe these signals.

As an electron traverses the calorimeter, a shower develops as a result of cascades of Bremsstrahlung ($e \to e\gamma$) and photon conversions ($\gamma \to e^+e^-$). Showers of EM energy will leave energy deposits across multiple cells and layers, forming calorimeter clusters. Standard electron reconstruction [54, 55] is based on the idea of matching clusters of energy from the EM calorimeter to tracks from charged particles in the ID (see Sections 4.2 and 4.3.1). The use of both systems serves to reduce backgrounds[1] from many sources. The seed clusters are found via a so-called *sliding window* algorithm,

[1] As a general rule, a larger background rejection rate will come at a loss in identification efficiency. The optimal combination of these is analysis-dependent.

which finds clusters having widths of 3×5 in cells of $\eta \times \phi$. This corresponds to $\Delta\eta \times \Delta\phi = 0.025 \times 0.025$. The cluster energies, found by summing up the measured energy from the calorimeter cells contained within, are required to be above 2.5 GeV. Inside $|\eta| < 2.5$, where the ID provides detection capabilities, electrons are defined by such a cluster matched to one or more tracks. Therefore, track-to-cluster matching is central to robust electron reconstruction.

Track-to-cluster matching proceeds in several steps. First, all tracks from the ID are extrapolated to the second EM calorimeter layer. Using this impact point, the (η, ϕ) of the tracks are compared to the (η, ϕ) of the cluster. If the difference in these coordinates is small, then the track and cluster are considered matched. If no hits are found for a track in the silicon detectors, leaving only TRT measurements, then the requirement on $\Delta\eta$ is ignored (because the accuracy of η measurements from the TRT is limited). If multiple tracks are associated with a cluster, this information is stored with the electron object, but the track with the smallest $\Delta R = \sqrt{(\Delta\eta)^2 + (\Delta\phi)^2}$ is chosen as the primary track. The various track-to-cluster matching quantities are used for electron identification, as well. The resultant track-cluster system is considered an electron candidate. Once a candidate is formed, the energy is recomputed using a re-formed cluster, with a 3×7 (5×5) window of barrel (endcap) calorimeter cells. Together with the η and ϕ measurement from the track, this provides the full set of quantities for four-momentum computations.

ATLAS employs a cut-based identification (ID) approach that uses variables useful in separating real, isolated electrons from fake electrons (*i.e.*, jets). The variables used make use of information from the calorimeter cluster used in electron reconstruction and the track matched to the cluster, as well as combined quantities. Using the ROOT TMVA [56] software, the set of variables used for the `loose` and `medium` electron classifications were used as input to an optimization over 10 bins in η and 11 bins in E_{T}, taking full advantage of knowledge of correlations amongst the quantities. The resulting identification selections are labeled as `loose`, `medium`, and `tight`. The `tight` selection has the highest background rejection power, and the `loose` selection accepts electrons with the highest efficiency.

The `loose` criteria are based off of three variables.

- $\mathbf{R_{had}}$, $\mathbf{R_{had1}}$: the energy leakage into the hadronic calorimeter (or in the first layer thereof) divided by the cluster E_{T} measured in the EM calorimeter

- $\mathbf{w_{\eta 2}}$: the lateral width of the EM shower as measured by the second layer of the

calorimeter, defined as $\sqrt{(\Sigma E_i \eta_i^2)/(\Sigma E_i) - ((\Sigma E_i \eta_i)/(\Sigma E_i))^2}$, where the sum runs over all cells inside the cluster window, and E_i (η_i) is the measured energy (pseudorapidity) of cell i.

- $\mathbf{R_\eta}$: the ratio of energies in 3×7 clusters to those of 7×7 clusters in the second EM calorimeter layer

The `medium` selection requires the electron candidate to satisfy the `loose` criteria, as well as passing cuts on several additional variables.

- $\mathbf{w_{stot}}$: the shower width of the total cluster, defined as $\sqrt{(\Sigma E_i (i - i_{\max})^2)(\Sigma E_i)}$, where the sum runs over approximately 20 η strips, and $i_{\max}$ is the index of the highest-energy strip

- $\mathbf{E_{ratio}}$: the ratio of the difference in energy between the largest and second largest deposits in the cluster to the sum of these energies

- $\mathbf{N_{hits,pix}}, \mathbf{N_{hits,Si}}$: the number of hits required for the electron track in the pixel system and in the combination of pixels and SCT

- $\mathbf{d_0}$: the transverse impact parameter, defined as the track's distance away from the primary vertex in the transverse plane

- $\mathbf{\Delta}\eta$: the $\Delta\eta$ between the cluster position and the impact point of the extrapolated track ($|\Delta\eta| < 0.01$)

Finally, the hardest level of ID cuts are defined for the `tight` selection. In addition to the `medium` requirements, the following variables are used for the `tight` electron classification:

- $\mathbf{\Delta}\phi$: the $\Delta\phi$ between the cluster position and the impact point of the extrapolated track ($|\Delta\phi| < 0.02$)

- $\mathbf{E/p}$: the ratio of measured cluster energy to the track momentum

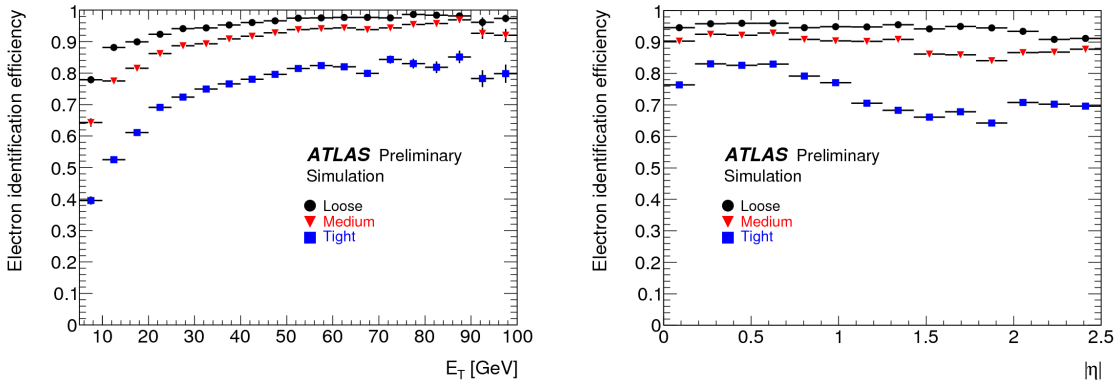

Figure 5.1: Electron identification efficiencies for the `loose`, `medium`, and `tight` selections, as a function of electron E_{T} (left) and η (right).

- $\mathbf{\Delta\eta}$: tighter cut on $\Delta\eta(< 0.005)$

$\mathbf{d_0}$ tighter cut on impact parameter, $d_0 < 1$ mm

- $\mathbf{N_{TRT}}$: the number of hits required for the electron track in the TRT

- $\mathbf{f_{HT}}$: the ratio of high-threshold TRT hits to N_{TRT}

- $\mathbf{N_{BL}}$: to reduce the effect of conversion photons, require ≥ 1 hits in the pixel b-layer

- `isConversion` bit: if the electron is flagged as a conversion photon, it is not considered

Figure 5.1 shows the performance of the three electron ID selections, as a function of electron kinematics. The electrons for these distributions come from simulated $Z \to ee$ events.

Early data studies with electrons demonstrated the need for more robust identification criteria, due to high trigger rates and the presence of multiple parton-parton interactions within a given bunch crossing. These robust EM ID criteria became known as the "`++`" menu [57], re-defining the classifications to be `loose++`, `medium++`, and `tight++`. The differences with respect to the standard ID menu mostly involve tightening cuts and migrating some selections *e.g.*, from the `medium` to the `loose` cuts. For the 2011 analysis presented in Chapter 6, the `++` menu was the standard.

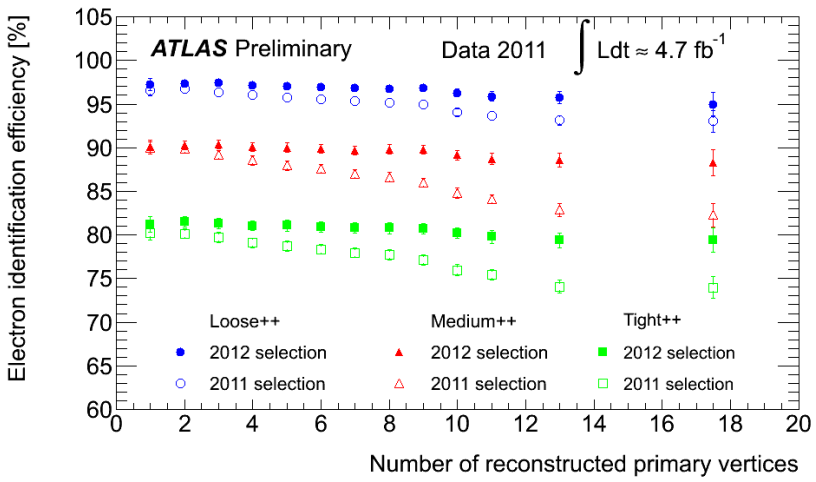

Figure 5.2: Electron identification efficiency dependence on pileup, showing both the 2011 and 2012 ID selection results.

The 2012 analysis, as discussed in Chapter 7, the ID menu was altered again to keep up with the ever-changing luminosity conditions in the LHC. To reduce effects from pileup, for example, the shower shape (R_{had}, R_{η}) cuts for were loosened, and tighter cuts on shower widths ($w_{\eta 2}$, w_{stot}) and E_{ratio} were implemented. Figure 5.2 shows a comparison of the `++` efficiencies for 2011 and 2012 data, as a function of the number of reconstructed primary vertices. The robustness of the 2012 ID selections with respect to pileup effects is clearly improved compared with the 2011 results.

For both analyses discussed later, electrons passing the `medium++` and `tight++` criteria are the only collections used.

5.2 Photons

Similarly to electrons, photons play a major role in many SM and new physics processes. Indeed, the combinatoric diphoton background is a major component of the Higgs search in the $H \to \gamma\gamma$ channel, and precise measurement of direct photon production is important for the study of perturbative QCD. The identification of prompt photons at a hadron collider is faced with many challenges, however, since an overwhelming fraction of photons detected are from neutral hadron decays (*e.g.*, in $\pi^0 \to \gamma\gamma$) or from initial or final state radiation originating from other electromagnetic particles.

Photon reconstruction [58] proceeds in a similar fashion to electrons, as they have obvious similarities from the calorimeter signal point of view. However, there are some complicating features to the reconstruction, since photons can be classified as either

"converted" or "unconverted." Converted photons, having undergone an interaction with an electron, result in electrons originating from some vertex inside the ID volume. Thus, converted photons have at least one track matching their EM calorimeter clusters, whereas unconverted photons are characterized by their lack of matched tracks. As a result of these features, there is a clear ambiguity in reconstruction of electrons and converted photons that has to be resolved, as explained in the following.

The first step in reconstructing a converted photon is performing vertex reconstruction, and looking for conversion vertices in the inner detector volume. Conversion vertices can be double- or single-track vertices. Double-track vertices are reconstructed by performing a vertex fit with the two tracks, assuming the parent particle (the photon) is massless ($m_\gamma = 0$). In contrast, single-track vertices are found typically at larger radial values, and are due either to an asymmetric electron pair with one of them being too soft for track reconstruction or to both electrons being highly collimated and not well separated. In this case, the vertex is simply placed at the point of the first momentum measurement of the track.

After classification of the conversion vertex as single- or double-track, the candidate is matched to an EM cluster [55] using matching in (η, ϕ). A window of 0.05 is required on each side of the track impact point in both coordinates, with the exception that, in the case of Bremsstrahlung radiation from one of the tracks, a window of 0.1 is used for the ϕ coordinate on the side affected by the Bremsstrahlung. After this matching is performed, the full set of conversion photons has been considered, but they are all simultaneously reconstructed as electrons at this stage, and thus have to be recovered. Clusters in the EM calorimeter without tracks are simply reconstructed as unconverted photons.

To recover the converted photons from the electron collection, a search through the electron candidates is performed to find tracks emanating from a conversion vertex. Once found, the best track from a conversion vertex is then checked against tracks coming from the best conversion vertex associated with a EM cluster. If the track matches any of the cluster tracks, then this object is considered a conversion photon. Otherwise, it remains in the electron collection. Furthermore, if an electron track is reconstructed using only hits from the TRT, while also having $p_{\mathrm{T}} > 2$ GeV and $E/p < 10$, it is marked as a converted photon. The photon clusters are then rebuilt, using a larger cluster size to accommodate larger showers in the ϕ coordinate. Finally, the conversion vertices are re-reconstructed, correcting for Bremsstrahlung effects.

As in the case of electrons, photon identification is of crucial importance for discriminating against backgrounds. A two level identification scheme has been

implemented to separate real, isolated photons from QCD jets, the most common fakes. Most of the variables used for the `loose` and `tight` photon selection criteria are the same as in the electron ID criteria, with the notable difference that track quality cuts are not used in the case of photon ID.

The `loose` photon ID criteria [58] impose requirements on $\mathbf{R_{had1}}$, $\mathbf{R_{had}}$, $\mathbf{R}_\eta$, and $\mathbf{w}_{\eta\mathbf{2}}$. See the definitions of these quantities in Section 5.1. Similar performance is found for this ID classification for both converted and unconverted photons. The more stringent photon ID requirements are found in the `tight` criteria, which are a superset of the `loose` selections. The cuts defined for `loose` photons are also present for the `tight` level, but with stricter requirements. The `tight` photon selection also relies on familiar quantities from electron ID, such as $\mathbf{w_{stot}}$ and $\mathbf{E_{ratio}}$. However, there are additional variables used for photons that are not used in the electron case.

$\mathbf{R}_\phi$ ratio of energies in 3×3 cells to those of 3×7 cells

$\mathbf{w_{s3}}$ shower width for the three EM calorimeter strips around the strip with maximum energy in the EM cluster

$\mathbf{F_{side}}$ the fraction of energy found outside the three core strips of the EM cluster, but within seven strips

$\mathbf{\Delta E}$ energy difference between second maximum strip energy and smallest strip energy between first and second maximum strips

These variables and their cuts are optimized for rejecting leading isolated neutral pions (π^0), and are separately optimized for converted and unconverted photons. Additionally, acceptance cuts are required ($|\eta| < 2.37$ and $1.37 < |\eta| < 1.52$) such that the photon is found in a region with a finely segmented first calorimeter layer.

Figure 5.3 shows the performance of the photon ID requirements, for both unconverted and converted photons. The photons used in Chapter 6 are all required to pass the `tight` selection criteria.

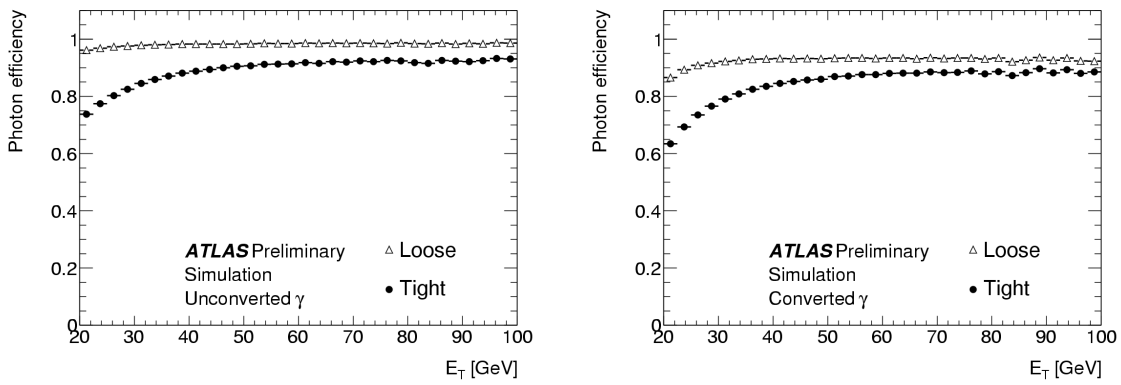

Figure 5.3: Photon identification efficiencies for the `loose` and `tight` selections, as a function of photon E_{T}, for unconverted (left) and converted (right) photons.

5.3 Muons

The ATLAS Muon Spectrometer allows for robust muon detection and triggering, and provides coverage out to $|\eta| < 2.7$. Using tracking algorithms in the MS and the ID, four muon candidate types are used in ATLAS [59, 60]:

Stand-alone the momentum and trajectory for stand-alone (SA) muons is only reconstructed in the MS. The momentum is corrected for the muon energy loss in the calorimeter system (to acquire the momentum at the IP), and the direction and impact parameter information is determined by extrapolation through the B-field from the MS to the IP.

Combined the SA muon momentum is combined with a measurement of momentum from the ID. The ID track is used for the direction and impact parameter measurements.

Segment-tagged without a fully-reconstructed MS track, an ID track can be extrapolated to the MS and associated with segments in the muon chambers.

Calorimeter-tagged similar to a segment-tagged muon, except that the ID track is associated with calorimeter deposits consistent with a muon, a minimum-ionizing particle.

For the purposes of the analyses presented in later chapters, only combined and segment-tgged muons will be used, so calorimeter-tagged muons will not be discussed

further. For all the muon types, two reconstruction chains were maintained for ATLAS analyses for early data-taking. These chains are known as STACO, or Chain 1 [61], and MUID, or Chain 2 [62]. For simplicity, only the STACO algorithm will be described in detail, as this is the muon track reconstruction algorithm used in the analyses presented in Chapters 6 and 7.

STACO (STAtistical COmbination) relies on performing the combination of a track from the ID with a track from the MS, using knowledge of the individual track parameters and their associated covariances. In general, the ID and MS measurements provide independent track parameter vectors, P_{ID} and P_{MS}. Each of these vectors then has a corresponding covariance matrix, called C_{ID} and C_{MS}[2]. The solution to the parameter vector for the combined track, P, can be found by:

$$C^{-1}P = \left(C_{\mathrm{ID}}^{-1} + C_{\mathrm{MS}}^{-1}\right) P = C_{\mathrm{ID}}^{-1} P_{\mathrm{ID}} + C_{\mathrm{MS}}^{-1} P_{\mathrm{MS}}, \tag{5.1}$$

and the corresponding χ^2 is expressed as:

$$\chi^2 = (P - P_{\mathrm{ID}})^T C_{\mathrm{ID}}^{-1} (P - P_{\mathrm{ID}}) + (P - P_{\mathrm{MS}})^T C_{\mathrm{MS}}^{-1} (P - P_{\mathrm{MS}}). \tag{5.2}$$

The combination in Equation 5.1 is performed at the point of closest approach to the beam, and the parameter vectors use the perigee representation commonly used in tracking algorithms. The individual tracking parameters for the ID and MS are reconstructed by the iPatRec and MuonBoy packages, respectively.

The preliminary ID/MS matching is done with (η, ϕ) matching. Then, the combination of tracks is attempted, and is accepted if its χ^2 is below some threshold. In case of ambiguities, the pair of tracks with the minimum χ^2 is flagged as combined, and the individual tracks removed from the ID/MS tracks to be considered for combination. The algorithm iterates over these tracks until no more ID/MS pairs exist to combine.

For STACO segment-tagged muons, the MuTag algorithm is used [63]. MuTag is designed to tag ID tracks and merge them with segments from the MS. Low p_{T} muons that make it through the calorimeters can have challenging trajectories for reconstruction because of the toroidal field. Thus, MuTag can help to recover muon reconstruction efficiency at low p_{T}. Furthermore, some regions (for example, around $|\eta| \sim 1.1$) are constructed with fewer precision chambers, making full reconstruction challenging. For these poorly equipped regions, MuTag helps to increase tracking efficiency. MuTag is run after the combined muon algorithm.

[2]In general, $C = \mathrm{cov}(X_i, X_j) = E\left[(X_i - \mu_i)(X_j - \mu_j)\right]$, where μ_i is the expectation value of X_i.

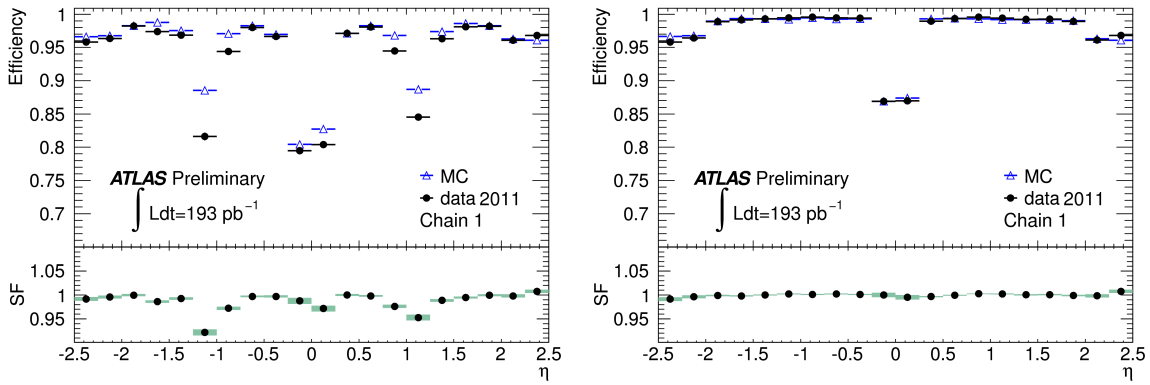

Figure 5.4: The muon identification efficiency versus pseudorapidity for combined (left) and combined+segment-tagged muons (right) in the STACO chain, or Chain 1.

Figure 5.4 shows the efficiency of the STACO algorithm, both for combined muons and the collection of combined and segment-tagged muons, as a function of muon η. The gain in efficiency in various $|\eta|$ regions measured when including segment-tagged muons is clearly seen.

5.4 Jets

Jets of hadronic activity are a dominant feature in high-energy proton-proton collisions, due to the process of fragmentation in QCD systems. They are also key ingredients in many analyses for precision SM measurements, as well as searches for new phenomena. Jets in ATLAS are reconstructed from topological clusters [55], and are found with the anti-k_t algorithm [64] with the FastJet software. Due to effects such as hadronic leakage in the detector and multiple parton interactions, a jet energy scale (JES) is applied to the reconstructed jets to correct them to their true energies, and not simply the measured EM-scale energies.

The reconstructed jets used in this work are seeded by topological clusters of hadronic calorimeter cells. The use of topo clusters takes full advantage of the finely-segmented nature of the hadronic calorimeter. The cluster algorithm proceeds in several steps. First, a collection of seed cells is formed for each event. A seed cell is one for which there is a signal to noise ratio satisfying $S/N \geq 4$. S/N is defined as the absolute value of the measured cell energy divided by the RMS of a cell-specific energy distribution for events triggered randomly. This collection of seed cells is sorted by S/N, and an iterative procedure forms jet candidates for each cell in the collection. For each seed cell, neighbor cells having $S/N \geq 2$ are added. Then, all cells surrounding

the proto-cluster are added, regardless of the S/N value. For the resultant topocluser, the energy computed is simply the sum over energies of the constituent cells. The mass is taken to be zero, and the direction (η, ϕ) is computed as an energy-weighted average of the (η, ϕ) values of the cells. In contrast to the sliding window algorithms used for clustering EM objects (see Sections 5.1 and 5.2), the topocluster algorithm results in clusters of variable sizes. In the case that two individual hadronic showers overlap, a cluster splitting algorithm is run to try and recover both signals separately.

With the clusters reconstructed, the next step in jet identification is to run a jet-finding algorithm. ATLAS uses the anti-k_t algorithm, part of a broader class of sequential recombination jet algorithms that includes the k_t and Cambridge/Aachen approaches [64]. The anti-k_t algorithm relies on the definition of two distance parameters,

$$d_{ij} = \min(\frac{1}{k_{ti}^2}, \frac{1}{k_{tj}^2})\frac{(y_i - y_j)^2 + (\phi_i - \phi_j)^2}{R^2}, \tag{5.3}$$

and

$$d_{iB} = \frac{1}{k_{ti}^2}. \tag{5.4}$$

d_{ij} serves as a measure of the separation between the i^{th} and j^{th} clusters, and d_{iB} represents the distance between the i^{th} cluster and the LHC beam. y_i (ϕ_i) is the rapidity (azimuthal angle) of the i^{th} cluster, and R is a parameter chosen as input to the algorithm (ATLAS uses $R = 0.4, 0.6$). For each pair of clusters, d_{ij} is computed, and compared to d_{iB}. If $d_{ij} < d_{iB}$, then the clusters i and j are combined, and form a new cluster. Then, the next-closest cluster j is chosen, and the comparison is made again. This procedure repeats until $d_{iB} < d_{ij}$, at which point cluster i is called a jet, and the constituent clusters are removed from the list to be considered. This process begins again with the next most energetic cluster, and is repeated until no clusters remain.

A notable benefit of the anti-k_t algorithm is the resilience of jet boundaries to soft radiation. Thus, soft divergences are avoided, because softer particles tend to cluster with harder particles. The R parameter describes the radius of the perfectly conical jet that results from a hard cluster having no hard neighbors within a distance of $2R$.

Jets in ATLAS analyses must satisfy several quality requirements in order to minimize contamination from fake jets due to detector problems or non-collision backgrounds [65]. Before this, however, the jets are calibrated to a certain energy scale to account for the non-compensating nature of the ATLAS calorimeters. The response for jets in ATLAS reconstruction is defined as the ratio of measured energy to the true jet energy, $R = E^{\text{reco}}/E^{\text{truth}}$. This value is usually be less than one when

reconstructing jets at the detector measurement level. Reconstruction inefficiencies and energy loss outside the calorimeter will lower the response value, and this effect must be accounted for.

The 2011 analysis presented in Chapter 6 makes use of the `AntiKt4TopoEM` jet collection, which contains jets calibrated with the so-called EM+JES approach [66]. EM+JES jets are reconstructed first without corrections (*i.e.*, at the electromagnetic scale), after which the energy and direction of the jets are adjusted for several effects. First, an energy correction is applied to account for extra energy in the calorimeters due to additional $p-p$ interactions in an event. The average expected energy from these interactions is measured *in situ*, and is subtracted from the measured energy. Next, the jet direction is recomputed such that the jet originates from the measured primary vertex, instead of the geometrical center of the detector (the standard origin for jet reconstruction). Finally, the energy and direction are both corrected with constants derived from comparisons between reconstructed jet kinematics and the corresponding truth information from MC simulations. These JES corrections are parametrized as a function of energy and pseudorapidity. At this point, EM+JES jets are ready for use in analysis.

The 2012 analysis presented in Chapter 7 employs jets from the `AntiKt4LCTopo` jet collection. These jets are calibrated with a local cell weighting (LCW) technique, which provides a more complex and robust way of accounting for the non-compensating nature of the detectors. In LCW jets, the corrections are applied at the calorimeter cell and topocluster level (as opposed to at the jet object level, as in EM+JES jets). Non-compensation, dead material, and deposits of energy outside the clusters are all corrected in separate steps. After this, the jets are re-built with the corrected clusters. In LCW jets, a (E, η)-dependent JES correction is still needed, but is numerically smaller than in the case of jets at the EM scale. At this point, these LCW+JES are analysis-ready.

A schematic briefly illustrating the reconstruction flow for both kinds of jets can be found in Figure 5.5.

5.5 Missing transverse energy

The missing transverse energy (the magnitude of the missing transverse momentum), or $E_{\mathrm{T}}^{\mathrm{miss}}$, is a quantity of crucial importance in ATLAS analyses. In particular, for searches for R-parity conserving SUSY signal, a keen understanding of this value

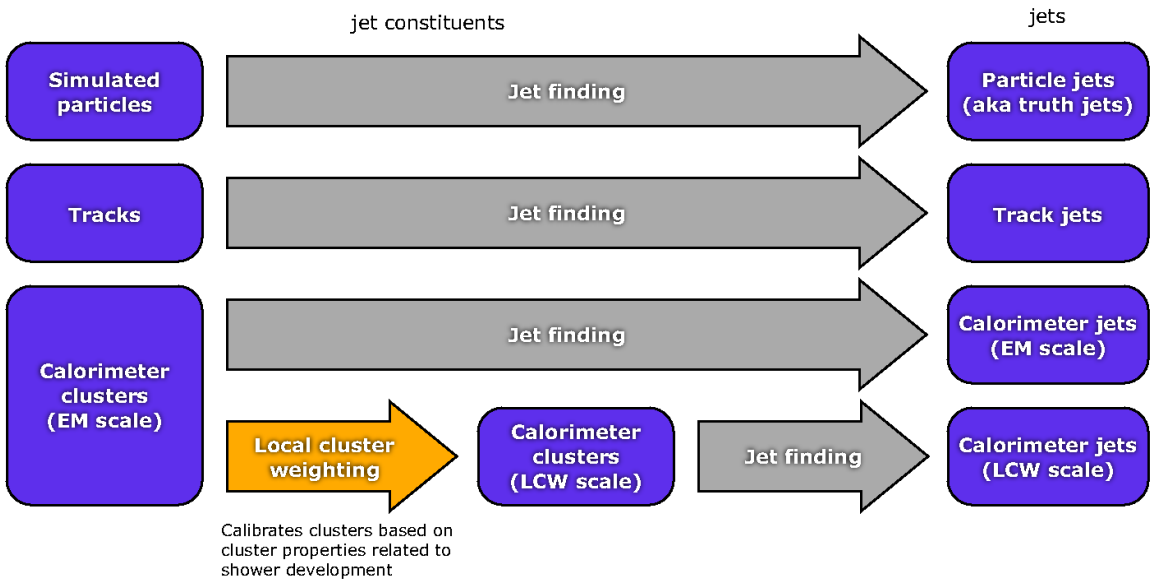

Figure 5.5: The ATLAS jet reconstruction scheme [66].

is paramount, given that excesses in this distribution may be due to new physics processes. $E_{\mathrm{T}}^{\mathrm{miss}}$ is defined as the overall imbalance in transverse energy in an event. Since $\vec{p_{\mathrm{T}}} = 0$ before the $p-p$ collision, it is expected to be the same after summing up the momenta of all particles in the event. However, if some particles, such as neutrinos or many possible theoretical particles, escape without detection, the signature will arise in the $E_{\mathrm{T}}^{\mathrm{miss}}$ quantity. As such, it is important that the reconstruction of $E_{\mathrm{T}}^{\mathrm{miss}}$ be minimally impacted by incomplete detector coverage, poor resolution, or noisy detectors. These effects would contribute to fake values of $E_{\mathrm{T}}^{\mathrm{miss}}$, or $E_{\mathrm{T}}^{\mathrm{miss,fake}}$. For the analyses presented in this work, two $E_{\mathrm{T}}^{\mathrm{miss}}$ algorithms are relevant in ATLAS reconstruction. For 2011, a cell-based $E_{\mathrm{T}}^{\mathrm{miss}}$ reconstruction was used, while a physics object-based $E_{\mathrm{T}}^{\mathrm{miss}}$ was the standard for 2012 [67].

In general, the x- and y-components of the missing energy are calculated, known as E_x^{miss} and E_y^{miss}, respectively. Typically, however, the polar representation is used, resulting in a value of $E_{\mathrm{T}}^{\mathrm{miss}}$ and ϕ^{miss}, computed as

$$E_{\mathrm{T}}^{\mathrm{miss}} = \sqrt{\left(E_x^{\mathrm{miss}}\right)^2 + \left(E_y^{\mathrm{miss}}\right)^2} \tag{5.5}$$

and

$$\phi^{\mathrm{miss}} = \tan^{-1}\left(\frac{E_y^{\mathrm{miss}}}{E_x^{\mathrm{miss}}}\right). \tag{5.6}$$

Since the assumption is that the transverse energy components must sum to 0, $E_{x,y}^{\mathrm{measurements}} + E_{x,y}^{\mathrm{miss}} = 0$, the calculation of $E_{\mathrm{T}}^{\mathrm{miss}}$ involves taking the values of mea-

surements in the detector and applying a factor of -1, since $E_{x,y}^{\text{miss}} = -E_{x,y}^{\text{measurements}}$.

Both approaches to $E_{\text{T}}^{\text{miss}}$ calculation will be described in the following sections.

5.5.1 Cell-based $E_{\text{T}}^{\text{miss}}$

The cell-based calculation is known as `MET_LocHadTopo`. The calculation is a sum of three contributions:

$$E_{x,y}^{\text{miss}} = E_{x,y}^{\text{miss,calo}} + E_{x,y}^{\text{miss,cryo}} + E_{x,y}^{\text{miss,muon}} \tag{5.7}$$

As the terms imply, a contribution is taken from the calorimeter system, from the energy loss in the cryostat structure between the LAr and tile calorimeters, and from the muon system.

The first term in the sum in Equation 5.7 represents the $E_{\text{T}}^{\text{miss}}$ contribution from calorimeter cells,

$$E_{x,y}^{\text{miss,calo}} = -\sum_{\text{cells}} E_{x,y}. \tag{5.8}$$

The sum iterates over all cells in clusters used to reconstruct both electromagnetic and hadronic physics objects. Note that the transverse components are computed using total energy and direction, as

$$E_{x}^{\text{miss,calo}} = -\sum_{\text{i}} E_i \sin\theta_i \cos\phi_i \tag{5.9}$$

and

$$E_{y}^{\text{miss,calo}} = -\sum_{\text{i}} E_i \sin\theta_i \sin\phi_i. \tag{5.10}$$

The muon term is computed using the measured momenta of combined muons measured within $|\eta| < 2.7$:

$$E_{x,y}^{\text{miss,muon}} = -\sum_{\text{muons}} p_{x,y}. \tag{5.11}$$

The energy lost by the muons in the calorimeter is accounted for by the calorimeter term.

To account for the thickness of the cryostat between the LAr and tile calorimeters, a correction is applied that uses the correlation of energies between the last LAr layer and the first hadronic layer. This correction is applied both in the barrel and in the

endcap. The term is defined as

$$E_{x,y}^{\text{miss,cryo}} = -\sum_{\text{jets}} E_{x,y}^{\text{cryo}}(\text{jet}) \tag{5.12}$$

$$= -\sum_{\text{jets}} w^{\text{cryo}}(\text{jet})\sqrt{E_{x,y}^{\text{EM3}}(\text{jet}) \times E_{x,y}^{\text{HAD}}(\text{jet})}, \tag{5.13}$$

where w^{cryo} is a calibration weight for each jet, and $E_{x,y}^{\text{EM3}}$ ($E_{x,y}^{\text{HAD}}$) is the jet energy in the third (first) layer of the EM (hadronic) calorimeter. Although this is a small correction, the cryostat term can contribute up to 5% for jets with $p_{\text{T}} > 500$ GeV. This calculation for $E_{\text{T}}^{\text{miss}}$ can be improved significantly, with a further calibration of the calorimeter cells dependent on the object to which they are associated. This refined calibration for $E_{\text{T}}^{\text{miss}}$ is discussed in the next section.

5.5.2 Object-based $E_{\text{T}}^{\text{miss}}$

The object-based $E_{\text{T}}^{\text{miss}}$ computation, known as `MET_RefFinal` [68], performs a sum similar to the `MET_LocHadTopo` approach (see Equation 5.7), but takes care to calibrate the calorimeter cells used according to the object to which they are associated. Cells are associated with a reconstructed and identified high-p_{T} object in the following order: electrons, photons, hadronically decaying τ leptons, hadronic jets, and muons. In addition, energies from cells not associated to any particular high-p_{T} object are taken into account in a term known as $E_{\text{T}}^{\text{miss,CellOut}}$. The calorimeter term in `MET_RefFinal` is written as

$$E_{x,y}^{\text{miss,calo}} = E_{x,y}^{\text{miss},e} + E_{x,y}^{\text{miss},\gamma} + E_{x,y}^{\text{miss},\tau} + E_{x,y}^{\text{miss,jets}} + E_{x,y}^{\text{miss,softjets}} + E_{x,y}^{\text{miss,calo},\mu} + E_{x,y}^{\text{miss,CellOut}}. \tag{5.14}$$

Similarly to before, these transverse components are taken from sums over all cells (see Equations 5.9 and 5.10), but are now summed separately, allowing for different cells to be calibrated depending on the cluster type. Performing these sums over the object topoclusters allows the $E_{\text{T}}^{\text{miss}}$ reconstruction to suppress contributions from noisy cells, and provides a better resolution for the $E_{\text{T}}^{\text{miss}}$ values.

$E_{x,y}^{\text{miss},e}$, $E_{x,y}^{\text{miss},\gamma}$, and $E_{x,y}^{\text{miss},\tau}$ are reconstructed from cells associated to electrons, photons, and hadronic τ leptons, respectively. $E_{x,y}^{\text{miss},e}$ is calculated using `medium` reconstructed electrons with $p_{\text{T}} > 10$ GeV that use the default EM calibration. $E_{x,y}^{\text{miss},\gamma}$ is calculated from photons passing the `tight` selection criteria having $p_{\text{T}} > 10$ GeV. $E_{x,y}^{\text{miss},\tau}$ is calculated using τ-jets reconstructed with the tightest τ identification

requirements that have $p_{\mathrm{T}} > 10$ GeV. The cells for τ-jets are calibrated with the LCW scheme.

$E_{x,y}^{\mathrm{miss,jets}}$ is reconstructed from cells in topoclusters from jets with a calibrated $p_{\mathrm{T}} > 20$ GeV. These jets are calibrated using LCW calibration, and have the JES correction applied. $E_{x,y}^{\mathrm{miss,softjets}}$ comes from cells in clusters associated with low-p_{T} jets, using the range $7 < p_{\mathrm{T}} < 20$ GeV. These jets are calibrated with the LCW scheme.

$E_{x,y}^{\mathrm{miss,calo},\mu}$ accounts for the energy lost by muons traveling through the calorimeter. However, the true muon momenta must also be included in the calculation of $E_{\mathrm{T}}^{\mathrm{miss}}$. As in the case of `MET_LocHadTopo`, the muon term is a sum over muon momenta,

$$E_{x,y}^{\mathrm{miss,muon}} = -\sum_{\mathrm{muons}} p_{x,y}. \tag{5.15}$$

Care must be taken when computing $E_{x,y}^{\mathrm{miss,calo},\mu}$ to avoid double counting. For the case of isolated muons[3], the p_{T} is taken from the combined muon measurement, which corrects for energy lost in the calorimeter. In this case, $E_{x,y}^{\mathrm{miss,calo},\mu}$ is not added to the calorimeter term in Equation 5.14. For a non-isolated muon, the energy deposited in the calorimeter cannot be separated from the jet deposits. Thus, the MS measurement of the muon p_{T} is used, implicitly adding the $E_{x,y}^{\mathrm{miss,calo},\mu}$ term to the calorimeter $E_{\mathrm{T}}^{\mathrm{miss}}$.

Finally, the `MET_RefFinal` calculation for $E_{\mathrm{T}}^{\mathrm{miss}}$can be written as

$$E_{x,y}^{\mathrm{miss}} = E_{x,y}^{\mathrm{miss,calo}} + E_{x,y}^{\mathrm{miss,muon}}. \tag{5.16}$$

[3]In this case, isolation implies that no jets are found within $\Delta R = \sqrt{(\Delta\eta)^2 + (\Delta\phi)^2} = 0.3$ of a muon.

Chapter 6

Searches for SUSY in the $Z + E_T^{\text{miss}}$ final state with 2011 data

6.1 Introduction

This chapter presents a search for GMSB signals involving at least one Z boson which decays to a pair of muons or electrons in association with large missing transverse energy ($E_{\text{T}}^{\text{miss}}$) using data recorded by the ATLAS detector in 2011, from data periods B through H. The analysis presented here is largely based off the 2011 ATLAS SUSY dilepton search [69], allowing us to employ well-understood MC and data samples. Furthermore, the dilepton analysis provides much of the object definition and event selection used in this search. The three-body gluino decays $\tilde{g} \to q\bar{q}\tilde{\chi}_1^0$ and $\tilde{g} \to q\bar{q}\tilde{\chi}_2^0$ followed by the higgsino-like $\tilde{\chi}_2^0$ decay $\tilde{\chi}_2^0 \to \tilde{\chi}_1^0 f\bar{f}$ and $\tilde{\chi}_1^0$ decay $\tilde{\chi}_1^0 \to Z\tilde{G}$ are expected to lead to final states that are characterised by the presence of at least one Z boson, which decays to a pair of electrons or muons, and large $E_{\text{T}}^{\text{miss}}$. The $E_{\text{T}}^{\text{miss}}$ results from the undetected gravitinos. The main SM backgrounds are the Z/γ^*+jets, $t\bar{t}$, single-top, and diboson processes. The evaluation of the instrumental $Z/\gamma^* +$ jets background, which has $E_{\text{T}}^{\text{miss}}$ that is mostly due to hadronic mismeasurement, was made using a sample of $\gamma +$ jets events. The top quark and diboson backgrounds were estimated using Monte Carlo (MC) simulation.

6.2 Data and Monte Carlo samples

6.2.1 Dataset and Trigger Selection

The analysis is performed using a dataset corresponding to an integrated luminosity of $\int \mathcal{L}\, dt = 1.04$ fb^{-1}.

Parameters	M_1	M_2	$\tan\beta$	$c\tau_{\text{NLSP}}$	μ	$m_{\tilde{g}}$
Values	1 TeV	1 TeV	1.5	0.1 mm	vary	vary

Table 6.1: Parameters of the GGM models used for production at $\sqrt{s} = 7$ TeV.

The trigger strategy adopted here mimics that of the 2011 ATLAS SUSY dilepton analysis [69]. For events in the ee channel, data is collected using the lowest unprescaled electron trigger for the runs considered here: `EF_e20_medium`, which selects events having at least one medium electron with a transverse momentum above 20 GeV. In the $\mu\mu$ channel, we use the `EF_mu18` trigger, which selects events having at least one muon with a transverse momentum above 18 GeV. The same trigger strategy is used for the MC, as well. In addition to the lepton triggers used for the event selection, we employ the use of a single photon trigger, `EF_g40_loose`, in order to collect a $\gamma +$ jets sample for the data-driven estimate of the $Z/\gamma^* +$ jets background (see Section 6.5.2).

Luminosity blocks in the triggered data samples are further required to be included in a Good Runs List (GRL), ensuring that we select events from valid physics runs.

6.2.2 Monte Carlo simulation

The use of MC is important for several reasons: production and simulation of GGM signal events, comparison of the selected data to SM expectation, and for the final evaluation of some backgrounds' contribution in the signal regions. For this analysis, the generation and simulation of signal and background samples is based on the `mc10b` configuration.

The MC events, after generation, are passed to the full ATLAS detector simulation, which uses GEANT4 [70]. Signal and background MC events are reconstructed using standard ATLAS reconstruction software from release 16 [71].

Background MC

As this analysis is largely structured around the 2011 ATLAS SUSY dilepton analysis [69], we have used the same background MC samples, cross sections, and k-factors as defined there.

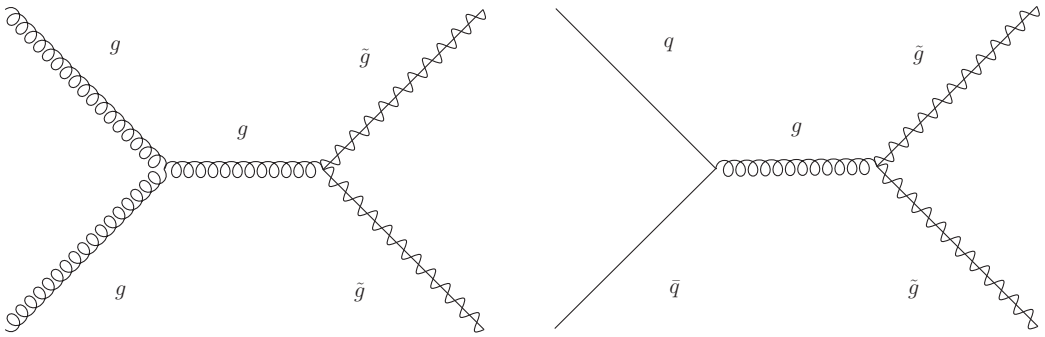

Figure 6.1: Example of gluino pair production.

Signal MC

To interpret the results of this search, we consider GGM higgsino-like neutralino models (see Sections 2.3.2 and 2.3.3). Table 7.1 shows the values of the parameters used for production. The gluino mass and μ (the higgsino mass parameter, also written $m(\tilde{h})$) are free parameters. All unspecified soft SUSY breaking masses are set to 1.5 TeV. The Higgs is in the decoupling regime with $M_{A^0} = 1.5$ TeV. The $\tan\beta$ value of 1.5 was chosen to ensure $\tilde{\chi}_1^0 \to Z\tilde{G}$ is the dominant NLSP decay [31]. We have $BR(\tilde{\chi}_1^0 \to Z\tilde{G}) \sim 97\%$. In this particular region of parameter space, the two lightest neutralinos ($\tilde{\chi}_1^0$ and $\tilde{\chi}_2^0$) and lightest chargino ($\tilde{\chi}_1^\pm$) become higgsino-like. By fixing μ and increasing M_1, M_2 we decouple the $U(1)$ and $SU(2)$ gauginos, leaving behind just the higgsinos. In the limit $(M_1,\ M_2) \to \infty$ we have the exact relations $m(\tilde{\chi}_1^0) = m(\tilde{\chi}_{12}^0) = m(\tilde{\chi}_1^\pm) = \mu$; in practice, M_1 and M_2 are never infinite, of course. For any reasonably large value, the effect of neutralino and chargino mixing will be to push the masses of $\tilde{\chi}_1^0$, $\tilde{\chi}_2^0$ and $\tilde{\chi}_1^\pm$ away from μ.

The full mass spectrum, the gluino branching ratios, and the decay width are calculated from this set of parameters using SUSPECT 2.41 [72] and SDECAY 1.3 [73]. For each signal point, 50000 events were generated with PYTHIA 6.423 [74] which completes the decay table correctly.

In total, 59 signal points in the $m(\tilde{g}) - m(\tilde{h})$ plane are generated. The $\tilde{g}$ mass ranges from 300 to 900 GeV, and the higgsino mass from 110 GeV up to 890 GeV. As an example, the full SUSY particle mass spectrum for the $\mu = 120$ GeV, $m(\tilde{g}) = 300$ GeV signal point is listed in Table 7.7.

Next-to-leading order (NLO) production cross sections for the GGM signal points are calculated with Prospino 2.1 [75]. The mechanisms for superpartner production in these GGM signal points can be grouped into two categories: strong production ($\tilde{g}\tilde{g}$),

Names	Mass Eigenstates	m [GeV]
squarks	$\tilde{u}_L$	1499.63
	$\tilde{u}_R$	1499.83
	$\tilde{d}_L$	1500.45
	$\tilde{d}_R$	1500.08
	$\tilde{s}_L$	1500.45
	$\tilde{s}_R$	1500.08
	$\tilde{c}_L$	1499.63
	$\tilde{c}_R$	1499.83
	$\tilde{t}_1$	1503.84
	$\tilde{t}_2$	1512.23
	$\tilde{b}_1$	1500.02
	$\tilde{b}_2$	1500.52
sleptons	$\tilde{e}_L$	1500.28
	$\tilde{e}_R$	1500.25
	$\tilde{\mu}_L$	1500.28
	$\tilde{\mu}_R$	1500.25
	$\tilde{\tau}_1$	1500.16
	$\tilde{\tau}_2$	1500.38
neutralinos	$\tilde{\chi}_1^0$	110.97
	$\tilde{\chi}_2^0$	120.30
	$\tilde{\chi}_3^0$	1000.00
	$\tilde{\chi}_4^0$	1009.32
charginos	$\tilde{\chi}_1^\pm$	113.30
	$\tilde{\chi}_2^\pm$	1007.14
Higgs bosons	h^0	120.00
	H^0	2004.00
	A^0	2000.00
	$H^\pm$	2002.09

Table 6.2: SUSY particle mass spectrum for the higgsino-like NLSP GGM model which is characterized by the following parameters: $M_1 = 1$ TeV, $M_2 = 1$ TeV, $\mu = 120$ GeV, $\tan(\beta) = 1.5$, $c\tau_{NLSP} = 0.1mm$, $m(\tilde{g}) = 300$ GeV

$m(\tilde{g})$ [GeV]	$m(\tilde{h})$ [GeV]	$m(\tilde{\chi}_1^0)$ [GeV]	$\sigma(NLO)$ [pb]	$\sigma(NLO) \times \epsilon$ [pb]
300	110	101.1	69.56 ± 0.06	13.3 ± 0.6
	115	106.0	68.19 ± 0.06	12.9 ± 0.3
	120	110.9	67.08 ± 0.06	12.8 ± 0.4
	150	140.7	63.56 ± 0.06	12.1 ± 0.4
	200	190.1	61.87 ± 0.06	11.7 ± 0.4
	290	278.9	61.26 ± 0.06	11.4 ± 0.3
400	110	101.1	18.46 ± 0.01	3.5 ± 0.1
	115	106.0	17.09 ± 0.01	3.3 ± 0.1
	120	110.9	15.98 ± 0.01	3.06 ± 0.06
	150	140.7	12.46 ± 0.01	2.4 ± 0.1
	200	190.1	10.77 ± 0.01	2.03 ± 0.04
	300	288.7	10.13 ± 0.01	1.90 ± 0.06
	390	377.1	10.04 ± 0.01	1.86 ± 0.06
500	110	101.1	10.63 ± 0.004	2.02 ± 0.08
	115	106.0	9.26 ± 0.004	1.77 ± 0.05
	120	110.9	8.15 ± 0.003	1.56 ± 0.04
	150	140.7	4.63 ± 0.003	0.88 ± 0.03
	200	190.1	2.94 ± 0.003	0.56 ± 0.02
	300	288.7	2.30 ± 0.003	0.43 ± 0.01
	400	386.9	2.20 ± 0.003	0.41 ± 0.01
	490	474.7	2.18 ± 0.003	0.405 ± 0.007
600	110	101.1	9.021 ± 0.002	1.69 ± 0.03
	115	106.0	7.655 ± 0.002	1.46 ± 0.06
	120	110.9	6.543 ± 0.002	1.25 ± 0.03
	150	140.7	3.023 ± 0.001	0.58 ± 0.01
	200	190.1	1.330 ± 0.001	0.25 ± 0.01
	300	288.7	0.695 ± 0.001	0.130 ± 0.005
	400	386.9	0.595 ± 0.001	0.111 ± 0.002
	500	484.5	0.571 ± 0.001	0.107 ± 0.004
	590	571.3	0.565 ± 0.001	0.105 ± 0.004
700	110	101.1	8.623 ± 0.002	1.64 ± 0.06
	115	106.2	7.257 ± 0.002	1.38 ± 0.05
	120	110.9	6.145 ± 0.001	1.17 ± 0.03
	150	140.7	2.625 ± 0.001	0.504 ± 0.015
	200	190.1	0.932 ± 0.0003	0.177 ± 0.005
	300	288.7	0.297 ± 0.0002	(55.7 ± 1.7)E-03
	400	386.9	0.197 ± 0.0002	(36.7 ± 0.8)E-03
	500	484.5	0.173 ± 0.0002	(32.4 ± 0.6)E-03
	600	580.9	0.166 ± 0.0002	(30.9 ± 0.6)E-03
	690	666.0	0.164 ± 0.0002	(30.5 ± 0.8)E-03

Table 6.3: The total and effective (*i.e.*, including a $Z(\ell\ell)$ event filter) NLO cross sections for the higgsino-like NLSP grid.

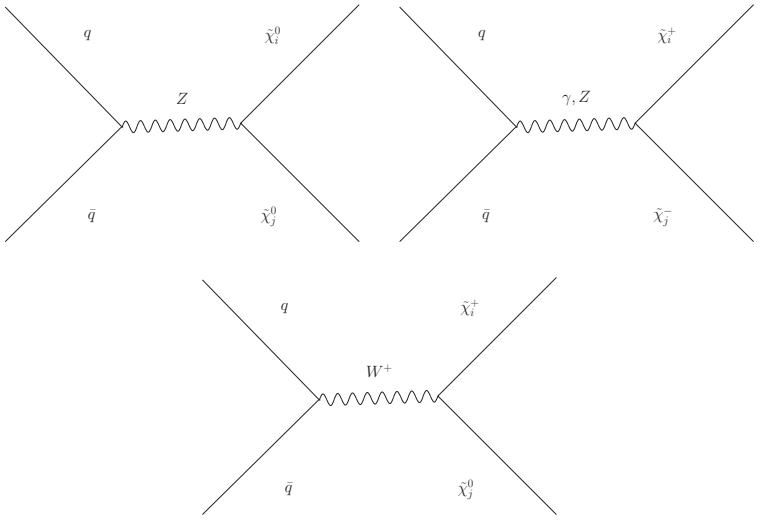

Figure 6.2: Example of electroweak production.

see Figure 6.1, and electroweak production ($\tilde{\chi}_1^0\tilde{\chi}_2^0$, $\tilde{\chi}_1^\pm\tilde{\chi}_1^\mp$, $\tilde{\chi}_1^0\tilde{\chi}_1^\pm$, $\tilde{\chi}_2^0\tilde{\chi}_1^\pm$), see Figure 6.2. All processes are considered for the LO and NLO calculations. CTEQ6.6m and CTEQ6L1 parton density distributions are used for the NLO and LO calculations, respectively. Tables 6.3, 6.4 present the total NLO cross sections for each GGM point. To select events with at least one Z boson which decays to pair of electrons, muons, or taus, the `ZtoLeptonFilter` is used at generator level. The lepton $|\eta|$ is required to be less than 10. This filter has an efficiency of $18.8 \pm 0.5\%$. The effective cross section, after applying the filter efficiency, is also given in Tables 6.3, 6.4.

Table 6.5 shows the NLO cross sections for $\tilde{g}\tilde{g}$ production as a function of $m_{\tilde{g}}$. $\tilde{g}\tilde{g}$ production is expected to have no dependence on higgsino mass. Table 7.6 shows the NLO cross section for the electroweak processes. Electroweak production cross sections depends on the higgsino mass, but there is no gluino mass dependence. The net result of these effects is that the total NLO cross section depends on both gluino and higgsino masses.

6.3 Object definitions

As this analysis overlaps largely with the 2011 ATLAS SUSY dilepton analysis, most of these definitions are identical to those given in [69]. For simplicity, we provide here the details of the object definitions for those which are distinct from the dilepton analysis, namely photons and $E_{\mathrm{T}}^{\mathrm{miss}}$. $E_{\mathrm{T}}^{\mathrm{miss}}$ is computed using the `MET_LocHadTopo` algorithm. Section 5.5.1 provides details on this calculation. The definitions which

$m(\tilde{g})$ [GeV]	$m(\tilde{h})$ [GeV]	$m(\tilde{\chi}_1^0)$ [GeV]	$\sigma(NLO)$ [pb]	$\sigma(NLO) \times \epsilon$ [pb]
800	120	110.9	6.033 ± 0.001	1.15 ± 0.05
	150	140.7	2.51 ± 0.001	0.48 ± 0.01
	200	190.1	0.8197 ± 0.0002	0.155 ± 0.003
	300	288.7	(184.7 ± 0.08)E-03	0.035 ± 0.001
	400	386.9	(84.75 ± 0.07)E-03	(15.8 ± 0.4)E-03
	500	484.5	(61.37 ± 0.07)E-03	(11.4 ± 0.5)E-03
	600	580.9	(54.64 ± 0.07)E-03	(10.1 ± 0.3)E-03
	700	675.3	(52.24 ± 0.07)E-03	(9.8 ± 0.4)E-03
	790	757.0	(51.22 ± 0.07)E-03	(9.6 ± 0.2)E-03
900	120	110.9	5.999 ± 0.001	1.14 ± 0.02
	150	140.7	2.479 ± 0.001	0.48 ± 0.01
	200	190.1	(785.6 ± 0.2)E-03	0.149 ± 0.003
	300	288.7	(150.6 ± 0.04)E-03	(28.1 ± 0.6)E-03
	400	386.9	(50.65 ± 0.03)E-03	(9.4 ± 0.2)E-03
	500	484.5	(27.27 ± 0.03)E-03	(5.1 ± 0.2)E-03
	600	580.9	(20.54 ± 0.03)E-03	(3.8 ± 0.1)E-03
	700	675.3	(18.35 ± 0.03)E-03	(3.4 ± 0.1)E-03
	800	765.8	(17.59 ± 0.03)E-03	(3.3 ± 0.1)E-03
	890	839.9	(17.20 ± 0.03)E-03	(3.2 ± 0.1)E-03

Table 6.4: The total and effective (*i.e.*, including a $Z(\ell\ell)$ event filter) NLO cross sections for the higgsino-like NLSP grid.

$m(\tilde{g})$ [GeV]	NLO $\sigma(\tilde{g}\tilde{g})$ [pb]
300	61.1 ± 0.06
400	10.0 ± 0.01
500	2.17 ± 0.003
600	0.561 ± 0.001
700	0.163 ± 0.0002
800	(51.2±0.07)E-03
900	(17.1±0.03)E-03

Table 6.5: The NLO cross sections for $\tilde{g}\tilde{g}$ production only.

$m(\tilde{h})$ [GeV]	$\sigma(\tilde{\chi}_1^0\tilde{\chi}_2^0)$ [pb]	$\sigma(\chi_1^\pm\chi_1^\mp)$ [pb]	$\sigma(\tilde{\chi}_1^0\chi_1^\pm)$ [pb]	$\sigma(\tilde{\chi}_2^0\chi_1^\pm)$ [pb]
110	1.06	2.20	2.84	2.36
115	0.88	1.85	2.36	1.98
120	0.74	1.56	1.99	1.68
150	0.29	0.64	0.82	0.706
200	0.09	0.19	0.26	0.226
290	0.017	0.04	0.05	0.047
300	0.014	0.033	0.045	0.040
390	0.004	0.009	0.013	0.012
400	3.5E-03	8.2E-03	0.012	0.010
490	1.1E-03	2.7E-03	0.004	0.0035
500	1.0E-03	2.46E-03	3.56E-03	3.15E-03
590	0.37E-03	0.93E-03	1.35E-03	1.2E-03
600	0.33E-03	0.84E-03	1.22E-03	1.04E-03
690	0.13E-03	0.34E-03	0.49E-03	0.41E-03
700	0.12E-03	0.31E-03	0.45E-03	0.37E-03
790	0.05E-03	0.14E-03	0.19E-03	0.15E-03
800	0.04E-04	0.125E-03	0.17E-03	0.15E-03
890	0.02E-04	0.058E-03	0.08E-03	0.05E-03

Table 6.6: The NLO cross sections for the electroweak processes.

are identical to those used in the dilepton analysis (jets, electrons, and muons) are given in Appendix A.

Photons are reconstructed using the standard clustering algorithm presented in Sections 5.1 and 5.2. Photons must satisfy the `PhotonTightAR` criteria [76] which helps with additional photon/electron discrimination. The p_{T} of photons is required to be greater than 45 GeVand $|\eta^{\mathrm{cl}}| < 1.81$, removing $|\eta^{\mathrm{cl}}| \in [1.37, 1.52]$, where p_T^{cl} (η^{cl}) refer to the p_T (η) of the calorimeter cluster.

As recommended by the egamma group, we exclude photons if their cluster core, defined as the 3×5 cells for unconverted photons in the barrel, the 3×7 cells for converted photons in barrel and the 5×5 cells in the endcap, overlaps with a missing calorimeter Front End Board (FEB) in the first or second layer. We also exclude photons if the cluster core overlaps with a dead HV region. We further exclude photons if there is a dead or masked cell either in the core of the 3×3 cells cluster in the second layer or in the eight central strips in the first layer of the electromagnetic calorimeters. These quality tests area done by using the object quality (OQ) flag "ph_OQ & egammaPID::BADCLUSPHOTON != 0".

Additionally, we apply an isolation requirement that the calorimeter transverse

energy in a cone of $R(\eta, \phi) < 0.4$ around the photon candidate is less than 5 GeV, where the E_T^{cone40} calculation has been corrected for energy leakage and energy density. Furthermore, the photon must pass specific jet-cleaning cuts.

After selecting good quality isolated photons, we then perform overlap removal with electrons and jets. First, if a selected photon overlaps with a selected electron within a radius $\Delta R(e, \gamma) < 0.01$, the electron is removed. Next, if a jet overlaps with a selected photon within $\Delta R(j, \gamma) < 0.2$, the jet is discarded. Finally, if a photon overlaps with selected jets within $0.2 < \Delta R(j, \gamma) < 0.4$, the photon is removed.

6.4 Event selection

6.4.1 Z preselection

Due to dead Front-End-Board (FEB) electronics in the LAr calorimeter (from periods E onwards), the data in the range $-0.1 < \eta < 1.5$ and $-0.9 < \phi < -0.5$ cannot be used. We therefore veto events in data and MC if they contain a jet with $p_T > 20$ GeV[1] or a selected electron (that satisfies object selection) pointing to this $\eta - \phi$ region. We require that the first primary vertex in the event have at least 5 tracks. Since the d_0 and z_0 of the muons considered in the analysis are calculated using this first primary vertex, this cut reduces the chance of selecting a cosmic event. Any event containing a muon which fails the d_0 and z_0 requiremets, mentioned in Appendix A.2, is rejected. Event weights are applied to each signal electron or muon (in MC events only) to correct for the differing electron and muon reconstruction and identification efficiencies in data and MC. Events are selected which contain at least two selected leptons satisfying the leading p_T requirements described above. Figure 6.3 (top) shows the distribution of the $E_{\text{T}}^{\text{miss}}$ for data and MC events after this dilepton selection. Finally, the two leading leptons in the event are required to be opposite-sign same-flavor (OSSF) pairs, with an invariant mass in a Z mass window, $81 < m_{\ell\ell} < 101$ GeV. Figure 6.3 (bottom) shows the $E_{\text{T}}^{\text{miss}}$ distribution after the Z mass requirement.

Three GGM signal points, which represent the endpoints of the $\tilde{g}/\tilde{h}$ mass ranges, are chosen to illustrate the SUSY contribution:

- $m(\tilde{g}) = 300$ GeV, $m(\tilde{h}) = 120$ GeV point represents the region with a relatively low $m(\tilde{g})$ and low mass of $\tilde{h}$, where the $\tilde{g}\tilde{g}$ process is a dominant production mechanism.

[1]For data, the jet p_T threshold is 20×(1-BCH_CORR_JET)/(1-BCH_CORR_CELL) GeV.

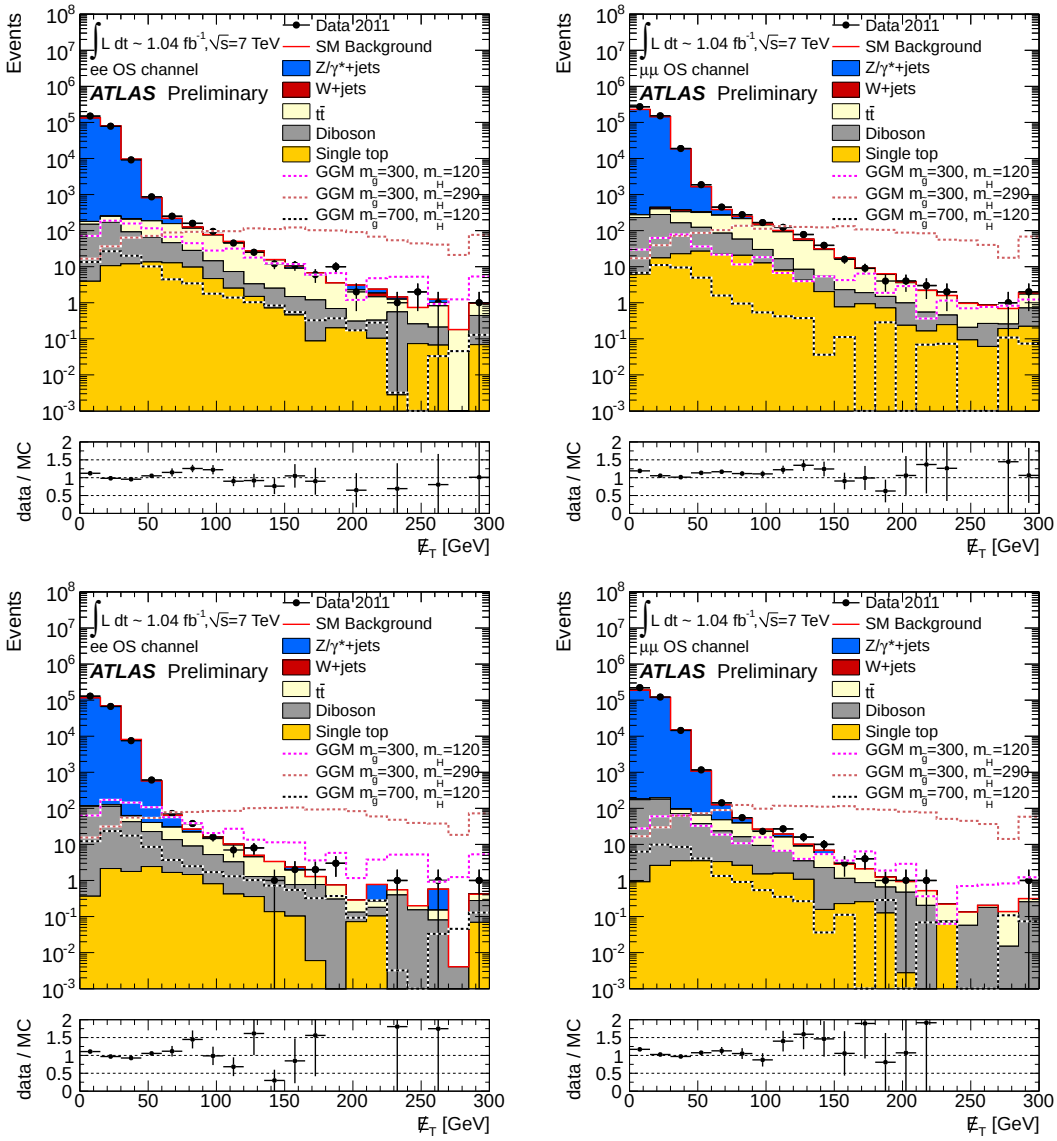

Figure 6.3: Distribution of the $E_{\mathrm{T}}^{\mathrm{miss}}$ for data and MC events after $e^{\pm}e^{\mp}$ (left) and $\mu^{\pm}\mu^{\mp}$ (right) selections (top) and after $Z(e^{\pm}e^{\mp})$ (left) and $Z(\mu^{\pm}\mu^{\mp})$ (right) selections (bottom). Three GGM signal points illustrate the SUSY contribution.

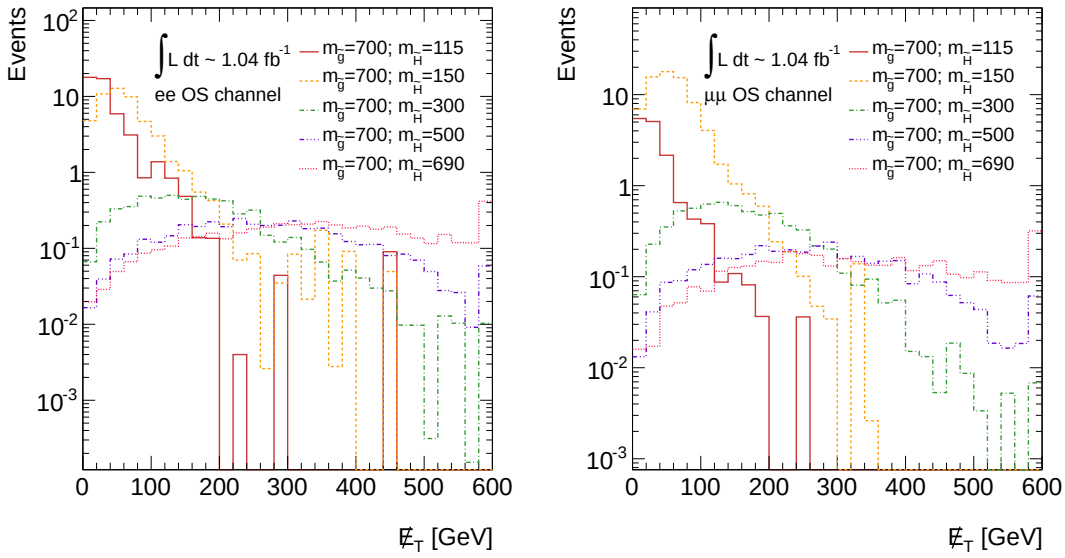

Figure 6.4: Distribution of the $E_{\mathrm{T}}^{\mathrm{miss}}$ for several GGM signal points with $m(\tilde{g}) = 700$ GeV after $Z(e^{\pm}e^{\mp})$ (left) and $Z(\mu^{\pm}\mu^{\mp})$ (right) selections. As can be seen here, for a fixed $m(\tilde{g})$, the $E_{\mathrm{T}}^{\mathrm{miss}}$ distribution gets harder as one increases $m(\tilde{h})$. This is due to the fact that the $\tilde{G}$, the true source of $E_{\mathrm{T}}^{\mathrm{miss}}$, is produced via $\tilde{\chi}_1^0 \to Z\tilde{G}$.

- $m(\tilde{g}) = 700$ GeV, $m(\tilde{h}) = 120$ GeV represents the region where $m(\tilde{g}) \gg m(h)$ with dominant chargino and neutralino pair production mechanism.
- $m(\tilde{g}) = 300$ GeV, $m(\tilde{h}) = 290$ GeV point represents the region $m(\tilde{g}) \approx m(\widetilde{h})$, where the $\tilde{g}\tilde{g}$ process is a dominant production mechanism.

By examining these extrema in the GGM grid, we can see how the SUSY contributions from different kinematic regions behave in distributions of interest. The source of the $E_{\mathrm{T}}^{\mathrm{miss}}$ in the GGM models is $\tilde{G}$, which is produced in the decay $\tilde{\chi}_1^0 \to Z\tilde{G}$. As a result, $E_{\mathrm{T}}^{\mathrm{miss}}$ depends on the $m(\tilde{h})$, which can be illustrated in Figure 6.3. Distributions of jet multiplicity, leading jet p_{T}, leading lepton p_{T}, H_T (scalar sum of the p_{T} of all selected objects in an event) and ΔR between the pair of leading leptons show the agreement between data and MC after Z preselection within the errors over the full range (see Figures 6.5 - 6.10). Reconstructed objects, which satisfy the object selection in Appendix A, were used in histograms.

6.4.2 Signal regions

Due to the different production mechanisms and different kinematics of the GGM grid points, as shown in figures 6.3 - 6.9, different signal regions should be selected to

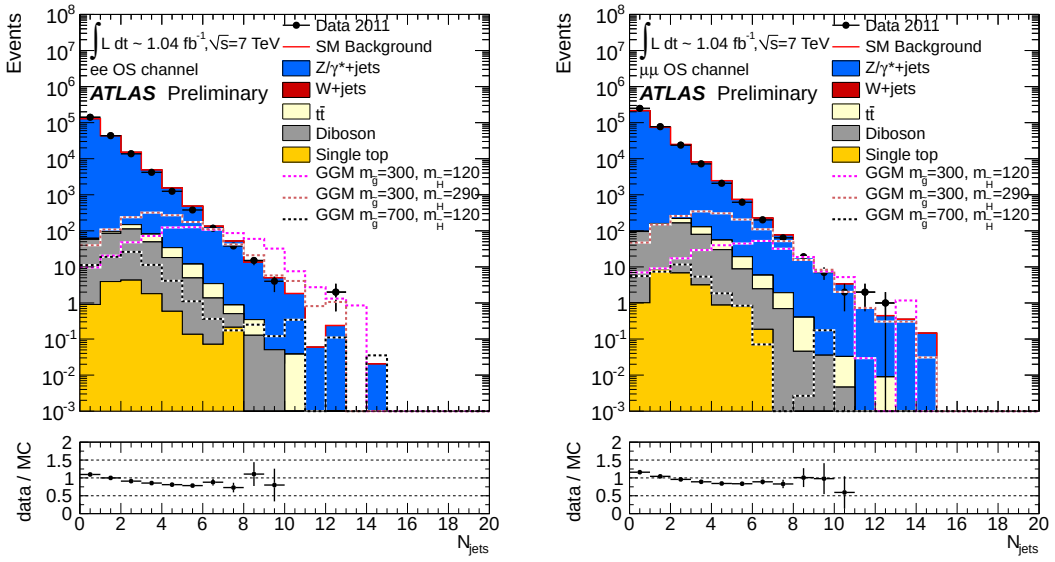

Figure 6.5: Distribution of the jet multiplicity for data and MC events after $Z(e^{\pm}e^{\mp})$ (left) and $Z(\mu^{\pm}\mu^{\mp})$ (right) selections. Three GGM signal points illustrate the SUSY contribution.

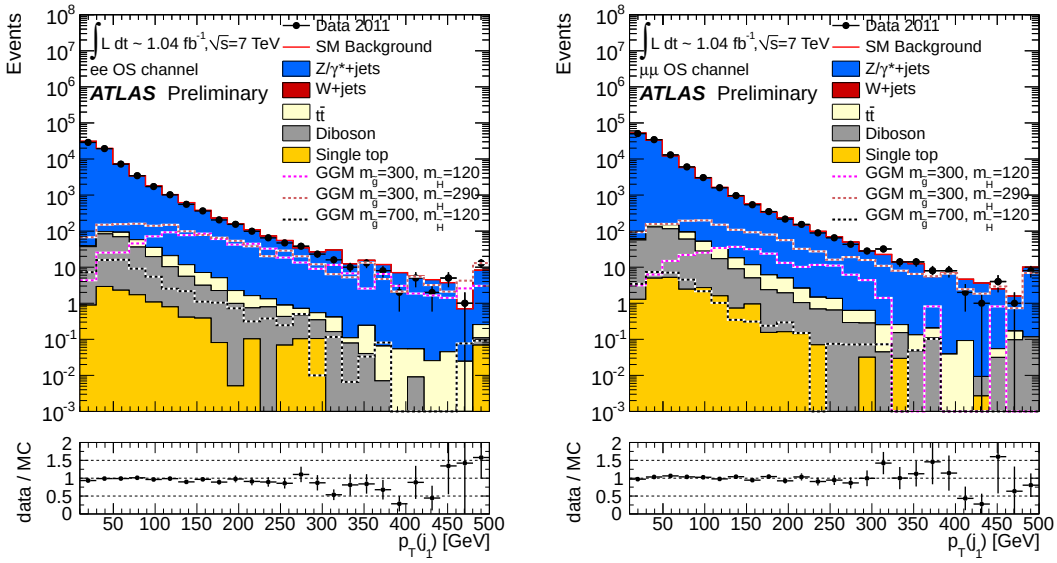

Figure 6.6: Distribution of the p_{T} of the leading jet for data and MC events after $Z(e^{\pm}e^{\mp})$ (left) and $Z(\mu^{\pm}\mu^{\mp})$ (right) selections. Three GGM signal points illustrate the SUSY contribution.

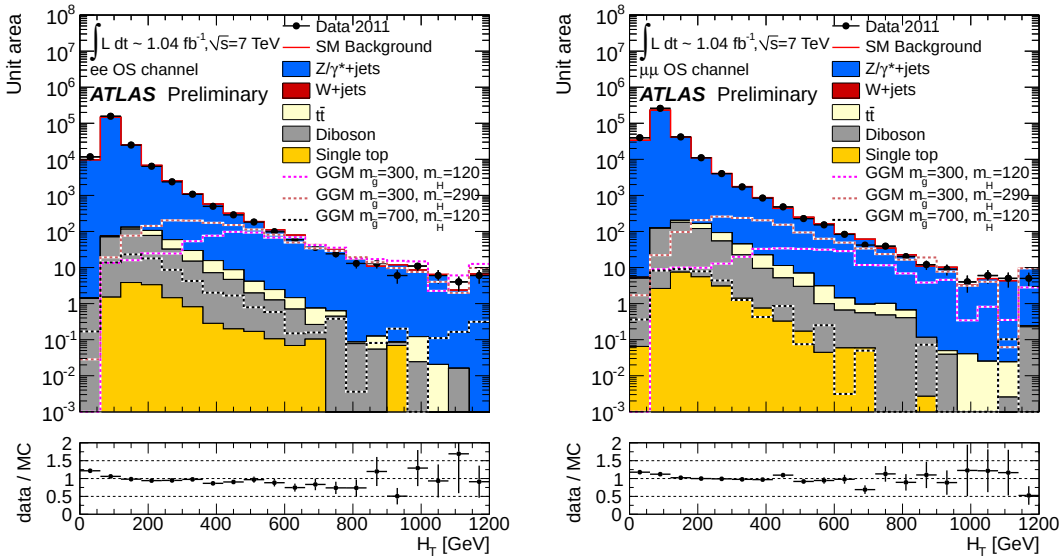

Figure 6.7: Distribution of the H_T for data and MC events after $Z(e^{\pm}e^{\mp})$ (left) and $Z(\mu^{\pm}\mu^{\mp})$ (right) selections. Three GGM signal points illustrate the SUSY contribution.

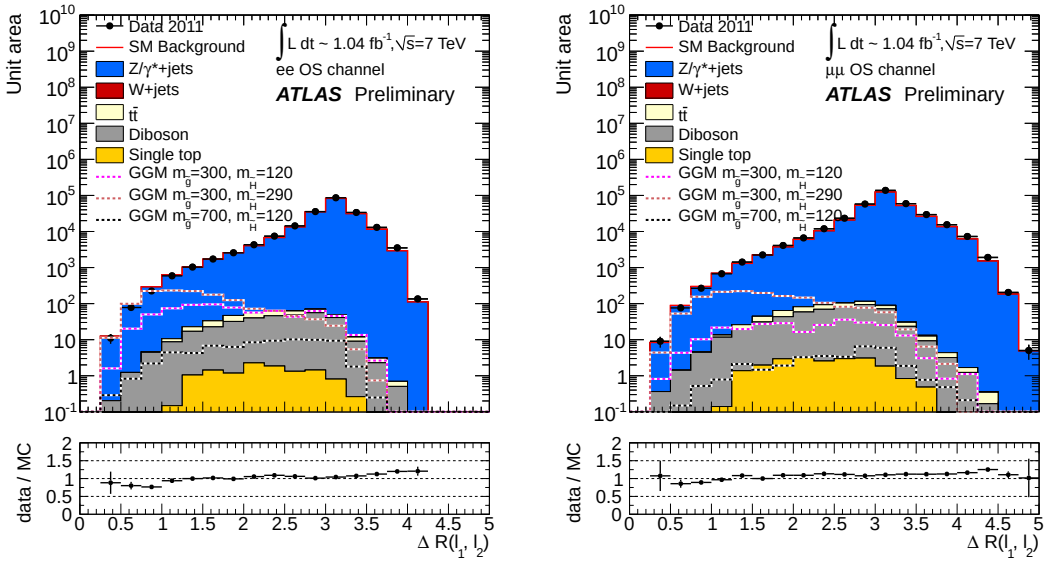

Figure 6.8: Distribution of the ΔR between pair of leading leptons for data and MC events after $Z(e^{\pm}e^{\mp})$ (left) and $Z(\mu^{\pm}\mu^{\mp})$ (right) selections. Three GGM signal points illustrate the SUSY contribution.

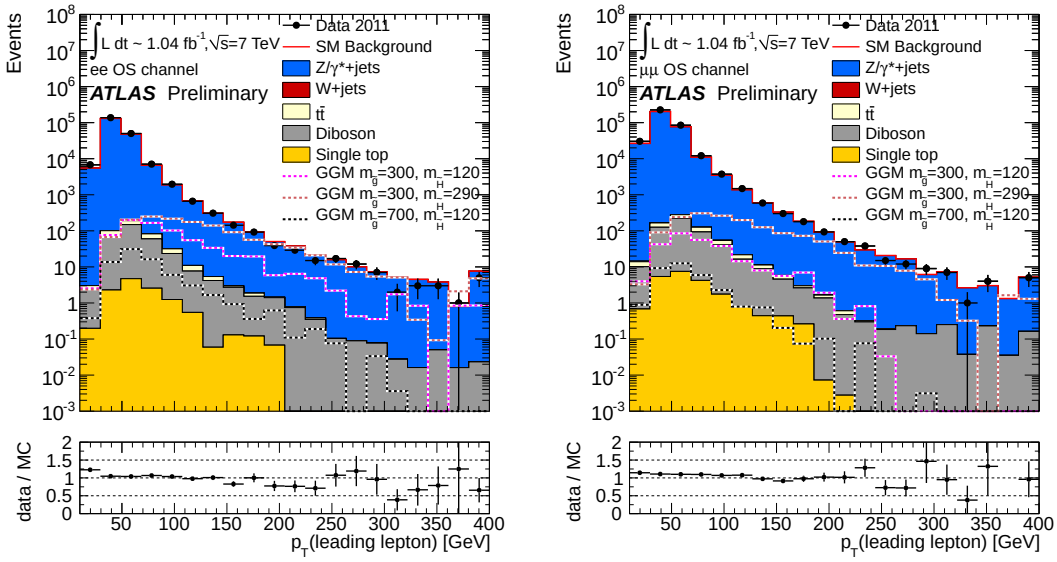

Figure 6.9: Distribution of the p_{T} of the leading lepton for data and MC events after $Z(e^{\pm}e^{\mp})$ (left) and $Z(\mu^{\pm}\mu^{\mp})$ (right) selections. Three GGM signal points illustrate the SUSY contribution.

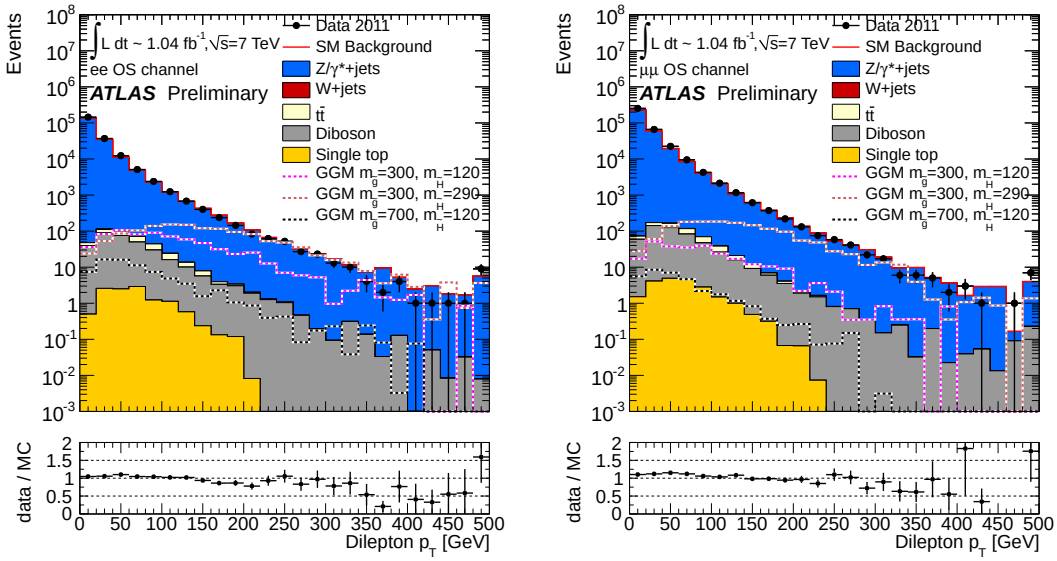

Figure 6.10: Distribution of the p_{T} of Z for data and MC events after $Z(e^{\pm}e^{\mp})$ (left) and $Z(\mu^{\pm}\mu^{\mp})$ (right) preselections. Three GGM signal points illustrate the SUSY contribution.

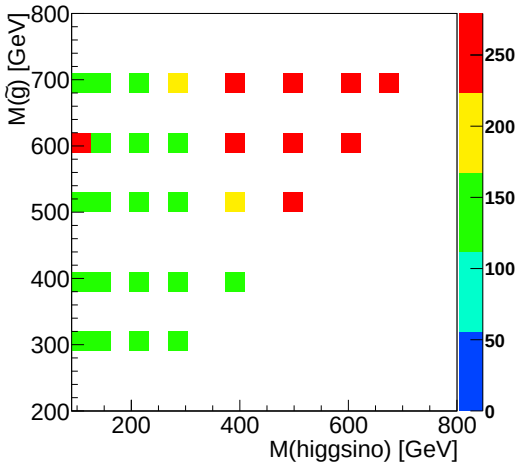

Figure 6.11: Values of the cut on $E_{\mathrm{T}}^{\mathrm{miss}}$ which give maximum reach for each GGM signal point.

optimize the GGM search throughout the parameter space.

For the signal region optimization, we used only $E_{\mathrm{T}}^{\mathrm{miss}}$, H_T and $\Delta R(\ell\ell)$ as discriminating quantities. Choosing more variables would lead to a strong model dependence on GGM kinematics when deciding on the best signal region for each point. The ranges of $0 - 220$ GeV for $E_{\mathrm{T}}^{\mathrm{miss}}$, $50 - 500$ GeV for H_T and $1.6 - 4$ for $\Delta R(\ell\ell)$ were scanned and for each combination of $E_{\mathrm{T}}^{\mathrm{miss}}$, H_T and ΔR the significance was calculated using the following formula:

$$Z_{LLR} = \sqrt{2((S+B)\ln(1+S/B) - S)}, \tag{6.1}$$

where $S(B)$ is the number of signal (SM background) MC events passing the selection. The combination of cuts on $E_{\mathrm{T}}^{\mathrm{miss}}$, H_T and ΔR which provides the maximum significance was chosen for each point. Figure 6.11 shows the values of the cut on $E_{\mathrm{T}}^{\mathrm{miss}}$ which maximize significance for each GGM point. $E_{\mathrm{T}}^{\mathrm{miss}}$ can be divided into two regions, as shown in Figure 6.11. The optimal cut values of H_T and $\Delta R(\ell\ell)$ are presented in Figure 6.12. For most of the grid points with $\tilde{g}\tilde{g}$ dominant production, we have maximum discovery reach with $H_T \backsim 300$ GeV. The grid points dominated by electroweak production have low jet multiplicity and consequently low H_T. With the integrated luminosity used for this analysis, we are not sensitive to these grid points, characterized by low-$m(\tilde{h})$ and high-$m(\tilde{g})$. As such, we will focus primarily on the regions characterized by strong production. Finally, $\Delta R(\ell\ell)$ is used to select events with boosted Z's.

After the optimization, the signal regions are defined as follows:

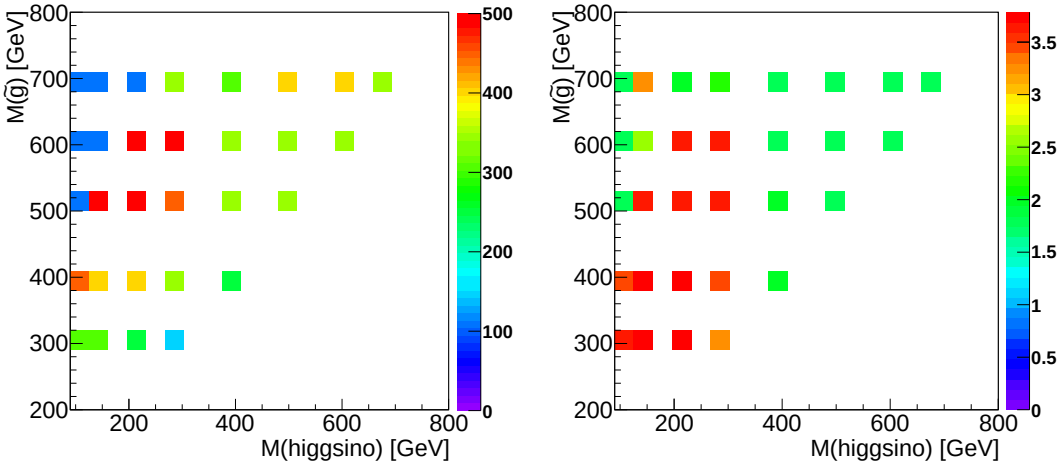

Figure 6.12: Values of the H_T (left) and $\Delta R(\ell\ell)$ (right) which give maximum reach for each GGM signal points.

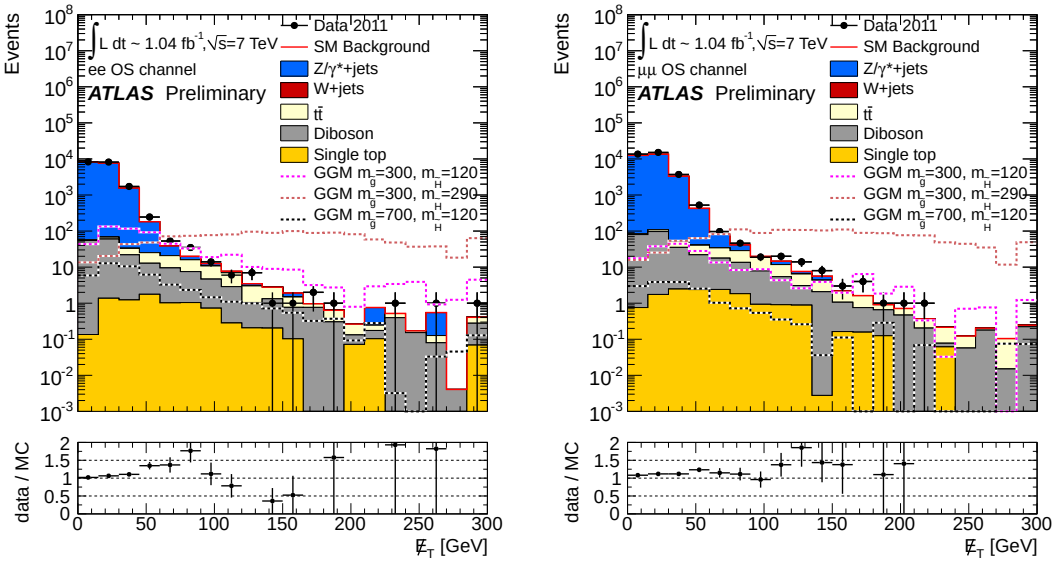

Figure 6.13: Distribution of the $E_{\mathrm{T}}^{\mathrm{miss}}$ for data and MC events after $Z(e^{\pm}e^{\mp})$ (left) and $Z(\mu^{\pm}\mu^{\mp})$ (right) selections and after applying $p_T(Z) > 45$ GeV cut. Three GGM signal points illustrate the SUSY contribution.

SR1		
	ee	$\mu\mu$
Data	2	0
SM total	0.64 ± 0.44(stat.) ± 0.55(syst.)	0.15 ± 0.03(stat.) ± 1.04(syst.)
$Z/\gamma^* + \text{jets}$	0.42 ± 0.42(stat.) ± 0.52(syst.)	0.00 ± 0.00(stat.) ± 1.04(syst.)
$W + \text{jets}$	-	-
$t\bar{t}$	0.12 ± 0.03(stat.) ± 0.11(syst.)	0.15 ± 0.03(stat.) ± 0.10(syst.)
single top	0.10 ± 0.10(stat.) ± 0.15(syst.)	-
dibosons	-	0.00 ± 0.00(stat.) ± 0.10(syst.)
non-Z	0.22 ± 0.11(stat.) ± 0.19(syst.)	0.15 ± 0.03(stat.) ± 0.14(syst.)

Table 6.7: The MC SM background expectations for $\int \mathcal{L}\, dt = 1.04$ fb^{-1}for the ee and $\mu\mu$ channels are shown for SR1, including systematic uncertainties. The final row shows the total non-Z MC expectation.

SR1: $p_T(Z) > 45$ GeV, $E_{\mathrm{T}}^{\mathrm{miss}} > 220$ GeV, and 3 jets with $p_{\mathrm{T}} > 80,\ 40,\ 40$ GeV

SR2: $p_T(Z) > 45$ GeV, $E_{\mathrm{T}}^{\mathrm{miss}} > 140$ GeV, and $H_T > 300$ GeV

SR3: $p_T(Z) > 45$ GeV, $E_{\mathrm{T}}^{\mathrm{miss}} > 140$ GeV, $H_T > 300$ GeV, and $\Delta R(\ell_1, \ell_2) < 2$

The 45 GeV cut on the $p_T(Z)$ is motivated by the data-driven method used to estimate $Z/\gamma^* + \text{jets}$, summarized in section 7.4.3. The distributions of the $E_{\mathrm{T}}^{\mathrm{miss}}$ after Z preselection and $p_T(Z) > 45$ GeV are shown in Figure 6.13.

The other kinematic requirements for each SR are motivated by Figures 6.11 and 6.12. Figure 6.11 shows that there are two clear regions which are optimized by two different cut values for $E_{\mathrm{T}}^{\mathrm{miss}}$. For low-$m(\tilde{h})$ signal points, a lower $E_{\mathrm{T}}^{\mathrm{miss}}$ cut is optimal than for high-$m(\tilde{h})$ points. This is due to the direct relation between $m(\tilde{h})$ and $E_{\mathrm{T}}^{\mathrm{miss}}$. The cuts for SR1 are designed to probe the high-$m(\tilde{h})$ region. In addition, since these cuts, except for the $p_T(Z) > 45$ GeV requirement, are identical to the opposite sign SR2 for the 2011 SUSY dilepton analysis, SR1 provides a chance to compare and validate our results. The cuts for SR2 are designed to probe the low-$m(\tilde{h})$ region, defined with a softer $E_{\mathrm{T}}^{\mathrm{miss}}$ requirement. The additional $\Delta R(\ell_1, \ell_2)$ cut is designed to probe regions with boosted Z's, see Figure 6.12 (right).

The MC estimatons of the SM background for the $e^+e^-$and $\mu^+\mu^-$channels are shown in Tables 6.7, 6.8, and 6.9 for SR1, SR2, and SR3, respectively. The systematic uncertainties, presented in the tables, are described in detail in section 7.5.

SR2		
	ee	$\mu\mu$
Data	4	7
SM total	4.43 ± 0.83(stat.) ± 3.78(syst.)	3.87 ± 0.23(stat.) ± 11.87(syst.)
$Z/\gamma^* + \text{jets}$	1.36 ± 0.78(stat.) ± 3.64(syst.)	0.00 ± 0.00(stat.) ± 11.80(syst.)
$W + \text{jets}$	-	-
$t\bar{t}$	1.79 ± 0.14(stat.) ± 0.99(syst.)	2.71 ± 0.16(stat.) ± 1.29(syst.)
single top	0.45 ± 0.20(stat.) ± 0.23(syst.)	0.26 ± 0.10(stat.) ± 0.09(syst.)
dibosons	0.84 ± 0.14(stat.) ± 0.11(syst.)	0.89 ± 0.13(stat.) ± 0.35(syst.)
non-Z	3.07 ± 0.28(stat.) ± 1.02(syst.)	3.87 ± 0.23(stat.) ± 1.34(syst.)

Table 6.8: The MC SM background expectations for $\int \mathcal{L}\, dt = 1.04$ fb^{-1}for the ee and $\mu\mu$ channels are shown for SR2, including systematic uncertainties. The final row shows the total non-Z expectation.

SR3		
	ee	$\mu\mu$
Data	2	4
SM total	2.87 ± 0.80(stat.) ± 3.27(syst.)	2.13 ± 0.19(stat.) ± 11.51(syst.)
$Z/\gamma^* + \text{jets}$	1.36 ± 0.78(stat.) ± 3.25(syst.)	0.00 ± 0.00(stat.) ± 11.49(syst.)
$W + \text{jets}$	-	-
$t\bar{t}$	0.75 ± 0.09(stat.) ± 0.41(syst.)	1.13 ± 0.12(stat.) ± 0.69(syst.)
single top	-	0.14 ± 0.06(stat.) ± 0.01(syst.)
dibosons	0.77 ± 0.14(stat.) ± 0.08(syst.)	0.86 ± 0.13(stat.) ± 0.30(syst.)
non-Z	1.52 ± 0.16(stat.) ± 0.41(syst.)	2.13 ± 0.19(stat.) ± 0.75(syst.)

Table 6.9: The MC SM background expectations for $\int \mathcal{L}\, dt = 1.04$ fb^{-1}for the ee and $\mu\mu$ channels are shown for SR3, including systematic uncertainties. The final row shows the total non-Z expectation.

6.5 Backgrounds

6.5.1 Non-Z background estimation

The estimates of most of the SM backgrounds ($t\bar{t}$, single-top, dibosons, and W + jets) are taken directly from MC. The SM background samples are weighted to an integrated luminosity of $\int \mathcal{L}\, dt = 1.04$ fb^{-1} using either next-to-next-to-leading order (NNLO) or NLO cross sections, and the results of the signal region selection are shown in Tables 6.7, 6.8, and 6.9 for both the $e^+e^-$and $\mu^+\mu^-$channels.

6.5.2 Z/γ^* + jets background estimation

We present here a data-driven estimate of the Z/γ^* + jets contribution to the signal regions defined for this analysis.

After Z preselection, one of the dominant SM backgrounds is Z/γ^* + jets. Since we are only considering Z decays to electrons or muons, there is no source of real $E_{\mathrm{T}}^{\mathrm{miss}}$. The $E_{\mathrm{T}}^{\mathrm{miss}}$ in these events mostly stems from mismeasurement of the reconstructed objects. Therefore, we do not trust the modeling of the instrumental $E_{\mathrm{T}}^{\mathrm{miss}}$ in Z/γ^* + jets from MC. Instead, we used a data control sample of γ + jets events, which have a similar topology as Z/γ^* + jets events. Contamination from sources with real $E_{\mathrm{T}}^{\mathrm{miss}}$, such as W + jets, $t\bar{t}$, dibosons, and single-top, is subtracted from the photon data sample.

The method utilizes templates, performing a fit of the $E_{\mathrm{T}}^{\mathrm{miss}}$ distributions of two background components, Z/γ^* + jets and non-Z sources, to that of the Z-preselected data. The γ + jets sample is used as a template for the Z/γ^* + jets component. The template for the non-Z sources comes from MC. This method consists of several steps, which will be discussed in detail in the following sections. The steps to be completed are as follows:

1. selection of the control sample,
2. subtraction of the events with real $E_{\mathrm{T}}^{\mathrm{miss}}$,
3. acquiring template for modeling Z/γ^* + jets component,
4. the template fit.

Selection of the control sample

Since the signal regions for this analysis are based on a $E_{\mathrm{T}}^{\mathrm{miss}}$ cut, we need to ensure that we have an adequate description of the $E_{\mathrm{T}}^{\mathrm{miss}}$ in background events. In the $Z/\gamma^* + \mathrm{jets}$ process, there is no source of real $E_{\mathrm{T}}^{\mathrm{miss}}$, considering Z decays to electrons or muons only. $E_{\mathrm{T}}^{\mathrm{miss}}$ in these events is dominated by effects of jet mismeasurement. Standard Model $\gamma + \mathrm{jets}$ events are similar in that a high p_T boson recoils against the hadronic system in the transverse plane. Therefore, $\gamma + \mathrm{jets}$ events are natural candidates to use for modeling the tail of $E_{\mathrm{T}}^{\mathrm{miss}}$ in $Z/\gamma^* + \mathrm{jets}$ events.

The photon data sample is collected using the `EF_g40_loose` photon trigger, which selects a stream of photon events using a p_{T}threshold of 40 GeV. The standard photon selection, described in Section 6.3, is applied on the photon data sample. Each event is required to have exactly one photon candidate with p_{T}greater then 45 GeV. The latter cut is necessary to have uniform trigger efficiency. The $E_{\mathrm{T}}^{\mathrm{miss}}$ distribution of the photon sample is plotted in Figure 6.14 (left). In addition, the $E_{\mathrm{T}}^{\mathrm{miss}}$ distributions after applying the non-$E_{\mathrm{T}}^{\mathrm{miss}}$ cuts for both SR1 and SR2 are shown in the same plot. Alternatively, one could consider using $\gamma\gamma + \mathrm{jets}$ events, considering the two photons in analogy to the two decay products of the Z. Figure 6.14 (right) shows the $E_{\mathrm{T}}^{\mathrm{miss}}$ distributions of data after $\gamma\gamma$ and signal region selections. The lack of statistics in the $\gamma\gamma$ sample at high $E_{\mathrm{T}}^{\mathrm{miss}}$ range prevents us from using this sample in the method.

Since the `L2_g40_loose` photon trigger was prescaled during the much of 2011 data taking, the effect of the prescale on the shape of the $E_{\mathrm{T}}^{\mathrm{miss}}$ distribution was investigated. For this purpose we used three runs from periods B, F and H with different prescale scenarios. The $E_{\mathrm{T}}^{\mathrm{miss}}$ distributions of the single photon samples from these runs have a good agreement in their shapes. This suggests that the different prescale scenarios do not affect the shape of the $E_{\mathrm{T}}^{\mathrm{miss}}$ distribution.

Subtraction of the events with real $E_{\mathrm{T}}^{\mathrm{miss}}$

Due to bremsstrahlung and electron-photon conversion, there is some probability for an electron to be misidentified as a tight photon. As a result, events from $W + \mathrm{jets}$, $t\bar{t}$, diboson, and single top processes, which have real $E_{\mathrm{T}}^{\mathrm{miss}}$, contaminate the control sample, rendering it invalid for the estimation of the instrumental $Z/\gamma^* +$ jets background. The fraction of the photon events with misidentified electrons was estimated using two methods:

1. applying the photon selection on the MC $W + \mathrm{jets}$, $t\bar{t}$, diboson, single top

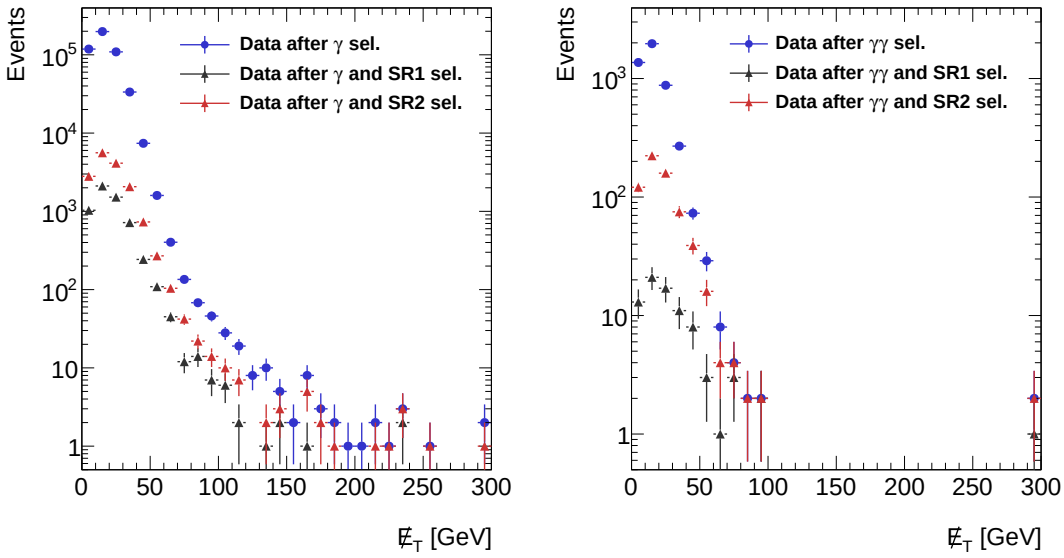

Figure 6.14: $E_{\mathrm{T}}^{\mathrm{miss}}$ distributions for single photon (left) and diphoton events (right) from data, using $\int \mathcal{L}\, dt = 1.04$ fb^{-1}. In addition the $E_{\mathrm{T}}^{\mathrm{miss}}$ distributions after a 3-jet ($p_T > 80,\ 40,\ 40$ GeV) (black) and a $H_T > 300$ GeV (red) requirements are shown. These latter two are meant to mimic the $E_{\mathrm{T}}^{\mathrm{miss}}$ distributions for SR1 and SR2, respectively.

	γ selection	SR1	SR2
W + jets	0.4804 ± 0.0024%	42 ± 31%	54 ± 13%
$t\bar{t}$	0.0199 ± 0.0001%	14 ± 10%	13 ± 3%
dibosons	0.0043 ± 0.00004%	0.49 ± 0.40%	0.90 ± 0.23%

Table 6.10: The fraction of the W + jets, $t\bar{t}$, and diboson processes relative to the photon sample, after inclusive photon, SR1, and SR2 selections.

samples,

2. applying e selection on MC, scaling each event with data derived scale factors describing the rate for electrons faking photons,

and the corresponding sample was then subtracted from the photon data sample.

The first method is based on the MC estimation of probability of an electron to be misidentified as a tight photon. To perform this estimation, we applied the photon selection on the W + jets, $t\bar{t}$, single top and diboson MC and then calculated the total contribution of these processes in each SR. Table 6.10 summarizes the fraction of these processes, relative to the photon sample, after the inclusive photon, SR1, and SR2 selections. In total, these processes make up less than 0.6% of the photon sample,

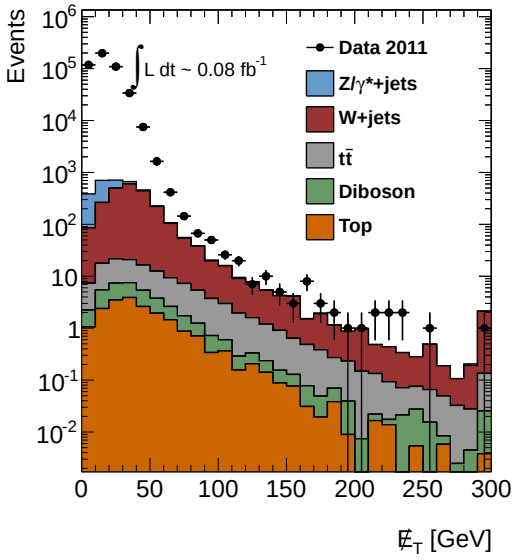

Figure 6.15: $E_{\mathrm{T}}^{\mathrm{miss}}$ distributions for single photon events from data and MC. The same selection was applied to both.

but in large $E_{\mathrm{T}}^{\mathrm{miss}}$ regions their contributions are significant and should be removed. Figure 6.15 shows the $E_{\mathrm{T}}^{\mathrm{miss}}$ distribution of the photon data sample and contribution of these MC samples after applying the photon selection. The total MC contribution was then subtracted from the photon data sample. Performing the subtraction in this way is disadvantageous in that it relies on the MC description of the $e \to \gamma$ fake rate, which we do not trust.

The second method is based on a data-driven estimation of the electron-photon fake rate. This fake rate, as derived in [77], varies between 5% and 17% as a function of η, due to the distribution of material in front of the calorimeter. The fake rate is applied on a single electron selection from MC. The $E_{\mathrm{T}}^{\mathrm{miss}}$ distribution for the photon data as well as scaled electron control sample is shown in Figure 6.16 (top). The $E_{\mathrm{T}}^{\mathrm{miss}}$ distributions after SR1 and SR2 selections without the $E_{\mathrm{T}}^{\mathrm{miss}}$ requirement are also shown.

The data-driven estimation of contamination from the misidentified electron was subtracted from the photon sample. Figure 6.17 shows the $E_{\mathrm{T}}^{\mathrm{miss}}$ distribution of the photon data sample after subtraction of events with real $E_{\mathrm{T}}^{\mathrm{miss}}$, using the two methods described above.

The photon data sample, after subtraction of the events with real $E_{\mathrm{T}}^{\mathrm{miss}}$ estimated using the data-driven method, will be used hereafter to model instrumental $Z/\gamma^* +$ jets background. This sample will be referred to as the "corrected" photon sample.

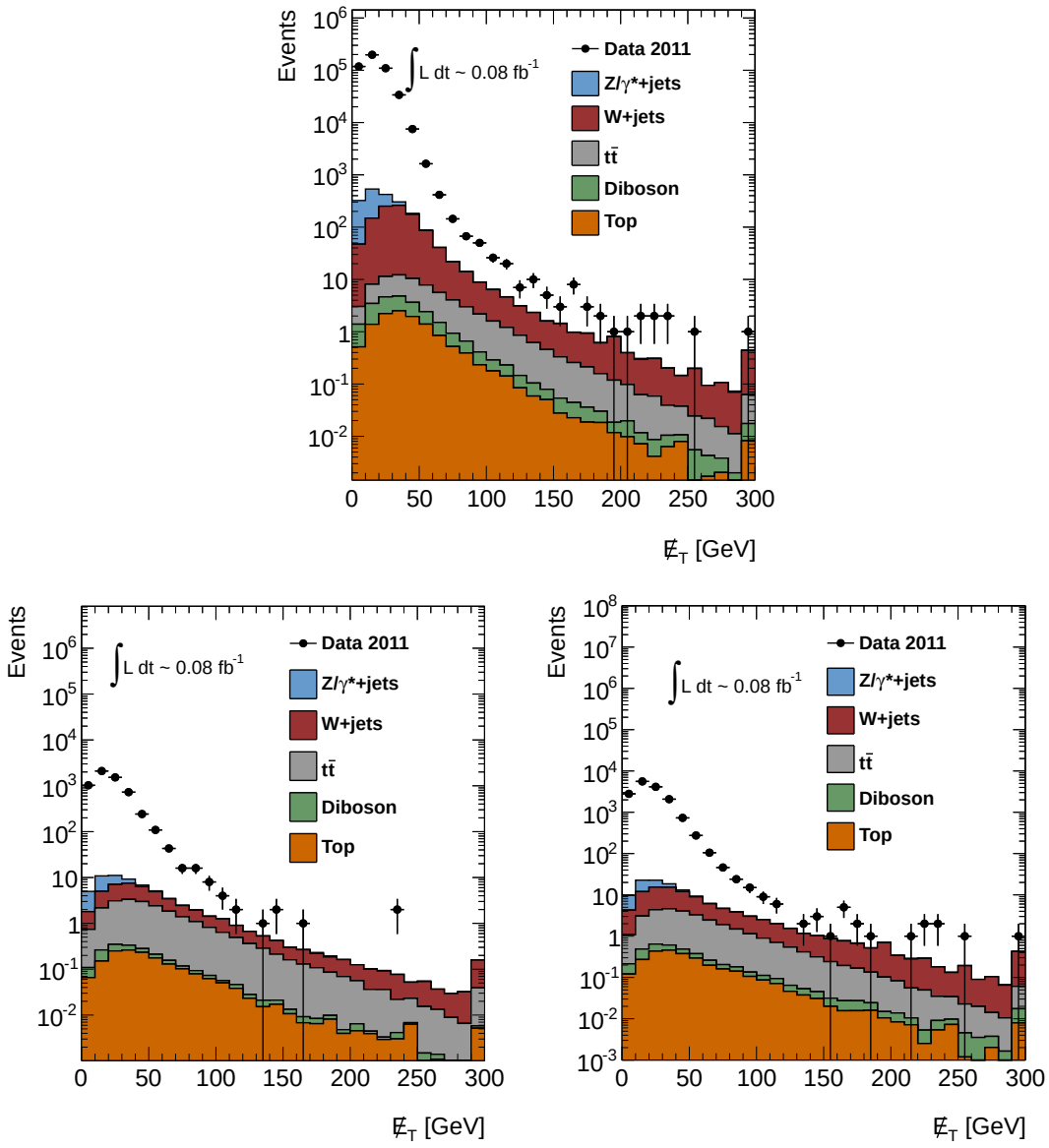

Figure 6.16: $E_{\mathrm{T}}^{\mathrm{miss}}$ distributions for single photon events from data and for electron events from MC, scaled with the electron-photon scale factors. The $E_{\mathrm{T}}^{\mathrm{miss}}$ distributions after SR1 and SR2 selections without the $E_{\mathrm{T}}^{\mathrm{miss}}$ requirement are shown on bottom.

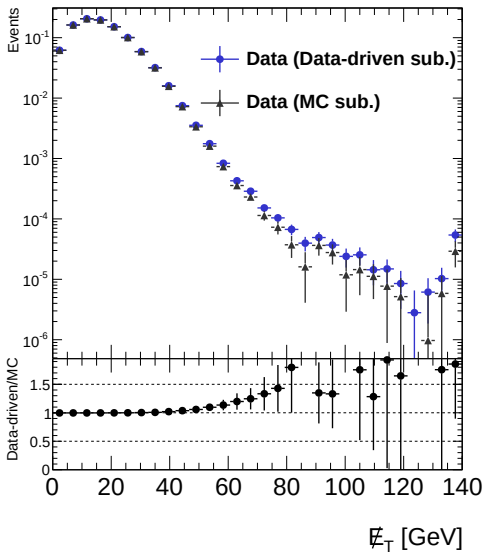

Figure 6.17: $E_{\mathrm{T}}^{\mathrm{miss}}$ distributions for single photon data sample after MC subtraction (black) and after subtraction of the data-driven estimation of the electron-photon fake contribution (blue).

Differences due to the different subtraction methods and shape uncertainties in the MC used for subtraction were taken into account in the assessment of systematic uncertainties.

Acquiring templates for $E_{\mathrm{T}}^{\mathrm{miss}}$ in $Z/\gamma^* + \mathbf{jets}$

The $E_{\mathrm{T}}^{\mathrm{miss}}$ distributions of the corrected photon sample and $Z/\gamma^* + \mathrm{jets}$ sample, after subtracting non-Z expectations, should have a similar shape due to their similar hadronic activity. Figure 6.18 shows the $E_{\mathrm{T}}^{\mathrm{miss}}$ distributions for data after Z preselection for both the ee and $\mu\mu$ channels, Z preselected data after subtracting the non-Z contribution, and the corrected photon sample. The non-Z contribution was estimated using MC.

One possible implication of the difference in the shape of these $E_{\mathrm{T}}^{\mathrm{miss}}$ distributions is that the kinematics of the $\gamma + \mathrm{jets}$ events are not the same as in the $Z/\gamma^* + \mathrm{jets}$ events due to the mass of the Z boson. To illustrate this, we plot the scalar sum of the p_T of all jets in the event for both Z and γ preselected events (see Figure 6.19). The difference in the jet kinematics contribute to the disagreement in $E_{\mathrm{T}}^{\mathrm{miss}}$ seen in Figure 6.18.

Furthermore, there is a disagreement in the shape of the p_T distributions of the Z and γ due to the Z being massive (see Figure 6.20). If the kinematic properties of

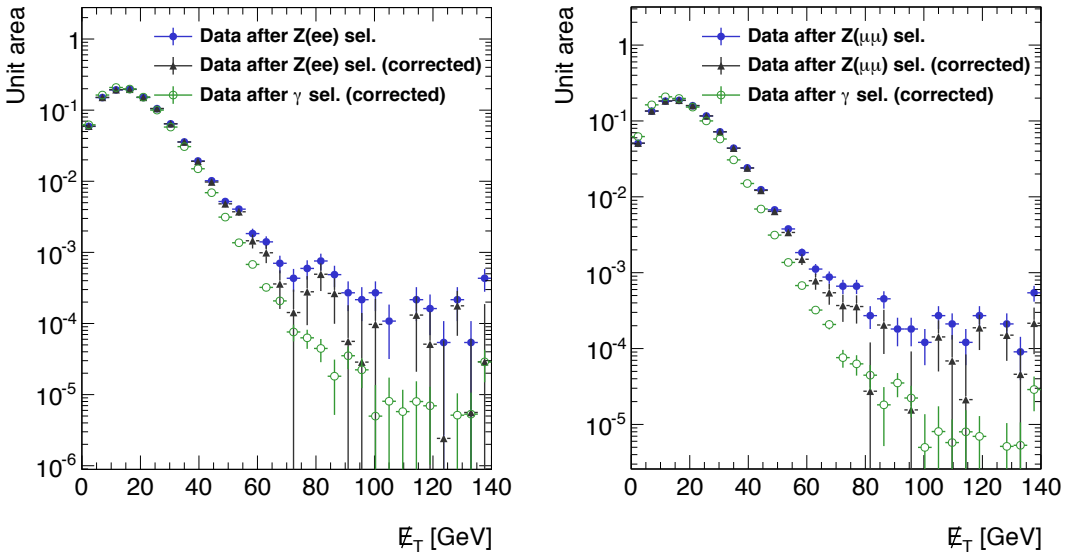

Figure 6.18: $E_{\mathrm{T}}^{\mathrm{miss}}$ distributions for data after Z preselection for the ee (left) and the $\mu\mu$ (right) channels. In addition, $E_{\mathrm{T}}^{\mathrm{miss}}$ distributions after correcting for non-Z sources are included, as well as $E_{\mathrm{T}}^{\mathrm{miss}}$ distribution from corrected photon data sample.

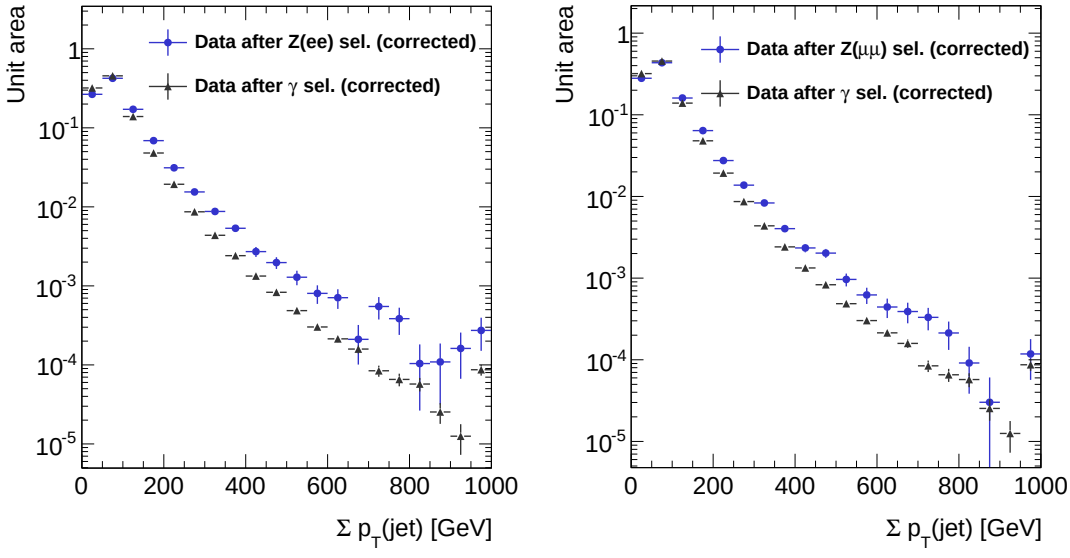

Figure 6.19: The scalar sum of the p_T of jets in Z and γ data samples.

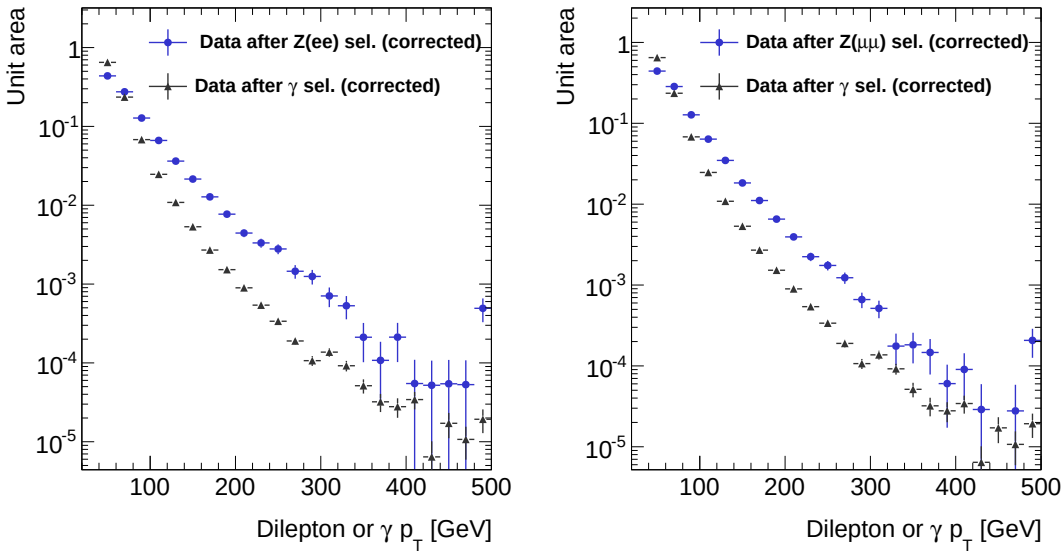

Figure 6.20: The p_T of the Z or γ in Z and γ data samples.

these two samples were comparable, we would expect the $E_{\mathrm{T}}^{\mathrm{miss}}$ distributions to be the same. The differences in both the hadronic recoil and the electromagnetic system (the γ or Z) can be jointly described by the differences in the H_T variable between the Z and photon samples. H_T is defined as the scalar sum of the p_T of all selected objects in a given event. The distributions for H_T are shown in Figure 6.21, and demonstrate the overall kinematic differences in the two classes of events.

To get a template for the $E_{\mathrm{T}}^{\mathrm{miss}}$ distribution in $Z/\gamma^* + \mathrm{jets}$ events, the kinematic differences between the Z and photon samples were corrected by reweighting the H_T distribution of the corrected photon sample to that of the Z data sample. Due to the fact that there is not a strong correlation between H_T and $E_{\mathrm{T}}^{\mathrm{miss}}$ (the correlation factor is ~ 0.15 for both ee and $\mu\mu$ samples), a reweighting function, illustrated at Figure 6.24, derived from events with $E_{\mathrm{T}}^{\mathrm{miss}} < 30$ GeV can be applied to events with any value of $E_{\mathrm{T}}^{\mathrm{miss}}$. Figure 6.22 shows the H_T distribution as function of $E_{\mathrm{T}}^{\mathrm{miss}}$ for ee and $\mu\mu$ samples. The profile of $H_T(E_{\mathrm{T}}^{\mathrm{miss}})$ versus $E_{\mathrm{T}}^{\mathrm{miss}}(H_T)$ is shown on Figure 6.23.

Figure 6.25 shows the reweighted H_T of the corrected photon sample, for events in the whole $E_{\mathrm{T}}^{\mathrm{miss}}$ range, compared to the H_T of the Z data sample. By only considering the low-$E_{\mathrm{T}}^{\mathrm{miss}}$ region, we ensure that the reweighting factors, plotted in Figure 6.24, are not contaminated by possible high-$E_{\mathrm{T}}^{\mathrm{miss}}$ signal in the photon or Z data samples. This is important when considering the possibility of bino-like neutralinos in the photon sample, and higgsino-like neutralinos (*i.e.*, the models we consider for interpretation in this analysis) in the Z sample. Using the $E_{\mathrm{T}}^{\mathrm{miss}} < 30$ GeV control region removes

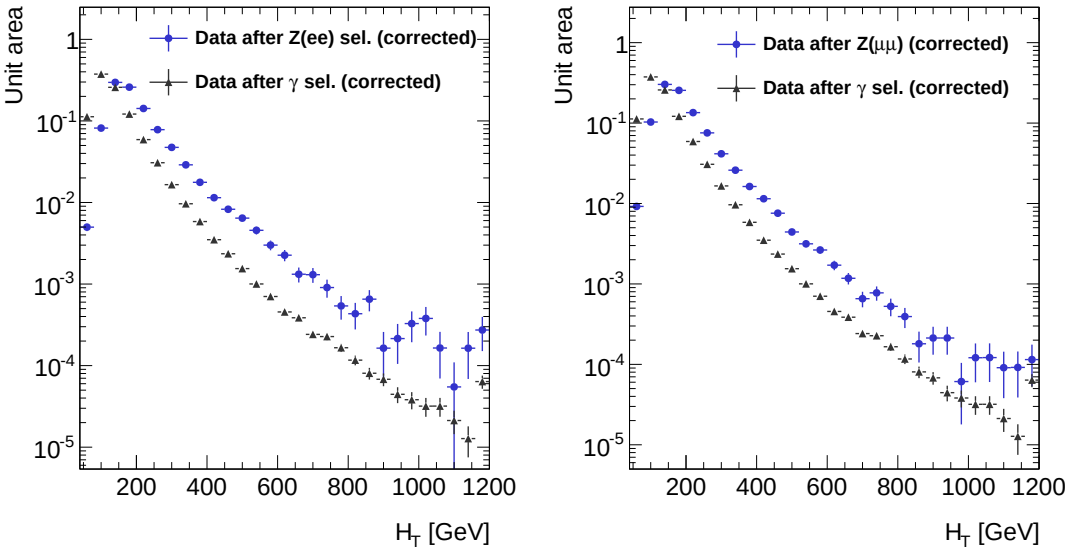

Figure 6.21: H_T distributions for Z and γ data samples. The kinematic differences in both the jet system and the Z/γ system manifest as differences in this quantity.

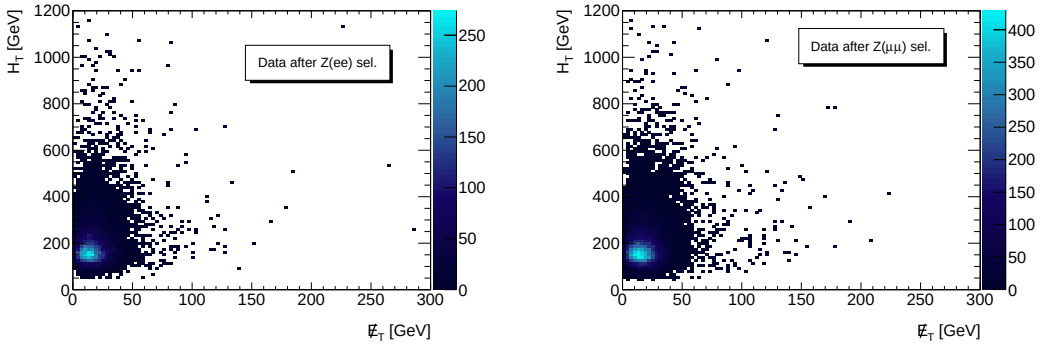

Figure 6.22: H_T distributions as function of $E_{\mathrm{T}}^{\mathrm{miss}}$ for Z data samples.

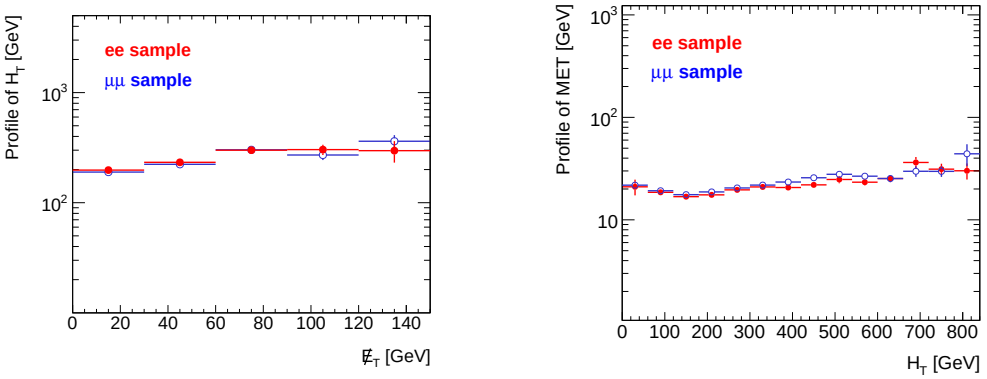

Figure 6.23: The profile distributions of H_T versus $E_{\mathrm{T}}^{\mathrm{miss}}$ (left) and $E_{\mathrm{T}}^{\mathrm{miss}}$ versus H_T (right).

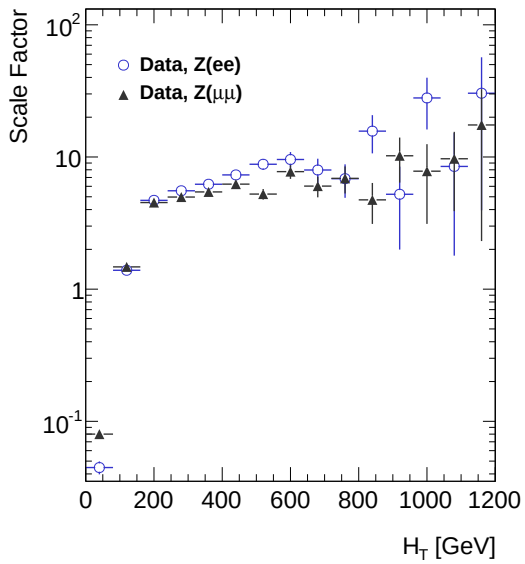

Figure 6.24: The reweighting function derived from data events with $E_{\mathrm{T}}^{\mathrm{miss}} < 30$ GeV.

almost all contamination from GGM signals dominated by strong production (see Figure 6.4). In these figures, the GGM points dominated by strong production are those with $m_{\tilde{h}} > 300$ GeV.

The reweighting function, when applied to the corrected photon sample, results in a $E_{\mathrm{T}}^{\mathrm{miss}}$ distribution which is a sufficient description of the $E_{\mathrm{T}}^{\mathrm{miss}}$ in $Z/\gamma^* +$ jets events in the case of the ee channel (see Figure 6.26, left). From Figure 6.26 (right), one can see that the ratio between the $E_{\mathrm{T}}^{\mathrm{miss}}$ of the reweighted corrected photon sample and that of the $\mu\mu$ Z-preselected events is not constant, but instead hints that there is a difference in $E_{\mathrm{T}}^{\mathrm{miss}}$ resolution between electromagnetic calorimeter objects and muon objects. To account for this difference, we smear the $E_{\mathrm{T}}^{\mathrm{miss}}$ of the selected photon events according to a Gaussian distribution with a width of 5 GeV. The resultant $E_{\mathrm{T}}^{\mathrm{miss}}$ distribution can be seen in Figure 6.27, and serves as the template for the $\mu\mu$ channel estimates.

To demonstrate the effect of reweighting on other distributions, we include the reweighted plots of the scalar sum p_T of jets and Z/γ p_T distribution in Figures 6.28, and 6.29, respectively. The discrepancy in the jet distribution is due to the fact that H_T incorporates the momentum of the Z decay products instead of the momentum of the Z itself.

We also considered the possibility of using other variables for the kinematic reweighting of the corrected photon sample. The H_T distribution characterizes each event in a global sense, taking into account all high-p_T objects, and therefore is a

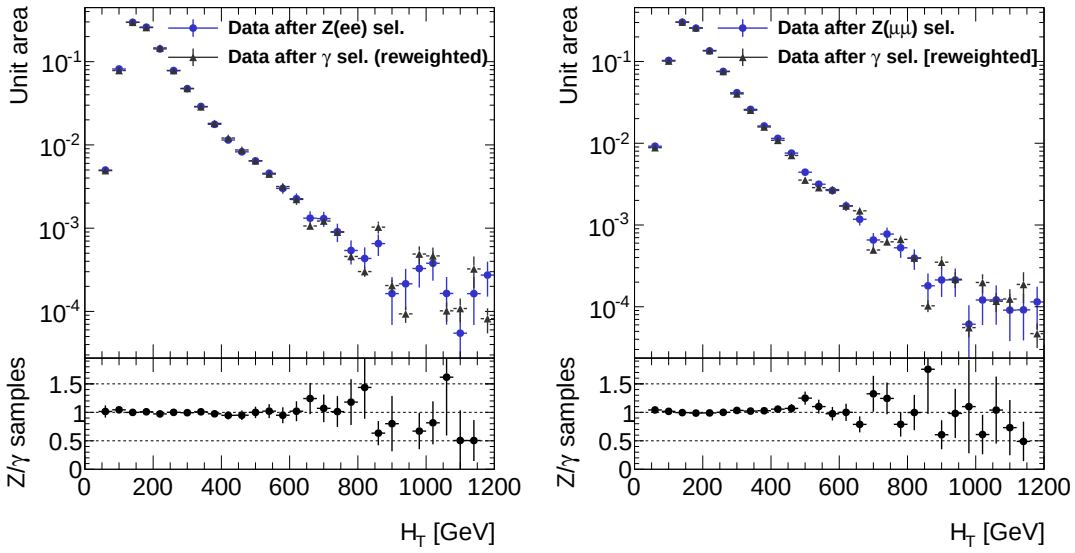

Figure 6.25: H_T distributions for Z and γ data samples in all $E_{\mathrm{T}}^{\mathrm{miss}}$ range. The H_T distributions of γ data samples are reweighted to match the H_T distributions of Z data in the region with $E_{\mathrm{T}}^{\mathrm{miss}} < 30$ GeV.

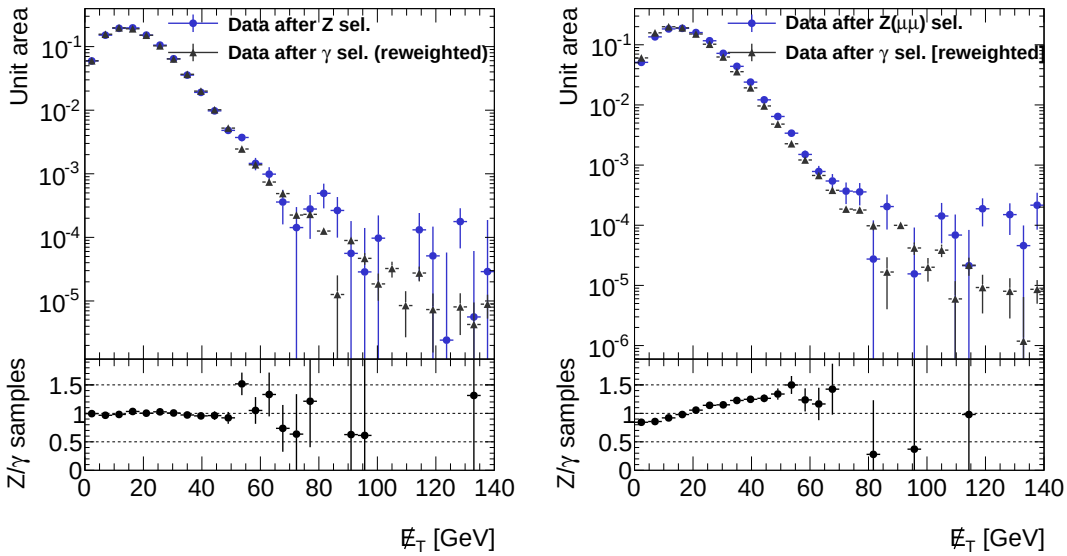

Figure 6.26: $E_{\mathrm{T}}^{\mathrm{miss}}$ of Z data sample compared to the H_T-reweighted $E_{\mathrm{T}}^{\mathrm{miss}}$ distribution of the photon sample, for both ee (left) and $\mu\mu$ (right) channels. The $E_{\mathrm{T}}^{\mathrm{miss}}$ distributions of the photon sample will serve as the templates for the fit of $E_{\mathrm{T}}^{\mathrm{miss}}$ which will provide the final estimate of $Z/\gamma^* + \mathrm{jets}$.

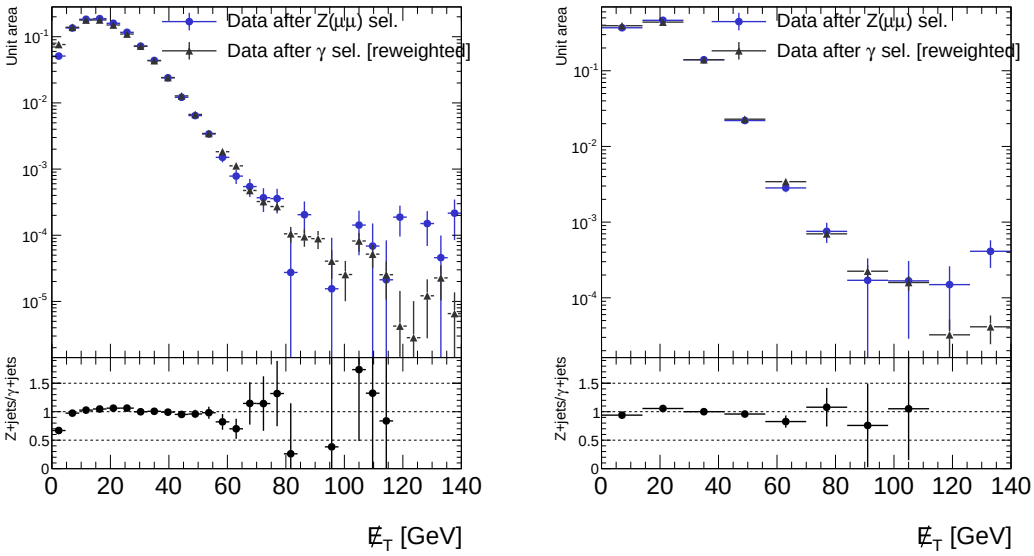

Figure 6.27: $E_{\mathrm{T}}^{\mathrm{miss}}$ of Z data sample compared to the H_T-reweighted $E_{\mathrm{T}}^{\mathrm{miss}}$distribution of the photon sample, for the $\mu\mu$ channel, where the $E_{\mathrm{T}}^{\mathrm{miss}}$ in the photon sample events has been smeared according to a Gaussian with a width of 5 GeV. The left distribution has a bin width of 10 GeV, and the right has a bin width of 30 GeV. The $E_{\mathrm{T}}^{\mathrm{miss}}$ distribution of the photon sample will serve as the templates for the fit of $E_{\mathrm{T}}^{\mathrm{miss}}$ which will provide the final estimate of $Z/\gamma^* + \mathrm{jets}$ in this channel.

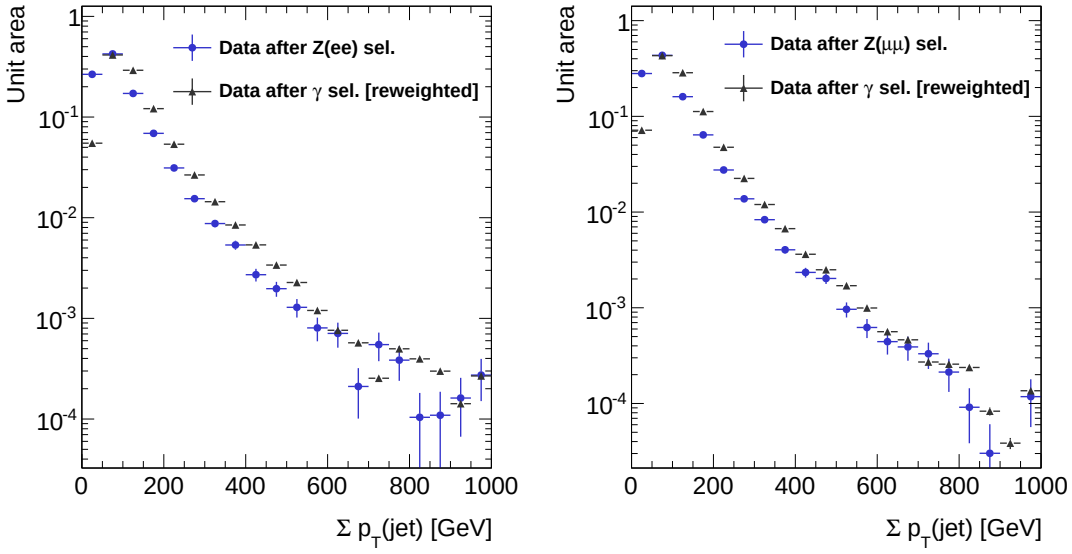

Figure 6.28: Scalar sum of jet p_T of Z data sample compared to the H_T-reweighted photon distribution.

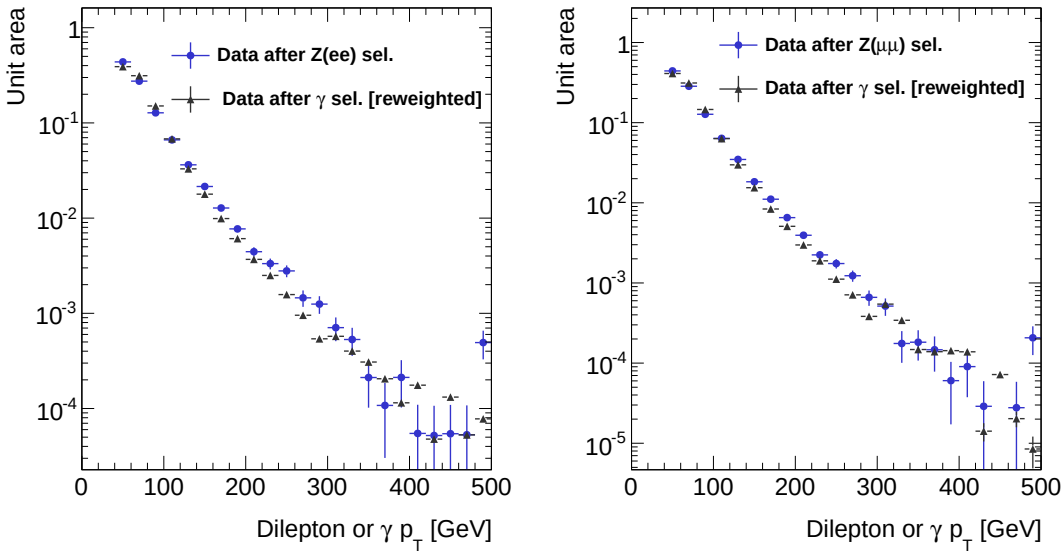

Figure 6.29: p_T of the Z in Z data sample compared to the H_T-reweighted γ p_T from photon sample.

well-motivated distribution to use in order to synchronize the photon $E_{\mathrm{T}}^{\mathrm{miss}}$ with that of the Z spectrum. Similarly, the p_T of the Z (photon) in the Z (photon) data sample can also be used to accomplish the same goal due to the similarities in the hadronic recoil in the $Z/\gamma^* +$jets and $\gamma +$jets processes. Figure 6.30 shows the photon $E_{\mathrm{T}}^{\mathrm{miss}}$ distribution, reweighted according to the $p_T(Z/\gamma)$ distribution, compared with the $E_{\mathrm{T}}^{\mathrm{miss}}$ distribution of the Z sample.

Later we will show that H_T reweighting yields consistent results with p_T reweighting. We will use the H_T reweighting method for the final estimation.

Estimate of $Z/\gamma^* +$ jets in the signal regions

The $E_{\mathrm{T}}^{\mathrm{miss}}$ distributions from the photon events, after reweighting with the H_T distribution for $E_{\mathrm{T}}^{\mathrm{miss}} < 30$ GeV, serve as the templates for $Z/\gamma^* +$ jets events in a global fit to the data. The non-Z backgrounds are represented by the distributions from MC. To get the estimates in the signal regions, the $E_{\mathrm{T}}^{\mathrm{miss}}$ templates which model Z and non-Z components are created after all cuts *except* the $E_{\mathrm{T}}^{\mathrm{miss}}$ cut. For each SR, we performed an extended maximum likelihood (ML) fit of the two $E_{\mathrm{T}}^{\mathrm{miss}}$ templates, as a composite PDF, to the $E_{\mathrm{T}}^{\mathrm{miss}}$ observed in data. The composite PDF can be described by

$$N_{\mathrm{obs}}(E_{\mathrm{T}}^{\mathrm{miss}}) = N_Z f_Z(E_{\mathrm{T}}^{\mathrm{miss}}) + N_{\text{non-}Z} f_{\text{non-}Z}(E_{\mathrm{T}}^{\mathrm{miss}}), \tag{6.2}$$

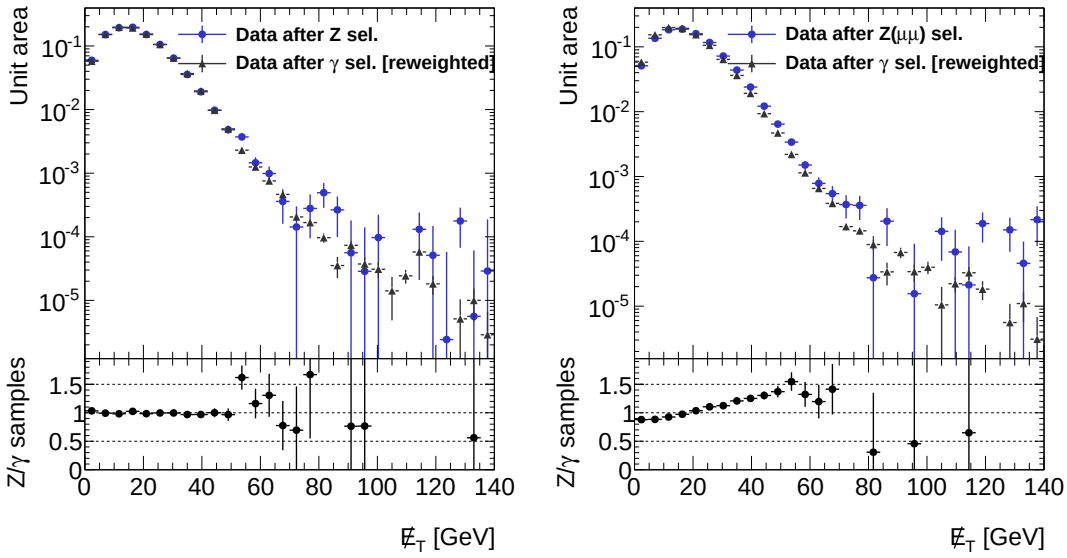

Figure 6.30: The $E_{\mathrm{T}}^{\mathrm{miss}}$ distribution for Z events, compared with the distribution for photon data reweighted using $p_T(Z/\gamma)$. The distribution for the e^+e^- ($\mu^+\mu^-$) channel is on the left (right).

where N_Z ($N_{\text{non-}Z}$) is the normalization of the Z (non-Z) component, and $f_Z(E_{\mathrm{T}}^{\mathrm{miss}})$ ($f_{\text{non-}Z}(E_{\mathrm{T}}^{\mathrm{miss}})$) is the PDF describing the shape of the $E_{\mathrm{T}}^{\mathrm{miss}}$ for Z (non-Z) fractions. The fit is performed over the range $0 < E_{\mathrm{T}}^{\mathrm{miss}} < 140$ GeV.

By using an *extended* ML fit, we ensure that $N_{\mathrm{obs}} = N_Z + N_{\text{non-}Z}$. The normalization of the non-Z component is constrained to the value from MC when performing the fits, and the statistical uncertainties on the MC prediction of the non-Z components are taken into account in the systematics. As a result, the only free parameter in the fit is the normalization of the Z component, which is an output of the fitting procedure.

Since the result of the fit in each SR provides the expectation for each component before the $E_{\mathrm{T}}^{\mathrm{miss}}$ cut, the efficiency of this cut, calculated from the photon template, is used in the calculation of the final expectation:

$$N_Z^{\text{exp, SR}} = N_Z^{\text{fit}} \times \epsilon^{E_{\mathrm{T}}^{\mathrm{miss}}\ \text{cut}} \tag{6.3}$$

Equation 6.3 gives the expression used to estimate the $Z/\gamma^* + \text{jets}$ contribution in SR1 and SR2. Since $\Delta R(\ell_1, \ell_2)$ cut can not be implemented in the single photon sample, the estimation of the $Z/\gamma^* + \text{jets}$ contribution in SR3 performed differently. Taking into account that the only difference between SR2 and SR3 is the $\Delta R(\ell_1, \ell_2)$ requirement, we use the result from SR2 and scale it by the efficiency of the ΔR cut found from $Z/\gamma^* + \text{jets}$ MC to calculate the expectation in SR3.

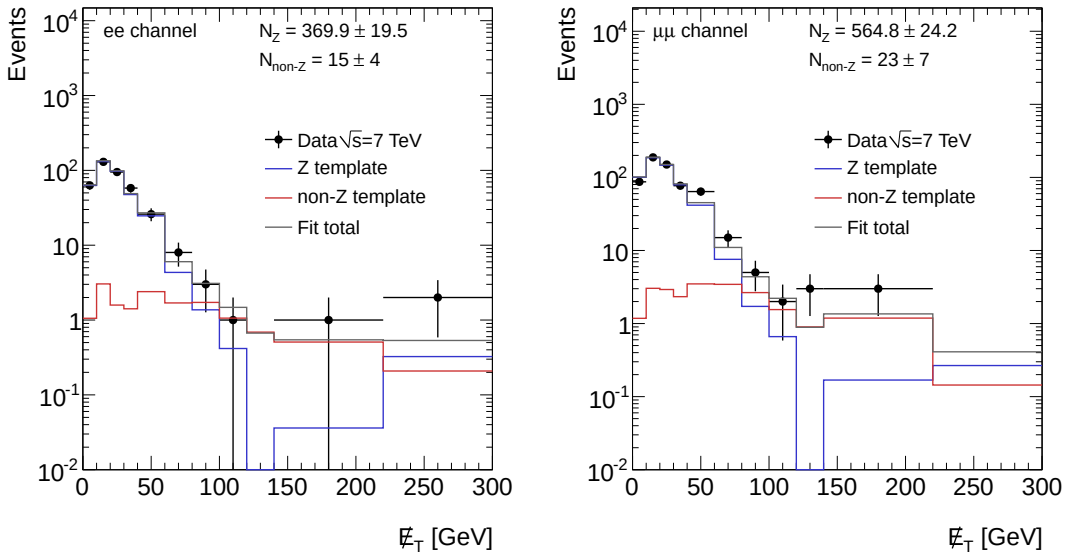

Figure 6.31: Results of the template fit of $E_{\mathrm{T}}^{\mathrm{miss}}$ to the selected data for ee (left) and $\mu\mu$ (right) in SR1, using a γ + jets template for Z/γ^* + jets and the MC distribution as a template for non-Z sources. Templates are created after the jet selection defined for SR1.

Template fit results

The results of the template fit for the estimate in SR1 are shown in Figure 6.31. In the ee channel, we find $N_Z^{\mathrm{exp}} = 369.9 \pm 19.5$ events before any cuts on $E_{\mathrm{T}}^{\mathrm{miss}}$. The efficiency of a cut of $E_{\mathrm{T}}^{\mathrm{miss}} > 220$ GeV, calculated using the photon template, is $\epsilon_{\mathrm{cut}} = 0.0009 \pm 0.0008$. This results in a final Z/γ^* + jets expectation of $N_Z^{\mathrm{exp,SR1}}(ee) = \epsilon_{\mathrm{cut}} \times N_Z^{\mathrm{exp}} = 0.32 \pm 0.29$. For the $\mu\mu$ channel, the fit result gives $N_Z^{\mathrm{exp}} = 563.5 \pm 24.2$, giving an SR1 expectation of $N_Z^{\mathrm{exp,SR1}}(\mu\mu) = 0.26 \pm 0.24$. Using p_{T}reweighting, described in Section 6.5.2, instead of H_T reweighting, the estimate is $N_Z^{\mathrm{exp,SR1}}(ee) = 0.05 \pm 0.04$ for the ee channel and $N_Z^{\mathrm{exp,SR1}}(\mu\mu) = 0.08 \pm 0.06$ for the $\mu\mu$ channel. These are consistent with the estimates above.

For SR2, the results of the template fit are shown in Figure 6.32. In this case, we find the estimates in the ee and $\mu\mu$ channels to be $N_Z^{\mathrm{exp,SR2}}(ee) = 2.08 \pm 0.82$ and $N_Z^{\mathrm{exp,SR2}}(\mu\mu) = 3.19 \pm 1.11$, respectively. The estimates using p_{T} reweighting are $N_Z^{\mathrm{exp,SR2}}(ee) = 1.3 \pm 0.5$ and $N_Z^{\mathrm{exp,SR2}}(\mu\mu) = 2.1 \pm 0.8$ in the ee and $\mu\mu$ channels, respectively, and they are consistent with the results obtained using H_T reweighting. Table 6.11 gives the detailed information regarding the results of these estimates. The sources of the systematic uncertainties will be discussed in Section 6.5.2.

Finally, the estimates for SR3 follow directly, using the efficiency from Z/γ^* +

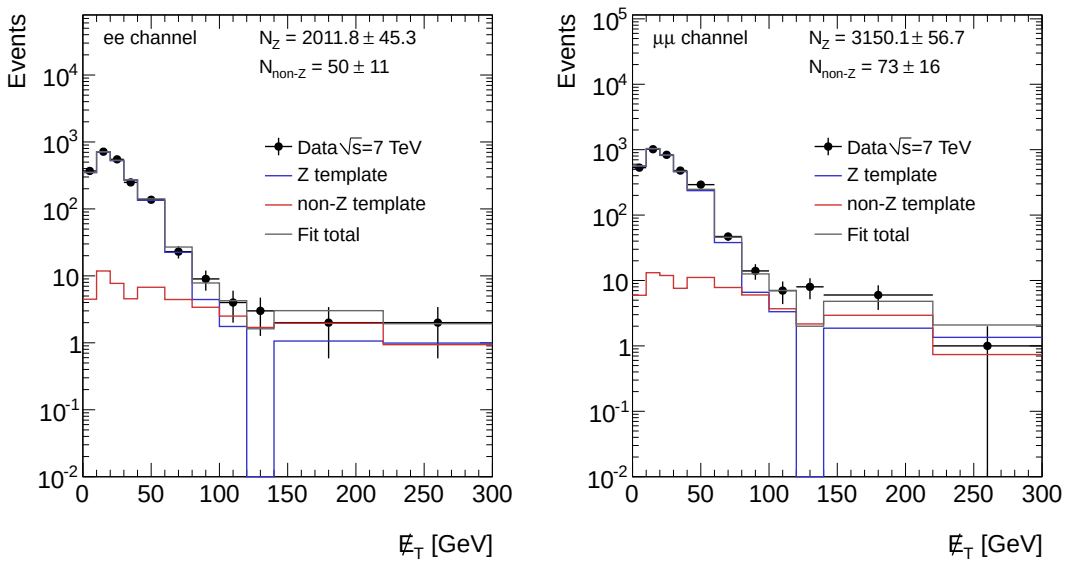

Figure 6.32: Results of the template fit of $E_{\mathrm{T}}^{\mathrm{miss}}$ to the selected data for ee (left) and $\mu\mu$ (right) in SR2, using a photon sample template for $Z/\gamma^* + \mathrm{jets}$ and the MC distribution as a template for non-Z sources. Templates are created after the H_T selection defined for SR2.

	SR1		
	$N_Z^{\text{no cut}}$	$N_{\text{non-}Z}^{\text{no cut}}$	N_Z^{exp}
ee	369.9±19.5	15.4±4.4	0.32±0.29(stat.)±0.21(sys.)
$\mu\mu$	564.8±24.2	22.8±6.8	0.26±0.24(stat.)±0.09(sys.)
	SR2		
	$N_Z^{\text{no cut}}$	$N_{\text{non-}Z}^{\text{no cut}}$	N_Z^{exp}
ee	2011.8±45.3	50.3±10.6	2.08±0.82(stat.)±1.04(sys.)
$\mu\mu$	3150.1±56.7	73.1±16.0	3.19±1.11(stat.)±1.53(sys.)
	SR3		
	$N_Z^{\text{no }\Delta\text{R cut}}$	$\epsilon^{\Delta\text{R cut}}$	N_Z^{exp}
ee	2.1±0.8	0.88±0.01	1.82±0.72(stat.)±0.92(sys.)
$\mu\mu$	3.2±1.1	0.77±0.01	2.44±0.85(stat.)±1.17(sys.)

Table 6.11: Results of the data-driven estimate for $Z/\gamma^* + \mathrm{jets}$ in SR1, SR2, and SR3 using $E_{\mathrm{T}}^{\mathrm{miss}}$ templates. In addition to the estimates themselves (N_Z^{exp}), the overall normalization before a $E_{\mathrm{T}}^{\mathrm{miss}}$ cut is given ($N_Z^{\text{no cut}}$).

jets MC for a $\Delta R(\ell_1, \ell_2) < 2.0$ cut after making the SR2 cuts. In the electron channel, we find $\epsilon^{\Delta\text{R cut}} = 0.88 \pm 0.01$, yielding $N_Z^{\text{exp,SR3}}(ee) = 1.82 \pm 0.72$. In the muon channel, we find $\epsilon^{\Delta\text{R cut}} = 0.77 \pm 0.01$, yielding $N_Z^{\text{exp,SR3}}(\mu\mu) = 2.44 \pm 0.85$.

Assessment of systematic uncertainties

Systematic uncertainties on the estimates derived here arise from several sources:

1. the effect of different binning schemes for the template histograms,
2. the uncertainties of the non-Z component in the fit,
3. the choice of CR used to define the H_T reweighting function,
4. the choice of subtraction scheme for removing sources of real $E_{\mathrm{T}}^{\mathrm{miss}}$ from the photon data sample,
5. the effect of $E_{\mathrm{T}}^{\mathrm{miss}}$ shape uncertainties on the MC used for subtraction from the photon data sample,
6. the effect of theoretical uncertainties on the MC used for subtraction from the photon data sample,
7. the difference in $E_{\mathrm{T}}^{\mathrm{miss}}$ resolution for $\mu\mu$ events in data and the reweighted photon data sample.

Given that the estimates for this analysis are performed in regions with such low statistics, the choice of binning of the $E_{\mathrm{T}}^{\mathrm{miss}}$ distributions used in the final template fits has an effect on the predicted number of events. The central value used in this analysis utilizes histograms with variable bin widths (see Figures 6.31, 6.32), with the bin widths increasing as $E_{\mathrm{T}}^{\mathrm{miss}}$ increases. The bin widths vary from 10 GeV in the $0 < E_{\mathrm{T}}^{\mathrm{miss}} < 50$ GeV range to 50 GeV in the $150 < E_{\mathrm{T}}^{\mathrm{miss}} < 300$ GeV range. However, we also perform the estimates with fixed-width binning, considering 7.5, 10, and 12 GeV widths. The fixed-width estimate with the largest discrepancy from the variable-width estimate is estimated is taken as a systematic uncertainty on the central value. The fixed-width bin estimate with the highest quality fit was taken as a systematic uncertainty on the central value. Figure 6.33 presents the results of the fits used to derive these systematic uncertainties for SR1 and SR2.

As discussed in section 6.5.2 the template fit method can be used to compute the overall normalization of $Z/\gamma^* + \text{jets}$. The non-Z backgrounds component is constrained to the value directly computed from MC. However, the cross sections used for these samples have some systematic uncertainties associated with them [78]. The uncertainties for the MC cross sections are taken as $^{+6.96\%}_{-9.59\%}$ [79, 80] for $t\bar{t}$ and 5% for the rest of the MC samples. We rerun the template fit after fluctuating the

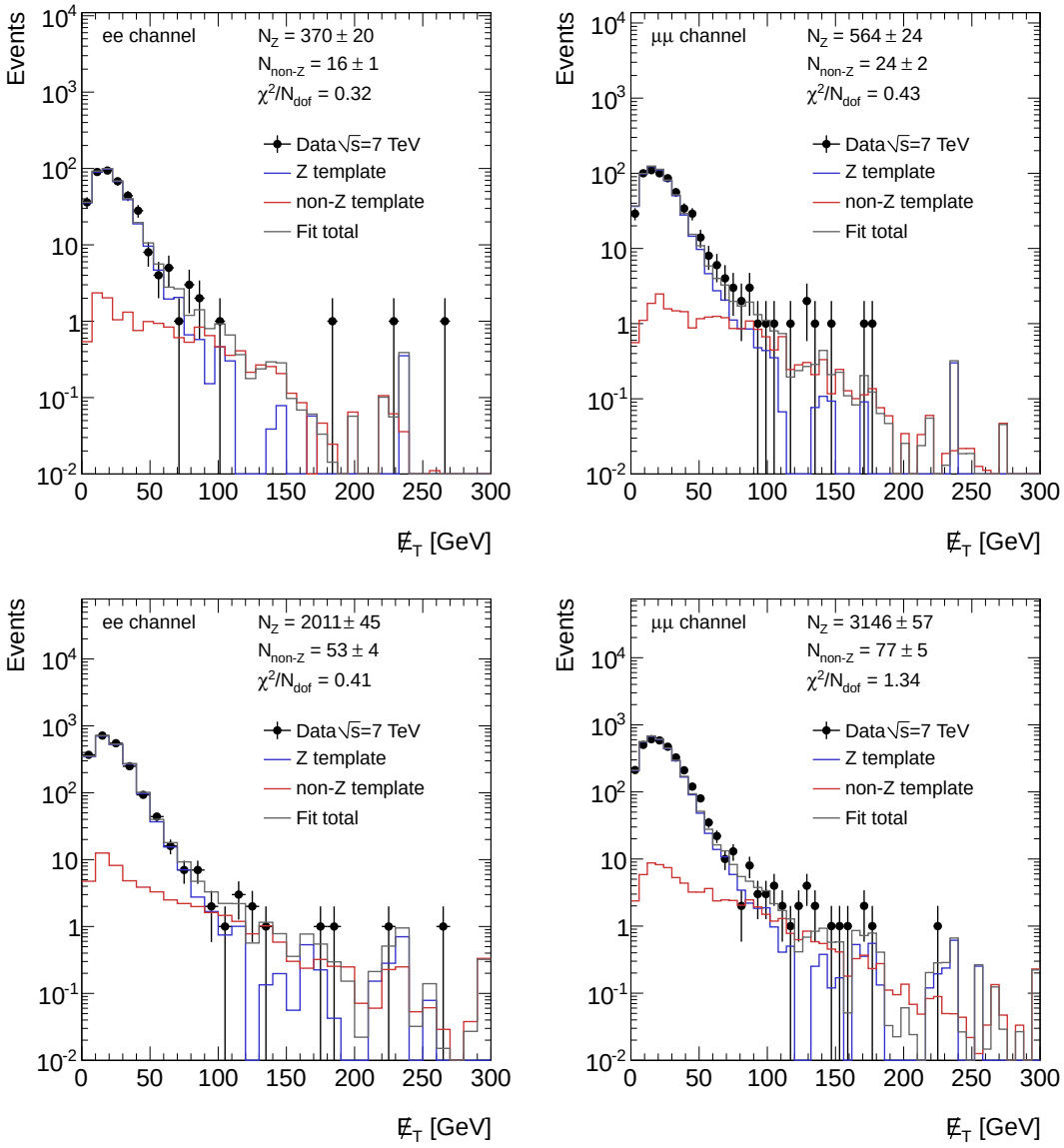

Figure 6.33: Results of the template fits to the selected data using fixed-width bins for ee (left) and $\mu\mu$ (right) in SR1 (top) and SR2 (bottom).

normalization according to these cross section uncertainties, and also according to the statistical uncertainty of the expected MC events. The difference in the result with these constraints on the template fits are taken as contributions to the overall systematic uncertainty.

Another potential uncertainty related to the non-Z component in the template fit is the shape of the $E_{\mathrm{T}}^{\mathrm{miss}}$ distribution. To account for this, we rerun the fit after varying the shape of the $E_{\mathrm{T}}^{\mathrm{miss}}$ due to effects like jet energy scale, jet energy resolution, and lepton energy scales. After combining these shape uncertainties with the above normalization uncertainties, the overall systematic due to the non-Z component in the template fit is less than 1%.

The choice of control region used to derive the reweighting as a function of H_T provides a source of uncertainty. To account for this, we vary the $E_{\mathrm{T}}^{\mathrm{miss}}$ cut used to define this region around the nominal value ($E_{\mathrm{T}}^{\mathrm{miss}} < 30$ GeV) and compute the $Z/\gamma^* + \mathrm{jets}$ estimate. We consider alternative cut values between 20 and 50 GeV, and take the largest discrepancy as another contribution to the overall systematic error. For SR1, defining the control region in the ee ($\mu\mu$) channels with $E_{\mathrm{T}}^{\mathrm{miss}} < 35$ GeV (50 GeV) yields the largest discrepancy. In SR2, the largest discrepancy in the ee ($\mu\mu$) channel comes from using $E_{\mathrm{T}}^{\mathrm{miss}} < 40$ GeV (50 GeV) as the control region. Figure 6.34 shows the results of the fits for each of these alternate CR cases.

The estimation of the contribution of events with real $E_{\mathrm{T}}^{\mathrm{miss}}$ in the photon data sample was performed by using two methods, as described in Section 6.5.2. The results with the MC-based method are consistent with those with the data-driven method, but the difference in these results was taken as a further source of systematic uncertainty.

The subtraction of the photon data sample relies on the $E_{\mathrm{T}}^{\mathrm{miss}}$ distribution of single electron events, scaled by electron-photon fake rates. In principle, the shape of this $E_{\mathrm{T}}^{\mathrm{miss}}$ distribution can change due to variations in jet energy scale, jet energy resolution, and electron energy scale. We must account for the effect these shape uncertainties have on the $Z/\gamma^* + \mathrm{jets}$ estimate. We do this by using each of the varied MC $E_{\mathrm{T}}^{\mathrm{miss}}$ distributions when performing the subtraction on the photon data sample. We take the sum in quadrature of these three uncertainties as an additional overall systematic uncertainty.

Additionally, the factorization and renormalization scales used in the generation of the $W + \mathrm{jets}$ MC events were varied by factors of two, changing the shape of the $E_{\mathrm{T}}^{\mathrm{miss}}$ distribution after electron selection. An additional $5 - 10\%$ (20%) uncertainty on the estimation is found to be from this source in SR1 (SR2).

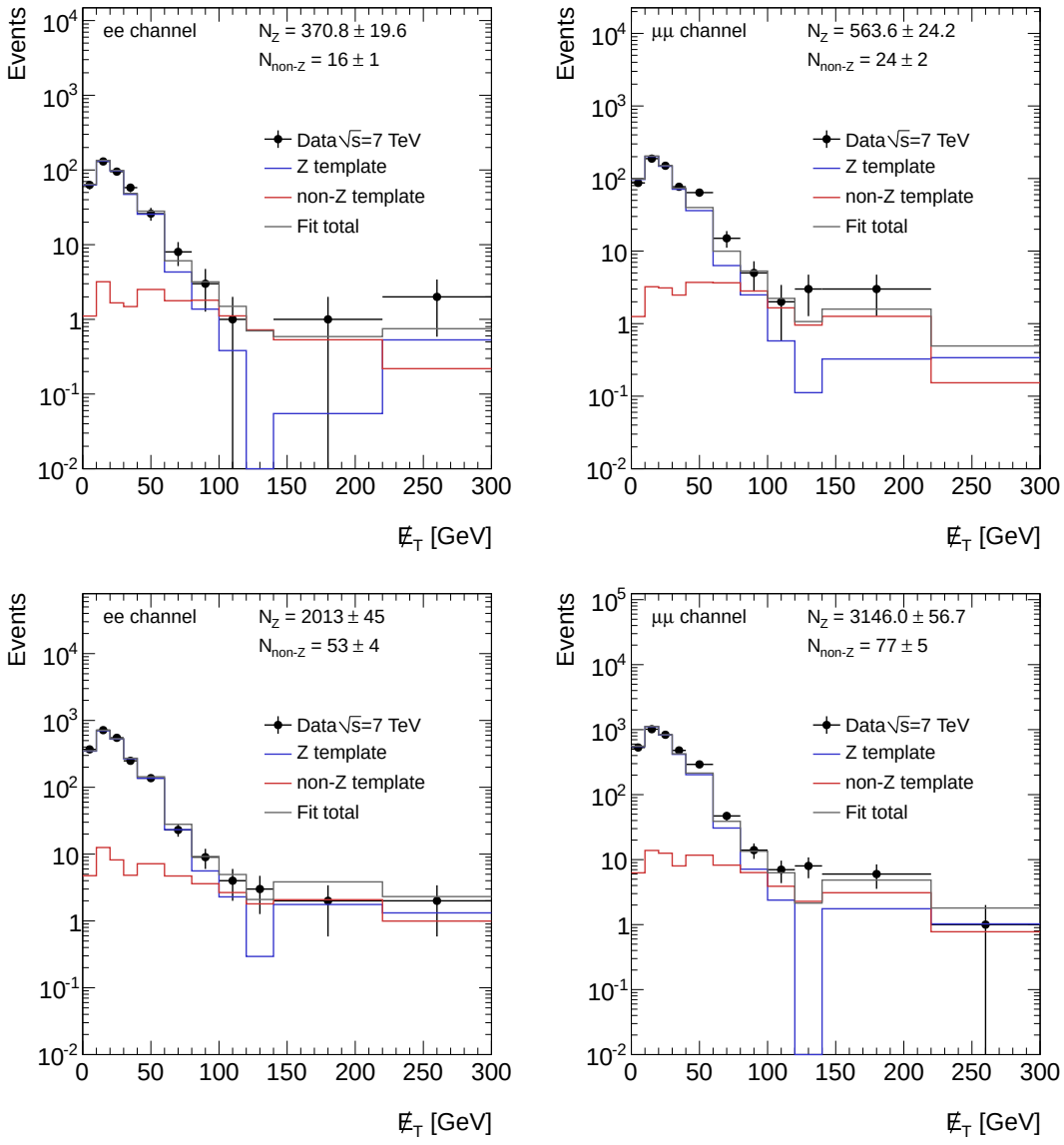

Figure 6.34: Results of the template fits to the selected data using alternate CR definitions which give the largest systematic uncertainty in both the ee (left) and $\mu\mu$ (right) channels for SR1 (top) and SR2 (bottom). For ee SR1, this corresponds to a CR choice of $E_{\mathrm{T}}^{\mathrm{miss}} < 35$ GeV. For $\mu\mu$ SR1, $E_{\mathrm{T}}^{\mathrm{miss}} < 50$ GeV. For ee SR2, $E_{\mathrm{T}}^{\mathrm{miss}} < 40$ GeV. And for $\mu\mu$ SR2, $E_{\mathrm{T}}^{\mathrm{miss}} < 50$ GeV.

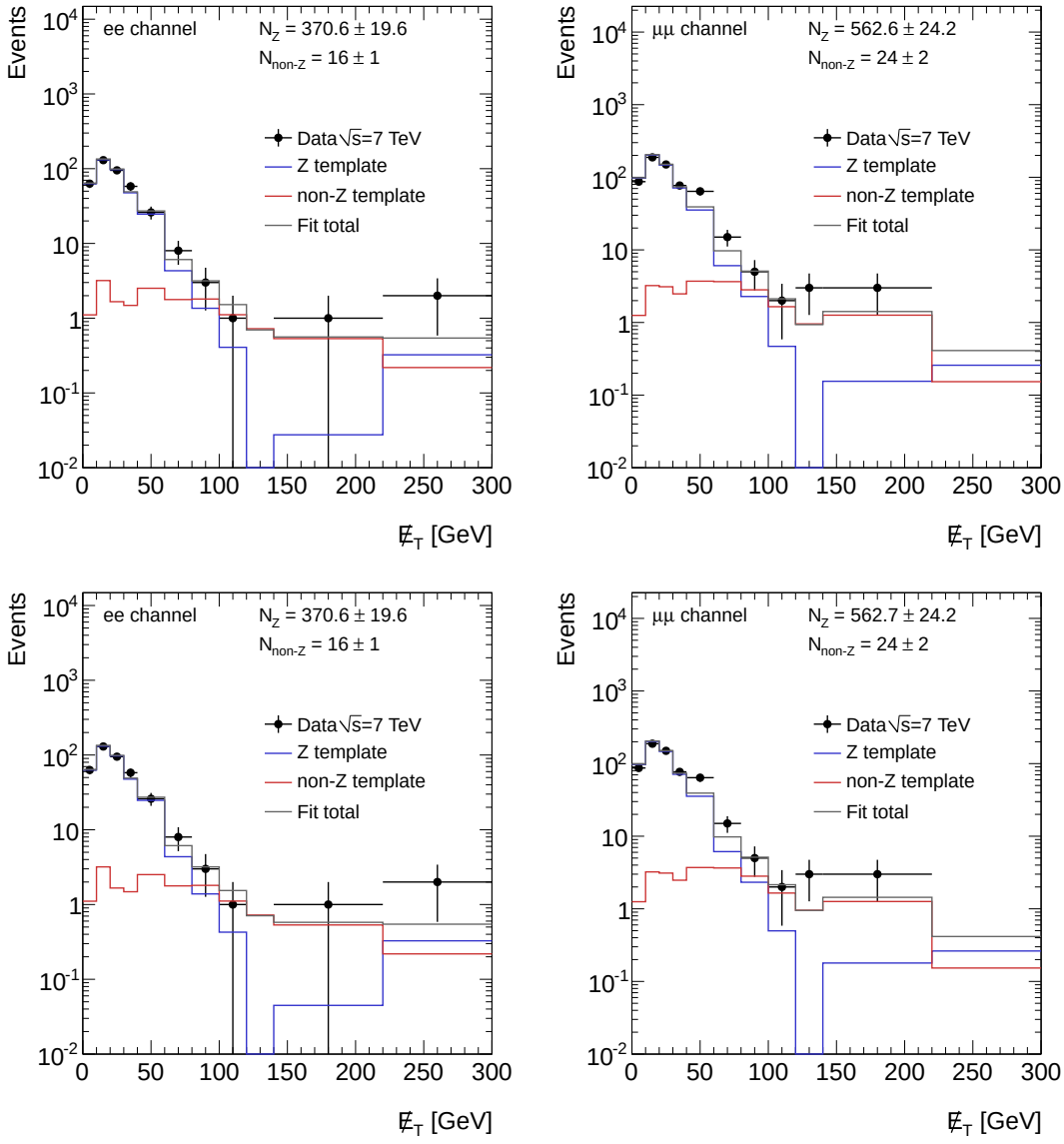

Figure 6.35: Results of the template fits to the selected data using for *ee* (left) and $\mu\mu$ (right) in SR1, fluctuating the MC cross sections used in the subtraction of the photon data sample up (top) and down (bottom).

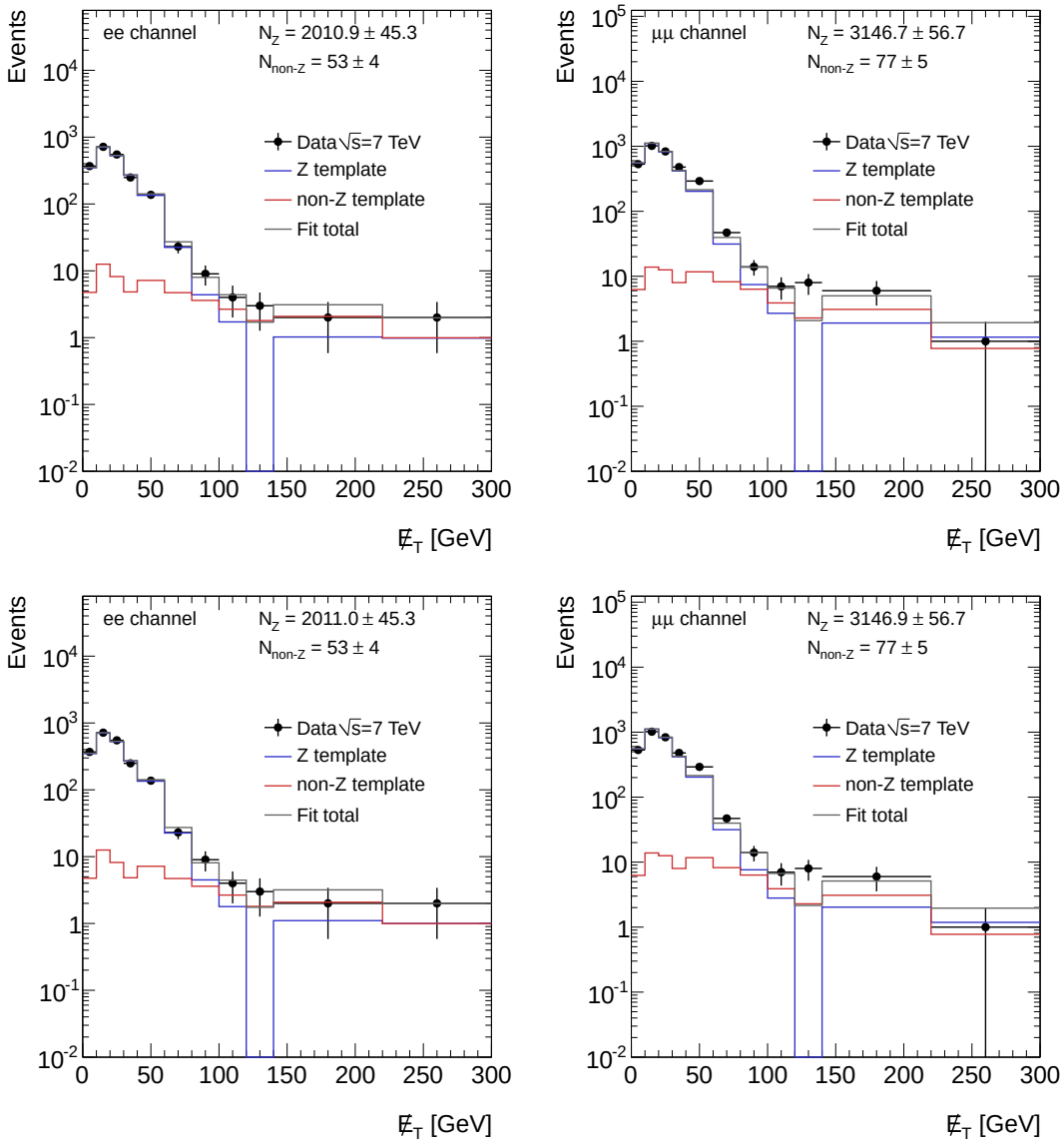

Figure 6.36: Results of the template fits to the selected data using for ee (left) and $\mu\mu$ (right) in SR2, fluctuating the MC cross sections used in the subtraction of the photon data sample up (top) and down (bottom).

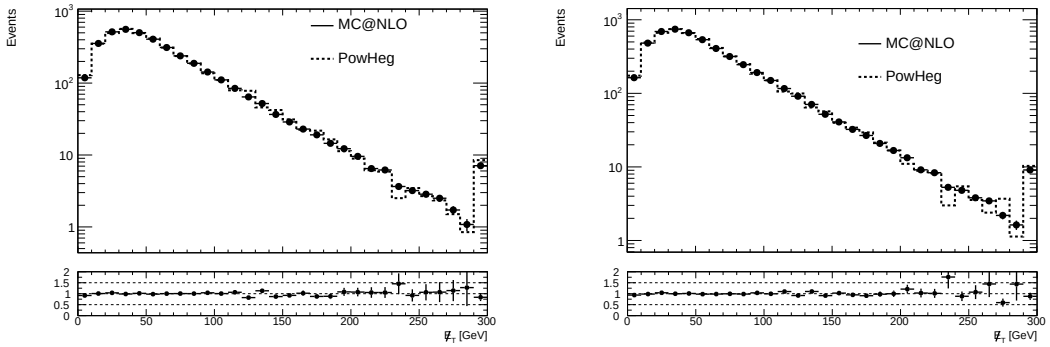

Figure 6.37: The $E_{\mathrm{T}}^{\mathrm{miss}}$ distribution of single electron $t\bar{t}$ events after SR1 (left) and SR2 (right) selection for both the MC@NLO and POWHEG [81] event generators.

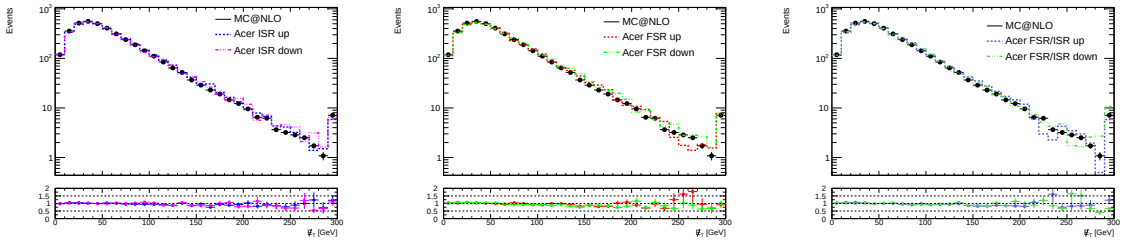

Figure 6.38: The $E_{\mathrm{T}}^{\mathrm{miss}}$ distribution of single electron $t\bar{t}$ events after SR1 selection, except $E_{\mathrm{T}}^{\mathrm{miss}}$, showing the nominal shape from `MC@NLO` along with the shapes from ISR/FSR varied Acer samples. Effects from ISR only (top left), FSR only (top right), and ISR+FSR together (bottom) are shown.

In either the data-driven or MC-based subtraction method for the photon data sample, we rely on the MC cross sections to quantify the contribution of events with real $E_{\mathrm{T}}^{\mathrm{miss}}$. To assess the effect of the MC cross section uncertainties have on the final $Z/\gamma^* + \mathrm{jets}$ results, we re-compute the estimate with all the MC cross sections varied up and down simultaneously according to the uncertainties discussed above. This simultaneous variation gives us a conservative estimate of the effect on the $Z/\gamma^* + \mathrm{jets}$ method's results. The larger of the two variations is taken as a systematic uncertainty on the central value. Figures 6.35 and 6.36 present the template fit results using these upward and downward variations of the MC cross sections used for subtraction in the photon data sample, for both SR1 and SR2. This uncertainty is included in the MC theory uncertainties given in Table 6.12.

Due to the scale of the $t\bar{t}$ process as a background in this analysis, we include two additional sources of uncertainty regarding the MC used for subtraction from the photon data sample:

- the uncertainty due to the choice of generators: MC@NLO versus POWHEG [81],

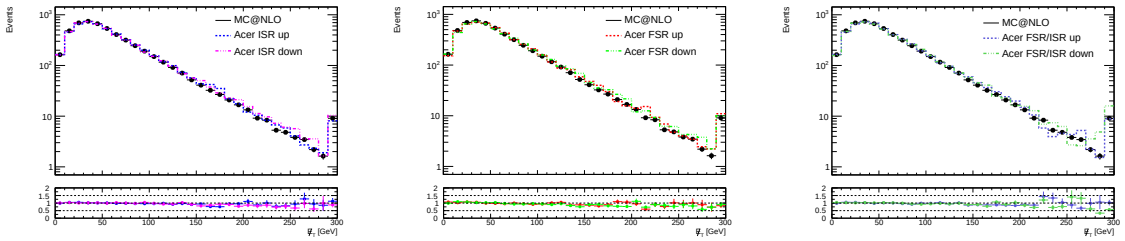

Figure 6.39: The $E_{\mathrm{T}}^{\mathrm{miss}}$ distribution of single electron $t\bar{t}$ events after SR2 selection, except $E_{\mathrm{T}}^{\mathrm{miss}}$, showing the nominal shape from `MC@NLO` along with the shapes from ISR/FSR varied AcerMC samples. Effects from ISR only (top left), FSR only (top right), and ISR+FSR together (bottom) are shown.

- the effect of initial and final state radiation (ISR/FSR) assessed by using AcerMC [82].

Figure 6.37 shows the shape of the $E_{\mathrm{T}}^{\mathrm{miss}}$ after single electron selection and SR1 and SR2 requirements, except $E_{\mathrm{T}}^{\mathrm{miss}}$, for $t\bar{t}$ MC events using the MC@NLO and PowHeg generators. Figures 6.38 and 6.39 show the shapes of $E_{\mathrm{T}}^{\mathrm{miss}}$ after single electron selection and SR1 and SR2 requirements, except $E_{\mathrm{T}}^{\mathrm{miss}}$, for $t\bar{t}$ MC events generated using MC@NLO and AcerMC [82] with ISR, FSR and ISR/FSR fluctuations. These effects do not have a significant impact on the shape of the $E_{\mathrm{T}}^{\mathrm{miss}}$ distribution of electron-selected events. As a result, we evaluated these uncertainties, estimated in Section 7.5, in the same manner as the uncertainty due to the MC cross section uncertainties used above.

As mentioned in Section 6.5.2, a Gaussian-smeared $E_{\mathrm{T}}^{\mathrm{miss}}$ distribution of the reweighted corrected photon data sample is used to derive the results for $Z/\gamma^* + \mathrm{jets}$ in the $\mu\mu$ channel. A smearing of 5 GeV is used for the central value. Smearing with widths of 3 GeV and 7 GeV was evaluated and the largest differences with respect to the central value were taken as a systematic uncertainty. Figures 6.40 and 6.41 show the template fit results having used Gaussian distributions with widths of 3 GeV and 7 GeV, respectively, to smear the $E_{\mathrm{T}}^{\mathrm{miss}}$ of the photon events.

A summary of systematic uncertainties on the $Z/\gamma^* + \mathrm{jets}$ estimation is shown in table 6.12. The final estimations take the sum of these uncertainties in quadrature.

6.5.3 Summary of SM backgrounds

Tables 6.13, 6.14, and 6.15 show the results from observed data and the total SM expectation for $\int \mathcal{L}\, dt = 1.04$ fb^{-1}for SR1, SR2, and SR3, respectively. The estimation of $Z/\gamma^* + \mathrm{jets}$ comes from the data-driven method which is summarized in section 7.4.3.

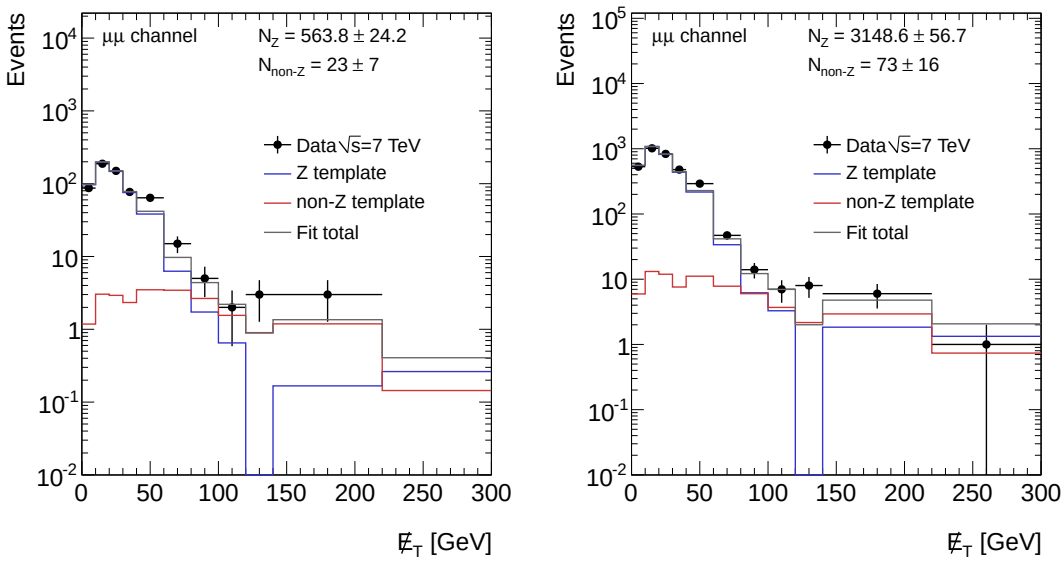

Figure 6.40: Results of the template fits to the selected data in the $\mu\mu$ channel for SR1 (left) and SR2 (right) using H_T-reweighted photon templates smeared with a Gaussian having a width of 3 GeV.

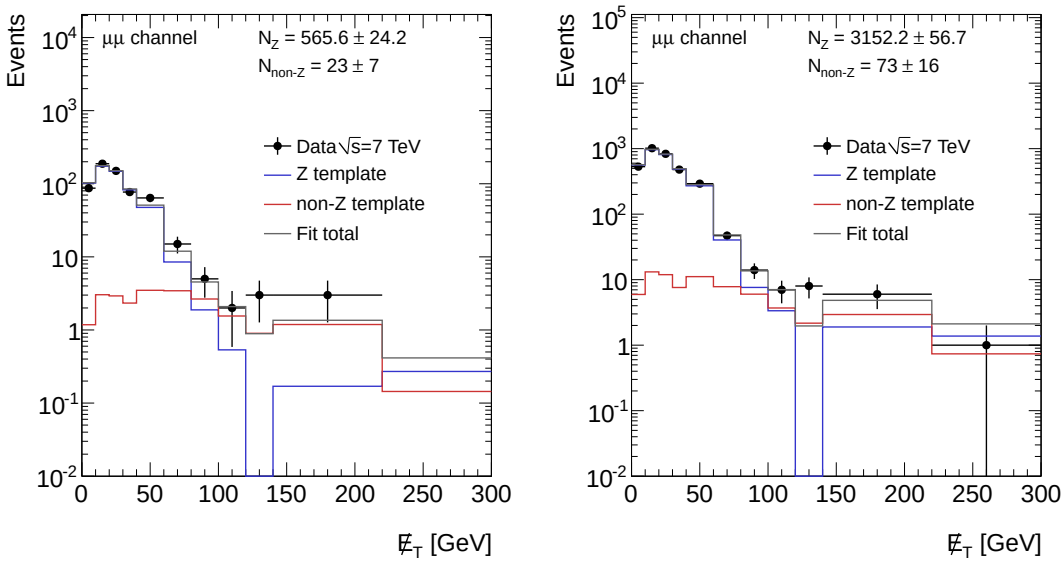

Figure 6.41: Results of the template fits to the selected data in the $\mu\mu$ channel for SR1 (left) and SR2 (right) using H_T-reweighted photon templates smeared with a Gaussian having a width of 7 GeV.

	SR1		SR2/SR3	
	ee	$\mu\mu$	ee	$\mu\mu$
binning	0.33%	1.35%	1.38%	1.61%
non-Z	<1%	<1%	<1%	<1%
CR	63.5%	21.2%	20.9%	11.5%
γ + jets subtraction	9.6%	20.8%	38.1%	39.2%
MC theory unc.	1.5%	3.1%	4.0%	4.1%
MC shape unc.	7.2%	13.8%	15.6%	15.6%
W + jets scale unc.	5.5%	10.6%	19.3%	19.1%
Muon $E_{\mathrm{T}}^{\mathrm{miss}}$	–	0.2%	–	0.2%
Total	64.90%	34.64%	50.17%	47.91%

Table 6.12: Systematic uncertainties (in %) on the estimate of Z/γ^* + jets contribution in SR1, SR2, and SR3. The sum in quadrature of these uncertainties is taken for the final result.

In SR1, the major backgrounds are the Z/γ^* + jets and top processes: ∼60% (∼63%) and ∼41% (∼37%), respectively, for the ee ($\mu\mu$) channel. Due to the stringent jet requirement in this region, the diboson contribution is negligible. Figure 6.42 (top) shows the distribution of the $E_{\mathrm{T}}^{\mathrm{miss}}$ after requirement of 3 jets with $p_T > 80, 40, 40$ GeV. After the requirement of $E_{\mathrm{T}}^{\mathrm{miss}} > 220$ GeV in SR1 we collect 2 events for $Z(\rightarrow e^{\pm}e^{\mp})$ final state, and zero events for $Z(\rightarrow \mu^{\pm}\mu^{\mp})$ final states, which is consistent with SM predictions in this region.

SR2 sees top, Z/γ^* + jets, and dibosons comprising ∼43% (∼42%), ∼40% (∼45%), and ∼16% (∼13%), of the total background, respectively, for the ee ($\mu\mu$) channel. Figure 6.42 (middle) shows the $E_{\mathrm{T}}^{\mathrm{miss}}$ distribution after a requirement of $H_T > 300$ GeV. After further selection of events with $E_{\mathrm{T}}^{\mathrm{miss}} > 140$ GeV, we observe 11 events in data, which is consistent with SM predictions. After adding the $\Delta R(\ell_1, \ell_2) < 2$ requirement for SR3, more than 50% of the $t\bar{t}$ background is removed. Figure 6.42 (bottom) shows the $E_{\mathrm{T}}^{\mathrm{miss}}$ distribution after requirement of $H_T > 300$ GeV and $\Delta R < 2$. In all signal regions, we find the contribution from QCD and W + jets to be negligible.

6.6 Systematic uncertainties for MC

Several sources of systematic uncertainties on both signal and background MC have been considered and quantified. These details of these uncertainties are given below.

Luminosity Uncertainty The uncertainty on the luminosity for 2011 data is 3.7%.

SR1		
	ee	$\mu\mu$
Data	2	0
SM total	0.54 ± 0.31(stat.) ± 0.28(syst.)	0.41 ± 0.24(stat.) ± 0.17(syst.)
non-Z	0.22 ± 0.11(stat.) ± 0.19(syst.)	0.15 ± 0.03(stat.) ± 0.14(syst.)
$Z/\gamma^* + \text{jets}$	0.32 ± 0.29(stat.) ± 0.21(syst.)	0.26 ± 0.24(stat.) ± 0.09(syst.)

Table 6.13: The results from observed data and the total SM background expectations for $\int \mathcal{L}\, dt = 1.04$ fb^{-1}. Results for the ee and $\mu\mu$ channels are shown for SR1.

SR2		
	ee	$\mu\mu$
Data	4	7
SM total	5.15 ± 0.87(stat.) ± 1.46(syst.)	7.06 ± 1.14(stat.) ± 2.03(syst.)
non-Z	3.07 ± 0.28(stat.) ± 1.02(syst.)	3.87 ± 0.23(stat.) ± 1.34(syst.)
$Z/\gamma^* + \text{jets}$	2.08 ± 0.82(stat.) ± 1.04(syst.)	3.19 ± 1.11(stat.) ± 1.53(syst.)

Table 6.14: The results from observed data and the total SM background expectations for $\int \mathcal{L}\, dt = 1.04$ fb^{-1}. Results for the ee and $\mu\mu$ channels are shown for SR2.

SR3		
	ee	$\mu\mu$
Data	2	4
SM total	3.34 ± 0.74(stat.) ± 1.01(syst.)	4.57 ± 0.87(stat.) ± 1.39(syst.)
non-Z	1.52 ± 0.16(stat.) ± 0.41(syst.)	2.13 ± 0.19(stat.) ± 0.75(syst.)
$Z/\gamma^* + \text{jets}$	1.82 ± 0.72(stat.) ± 0.92(syst.)	2.44 ± 0.85(stat.) ± 1.17(syst.)

Table 6.15: The results from observed data and the total SM background expectations for $\int \mathcal{L}\, dt = 1.04$ fb^{-1}. Results for the ee and $\mu\mu$ channels are shown for SR3.

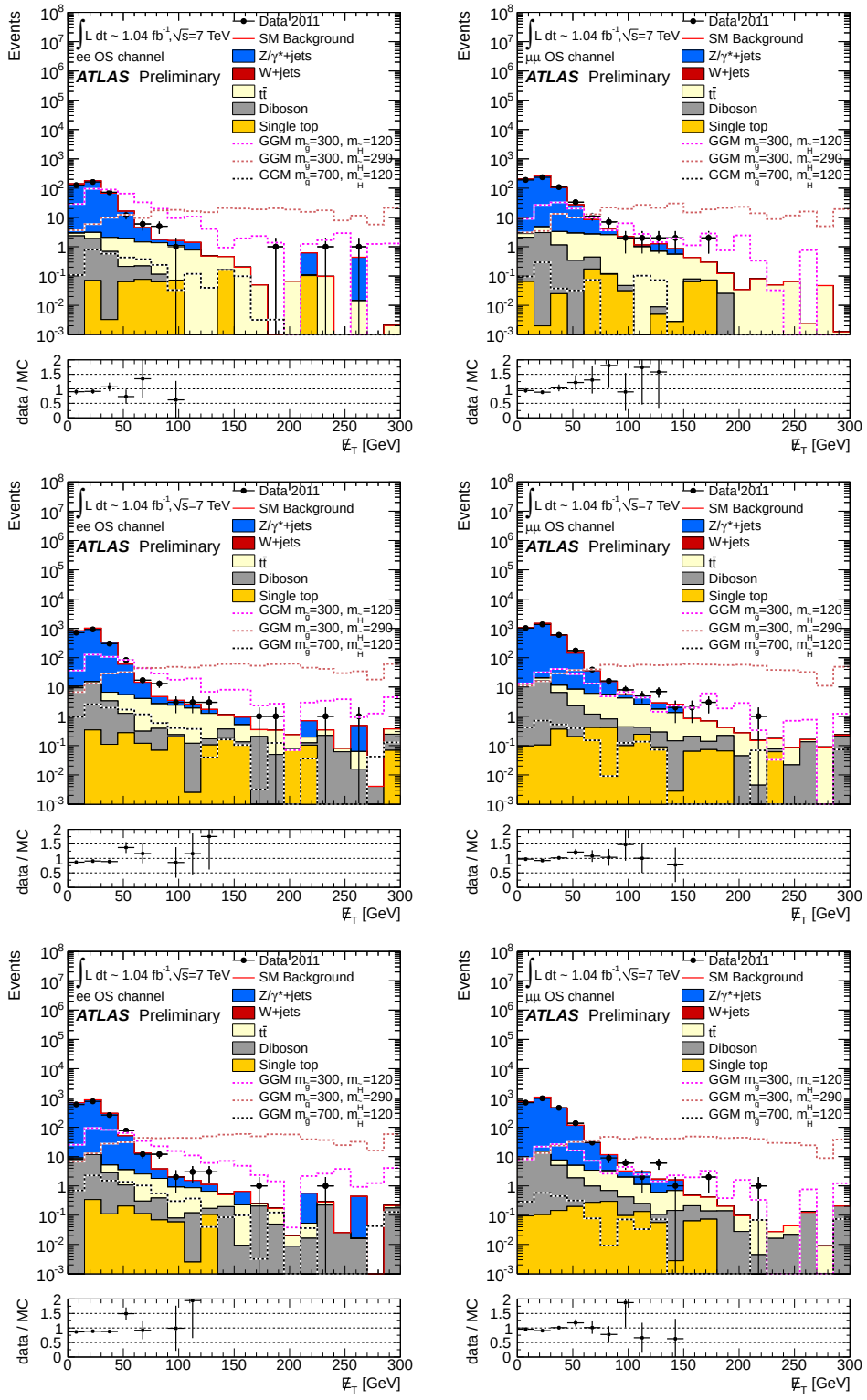

Figure 6.42: Distribution of the $E_{\mathrm{T}}^{\mathrm{miss}}$ for data and MC events after $Z(e^{\pm}e^{\mp})$ (left) and $Z(\mu^{\pm}\mu^{\mp})$ (right), $p_T(Z) > 45$ GeV, and additional requirements of 1) 3 jets with $p_T > 80, 40, 40$ GeV (top); 2) $H_T > 300$ GeV (middle); 3)$H_T > 300$ GeV and $\Delta R < 2$ (bottom). Three GGM signal points illustrate the SUSY contribution.

JES This is the asymmetric uncertainty due to the scaling of the jet energy up or down. The uncertainty due to the jet energy scale is evaluated using the MultijetJESUncertaintyProvider tool [83], which gives the uncertainties on the jet energy scale as a function of jet $p_{\mathrm{T}}$and η. In order to take into account the significant increase of out-of-time pile-up in 2011, another uncertainty has to be added. The numbers are derived from the expected difference from data and MC of the jet offset calculated from the mean tower energy in the zero-bias stream [83]. These pileup uncertainties were added in quadrature to the uncertainties provided by the MultijetJESUncertaintyProvider without the previous pileup term [84]. The uncertainties due to the in-time pile-up are included at the MultijetJESUncertaintyProvider tool [85].

JER This is the systematic uncertainty due to the jet energy resolution. It is evaluated following the recommendations given in [86]. Each jet is smeared according to a Gaussian distribution, with unit mean, and a width, sigma, given by the p_{T}(where $p_{\mathrm{T}}$is given in units of GeV) resolution function, as described in [69]. The JER provider provides JER uncertainties up to p_{T}= 500 GeVand $|\eta| = 2.8$. An extra absolute uncertainty of 7% has to be added, if the jet is in $|\eta| > 2.8$. All jets above the $\eta$and p_{T}boundaries are calculated with the boundary values.

EES This is an asymmetric uncertainty due to the scaling up or down of the electron energy scale. The uncertainty is evaluated using the EnergyRescaler tool [87].

EER This uncertainty considers the impact of additional electron energy resolution. This uncertainty is evaluated using the EnergyRescaler tool [87].

MES These are the asymmetric uncertainties from varying the MS and ID components of muon p_{T}.Based on the muon momenutm resolution measurements [88] MC muon momentum corrections have to be applied. The package MuonMomentumCorrections provides those corrections and the possibility to apply scale shifting and resolution smearing [89].

MC cross section The uncertainty due to the MC cross sections is chosen to be 5% for all MC samples except $t\bar{t}$, where the uncertainty in the cross section is taken $^{+7.0\%}_{-9.6\%}$ [79, 80].

For all the uncertainties which affect object definitions, the $E_{\mathrm{T}}^{\mathrm{miss}}$ is corrected accordingly. This means that each object in the container is removed (vectorially) from the missing energy, and the object added back in, but with systematic-varied x

and y components. In addition, uncertainties are considered on the $E_{\mathrm{T}}^{\mathrm{miss}}$ computation related to uncertainties in the `MET_CellOut`, used in `MET_RefFinal`. Since we use `MET_LocHadTopo`, the "CellOut" contribution to the overall $E_{\mathrm{T}}^{\mathrm{miss}}$ has to be approximated with a procedure recommended by the Jet/$E_{\mathrm{T}}^{\mathrm{miss}}$ group. The uncertainties considered here refer to the uncertainties in energy scale associated to the calorimeter clusters which are used in the $E_{\mathrm{T}}^{\mathrm{miss}}$ computation, but which are not associated to any hard objects in the event. These cluster energies are scaled, and the effect of this scaling is propagated to the overall $E_{\mathrm{T}}^{\mathrm{miss}}$ [90]. A flat 13.2% uncertainty is applied for this "CellOut" variation.

6.6.1 Systematic uncertainties for $t\bar{t}$ MC

Given that a large fraction of the background in the SRs is comprised of $t\bar{t}$ events, extra theoretical uncertainties were considered for this process:

- uncertainties due to the effect of Initial State Radiation (ISR) and Final State Radiation (FSR). AcerMC [82] samples were used to assess these uncertainties.
- uncertainties due to the choice of MC generator. The default MC@NLO MC is compared to POWHEG [81]. POWHEG gives the systematic uncertainty due to the use of a different NLO calculation.

The systematic uncertainties arising from possible mis-modeling of the ISR and FSR are studied using events generated with AcerMC interfaced with Pythia. The parameters controlling ISR and FSR were varied in a range consistent with experimental data. We considered samples characterized by six possible fluctuations:

1. ISR fluctuated upward
2. ISR fluctuated downward
3. FSR fluctuated upward
4. FSR fluctuated downward
5. ISR+FSR fluctuated upward
6. ISR+FSR fluctuated downward

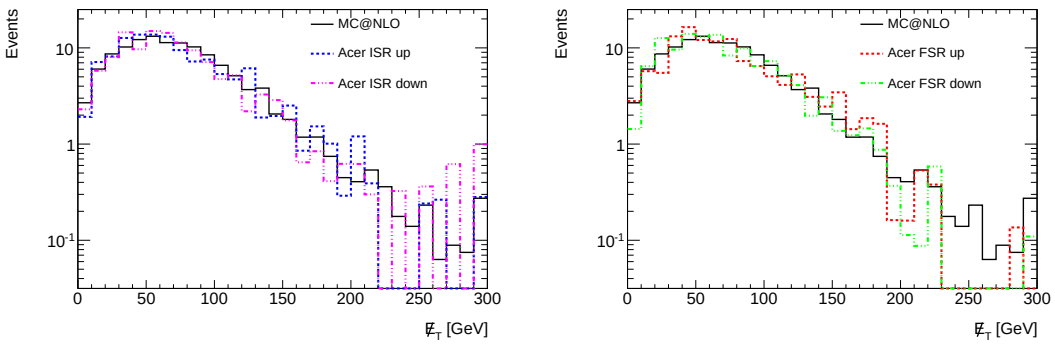

Figure 6.43: The $E_{\mathrm{T}}^{\mathrm{miss}}$ distribution for SR2 selection for $t\bar{t}$ MC, showing the nominal `MC@NLO` distribution along with ISR (left) and FSR (right) fluctuated distributions.

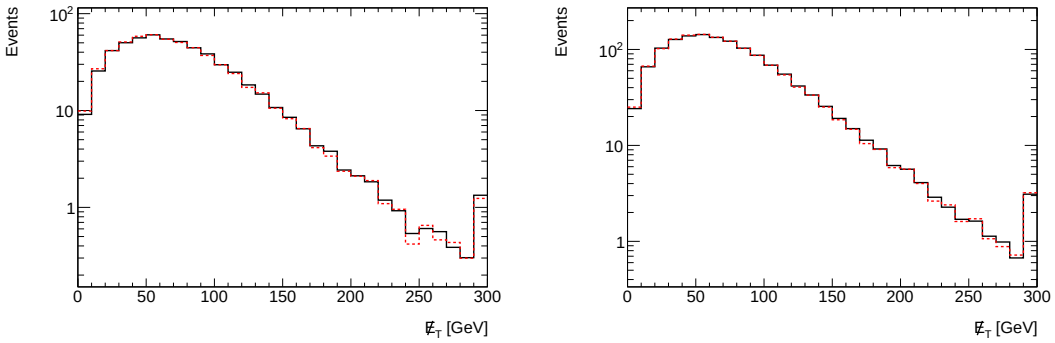

Figure 6.44: The $E_{\mathrm{T}}^{\mathrm{miss}}$ distribution of the $t\bar{t}$ samples generated using MC@NLO after SR1 (left) and SR2 (right) selections except $E_{\mathrm{T}}^{\mathrm{miss}}$ and dilepton mass cuts, with (black) and without (red) $p_T(Z) > 45$ GeV requirement.

The impact of the ISR and FSR fluctuations on the $E_{\mathrm{T}}^{\mathrm{miss}}$ distribution of the $t\bar{t}$ sample in SR2 are shown in Figure 6.43. Uncertainties due to the effect of ISR and FSR on the $t\bar{t}$ background prediction are computed by taking the largest variations up and down in the predicted event yield compared to the default Acer MC sample as a function of the $E_{\mathrm{T}}^{\mathrm{miss}}$cut. To increase the statistics in the Acer MC samples the dilepton mass and $p_{\mathrm{T}}(Z)$ requirements, which have no effect on the shape of the $t\bar{t}$ $E_{\mathrm{T}}^{\mathrm{miss}}$ distribution, were removed from the selection. Figure 6.44 shows the $E_{\mathrm{T}}^{\mathrm{miss}}$ distribution of the $t\bar{t}$ samples generated using MC@NLO after SR1 and SR2 requirements, except $E_{\mathrm{T}}^{\mathrm{miss}}$ and the dilepton mass cuts. To demonstrate that the $p_{\mathrm{T}}(Z) > 45$ GeV requirement has no effect on the shape of the $E_{\mathrm{T}}^{\mathrm{miss}}$, these distributions were plotted with and without this cut. Figure 6.45 shows the effect of ISR and FSR fluctuations on the $E_{\mathrm{T}}^{\mathrm{miss}}$ of $t\bar{t}$ events after SR2 selection without the dilepton mass, $p_{\mathrm{T}}(Z)$, and $E_{\mathrm{T}}^{\mathrm{miss}}$ requirements.

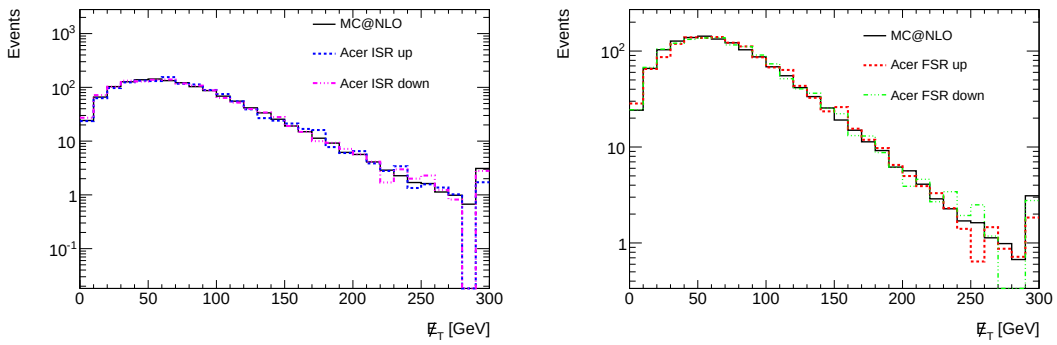

Figure 6.45: The $E_{\mathrm{T}}^{\mathrm{miss}}$ distribution for SR2 selection without the dilepton mass or dilepton p_T requirements for $t\bar{t}$MC, showing the nominal `MC@NLO` distribution along with ISR fluctuated (left) and FSR fluctuated (right) distributions.

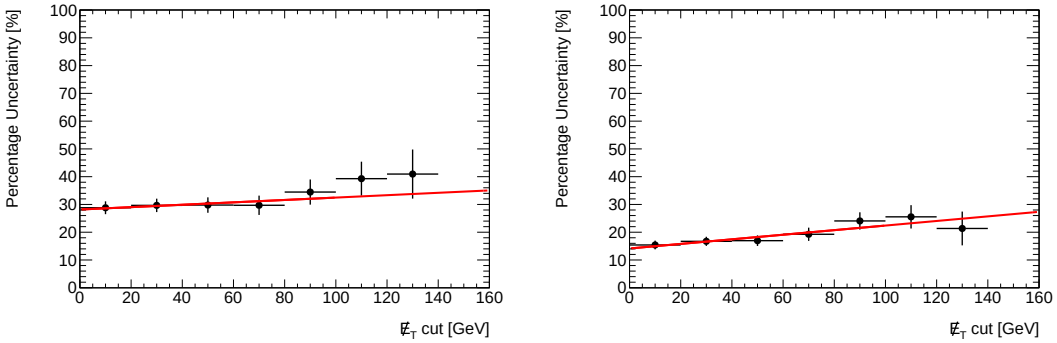

Figure 6.46: The % uncertainty on $t\bar{t}$ expectations using the Acer MC ISR and FSR varied samples for SR1 (left) and SR2 (right) as a function of $E_{\mathrm{T}}^{\mathrm{miss}}$ cut value. The red lines show a linear fit through the points in the $E_{\mathrm{T}}^{\mathrm{miss}} < 100$ GeV region. Both ee and $\mu\mu$ events are used together to increase statistics, in addition to having no requirement on dilepton mass and p_T.

Due to the stringent $E_{\mathrm{T}}^{\mathrm{miss}}$ requirements for the signal regions, the statistical error on the systematic uncertainty becomes considerable due to lack of Monte Carlo events and can not be calculated directly. To address this and limit the effect of statistical variations, the uncertainty was computed for several softer cuts in $E_{\mathrm{T}}^{\mathrm{miss}}$, and then extrapolated to the cut values used for the signal regions. For this extrapolation, a linear fit of the uncertainties as a function of $E_{\mathrm{T}}^{\mathrm{miss}}$ cut values was performed. The evolution of the uncertainties as a function of the $E_{\mathrm{T}}^{\mathrm{miss}}$ cut are shown in Figure 6.46 for SR1 and SR2. Uncertainties of 37.6%, 25.7%, and 39.7% were computed respectively for SR1, SR2, and SR3.

Generator uncertainties on the predicted yield of the $t\bar{t}$ background were assessed by comparing the nominal predictions, from MC@NLO, to the predictions of the POWHEG generator. These variations were studied as a function of the $E_{\mathrm{T}}^{\mathrm{miss}}$ cut,

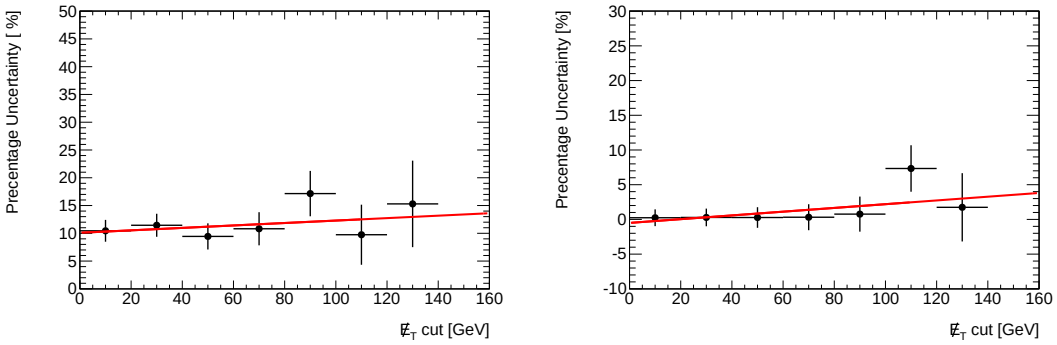

Figure 6.47: The % uncertainty on $t\bar{t}$ expectations using the POWHEG samples for SR1 (left) and SR2 (right) as a function of $E_{\mathrm{T}}^{\mathrm{miss}}$ cut value. The red lines show a linear fit through the points in the $E_{\mathrm{T}}^{\mathrm{miss}} < 100$ GeV region. Both ee and $\mu\mu$ events are used together to increase statistics, in addition to having no requirement on dilepton mass and p_T.

in an analogous fashion as for the ISR and FSR uncertainties above. The evolution of the generator uncertainties as a function of $E_{\mathrm{T}}^{\mathrm{miss}}$ cut are shown in Figure 6.47 for SR1 and SR2. The uncertainties of 14.9%, 3.2%, and 5.9% were computed respectively for SR1, SR2, and SR3.

Table 6.16 summarizes the systematic uncertainties due to all sources of the systematics uncertainties mentioned above.

6.6.2 Systematic uncertainties for signal MC

The signal systematic uncertainties which were considered in the analysis are detailed below.

Renormalization and Factorization scale The combined uncertainties on the cross section from the renormalization and factorization scales are estimated by comparing Prospino 2.1 [75] NLO cross section values obtained with or without scale variations. For the $\tilde{g}\tilde{g}$ production, the nominal scale is given by Q = m($\tilde{g}$). The scale uncertainties, is taken to be the difference in cross section between 2Q and Q, and between Q/2 and Q. The contribution from the each process is taken into account. Table 6.17 shows the scale relative uncertainties calculated only using $\tilde{g}\tilde{g}$ production processes.

PDF The central value of the NLO cross section was calculated by Prospino2.1 [75] with CTEQ6.6m PDF. The PDF are extrapolated from measurements and thus carry uncertainties. The uncertainties are represented by 22 variations which

Sources	SR1		SR2		SR3	
	ee	$\mu\mu$	ee	$\mu\mu$	ee	$\mu\mu$
Luminosity	3.7%					
MC cross section ($t\bar{t}$)	8%					
MC cross section (others)	5%					
JES	55.6%	39.2%	22.0%	19.8%	11.2%	12.4%
JER	12.1%	2.3%	3.1%	4.1%	1.9%	5.9%
EES and EER	18.8%	0.01%	2.9%	0.01%	3.5%	0.01%
MES and ID	0.0%	14.4%	1.9%	4.8%	0.0%	8.3%
Cell Out	55.6%	72.0%	18.3%	19.8%	13.4%	22.1%
ISR/FSR ($t\bar{t}$)	19.8%	37.6%	14.9%	18.0%	19.5%	21.2%
Generator uncertainty ($t\bar{t}$)	7.9%	15%	1.9%	2.3%	3.0%	3.2%
Total	84.8%	93.0%	33.3%	34.7%	27.4%	35.3%

Table 6.16: Relative systematic uncertainties from all sources on SM non-Z events for the ee and $\mu\mu$ channels.

$m(\tilde{g})$ [GeV]	Scale	PDF
300	0.15	0.12
400	0.16	0.12
500	0.17	0.15
600	0.18	0.18
700	0.18	0.21
800	0.20	0.25
900	0.19	0.29

Table 6.17: The scale and PDF relative uncertainties on the GGM signal cross sections for $\tilde{g}\tilde{g}$ production only.

span the range of the uncertainties coming from the experimental errors. The uncertainties are the 90% CL upper and lower bound variation of the PDF. The effect of these uncertainties on the NLO cross section is obtained by calculating the cross section for each of these variations while keeping the other parameters fixed. This leads to 44 different outcomes of the cross section $\sigma_{\pm}$ from which the PDF uncertainty is evaluated by using the Hessian method, based on the linear error propagation. The detailes can be found at [77]. Table 6.17 shows the PDF relative uncertainties calculated only using $\tilde{g}\tilde{g}$ production processes.

GGM MC cross section uncertainties The GGM MC cross section uncertainties was calculated by Prospino 2.1 [75]. The uncertainty on the filter efficiency was calculated using Pythia generator.

Tables 6.18 and 6.19 summarize the signal systematic uncertainties from the different sources mentioned above. The overal uncertainties change from 14% to 35%. In addition, for each GGM point we estimated the systematic uncertainties due to JES, JER, EES, EER, MES, and the CellOut sources. The $E_{\mathrm{T}}^{\mathrm{miss}}$ was corrected accordingly by varying the computation for each source, and then the estimates were compared against the nominal values.

6.7 Interpretation in the Context of SUSY

Having the observations from data and the estimations of backgrounds in the SRs, we now can quantify the level of agreement between the data and the prediction from the standard model or specific SUSY models. The frequentist approach followed here is outlined in [91], and is constructed based around a profile log likelihood ratio (LLR) test. The profile LLR is obtained by performing fits the likelihood to the measurements in the SRs. The `HistFitter` package is used to implement the creation of workspaces and the calculation of p-values using toy MC experiments.

		Relative uncertainties			
$m(\tilde{g})$[GeV]	$m(\tilde{h})$[GeV]	scale	PDF	MC cross section and efficiency	Total
300	110	0.13	0.12	0.04	0.18
	115	0.13	0.12	0.02	0.18
	120	0.14	0.12	0.03	0.18
	150	0.15	0.12	0.036	0.19
	200	0.15	0.12	0.035	0.20
	290	0.15	0.12	0.029	0.20
400	110	0.06	0.12	0.03	0.14
	115	0.07	0.12	0.025	0.14
	120	0.08	0.12	0.019	0.15
	150	0.12	0.12	0.035	0.17
	200	0.15	0.12	0.021	0.19
	300	0.16	0.12	0.031	0.20
	390	0.16	0.12	0.031	0.20
500	110	0.006	0.15	0.038	0.15
	115	0.002	0.15	0.027	0.15
	120	0.01	0.15	0.024	0.15
	150	0.06	0.15	0.035	0.16
	200	0.1	0.15	0.036	0.19
	300	0.16	0.15	0.027	0.22
	400	0.17	0.15	0.034	0.23
	490	0.17	0.15	0.017	0.23
600	110	0.04	0.18	0.017	0.18
	115	0.03	0.18	0.041	0.19
	120	0.03	0.18	0.027	0.18
	150	0.004	0.18	0.025	0.18
	200	0.06	0.18	0.032	0.19
	300	0.14	0.18	0.042	0.23
	400	0.17	0.18	0.016	0.25
	500	0.17	0.18	0.035	0.25
	590	0.17	0.18	0.038	0.25

Table 6.18: Summary of the scale, PDF, MC cross section and efficiency, and the total relative uncertainties on the GGM signal cross sections.

		Relative uncertainties			
$m(\tilde{g})$[GeV]	$m(\tilde{h})$[GeV]	Scale	PDF	MC cross section and efficiency	Total
700	110	0.05	0.21	0.037	0.22
	115	0.04	0.21	0.035	0.22
	120	0.04	0.21	0.027	0.22
	150	0.02	0.21	0.029	0.21
	200	0.01	0.21	0.030	0.21
	300	0.10	0.21	0.030	0.23
	400	0.15	0.21	0.022	0.26
	500	0.17	0.21	0.020	0.27
	600	0.18	0.21	0.020	0.28
	690	0.18	0.21	0.027	0.28
800	120	0.04	0.25	0.042	0.26
	150	0.03	0.25	0.023	0.25
	200	0.01	0.25	0.019	0.25
	300	0.05	0.25	0.024	0.26
	400	0.12	0.25	0.026	0.28
	500	0.17	0.25	0.042	0.30
	600	0.19	0.25	0.027	0.31
	700	0.20	0.25	0.044	0.32
	790	0.20	0.25	0.021	0.32
900	120	0.05	0.29	0.020	0.29
	150	0.04	0.29	0.021	0.29
	200	0.02	0.29	0.020	0.29
	300	0.01	0.29	0.020	0.29
	400	0.06	0.29	0.016	0.30
	500	0.12	0.29	0.036	0.32
	600	0.16	0.29	0.020	0.33
	700	0.18	0.29	0.031	0.34
	800	0.18	0.29	0.028	0.35
	890	0.19	0.29	0.038	0.35

Table 6.19: Summary of the scale, PDF, MC cross section and efficiency, and the total relative uncertainties on the GGM signal cross sections.

6.7.1 The likelihood function

The likelihood function is defined as a product over flavor channels:

$$L(\boldsymbol{n}_{\text{obs}}, \boldsymbol{\theta}^0|\mu, \boldsymbol{b}, \boldsymbol{\theta}) = \prod_{c\in\text{channels}} \text{Pois}(n_{\text{obs},c}|\lambda(\mu, \boldsymbol{b}_c, \boldsymbol{\theta})) \cdot G(L_0|L, \Delta_L) \cdot \prod_{p\in\text{syst}} G_p(\theta_p^0, \theta_p) \tag{6.4}$$

The Poisson function is defined as the probability that there are exactly $n_{\text{obs},c}$ events for channel c in the SR given an expectation of λ, $P(n_{\text{obs},c}|\lambda(\mu, \boldsymbol{b}_c, \boldsymbol{\theta}))$. The Poisson expectation λ depends on the following:

- background normalization factors for each channel, $\boldsymbol{b}_c$, such as the expected number of $t\bar{t}$ or diboson events in the SR;
- nuisance parameters, $\boldsymbol{\theta}$, which parametrize the systematic uncertainties;
- a signal strength factor, μ, which describes the signal model being considered. For $\mu = 0$, no signal is considered, whereas for $\mu = 1$, the signal expectation equals the nominal value of the expectation from the model under investigation.

The systematic uncertainties for both the signal and background expectations in the SR are described by a product of Gaussian distributions over the various sources taken into account. To ensure a proper treatment of correlated uncertainties among samples and flavor channels, all detector-related systematics (*e.g.*, jet energy scale, jet energy resolution, $E_{\text{T}}^{\text{miss}}$ `CellOut` uncertainty) are represented by a single term in the likelihood. Theory uncertainties are treated as uncorrelated. In the case of the data-driven $Z/\gamma^* + \text{jets}$ estimate, the uncertainties are treated as correlated between the two flavor channels.

6.7.2 The test statistic

The test statistic , q_μ, used to derive the p-values for exclusion or discovery is constructed from a profile LLR:

$$q_\mu \equiv q_\mu(\boldsymbol{n}_{\text{obs}}, \boldsymbol{\theta}^0) \equiv -2\left(\ln \frac{L(\boldsymbol{n}_{\text{obs}}, \boldsymbol{\theta}^0|\mu, \hat{\hat{\boldsymbol{b}}}, \hat{\hat{\boldsymbol{\theta}}})}{L(\boldsymbol{n}_{\text{obs}}, \boldsymbol{\theta}^0|\hat{\mu}, \hat{\boldsymbol{b}}, \hat{\boldsymbol{\theta}})}\right) \tag{6.5}$$

$$= -2\left(\ln L(\boldsymbol{n}_{\text{obs}}, \boldsymbol{\theta}^0|\mu, \hat{\hat{\boldsymbol{b}}}, \hat{\hat{\boldsymbol{\theta}}}) - \ln L(\boldsymbol{n}_{\text{obs}}, \boldsymbol{\theta}^0|\hat{\mu}, \hat{\boldsymbol{b}}, \hat{\boldsymbol{\theta}})\right) \tag{6.6}$$

In this notation, $\hat{\mu}, \hat{\boldsymbol{b}}, \hat{\boldsymbol{\theta}}$ are the values of the signal strength, background normalization, and nuisance parameters which maximize the likelihood function in a free fit. If the signal strength μ is held fixed, then the values which maximize the likelihood function with this constraint are given by $\hat{\hat{\boldsymbol{b}}}, \hat{\hat{\boldsymbol{\theta}}}$. Since each of the SRs in question for this analysis are characterized by low event counts, we do not assume a simple χ^2 distribution for q_μ; instead, pseudo-experiments are used to obtain the PDF for q_μ.

6.7.3 Pseudo-experiments

The goal of running pseudo-experiments is to acquire the PDFs for the test statistic q_μ assuming some specific hypothesis; these PDFs are known as sampling distributions. The calculation performed here is following the CL_s procedure, and therefore we are interested in the sampling distributions for both a signal+background hypothesis and a background-only hypothesis. We generate toy MC to simulate the measurement made with $\int \mathcal{L}\, dt = 1.04$ fb^{-1}, based on the likelihood above, to find the sampling distributions. The idea is to mimic the measurement scenario by obtaining values of the nuisance parameters and observables, $\boldsymbol{\theta}^0$ and $\boldsymbol{n}$, from a specified set of $\mu, \boldsymbol{b}, \boldsymbol{\theta}$ using the likelihood function $L(\boldsymbol{n}_{\text{obs}}, \boldsymbol{\theta}^0 | \mu, \boldsymbol{b}, \boldsymbol{\theta})$. With each pseudo-measurement (a value for the observable and the nuisance parameters, denoted $\boldsymbol{n}^{'}_{\text{obs}}, \boldsymbol{\theta}^{0'}$), a value for the test statistic can be obtained, q'_μ.

The distributions for $\mu = 0$ toy MC and $\mu = 1$ toy MC are both necessary for our formalism, since we employ the use of the CL_s value. The defintion of CL_s is

$$CL_s = \frac{p_{s+b}}{1 - p_b}. \tag{6.7}$$

Here, $p_{s+b} = \int_{q_{\text{obs}}}^{\infty} f_{s+b}(q^{'}_{\mu=1}) dq^{'}$ is the probability under the $s + b$ hypothesis of conducting an experiment whose test statistic value is larger than the observed test statistic, q_{obs}; the smaller this value is, the more compatible the measurement is with the signal+background hypothesis. Similarly, $p_b = \int_{-\infty}^{q_{\text{obs}}} f_b(q^{'}_{\mu=1}) dq^{'}$ is the probability under the b-only hypothesis of measuring a value for q_μ less than q_{obs}; the larger this value, the less compatible the measurement is with the background hypothesis (*i.e.*, the more compatible it is with the signal+background hypothesis).

With the value of CL_s, the question of exclusion at 95% confidence is simple: if CL_s is found to be < 0.05, we can exclude the signal hypothesis for the given model with 95% confidence.

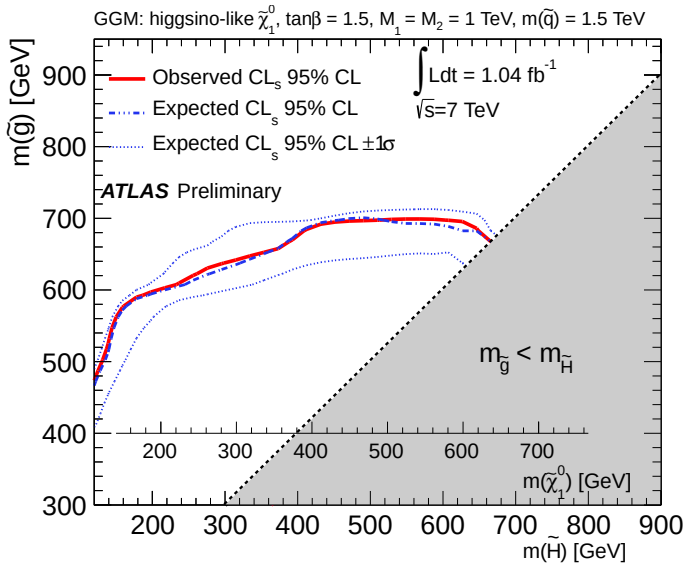

Figure 6.48: 95% CL mass limit contours, for $\int \mathcal{L}\, dt = 1.04$ fb^{-1}, for the combination of SR1 and SR2. For each grid point, the p-values from the SR which gives the strongest expected limit is used.

6.7.4 Interpretation in higgsino-like NLSP GGM

To produce 95% CL contours in the $m_{\tilde{h}} - m_{\tilde{g}}$ plane, we run 20,000 toy MC pseudo-experiments for each of our GGM grid points to obtain exclusion p-values. In performing this calculation, we consider both the individual flavor channels independently, as well as the statistical combination of the two. The results in SR3 provide no additional sensitivity over SR2, and therefore the exclusions have been calculated for SR1 and SR2 only. The exclusion calculation uses the statistical combination of the two flavor channels, and performs a scan over SR1 and SR2. At each signal point, the value corresponding to the SR having the strongest median expected limit (*i.e.*, the lowest expected p-value) is chosen. The results of this scan are shown in figure 6.48.

6.7.5 Exclusion limits

Figure 6.48 shows the 95% upper limits on the higgsino and gluino masses for the combination of the ee and $\mu\mu$ channels, taking the strongest expected limit from SR1 and SR2. For higgsino masses in the range $200 < m_{\tilde{\chi}} < 640$ GeV, we compute an upper limit on the gluino mass of $m_{\tilde{g}} < 600 - 700$ GeV.

Chapter 7

Searches for SUSY in the $Z + E_T^{\text{miss}}$ final state with 2012 data

7.1 Introduction

This chapter presents a continued search for SUSY in the $Z + \text{jets} + E_{\text{T}}^{\text{miss}}$ final state, based off of the analysis in the previous chapter. Data collected in 2012 at $\sqrt{s} = 8$ TeV amounting to a total integrated luminosity of 5.84 fb^{-1} is used. As before, the main SM backgrounds are the $Z/\gamma^* + \text{jets}$, $t\bar{t}$, single-top, and diboson processes. The evaluation of the instrumental $Z/\gamma^* + \text{jets}$ background, which has $E_{\text{T}}^{\text{miss}}$ that is mostly due to hadronic mismeasurement, was made using a data driven method known as "jet smearing." The WW, $t\bar{t}$, Wt, $\tau\tau$ backgrounds were estimated using $e\mu$ events. The ZZ and WZ backgrounds were estimated using Monte Carlo (MC) simulation. The QCD and inclusive $W + \text{jets}$ backgrounds are negligible.

7.2 Simulation

7.2.1 Signal MC

For the GGM models, the SUSY mass spectra, the gluino branching ratios, and the gluino decay width were calculated using SUSPECT 2.41 [72] and SDECAY 1.3 [73]. Table 7.1 shows the values of the parameters used for the signal MC production. All other sparticle masses are fixed at ∼1.5TeV.

The MC signal samples were generated using PYTHIA 6.423 [74] with MRST2007 LO* [92] parton distribution functions (PDF). Signal cross sections are calculated to next-to-leading order (NLO) in the strong coupling constant, adding the resummation of soft gluon emission at next-to-leading-logarithmic accuracy (NLO+NLL) [93–97].

Parameters	M_1	M_2	$\tan\beta$	$c\tau_{\text{NLSP}}$	μ	$m(\tilde{g})$
Values	1 TeV	1 TeV	1.5	0.1 mm	vary	vary
Values	1 TeV	1 TeV	30	0.1 mm	vary	vary

Table 7.1: Parameters of the GGM models used for the signal production at $\sqrt{s} =$ 8 TeV.

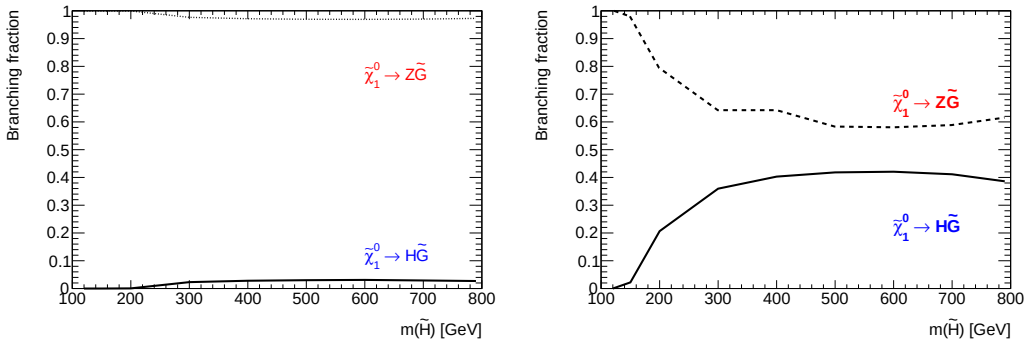

Figure 7.1: The branching fraction for $\tilde{\chi}_1^0 \to h\tilde{G}$ and $\tilde{\chi}_1^0 \to Z\tilde{G}$ processes as function of μ for GGM grid models characterized by the following parameters: $M_1 = 1$ TeV, $M_2 =$ 1 TeV, $m(\tilde{g}) = 800$ GeV, $\tan\beta = 1.5$(left), $\tan\beta = 30$(right).

The nominal cross section and the uncertainty are taken from an envelope of cross section predictions using different PDF sets and factorisation and renormalisation scales, as described in Ref. [98].

The mechanisms for sparticle production in the signal points can be grouped into two categories: strong production ($\tilde{g}\tilde{g}$), and electroweak production ($\tilde{\chi}_1^0\tilde{\chi}_2^0$, $\tilde{\chi}_1^\pm\tilde{\chi}_1^\mp$, $\tilde{\chi}_1^0\tilde{\chi}_1^\pm$, $\tilde{\chi}_2^0\tilde{\chi}_1^\pm$). All processes are considered for NLO calculations. To select events with at least one Z boson that decays to a pair of electrons, muons, or taus, the `ZtoLeptonFilter` is used at generator level. This filter has an efficiency of $18.8 \pm 0.5\%$ for models with $\tan\beta = 1.5$. The filter efficiency for the models with $\tan\beta = 30$ is dependent on μ, because $BR(\tilde{\chi}_1^0 \to h\tilde{G})$ increases with μ for these models, reaching a value of 0.39 for $\mu = 790$ GeV (see Figure 7.1 (right)). The $BR(\tilde{\chi}_1^0 \to h\tilde{G})$ and $BR(\tilde{\chi}_1^0 \to Z\tilde{G})$ for $\tan\beta = 1.5$ is also presented at Figure 7.1 (left). Tables 7.2, 7.3, 7.4, and 7.5 present μ, masses of $\tilde{\chi}_1^0$, $\tilde{\chi}_2^0$, $\tilde{\chi}_1^\pm$, the NLO+NLL cross section, the filter efficiency, and the effective NLO+NLL cross section for each generated GGM point. Table 7.6 presents the NLO+NLL cross section for for $\tilde{g}\tilde{g}$ production as a function of $m(\tilde{g})$. $\tilde{g}\tilde{g}$ production is expected to have no dependence on $m(\tilde{H})$.

In total, 101 signal samples were generated. As an example, the full SUSY particle mass spectrum for the model with $\tan\beta = 1.5$, $m(\tilde{g}) = 600$ GeV and $\mu = 120$ GeV is listed in Table 7.7.

$m(\tilde{g})$ [GeV]	μ [GeV]	$m(\tilde{\chi}_1^0)$ [GeV]	$\sigma(NLO+NLL)$ [pb]	ϵ [%]	$\sigma \times \epsilon$ [pb]
600	120	110.9	6.6 ± 0.3	18.8 ± 0.5	1.24± 0.05
	150	140.7	3.3 ± 0.2		0.62± 0.04
	200	190.1	1.9 ± 0.2		0.36± 0.04
	300	288.7	1.3 ± 0.2		0.25± 0.04
	400	386.9	1.2 ± 0.2		0.23± 0.04
	500	484.5	1.2 ± 0.2		0.22± 0.04
	590	571.3	1.2 ± 0.2		0.22± 0.04
700	120	110.9	5.8 ± 0.2	18.8 ± 0.5	1.09± 0.03
	150	140.7	2.7± 0.1		0.51±0.02
	200	190.1	1.1± 0.1		0.21±0.02
	300	288.7	0.51± 0.08		0.096±0.014
	400	386.9	0.40± 0.08		0.076±0.014
	500	484.5	0.38± 0.08		0.072±0.014
	600	580.9	0.38± 0.08		0.071±0.014
	690	666.0	0.37± 0.08		0.070±0.014
800	120	110.9	5.55± 0.15	18.8 ± 0.5	1.04±0.03
	150	140.7	2.44± 0.07		0.46± 0.01
	200	190.1	0.88±0.04		0.17± 0.007
	300	288.7	0.27±0.03		0.05± 0.006
	400	386.9	0.16±0.03		0.031± 0.006
	500	484.5	0.14±0.03		0.026± 0.006
	600	580.9	0.13± 0.03		0.025± 0.006
	700	675.3	0.13± 0.03		0.024± 0.006
	790	757.0	0.13± 0.03		0.024± 0.006

Table 7.2: μ, mass of $\tilde{\chi}_1^0$, the NLO+NLL cross section, the generation efficiency, and the effective NLO+NLL cross section after a $Z(\ell\ell)$ event filter for the GGM grid models characterized by the following parameters: $M_1 = 1$ TeV, $M_2 = 1$ TeV, $\tan\beta = 1.5$.

$m(\tilde{g})$ [GeV]	μ [GeV]	$m(\tilde{\chi}_1^0)$ [GeV]	$\sigma(NLO+NLL)$ [pb]	ϵ [%]	$\sigma \times \epsilon$ [pb]
900	120	110.9	5.46 ± 0.15	18.8 ± 0.5	1.03 ± 0.03
	150	140.7	2.02 ± 0.06		0.38 ± 0.01
	200	190.1	0.80± 0.02		0.15 ± 0.004
	300	288.7	0.09± 0.01		0.016 ± 0.002
	400	386.9	0.07± 0.01		0.014 ± 0.002
	500	484.5	0.05± 0.01		0.010 ± 0.002
	600	580.9	0.05± 0.01		0.009 ± 0.002
	700	675.3	0.05± 0.01		0.009 ± 0.002
	800	765.8	0.05± 0.01		0.009 ± 0.002
	890	839.9	0.05± 0.01		0.008 ± 0.002
1000	120	110.9	5.44± 0.015	18.8 ± 0.5	1.02±0.03
	150	140.7	2.33± 0.06		0.44± 0.01
	200	190.1	0.77± 0.02		0.145±0.004
	300	288.7	0.16± 0.01		0.030±0.001
	400	386.9	0.054± 0.006		0.010±0.001
	500	484.5	0.029± 0.006		0.0052±0.001
	600	580.9	0.022± 0.006		0.0037±0.001
	700	675.3	0.019± 0.0006		0.0032±0.001
	800	765.8	0.018± 0.0006		0.0030±0.001
	900	847.5	0.018± 0.0006		0.0029±0.001
	990	905.5	0.017± 0.0006		0.0029±0.001

Table 7.3: μ, mass of $\tilde{\chi}_1^0$, the NLO+NLL cross section, the generation efficiency, and the effective NLO+NLL cross section after a $Z(\ell\ell)$ event filter for the GGM grid models characterized by the following parameters: $M_1 = 1$ TeV, $M_2 = 1$ TeV, $\tan\beta = 1.5$.

$m(\tilde{g})$ [GeV]	μ [GeV]	$m(\tilde{\chi}_1^0)$ [GeV]	$\sigma(NLO+NLL)$ [pb]	ϵ [%]	$\sigma \times \epsilon$ [pb]
400	120	115.1	23.6 ± 2.8	19.0 ± 0.5	4.4 ± 0.5
	150	144.9	20.5 ± 2.8	18.8 ± 0.5	3.85± 0.5
	200	194.6	18.9 ± 2.8	16.2 ± 0.4	3.6 ± 0.5
	300	293.8	18.3 ± 2.8	13.2 ± 0.4	3.4± 0.5
	390	382.9	18.2 ± 2.8	11.2 ± 0.3	3.4± 0.5
500	120	115.1	9.7 ± 0.7	20.0 ± 0.5	1.8 ± 0.13
	150	144.9	6.5 ± 0.7	18.7 ± 0.5	1.2 ± 0.13
	200	194.6	4.9 ± 0.7	16.2 ± 0.4	0.9 ± 0.13
	300	293.8	4.4 ± 0.7	12.4 ± 0.3	0.82±0.13
	400	392.8	4.3 ± 0.7	12.6 ± 0.3	0.80±0.13
	490	481.5	4.2 ± 0.7	11.6 ± 0.3	0.80±0.13
600	120	115.1	6.6 ± 0.3	18.6 ± 0.5	1.24 ± 0.05
	150	144.9	3.3 ± 0.2	18.7 ± 0.5	0.62 ± 0.04
	200	194.6	1.9 ± 0.2	15.2 ± 0.4	0.36 ± 0.04
	300	293.8	1.3± 0.2	12.4 ± 0.3	0.25± 0.04
	400	392.8	1.2± 0.2	12.3 ± 0.3	0.23± 0.04
	500	491.4	1.2± 0.2	11.6 ± 0.3	0.22± 0.04
	590	579.5	1.2± 0.2	12.4 ± 0.3	0.22± 0.04
700	120	115.1	5.79 ± 0.17	18.4 ± 0.5	1.09 ±0.03
	150	144.9	2.70 ± 0.10	18.1 ± 0.5	0.51±0.02
	200	194.6	1.13± 0.8	15.5 ± 0.4	0.21±0.014
	300	293.8	0.51± 0.08	12.9 ± 0.3	0.09±0.014
	400	392.8	0.40± 0.08	12.2 ± 0.3	0.08±0.014
	500	491.4	0.38± 0.08	12.1 ± 0.3	0.07±0.014
	600	589.3	0.38± 0.08	11.9 ± 0.3	0.07±0.014
	690	676.4	0.37± 0.08	11.5 ± 0.3	0.07±0.014
800	120	115.1	5.55± 0.15	19.1 ± 0.5	1.04 ± 0.03
	150	144.9	2.44± 0.07	19.3 ± 0.5	0.46 ± 0.01
	200	194.6	0.88± 0.04	14.7 ± 0.4	0.17± 0.007
	300	293.8	0.27± 0.03	12.7 ± 0.3	0.05± 0.006
	400	392.8	0.16± 0.03	12.5 ± 0.3	0.03± 0.006
	500	491.4	0.14± 0.03	11.6 ± 0.3	0.025± 0.006
	600	589.3	0.13± 0.03	11.6 ± 0.3	0.025± 0.006
	700	686.0	0.13± 0.03	11.4 ± 0.3	0.024± 0.006
	790	770.9	0.13± 0.03	12.4 ± 0.3	0.024± 0.006

Table 7.4: μ, mass of $\tilde{\chi}_1^0$, the NLO+NLL cross section, the generation efficiency, and the effective NLO+NLL cross section after a $Z(\ell\ell)$ event filter for the GGM grid models characterized by the following parameters: $M_1 = 1$ TeV, $M_2 = 1$ TeV, $\tan\beta = 30$.

$m(\tilde{g})$ [GeV]	μ [GeV]	$m(\tilde{\chi}_1^0)$ [GeV]	$\sigma(NLO+NLL)$ [pb]	ϵ [%]	$\sigma \times \epsilon$ [pb]
900	120	115.1	5.46 ± 0.15	19.7 ± 0.5	1.03 ± 0.03
	150	144.9	2.02 ± 0.06	18.2 ± 0.5	0.38± 0.01
	200	194.6	0.80 ± 0.02	15.1 ± 0.4	0.15 ± 0.004
	300	293.8	0.09 ± 0.014	13.0 ± 0.3	0.016 ± 0.002
	400	392.8	0.07± 0.014	11.9 ± 0.3	0.014 ± 0.002
	500	491.4	0.05± 0.014	11.9 ± 0.3	0.010 ± 0.002
	600	589.3	0.048± 0.014	11.5 ± 0.3	0.009 ± 0.002
	700	686.0	0.046± 0.014	12.6 ± 0.3	0.009 ± 0.002
	800	780.1	0.046± 0.014	12.6 ± 0.3	0.009 ± 0.002
	890	859.9	0.046± 0.014	13.3 ± 0.4	0.009 ± 0.002
1000	120	115.1	5.4 ±0.15	20.3 ± 0.5	1.02± 0.03
	150	144.9	2.4 ± 0.06	18.5 ± 0.5	0.43± 0.01
	200	194.6	0.77 ± 0.02	16.2 ± 0.4	0.15± 0.004
	300	293.8	0.160 ± 0.007	13.1 ± 0.3	0.03± 0.001
	400	392.8	0.054±0.006	12.6 ± 0.3	0.010± 0.001
	500	491.4	0.029±0.006	11.7 ± 0.3	0.006± 0.001
	600	589.3	0.022± 0.006	11.9 ± 0.3	0.004± 0.001
	700	686.0	0.019± 0.006	12.1 ± 0.3	0.0036± 0.001
	800	780.1	0.018± 0.006	13.2 ± 0.3	0.0034± 0.001
	900	867.2	0.018± 0.006	14.3 ± 0.4	0.0033± 0.001
	990	929.2	0.017± 0.006	15.3 ± 0.4	0.0033± 0.001

Table 7.5: μ, mass of $\tilde{\chi}_1^0$, the NLO+NLL cross section, the generation efficiency, and the effective NLO+NLL cross section after a $Z(\ell\ell)$ event filter for the GGM grid models characterized by the following parameters: $M_1 = 1$ TeV, $M_2 = 1$ TeV, $\tan\beta = 30$.

$m(\tilde{g})$ [GeV]	(NLO+NLL) $\sigma(\tilde{g}\tilde{g})$ [pb]
400	18.2 ± 2.8
500	4.2 ± 0.7
600	1.2 ± 0.2
700	0.37 ± 0.08
800	0.13±0.03
900	0.046±0.014
1000	0.017±0.006

Table 7.6: The NLO+NLL cross sections for $\tilde{g}\tilde{g}$ production only.

Names	Mass Eigenstates	m [GeV]
squarks	$\tilde{u}_L$	≈ 1500
	$\tilde{u}_R$	
	$\tilde{d}_L$	
	$\tilde{d}_R$	
	$\tilde{s}_L$	
	$\tilde{s}_R$	
	$\tilde{c}_L$	
	$\tilde{c}_R$	
	$\tilde{t}_1$	
	$\tilde{t}_2$	
	$\tilde{b}_1$	
	$\tilde{b}_2$	
sleptons	$\tilde{e}_L$	≈ 1500
	$\tilde{e}_R$	
	$\tilde{\mu}_L$	
	$\tilde{\mu}_R$	
	$\tilde{\tau}_1$	
	$\tilde{\tau}_2$	
neutralinos	$\tilde{\chi}_1^0$	110.97
	$\tilde{\chi}_2^0$	120.30
	$\tilde{\chi}_3^0$	1000.00
	$\tilde{\chi}_4^0$	1009.32
charginos	$\tilde{\chi}_1^\pm$	113.30
	$\tilde{\chi}_2^\pm$	1007.14
Higgs bosons	h^0	126.00
	H^0	2004.00
	A^0	2000.00
	$H^\pm$	2002.09

Table 7.7: SUSY particle mass spectrum for the higgsino-like NLSP GGM model which is characterized by the following parameters: $M_1 = 1$ TeV, $M_2 = 1$ TeV, $\tan\beta = 1.5$, $c\tau_{NLSP} = 0.1$ mm, $\mu = 120$ GeV, $m(\tilde{g}) = 600$ GeV.

ID	physics process	Generator	cross section × BR [pb]	k-factor
147770	$Z(ee)$	SHERPA	1207.9	1.03
147771	$Z(\mu\mu)$	SHERPA	1207.8	1.03
147772	$Z(\tau\tau)$	SHERPA	1207.1	1.03
147774	$W(e\nu)$	SHERPA	11878.0	1.03
147775	$W(\mu\nu)$	SHERPA	11879.0	1.03
147776	$W(\mu\nu)$	SHERPA	11872.0	1.03
126892	WW	SHERPA	5.4982	1.07
126893	WZ	SHERPA	9.7534	1.06
126894	$ZZ(4l)$	SHERPA	8.7356	1.11
126895	$ZZ(2l2\nu)$	SHERPA	0.4962	1.14

Table 7.8: MC samples used in the analysis including cross section times branching ratio, the generator, and the k-factor.

7.2.2 Background MC

Single-top and $t\bar{t}$ production were simulated using MC@NLO [99] with the NLO PDF set CTEQ6.6 [100] and ACERMC [82]. The $Z/\gamma^* + \text{jets}$, W+jets, and diboson (ZZ, WZ and WW) samples were generated using SHERPA [101] with NLO CT10 parton density function set (PDF). The $Z/\gamma^* + \text{jets}$ samples were normalized to inclusive next-to-next-to-leading (NNLO) cross sections. The full list of simulated samples used in this analysis, including the cross sections, filter efficiencies, the generators, and the k-factors, is listed in Table 7.8.

All samples were processed through the GEANT4 simulation [70, 102] of the ATLAS detector [42]. The in-time and out-of-time pile-up conditions, which result from multiple proton-proton interactions per crossing, were taken into account by overlaying minimum-bias events on the hard-scattering process in each MC sample. The simulated events were then reweighted such that the distribution of the number of interactions per crossing in MC matched the one observed in data.

7.3 Object and Event Selection

The analysis is performed using data recorded in proton-proton collisions at a center-of-mass energy of 8 TeV, corresponding to an integrated luminosity of 5.8 fb^{-1} [103] after the application of beam, detector and data quality requirements. Events are selected using dilepton triggers that have constant efficiency as a function of lepton transverse momentum (p_{T}) above the offline p_{T} cuts used in the analysis. For the ee selection, each event must fire either the `EF_e24vh_medium1_e7_medium1` or `EF_2e12Tvh_loose1`

trigger. $\mu\mu$ events are selected if they fire the `EF_mu18_tight_mu8_EFFS` or `EF_2mu13` trigger. $e\mu$ events, which are used in the estimation of some SM backgrounds, are selected if they fire either `EF_e12Tvh_medium1_mu8` or `EF_mu18_tight_e7_medium1`.

Jets are reconstructed using the anti-k_t jet clustering algorithm [64] with a distance parameter of $R = 0.4$ (in $\eta - \phi$ space). Jets are required to have $p_{\mathrm{T}} > 20$ GeV and lie within $|\eta| < 4.5$. Electron candidates are required to have $p_{\mathrm{T}} > 10$ GeV and $|\eta| < 2.47$ and pass the "medium" shower shape and track selection criteria [54]. Muon candidates within $|\eta| < 2.4$ are considered, and their p_{T} must be greater than 10 GeV. Muons are identified by matching an extrapolated inner detector track and one or more track segments in the muon spectrometer [104]. The leading lepton is required to have $p_{\mathrm{T}} > 25$ GeV. To avoid overlap, any jet within $\Delta R < 0.2$ of any remaining electron is removed. Finally, electron or muon candidates within $\Delta R < 0.4$ of any remaining jet are also discarded. The $E_{\mathrm{T}}^{\mathrm{miss}}$ is computed using the `MET_RefFinal` algorithm, as explained in Section 5.5.2.

After performing the baseline object selection described above, including jet overlap removal, "signal" objects are selected with more stringent requirements. Signal electron candidates must pass the "tight" selection criteria. Furthermore, an isolation requirement is imposed by requiring that the sum of the p_{T} of tracks within $\Delta R < 0.2$ around an electron candidate must be less than 10% of the electron p_{T}. Signal muon candidates must have longitudinal and transverse impact parameter values within 1 mm and 0.2 mm of the primary vertex, respectively, and are required to be isolated. The isolation requirement is that the sum of the p_{T} of tracks within $\Delta R < 0.2$ around a muon candidate is less than 1.8 GeV. Signal jets are required to have $p_{\mathrm{T}} > 30$ GeV and $|\eta| < 2.5$. Furthermore a cut on the jet vertex fraction, JVF > 0.5, is implemented, which reduces the contamination of pileup effects.

Events that contain at least two leptons, with the two leading leptons having opposite charge and an invariant mass in a window around the Z boson mass, $[81, 101]$ GeV, are selected. Figures 7.2 and 7.3 show the mass and $E_{\mathrm{T}}^{\mathrm{miss}}$ distribution of data and MC events before the Z mass requirement for the ee and $\mu\mu$ channels.

When plotting kinematic distributions of the selected events, two representative GGM signal points, which are characterized by the $gg \to \tilde{g}\tilde{g}$ production mechanism, are chosen to illustrate the SUSY contribution:

- $m(\tilde{g}) = 600$ GeV, $\mu = 120$ GeV represents the region $m(\tilde{g}) \gg \mu$.
- $m(\tilde{g}) = 600$ GeV, $\mu = 590$ GeV represents the region $m(\tilde{g}) \approx \mu$.

By examining these GGM grid points, one can see how the SUSY contributions

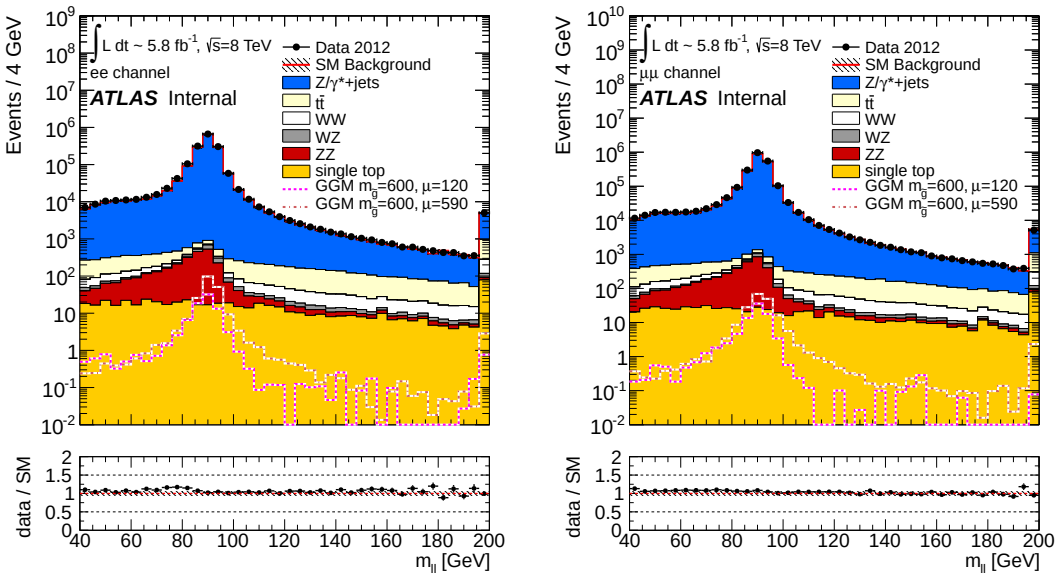

Figure 7.2: Invariant mass distribution of opposite charge electrons (left) and muons (right) for data and MC events. Two GGM signal points from the $\tan\beta = 1.5$ grid are included. The first point was produced with $m(\tilde{g}) = 600$ GeV and $\mu = 120$ GeV, and the second with $m(\tilde{g}) = 600$ GeV and $\mu = 590$ GeV. The plot labeled "Data/SM" shows the ratio of the distribution from data to that of the total SM background. The error bars on the data represent statistical uncertainties. The hatched grey band represents the systematic uncertainties on the MC expectations.

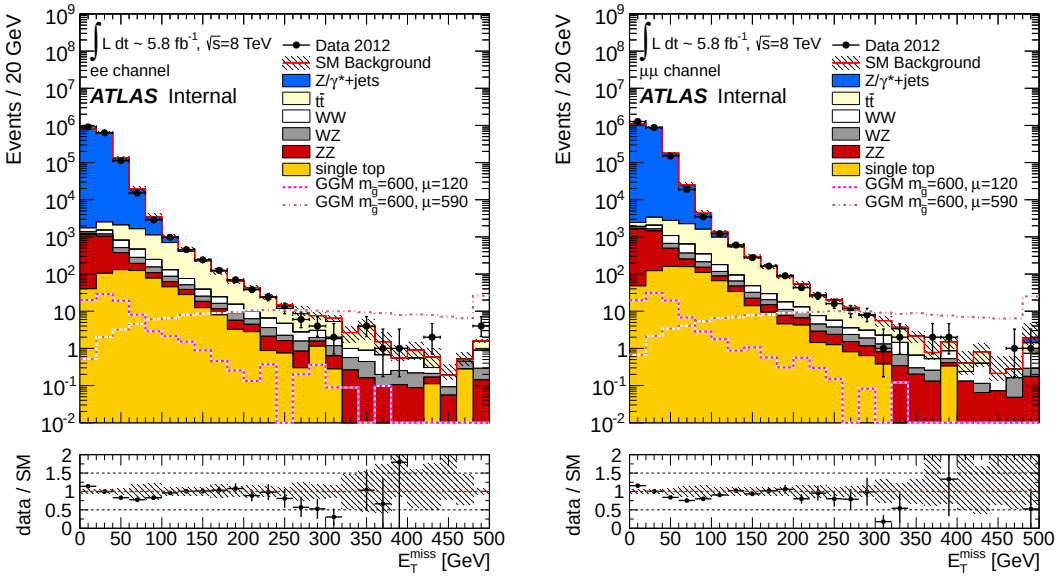

Figure 7.3: $E_{\mathrm{T}}^{\mathrm{miss}}$ distribution of opposite charge electrons (left) and muons (right) for data and MC events after $m(ll) > 40$ GeV requirement. Two GGM signal points from the $\tan\beta = 1.5$ grid are included. The first point was produced with $m(\tilde{g}) = 600$ GeV and $\mu = 120$ GeV, and the second with $m(\tilde{g}) = 600$ GeV and $\mu = 590$ GeV. The plot labeled "Data/SM" shows the ratio of the distribution from data to that of the total SM background. The error bars on the data represent statistical uncertainties. The hatched grey band represents the systematic uncertainties on the MC expectations.

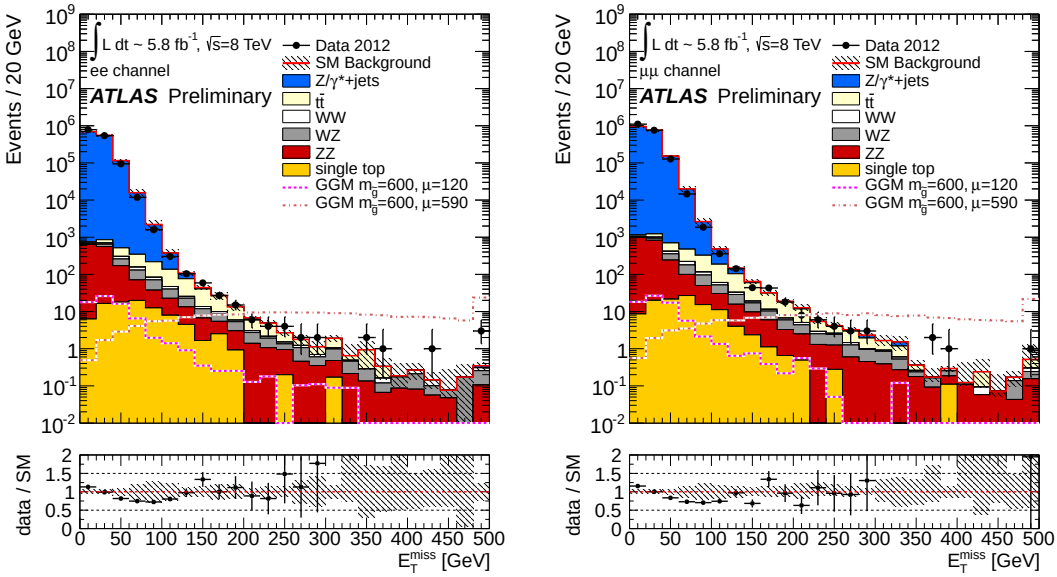

Figure 7.4: Distribution of $E_{\mathrm{T}}^{\mathrm{miss}}$ for data and MC events after $Z \to e^{\pm}e^{\mp}$ (left) and $Z \to \mu^{\pm}\mu^{\mp}$ (right) selections. Two GGM signal points from the $\tan\beta = 1.5$ grid are included. The first point was produced with $m(\tilde{g}) = 600$ GeV and $\mu = 120$ GeV, and the second with $m(\tilde{g}) = 600$ GeV and $\mu = 590$ GeV. The plot labeled "Data/SM" shows the ratio of the distribution from data to that of the total SM background. The error bars on the data represent statistical uncertainties. The hatched grey band represents the systematic uncertainties on the MC expectations.

from different kinematic regions behave in the distributions of interest. The source of the $E_{\mathrm{T}}^{\mathrm{miss}}$ in the GGM models is the $\tilde{G}$, which is produced in the decays $\tilde{\chi}_1^0 \to Z\tilde{G}$ and $\tilde{\chi}_1^0 \to H\tilde{G}$. As a result, $E_{\mathrm{T}}^{\mathrm{miss}}$ depends on μ. This can be seen in Figure 7.4, which shows the $E_{\mathrm{T}}^{\mathrm{miss}}$ distribution of data and MC events after the Z mass requirement for the ee and $\mu\mu$ channels.

Due to the different kinematics of the GGM signal points, two signal regions were selected to optimize the GGM search throughout the parameter space. The signal regions (SR), characterized by $E_{\mathrm{T}}^{\mathrm{miss}}$, jet multiplicity, and the scalar sum of the p_{T} of all reconstructed objects (denoted $H_{\mathrm{T}} \equiv \sum_i p_{\mathrm{T}}^{\mathrm{jet},i} + \sum_i p_{\mathrm{T}}^{\mathrm{lepton},i}$) are defined as shown in Table 7.9. In the H_{T} definition, the sums are over the signal jets and leptons. The SR optimization studies were performed in Chapter 6 [105]. The H_{T} , signal jet multiplicity, the p_{T} of the leading jet, p_{T} of sub-leading jet, and the p_{T} of the third jets distributions of data and MC events after the Z mass requirement for the ee and $\mu\mu$ channels are shown in Figures 7.5, 7.6, 7.7, 7.8, and 7.9. These variables are used in the signal region definitions to select events with high levels of hadronic activity. The p_{T} of the leading and sub-leading leptons are shown in Figures 7.10

Signal Region	SR1	SR2
$E_{\mathrm{T}}^{\mathrm{miss}}$[GeV]	>220	>140
Leading jet p_{T}[GeV]	>80	-
Second jet p_{T}[GeV]	>40	-
Third jet p_{T}[GeV]	>40	-
H_{T}[GeV]	-	>300

Table 7.9: Criteria for each of the signal regions.

and 7.11.

7.4 Background Evaluation

After the SR requirements, the SM backgrounds are $Z/\gamma^* + \text{jets}$, $t\bar{t}$, Wt, and dibosons. Data driven techniques were used to estimate the contribution from dominant backgrounds: instrumental $Z/\gamma^* + \text{jets}$, WW, $t\bar{t}$, Wt, $\tau\tau$. The contribution from ZZ and WZ processes were estimated using MC. The QCD and inclusive $W+\text{jets}$ backgrounds were estimated to be negligible.

7.4.1 WW, $t\bar{t}$, Wt, $\tau\tau$ background estimation

Since the leptonic decay branching fractions for the ee, $\mu\mu$ and $e\mu$ decays from WW, $t\bar{t}$, Wt, $\tau\tau$ are 1:1:2, $e\mu$ events were used to estimate the background in the ee and $\mu\mu$ channels from the WW, $t\bar{t}$, Wt, $\tau\tau$ processes in the signal regions. The estimation was performed using the following expressions:

$$N_{ee}^{\mathrm{est}} = \frac{1}{2} N_{e\mu}^{\mathrm{data,corr}} \times k_{ee}, \tag{7.1}$$

$$N_{\mu\mu}^{\mathrm{est}} = \frac{1}{2} N_{e\mu}^{\mathrm{data,corr}} \times k_{\mu\mu}, \tag{7.2}$$

where

$$k_{ee} = \sqrt{\frac{N_{ee}^{\mathrm{data}}}{N_{\mu\mu}^{\mathrm{data}}}}, \tag{7.3}$$

and

$$k_{\mu\mu} = \sqrt{\frac{N_{\mu\mu}^{\mathrm{data}}}{N_{ee}^{\mathrm{data}}}}. \tag{7.4}$$

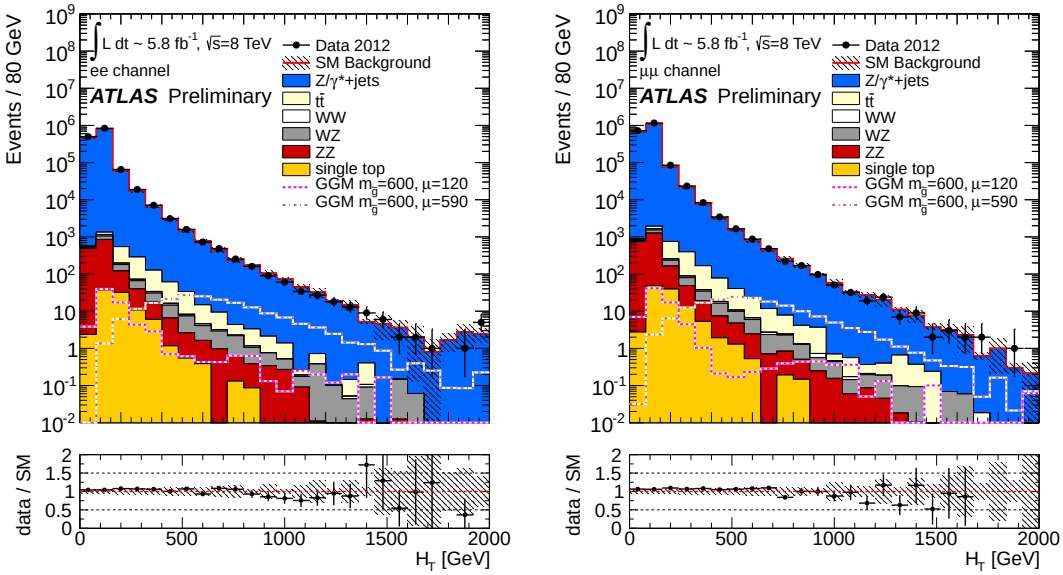

Figure 7.5: Distributions of H_{T} for data and MC events after $Z \to e^{\pm}e^{\mp}$ (left) and $Z \to \mu^{\pm}\mu^{\mp}$ (right) selections. The components labelled GGM correspond to GGM signal events having $\tan\beta = 1.5$ produced with $m(\tilde{g}) = 600$ GeV and $\mu = 120$ GeV, $m(\tilde{g}) = 600$ GeV and $\mu = 590$ GeV. The plot labeled "Data/SM" shows the ratio of the distribution from data to that of the total SM background. The error bars on the data represent statistical uncertainties. The hatched grey band represents the systematic uncertainties on the MC expectations.

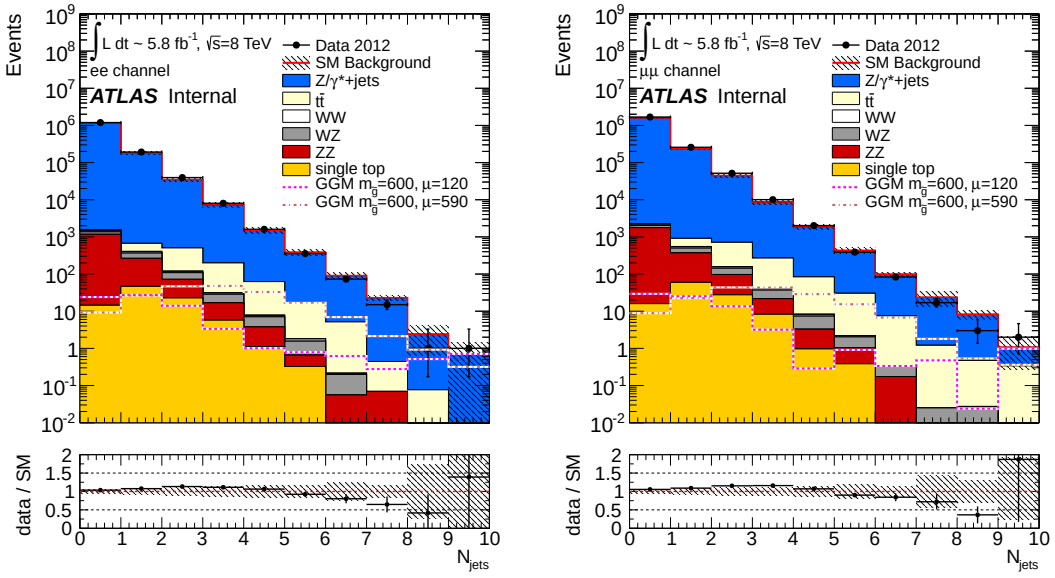

Figure 7.6: Distributions of jet multiplicity for data and MC events after $Z \to e^{\pm}e^{\mp}$ (left) and $Z \to \mu^{\pm}\mu^{\mp}$ (right) selections. The components labelled GGM correspond to GGM signal events having $\tan\beta = 1.5$ produced with $m(\tilde{g}) = 600$ GeV and $\mu = 120$ GeV, $m(\tilde{g}) = 600$ GeV and $\mu = 590$ GeV. The plot labeled "Data/SM" shows the ratio of the distribution from data to that of the total SM background. The error bars on the data represent statistical uncertainties. The hatched grey band represents the systematic uncertainties on the MC expectations.

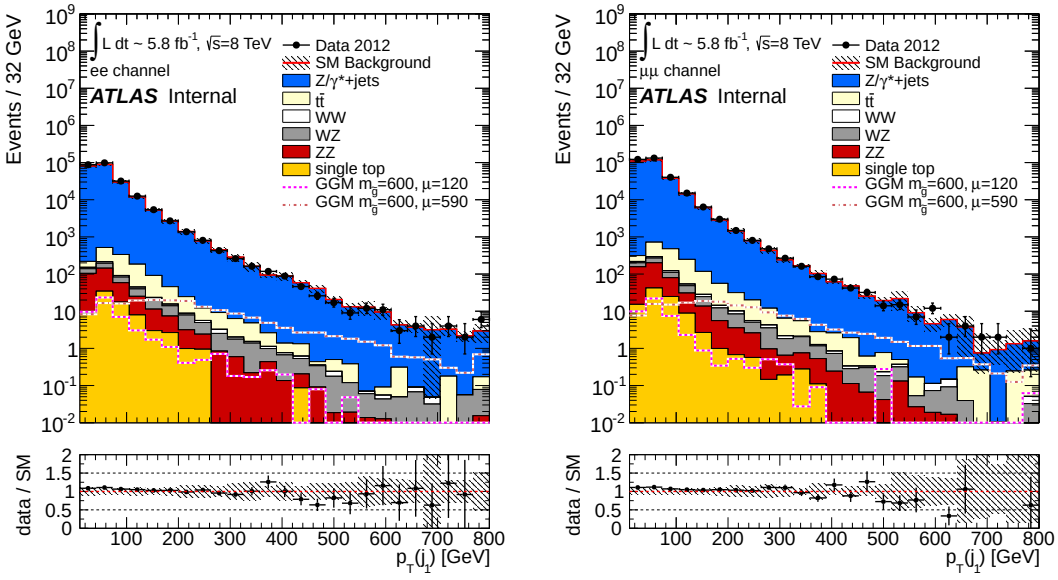

Figure 7.7: Distributions of p_{T} of the leading jet for data and MC events after $Z \to e^{\pm}e^{\mp}$ (left) and $Z \to \mu^{\pm}\mu^{\mp}$ (right) selections. The components labelled GGM correspond to the signal events having $\tan\beta = 1.5$ produced with $m(\tilde{g}) = 600$ GeV and $\mu = 120$ GeV, $m(\tilde{g}) = 600$ GeV and $\mu = 590$ GeV. The plot labeled "Data/SM" shows the ratio of the distribution from data to that of the total SM background. The error bars on the data represent statistical uncertainties. The hatched grey band represents the systematic uncertainties on the MC expectations.

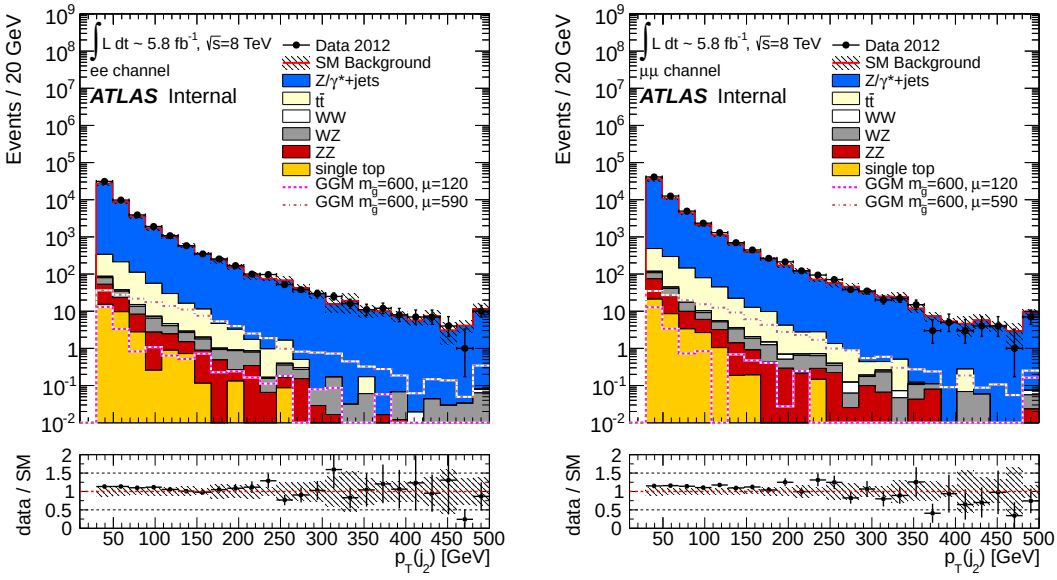

Figure 7.8: Distributions of p_{T} of the sub-leading jet for data and MC events after $Z \to e^{\pm}e^{\mp}$ (left) and $Z \to \mu^{\pm}\mu^{\mp}$ (right) selections. The components labelled GGM correspond to the signal events having $\tan\beta = 1.5$ produced with $m(\tilde{g}) = 600$ GeV and $\mu = 120$ GeV, $m(\tilde{g}) = 600$ GeV and $\mu = 590$ GeV. The plot labeled "Data/SM" shows the ratio of the distribution from data to that of the total SM background. The error bars on the data represent statistical uncertainties. The hatched grey band represents the systematic uncertainties on the MC expectations.

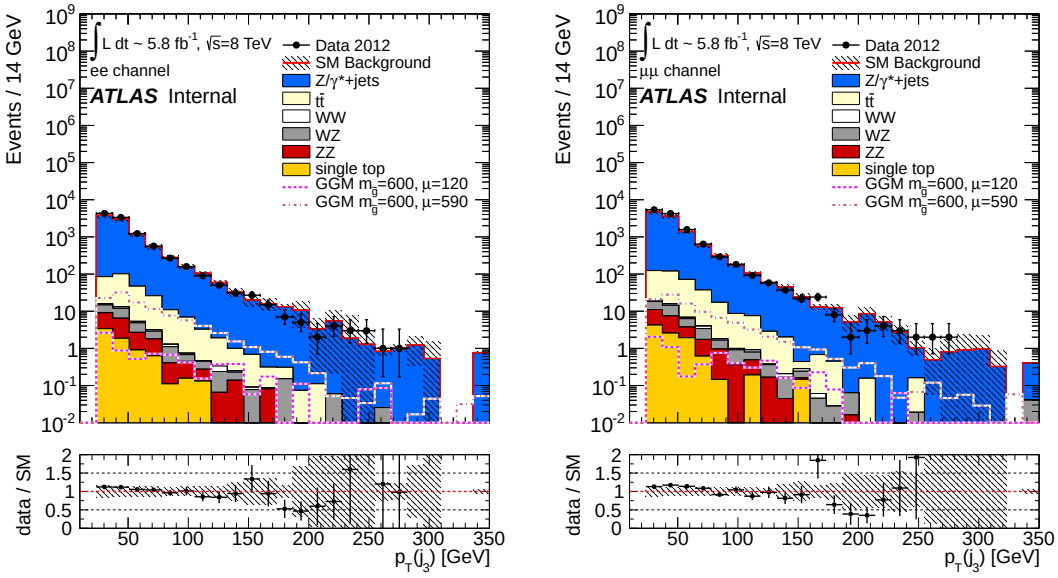

Figure 7.9: Distributions of p_{T} of the third jet for data and MC events after $Z \to e^{\pm}e^{\mp}$ (left) and $Z \to \mu^{\pm}\mu^{\mp}$ (right) selections. The components labelled GGM correspond to the signal events produced with $m(\tilde{g}) = 600$ GeV and $\mu = 120$ GeV, $m(\tilde{g}) = 600$ GeV and $\mu = 590$ GeV. The plot labeled "Data/SM" shows the ratio of the distribution from data to that of the total SM background. The error bars on the data represent statistical uncertainties. The hatched grey band represents the systematic uncertainties on the MC expectations.

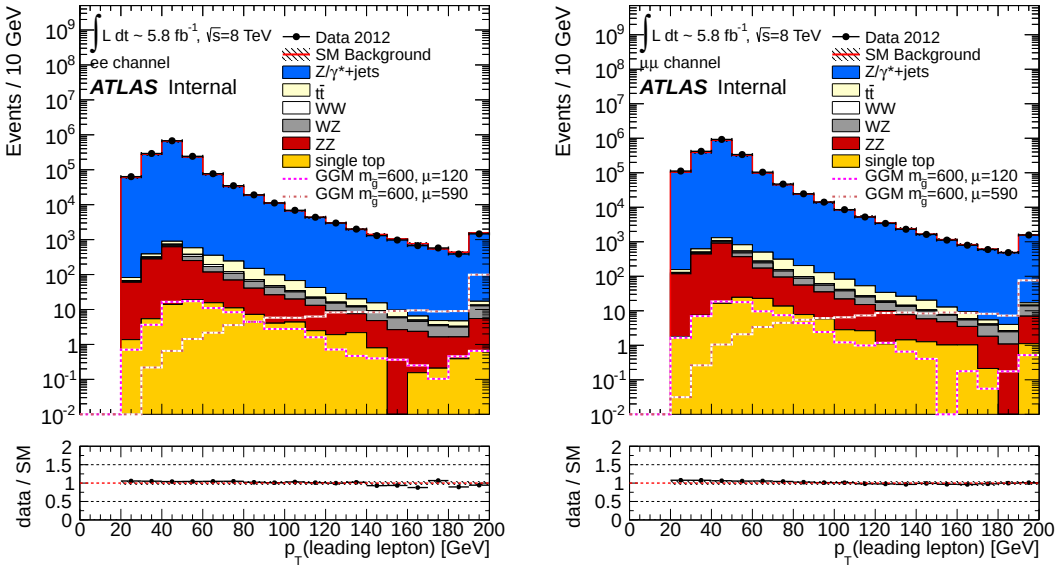

Figure 7.10: Distributions of p_{T} of the leading lepton for data and MC events after $Z \to e^{\pm}e^{\mp}$ (left) and $Z \to \mu^{\pm}\mu^{\mp}$ (right) selections. The components labelled GGM correspond to GGM signal events produced with $m(\tilde{g}) = 600$ GeV and $\mu = 120$ GeV, $m(\tilde{g}) = 600$ GeV and $\mu = 590$ GeV. The plot labeled "Data/SM" shows the ratio of the distribution from data to that of the total SM background. The error bars on the data represent statistical uncertainties.

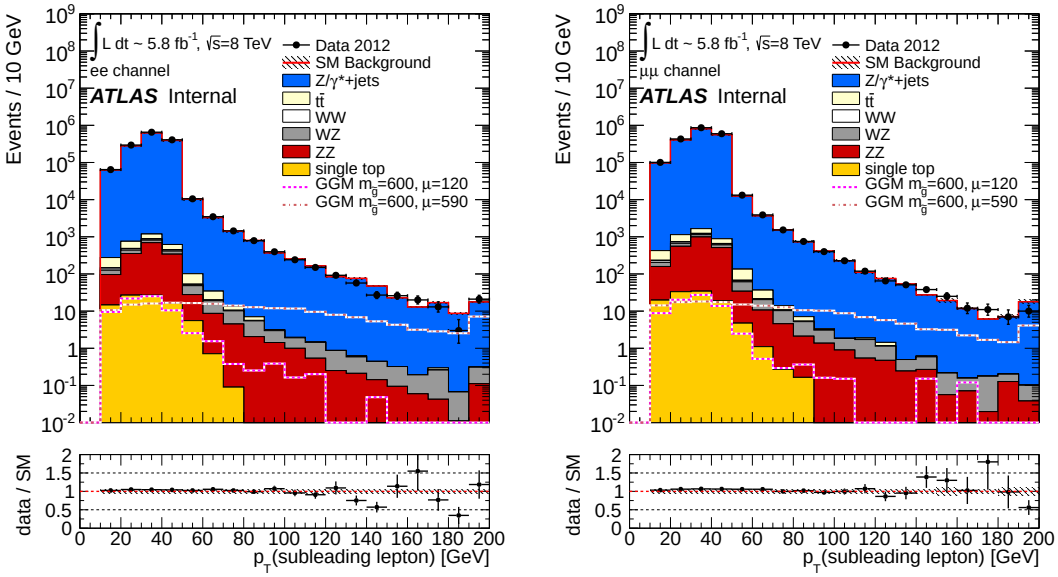

Figure 7.11: Distributions of p_{T} of the sub-leading lepton for data and MC events after $Z \to e^{\pm}e^{\mp}$ (left) and $Z \to \mu^{\pm}\mu^{\mp}$ (right) selections. The components labelled GGM correspond to GGM signal events produced with $m(\tilde{g}) = 600$ GeV and $\mu = 120$ GeV, $m(\tilde{g}) = 600$ GeV and $\mu = 590$ GeV. The plot labeled "Data/SM" shows the ratio of the distribution from data to that of the total SM background. The error bars on the data represent statistical uncertainties.

Control Region	N_{ee}^{data}	$N_{\mu\mu}^{\text{data}}$	k_{ee}	$k_{\mu\mu}$
CR1	3683	4503	0.91 ± 0.01(stat.)	1.11 ± 0.01(stat.)
CR2	16626	19142	0.93 ± 0.01(stat.)	1.07 ± 0.01(stat.)

Table 7.10: The number of ee and $\mu\mu$ events and the values of k_{ee} and $k_{\mu\mu}$ estimated from data in the control regions.

Control Region	N_{ee}^{MC}	$N_{\mu\mu}^{\text{MC}}$	k_{ee}^{MC}	$k_{\mu\mu}^{\text{MC}}$
CR1	3625.5	4351.9	0.912 ± 0.010(stat.)	1.096 ± 0.012(stat.)
CR2	16182	18975	0.924 ± 0.006(stat.)	1.082 ± 0.006(stat.)

Table 7.11: The number of ee and $\mu\mu$ events from MC and the values of k_{ee} and $k_{\mu\mu}$ estimated from MC in the control regions.

N_{ee}^{data} and $N_{\mu\mu}^{\text{data}}$ are the numbers ee and $\mu\mu$ events from data in the control regions: CR1 and CR2, defined as the signal regions, but with $E_{\text{T}}^{\text{miss}} < 140$ GeV. Figure 7.12 shows the distribution of $E_{\text{T}}^{\text{miss}}$ for ee and $\mu\mu$ events in the control regions. Signal contamination in the CRs was found to be negligible: less than 0.25% in CR1 and less than 0.15% in CR2. k_{ee} and $k_{\mu\mu}$ take into account the differences between the electron and muon reconstruction efficiencies. Table 7.10 summarizes the values of the N_{ee}^{data}, $N_{\mu\mu}^{\text{data}}$, k_{ee}, and $k_{\mu\mu}$ in the control regions. Table 7.11 summarize the values from the previous table estimated from MC in the control regions: N_{ee}^{MC}, $N_{\mu\mu}^{\text{MC}}$, k_{ee}^{MC}, and $k_{\mu\mu}^{\text{MC}}$. The data estimated values of k_{ee} and $k_{\mu\mu}$ are in a good agreement with the values estimated from MC. Figure 7.13 shows the distribution of H_{T} after control region requirements.

$N_{e\mu}^{\text{data,corr}}$ is the number of $e\mu$ events observed in data after applying the signal region requirements, corrected for the WZ, ZZ, $W+$jets, and $Z+$jets processes in the $e\mu$ channel, which were estimated with MC. Table 7.12 summarizes the contributions of these processes with the corresponding statistical uncertainties.

Due to the low statistics in SR1 and in SR2 for some MC processes, such as $W/Z+$ jet and ZZ processes, the estimated contributions in the $e\mu$ channel is zero. In such cases, the statistical uncertainty is taken as the average of the upper limit error and lower limit error using a Poisson distribution at 68% CL. The statistical uncertainties

Signal Region	WZ	ZZ	W+jets	Z+jets	Total
SR1	0.0 ± 0.64	0.0 ± 0.64	0.0 ± 0.64	0.0 ± 0.64	0.0 ± 1.28
SR2	0.37 ± 0.11	0.0 ± 0.64	1.86 ± 1.86	0.0 ± 0.64	2.2 ± 2.1

Table 7.12: The contribution of the subtracted processes estimated from MC in the signal regions.

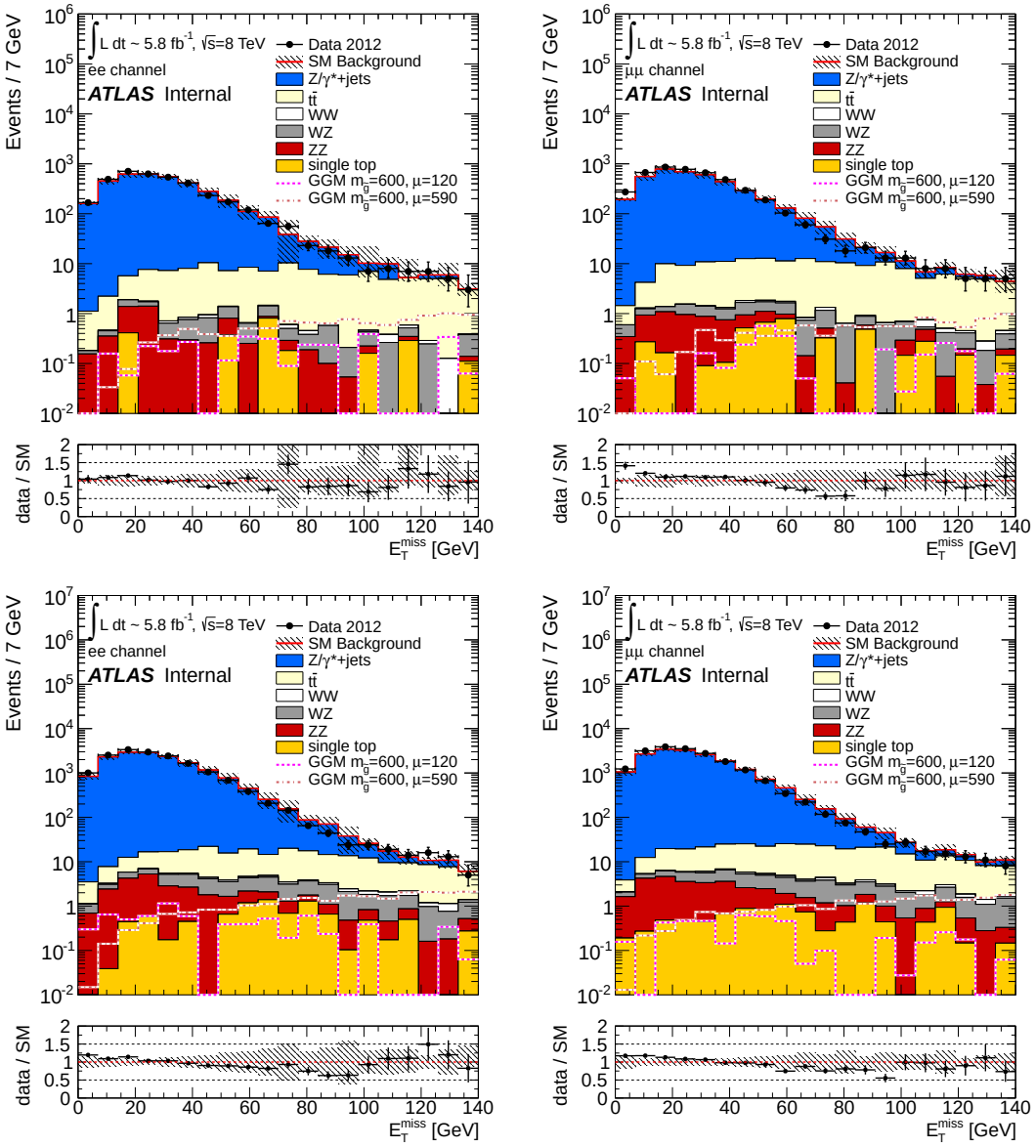

Figure 7.12: Distribution of $E_{\mathrm{T}}^{\mathrm{miss}}$ for data and MC events after CR1 (top) and CR2 (bottom) selections for ee(left) and $\mu\mu$ (right) events. Two GGM signal points from the $\tan\beta = 1.5$ grid are included. The first point was produced with $m(\tilde{g}) = 600$ GeV and $\mu = 120$ GeV, and the second with $m(\tilde{g}) = 600$ GeV and $\mu = 590$ GeV. The plot labeled "Data/SM" shows the ratio of the distribution from data to that of the total SM background. The error bars on the data represent statistical uncertainties. The hatched grey band represents the systematic uncertainties on the MC expectations.

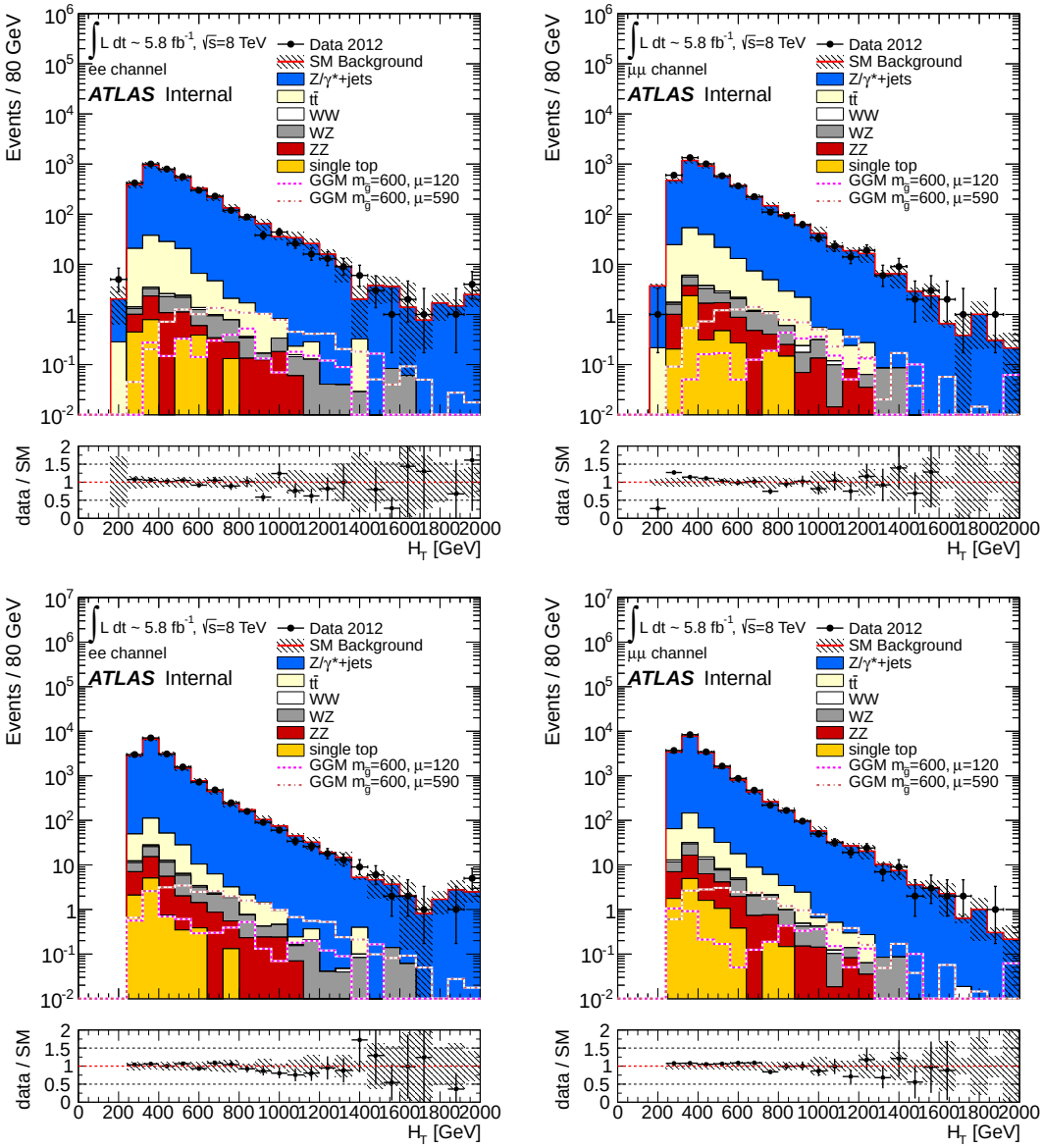

Figure 7.13: Distribution of H_{T} for data and MC events after CR1 (top) and CR2 (bottom) selections for ee(left) and $\mu\mu$ (right) events. The plot labeled "Data/SM" shows the ratio of the distribution from data to that of the total SM background. The error bars on the data represent statistical uncertainties. The hatched grey band represents the systematic uncertainties on the MC expectations.

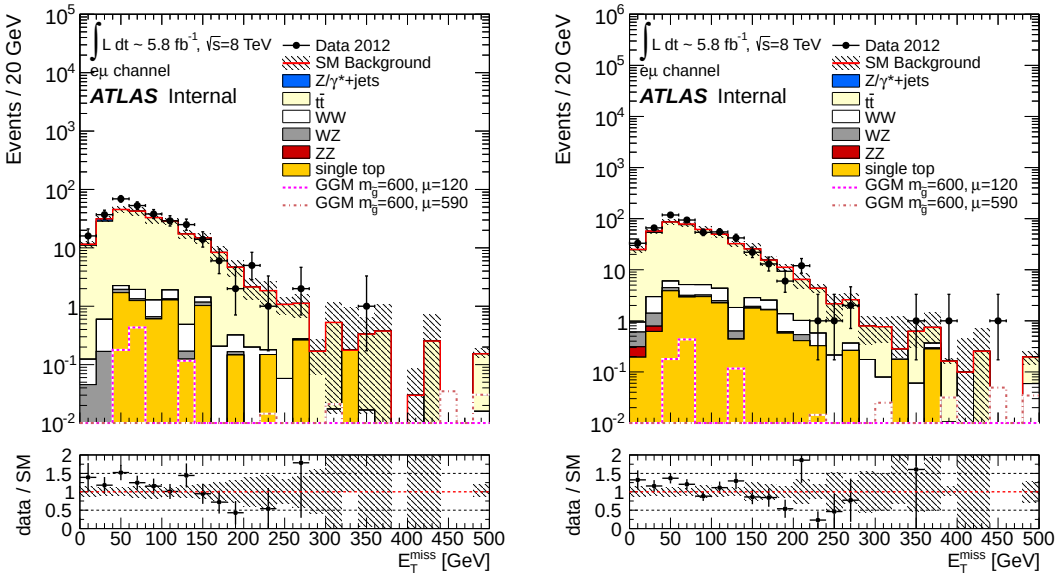

Figure 7.14: $E_{\mathrm{T}}^{\mathrm{miss}}$ distribution after SR1 (left) and SR2 (right) requirements without $E_{\mathrm{T}}^{\mathrm{miss}}$ cut for $e\mu$ events. The plot labeled "Data/SM" shows the ratio of the distribution from data to that of the total SM background. The error bars on the data represent statistical uncertainties. The hatched grey band represents the systematic uncertainties on the MC expectations.

from various subtracted MC sources are quadratically summed. Figure 7.14 shows the $E_{\mathrm{T}}^{\mathrm{miss}}$ distributions after signal region selection, but without the cut on $E_{\mathrm{T}}^{\mathrm{miss}}$, in the $e\mu$ channel. The distributions of H_{T}, $p_{\mathrm{T}}$of the leading jet are shown in Figures 7.15, 7.16 for the $e\mu$ channel in the signal regions. The contamination of the MC signal in the signal regions in the $e\mu$ channel is found to be less than 0.6% for SR1 and less than 0.1% for SR2 and was taken into account in the assessment of systematic uncertainties.

The statistical uncertainties of the estimate were calculated by using the formulas below:

$$\begin{aligned}\sigma^2_{N^{\mathrm{est}}_{ee}} &= \frac{1}{4}\left(\sigma^2_{N^{\mathrm{data,corr}}_{e\mu}} k^2_{ee} + \sigma^2_{k_{ee}} (N^{\mathrm{data,corr}}_{e\mu})^2\right) \\ &= \frac{1}{4}(N^{\mathrm{data}}_{e\mu} + \sigma^2_{N^{\mathrm{MC,sub}}_{e\mu}})\frac{N^{\mathrm{data}}_{ee}}{N^{\mathrm{data}}_{\mu\mu}} + \frac{1}{16}(N^{\mathrm{data}}_{e\mu} - N^{\mathrm{MC,sub}}_{e\mu})^2(N^{\mathrm{data}}_{ee} + N^{\mathrm{data}}_{\mu\mu})^2,\end{aligned} \tag{7.5}$$

$$\begin{aligned}\sigma^2_{N^{\mathrm{est}}_{\mu\mu}} &= \frac{1}{4}\left(\sigma^2_{N^{\mathrm{data,corr}}_{e\mu}} k^2_{\mu\mu} + \sigma^2_{k_{\mu\mu}} (N^{\mathrm{data,corr}}_{e\mu})^2\right) \\ &= \frac{1}{4}(N^{\mathrm{data}}_{e\mu} + \sigma^2_{N^{\mathrm{MC,sub}}_{e\mu}})\frac{N^{data}_{\mu\mu}}{N^{data}_{ee}} + \frac{1}{16}(N^{\mathrm{data}}_{e\mu} - N^{\mathrm{MC,sub}}_{e\mu})^2(N^{\mathrm{data}}_{ee} + N^{\mathrm{data}}_{\mu\mu})^2,\end{aligned} \tag{7.6}$$

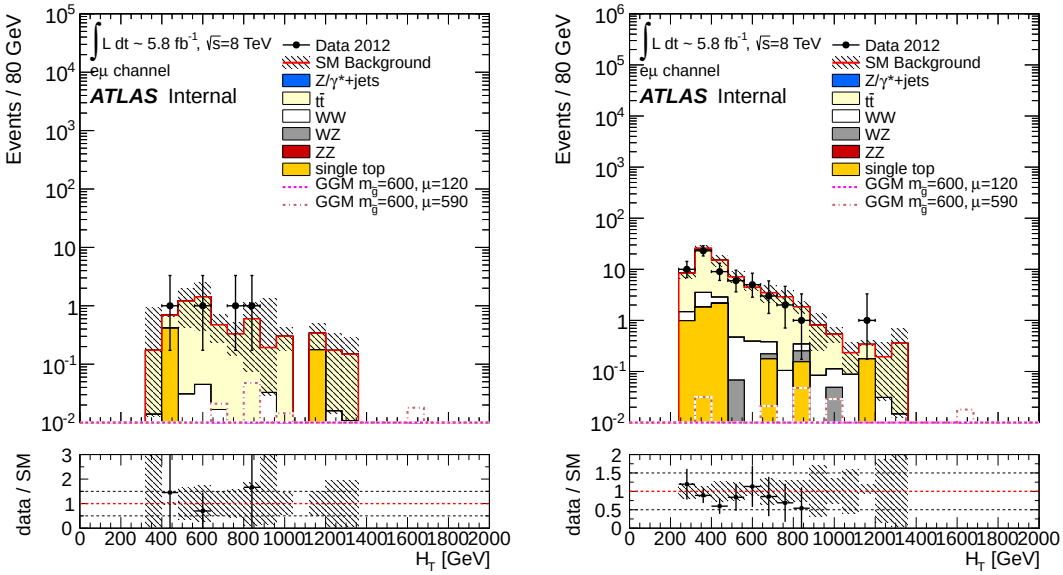

Figure 7.15: Distribution of H_{T} for data and MC events after SR1 (left) and SR2 (right) requirements for $e\mu$ events. The plot labeled "Data/SM" shows the ratio of the distribution from data to that of the total SM background. The error bars on the data represent statistical uncertainties. The hatched grey band represents the systematic uncertainties on the MC expectations.

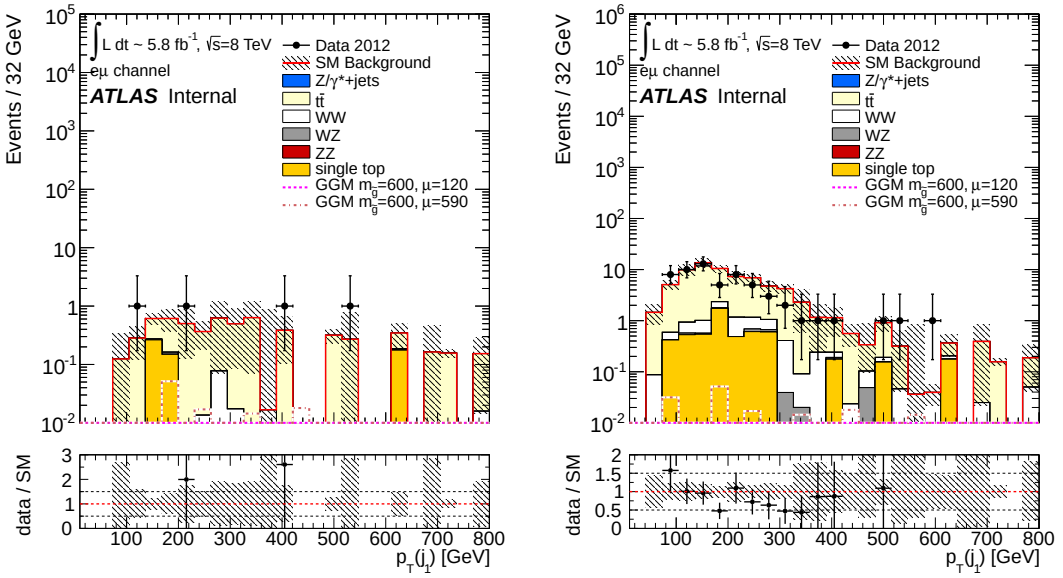

Figure 7.16: Distribution of p_{T} of the leading jet for data and MC events after SR1 (left) and SR2 (right) requirements for $e\mu$ events. The plot labeled "Data/SM" shows the ratio of the distribution from data to that of the total SM background. The error bars on the data represent statistical uncertainties. The hatched grey band represents the systematic uncertainties on the MC expectations.

Signal Region	$N_{e\mu}^{data,corr}$	N_{ee}^{est}	$N_{\mu\mu}^{est}$
SR1	4	1.80±1.07(stat.)±0.16(syst.)	2.20±1.31(stat.)±0.18(syst.)
SR2	57.8	26.9±3.8(stat.)±1.7(syst.)	30.9±4.3(stat.)±1.8(syst.)

Table 7.13: Summary of data driven estimation of the WW, $t\bar{t}$, Wt, $\tau\tau$ backgrounds in the signal regions for 5.84 fb^{-1}.

where $N_{e\mu}^{\mathrm{MC,sub}}$ and $\sigma^2_{N_{e\mu}^{\mathrm{MC,sub}}}$ are summarized in Table 7.12.

Systematic uncertainties

The main sources of systematic uncertainties in this method are due to the subtraction of MC events from the $e\mu$ data sample. The following sources of the systematics were considered: production cross section uncertainty (12% for top, 5% for ZZ, 7% for WZ and 5% for W+jets and Z+jets), luminosity (3.6%), lepton energy scale and resolution uncertainties, and jet energy scale (JES) and resolution (JER) uncertainties. The total systematic uncertainty due to subtraction of WZ, ZZ, W+jets, $Z(ee)$+jets and $Z(\mu\mu)$+jets process are estimated to be less than 0.8% (0.3%) in SR1 (SR2), where the dominant uncertainty is due to JES/JER. Another source of uncertainty is the signal contamination in the signal regions in the $e\mu$ channel. About 0.6% of MC signal was estimated in SR1 and 0.1% in SR2.

Since k_{ee} and $k_{\mu\mu}$ values were calculated in control regions, with lower $E_{\mathrm{T}}^{\mathrm{miss}}$requirements than the SRs, the $E_{\mathrm{T}}^{\mathrm{miss}}$dependence of k_{ee} and $k_{\mu\mu}$, and its effect on the estimate, was investigated. The CRs were divided into several regions and the estimation was re-evaluated using k_{ee} and $k_{\mu\mu}$ calculated for each region. Although the dominant uncertainties in these calculations are statistical, indeed a slight increase of N_{ee} estimate is observed toward larger $E_{\mathrm{T}}^{\mathrm{miss}}$for both SR's. To account for this effect, the maximum difference between the nominal estimate and the estimations in each $E_{\mathrm{T}}^{\mathrm{miss}}$region was assigned as a systematic. In SR1 (SR2), an 8% (5%) uncertainty on the $top, WW, \tau\tau$ estimate is observed due to this bias.

After combining the uncertainties from all sources, the total systematic uncertainty of the estimate for flavor symmetric backgrounds was found to be $\approx 9\%$ for SR1 and $\approx 5\%$ for SR1.

Signal Region	N_{ee}^{est}	$N_{\mu\mu}^{est}$
SR1	1.5 ± 0.6(stat.)	1.8 ± 0.7(stat.)
SR2	24.9 ± 0.8(stat.)	29.2 ± 0.9(stat.)

Table 7.14: Summary of the closure test.

Signal Region	N_{ee}^{MC}	$N_{\mu\mu}^{\mathrm{MC}}$
$t\bar{t}$	1.1 ± 0.2(stat.)	2.3 ± 0.3 (stat.)
Wt	0.0 ± 0.64(stat.)	0.0 ± 0.64(stat.)
WW	0.15 ± 0.04(stat.)	0.30 ± 0.07(stat.)
$\tau\tau$	0.0 ± 0.64(stat.)	0.0 ± 0.64(stat.)
Total	1.29 ± 0.92(stat.) ± 0.45(syst.)	2.59 ± 0.97(stat.) ± 1.2(syst.)

Table 7.15: The MC predicted values for WW, $t\bar{t}$, Wt, $\tau\tau$ processes in the SR1 for 5.84 fb^{-1}.

Results

The results of the $e\mu$ method for estimating the flavor-symmetric backgrounds are summarized in Table 7.13. The closure test were performed using this method. The results of the closure test are summarized in Table 7.14. The MC predictions for WW, $t\bar{t}$, Wt, and $\tau\tau$ backgrounds are listed in Tables 7.15 and 7.16 with the associated statistical and systematic uncertainties. For these estimations, the systematic uncertainties are found to be 35% and 47% for ee and $\mu\mu$ channels, respectively, in SR1. In SR2, the systematic uncertainties were estimated to be 26% (25%) for the ee ($\mu\mu$) channel. The dominant source of the systematics is due to JES: 32% (45%) in SR1 and 24% (22%) in SR2 for the ee ($\mu\mu$) channel.

Signal Region	N_{ee}^{MC}	$N_{\mu\mu}^{\mathrm{MC}}$
$t\bar{t}$	23.0 ± 1.0(stat.)	29.0 ± 1.2 (stat.)
Wt	2.4 ± 0.6 (stat.)	1.3 ± 0.4 (stat.)
WW	2.5 ± 0.2 (stat.)	3.1 ± 0.2 (stat.)
$\tau\tau$	0.0 ± 0.64 (stat.)	0.0 ± 0.64 (stat.)
Total	27.9 ± 1.4(stat.) ± 7.2(syst.)	33.4 ± 1.4(stat.) ± 8.3(syst.)

Table 7.16: The MC predicted values for WW, $t\bar{t}$, Wt, $\tau\tau$ processes in the SR2 for 5.84 fb^{-1}.

Signal Region	$N_{ee}^{WZ,\mathrm{MC}}$	$N_{\mu\mu}^{WZ,\mathrm{MC}}$
SR1	$0.65 \pm 0.14(\mathrm{stat.}) \pm 0.30(\mathrm{syst.})$	$0.52 \pm 0.12(\mathrm{stat.}) \pm 0.24(\mathrm{syst.})$
SR2	$8.4 \pm 0.5(\mathrm{stat.}) \pm 1.8(\mathrm{syst.})$	$9.0 \pm 0.5(\mathrm{stat.}) \pm 2.1(\mathrm{syst.})$

Table 7.17: The WZ MC predicted values in the signal regions for ee and $\mu\mu$ channels for 5.84 fb^{-1}.

Signal Region	$N_{ee}^{ZZ,\mathrm{MC}}$	$N_{\mu\mu}^{ZZ,\mathrm{MC}}$
SR1	$0.18 \pm 0.03(\mathrm{stat.}) \pm 0.05(\mathrm{syst.})$	$0.21 \pm 0.03(\mathrm{stat.}) \pm 0.08(\mathrm{syst.})$
SR2	$3.7 \pm 0.14(\mathrm{stat.}) \pm 0.4(\mathrm{syst.})$	$4.8 \pm 0.16(\mathrm{stat.}) \pm 0.9(\mathrm{syst.})$

Table 7.18: The ZZ MC predicted values in the signal regions for ee and $\mu\mu$ channels for 5.84 fb^{-1}.

7.4.2 WZ and ZZ backgrounds

The contribution from ZZ and WZ processes were estimated using MC. Tables 7.17 and 7.18 summarize the MC estimation for these processes in the signal regions with the associated statistical and systematic uncertainties. The dominant source of systematic uncertainty is the difference in MC generators. For the predictions in SR1, these uncertainties are estimated to be 41% (34%) for WZ and 11% (33%) for ZZ in the ee ($\mu\mu$) channel. In SR2, these generator uncertainties are 17% (18%) for WZ and 3% (18%) for ZZ in the ee ($\mu\mu$) channel.

7.4.3 $Z/\gamma^* +$ jets background estimation

After the Z mass requirement, one of the dominant SM backgrounds is $Z/\gamma^* +$ jets. Since only $Z \to ee$ and $Z \to \mu\mu$ (and not $Z \to \tau\tau$) decays were selected, this background has $E_{\mathrm{T}}^{\mathrm{miss}}$ that mostly stems from mismeasurement of the reconstructed objects, especially jets. To estimate the contribution of the instrumental $Z/\gamma^* +$ jets background in the signal regions, the jet smearing method was used, as described below.

This method implements a momentum smearing of well-measured jets with a function modeling the response of the calorimeters to determine the acceptance in the SRs for poorly measured $Z/\gamma^* +$ jets events. The jet response function quantifies the probability of fluctuation of the measured p_{T} of jets and takes into account both the effects of jet mis-measurement and contributions from neutrinos and muons in jets from heavy flavor decays. The response function was estimated in [106] and is based on the results of MC simulations but is modified in such a way as to give good

agreement between multi jet estimates and data in two additional dedicated analyses. This procedure minimizes the susceptibility of the multi jet background estimates in the main analysis to systematic uncertainties arising from the MC modeling of the initial response function.

The jet smearing method proceeds in the following steps:

- Definition of seed region where events with well measured jets were selected. Selection of low-$E_{\mathrm{T}}^{\mathrm{miss}}$seed events in the data. The jets in these events are well measured.

- Convolution of jets in the seed events with the response function to generate pseudo-data events. These events are used to describe the $E_{\mathrm{T}}^{\mathrm{miss}}$ and estimate the acceptance in the signal and control regions, which are defined in table 7.19.

Seed event selection

The selection of the seed events starts from the Z preselected data sample to provide similar topology between seed, control and signal regions. Since there are no jets in a significant fraction of Z preselected events, at least 3 signal jets were required in analogy to the seed requirement in [106]. The seed events were classified in two regions, one for each signal region: ZSeed1 and ZSeed2. Similar kinematics between the seed and the signal regions were ensured by applying the same H_T cut for ZSeed2 as in SR2.

Events with well measured jets were selected by using the $E_{\mathrm{T}}^{\mathrm{miss}}$ significance, which is defined as

$$S = \frac{E_{\mathrm{T}}^{\mathrm{miss}}}{\sqrt{\sum_{i}^{N_{\mathrm{jets}}} p_T^i}}, \tag{7.7}$$

where N_{jets} and p_{T} are the number and the transverse momentum of the reconstructed signal jets in a event. Figure 7.17 shows the $E_{\mathrm{T}}^{\mathrm{miss}}$ significance for Z preselected events having at least 3 jets and for Z events having at least 3 jets and $H_{\mathrm{T}} > 300$ GeV. The $E_{\mathrm{T}}^{\mathrm{miss}}$ significance is required to be less than 1.5 for both ZSeed1 and ZSeed2, which corresponds to $E_{\mathrm{T}}^{\mathrm{miss}}$ less than 50 GeV for events in both regions (see Fig. 7.18). To ensure similar hadronic activity in the seed, control and signal regions, the $E_{\mathrm{T}}^{\mathrm{miss}}$significance was used to select the well-measured jets instead of $E_{\mathrm{T}}^{\mathrm{miss}}$. Figures 7.19 show that the requirement of $S < 1.5$ GeV$^{1/2}$ has a negligible effect on

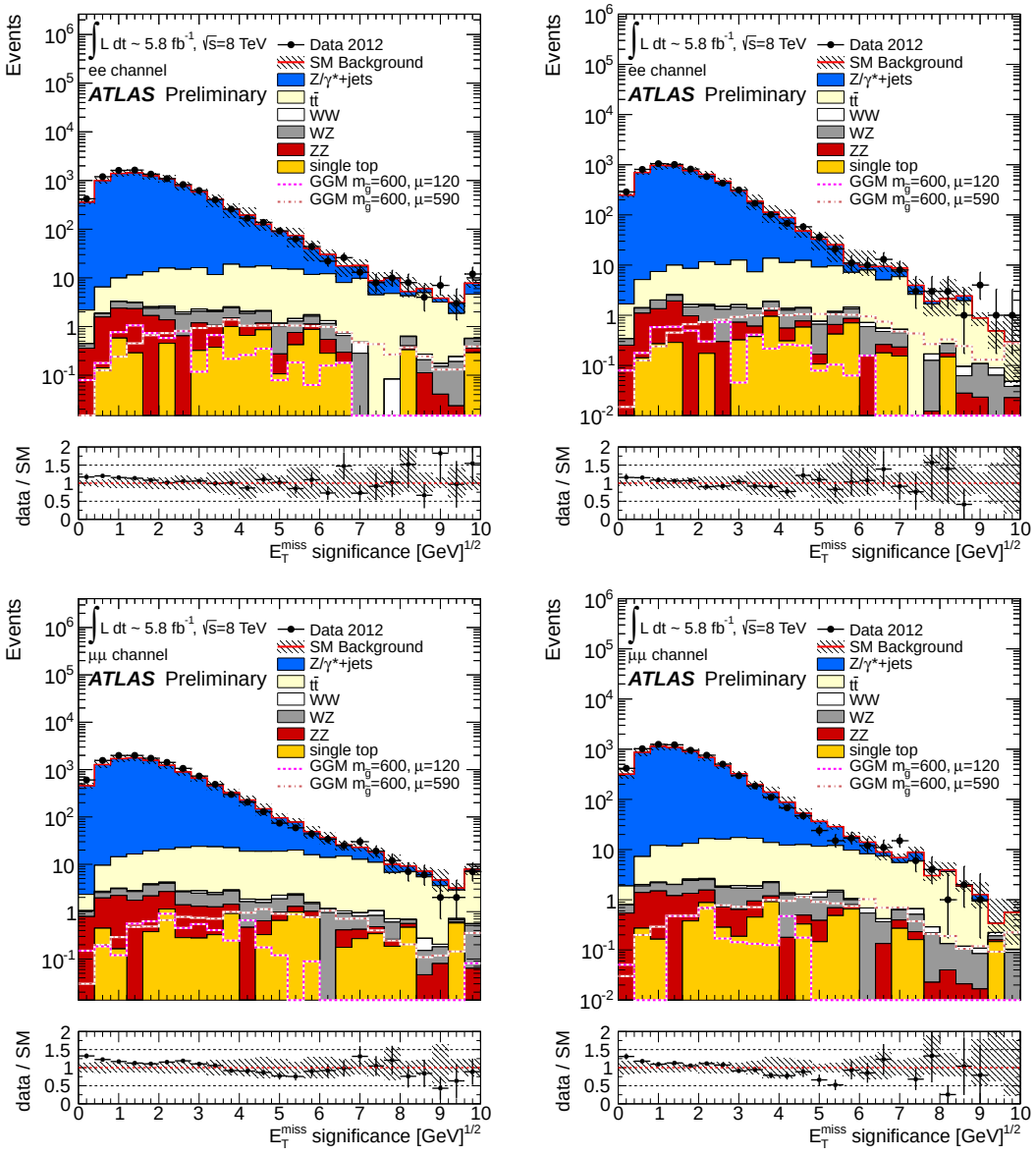

Figure 7.17: $E_{\mathrm{T}}^{\mathrm{miss}}$ significance for ee (top) and $\mu\mu$ (bottom) events passing Z preselection having $E_{\mathrm{T}}^{\mathrm{miss}} < 140$ GeV with at least 3 signal jets (left) or at least 3 jets and $H_{\mathrm{T}} > 300$ GeV (right).

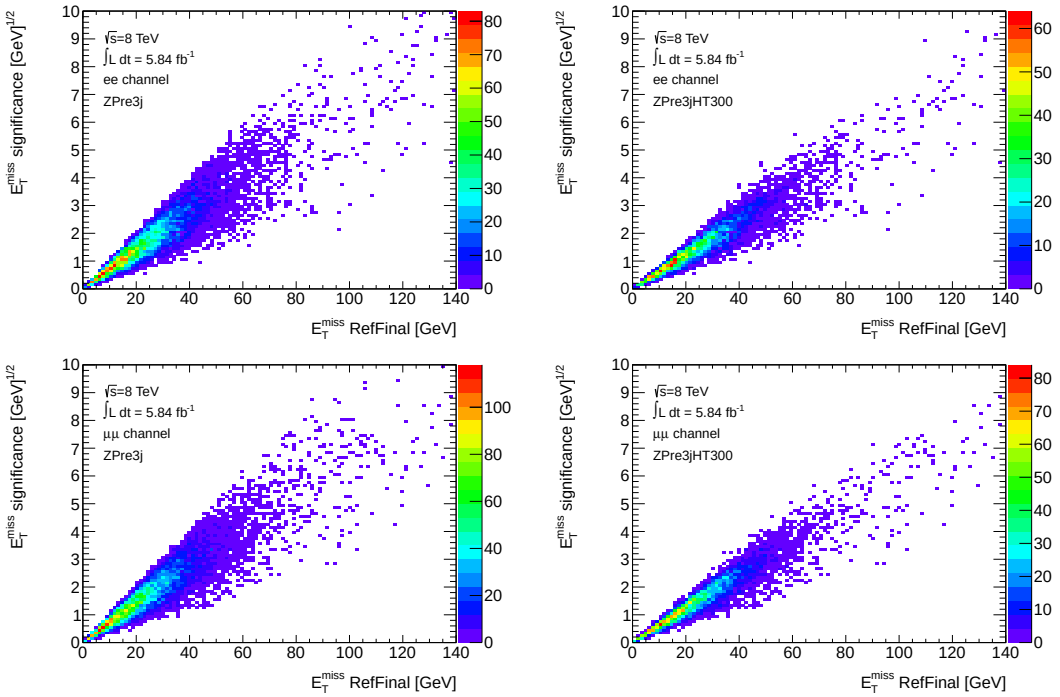

Figure 7.18: $E_{\mathrm{T}}^{\mathrm{miss}}$ significance vs. $E_{\mathrm{T}}^{\mathrm{miss}}$ for ee (top) and $\mu\mu$ (bottom) events passing Z preselection having $E_{\mathrm{T}}^{\mathrm{miss}} < 140$ GeV with at least 3 signal jets (left) or at least 3 jets and $H_{\mathrm{T}} > 300$ GeV (right).

the hadron activity.

As defined in Section 7.3, the contributions to the $E_{\mathrm{T}}^{\mathrm{miss}}$ not associated to any hard objects in the event are quantified in the `MET_CellOut` term. A cut on the ratio of the magnitude of `MET_CellOut` to the magnitude of `MET_RefFinal`, f_{CellOut}, is used in the definitions of both ZSeed1 and ZSeed 2. f_{CellOut} is defined as

$$f_{\mathrm{CellOut}} = \frac{\left|\mathbf{E}_{\mathrm{T}}^{\mathrm{miss,CellOut}}\right|}{\left|\mathbf{E}_{\mathrm{T}}^{\mathrm{miss,RefFinal}}\right|}. \tag{7.8}$$

Figure 7.20 shows the relationship between `MET_RefFinal` and f_{CellOut} for events passing Z preselection with at least 3 jets and for those events also having $H_{\mathrm{T}} > 300$ GeV. There is a strong correlation with large f_{CellOut} and low values of `MET_RefFinal`. Similarly, events with large `MET_RefFinal` values are characterized by low values of f_{CellOut}. Since the method described here is striving to reproduce the $E_{\mathrm{T}}^{\mathrm{miss}}$ at large values (*i.e.*, in the tail region), the region with low f_{CellOut} is the most interesting. Furthermore, considering events with low f_{CellOut} also ensures that the dominant source of the $E_{\mathrm{T}}^{\mathrm{miss}}$ is not due to soft sources, but instead is due to *e.g.*, the `MET_RefJet` term.

Since $Z/\gamma^* +$ jets events at high-$E_{\mathrm{T}}^{\mathrm{miss}}$ tend to have $E_{\mathrm{T}}^{\mathrm{miss}}$ dominated by hadronic

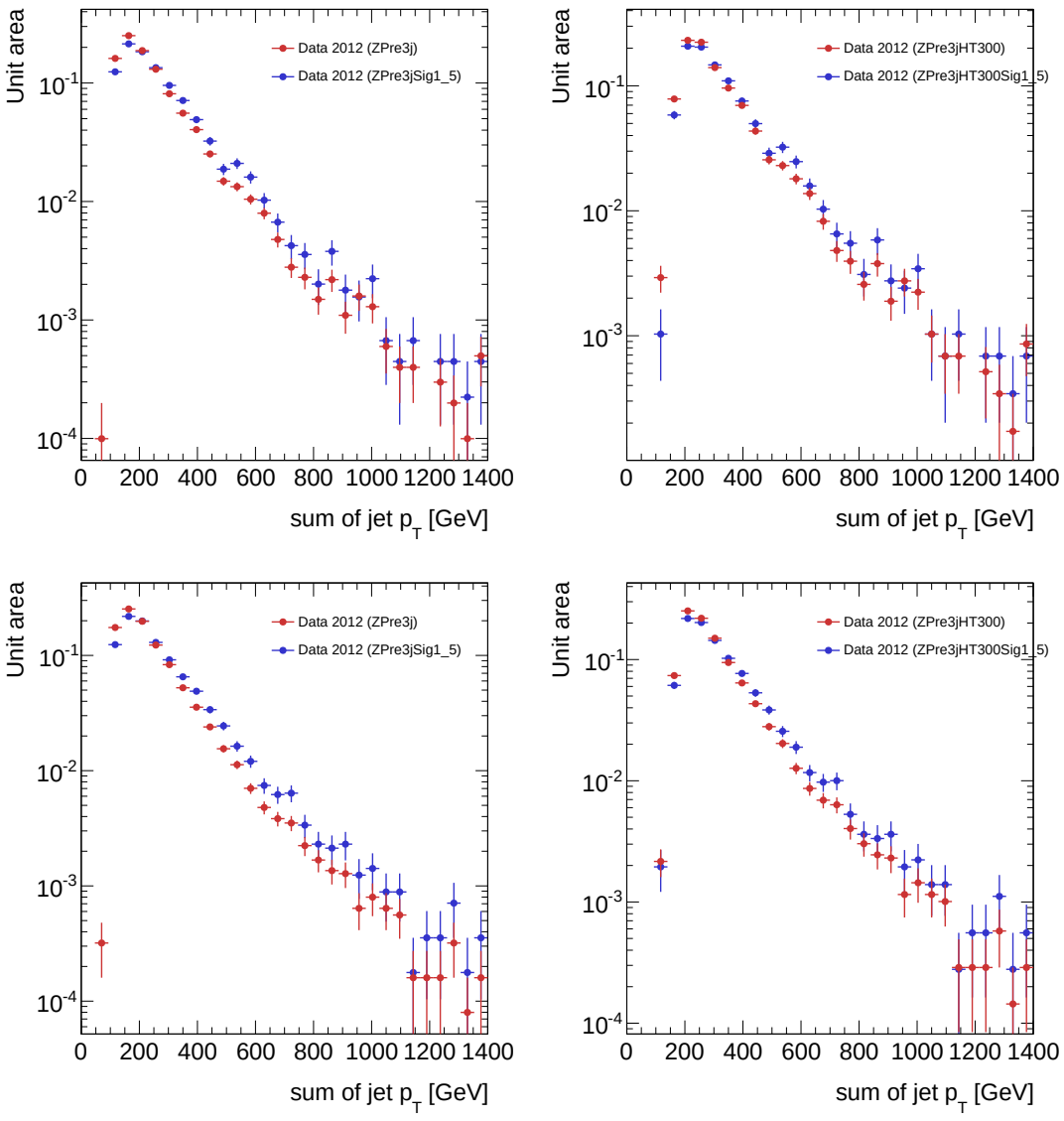

Figure 7.19: Sum of jet p_{T} for ee (top) and $\mu\mu$ (bottom) events passing Z preselection having $E_{\mathrm{T}}^{\mathrm{miss}} < 140$ GeV with at least 3 signal jets (left) or at least 3 jets and $H_{\mathrm{T}} > 300$ GeV (right). In addition, the blue data points include a cut on $S < 1.5$ GeV$^{1/2}$.

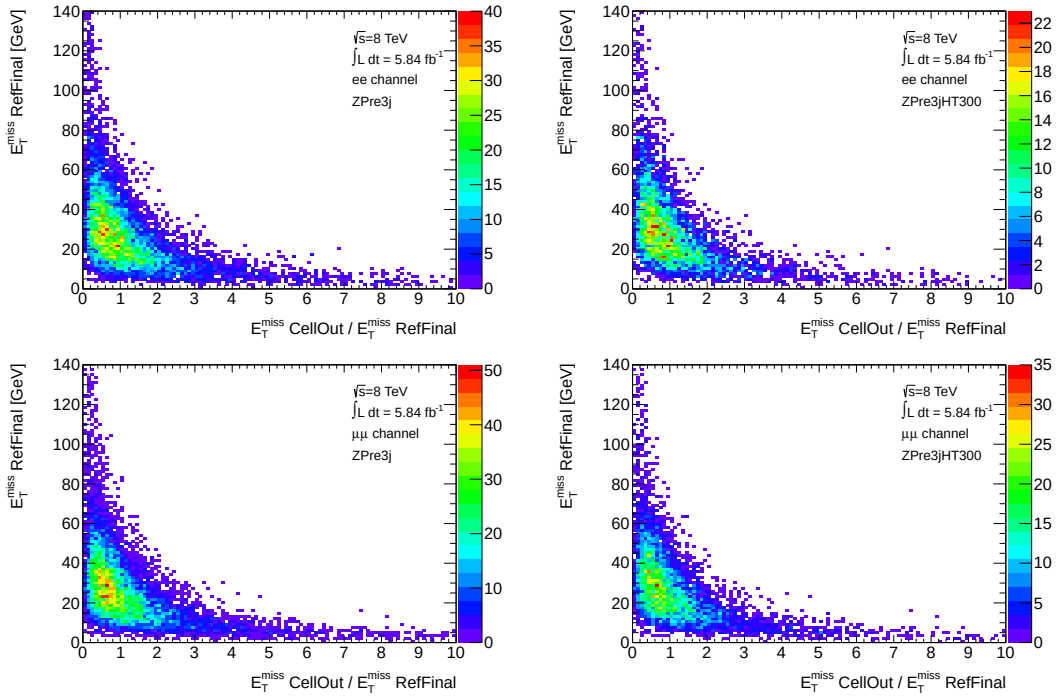

Figure 7.20: `MET_RefFinal` vs. `MET_CellOut`/`MET_RefFinal` for ee (top) and $\mu\mu$ (bottom) events passing Z preselection having $E_{\mathrm{T}}^{\mathrm{miss}} < 140$ GeV with at least 3 signal jets (left) or at least 3 jets and $H_{\mathrm{T}} > 300$ GeV (right).

mismeasurement, seed events whose $E_{\mathrm{T}}^{\mathrm{miss}}$ is mostly due to `MET_CellOut` should not be selected. Therefore, a requirement of $f_{\mathrm{CellOut}} < 0.4$ is added to the definitions for both the ZSeed1 and ZSeed2 regions.

Table 7.19 summarizes the definitions of seed, control, and signal regions used in this method. Figure 7.21 shows $E_{\mathrm{T}}^{\mathrm{miss}}$ vs. f_{CellOut} for two signal points: $(m(\tilde{g}), \mu) = (600, 120)$ GeV and $(m(\tilde{g}), \mu) = (600, 590)$ GeV. The signal contamination in the seed region is negligible, $< 1\%$, for both high- and low-μ points, due to the real source of $E_{\mathrm{T}}^{\mathrm{miss}}$ in these events.

Jet smearing and generation of the pseudo-data

To smear the momenta of jets in the ZSeed1 and ZSeed2 events, the response functions defined for `JetSmearing-00-01-12` were used [106]. The response function is composed of a Gaussian core and non-Gaussian tails. The response function is measured first with dijet MC, and then the shape is adjusted to match distributions in data. The Gaussian core component was tuned using dijet events and the non-Gaussian tails were adjusted using using 3-jet ("mercedes") events. Figure 7.22a shows the jet

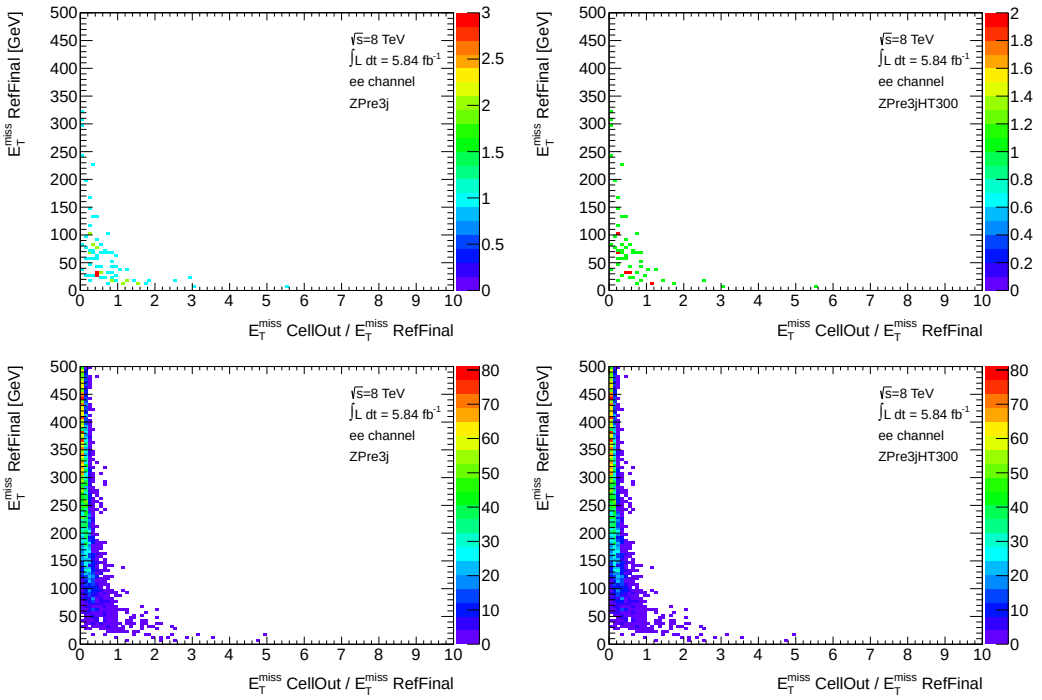

Figure 7.21: `MET_RefFinal` vs. `MET_CellOut`/`MET_RefFinal` for ee events from the GGM signal points with $(m(\tilde{g}), \mu) = (600, 120)$ GeV (top) and $(m(\tilde{g}), \mu) = (600, 590)$ GeV (bottom) passing Z preselection having $E_{\mathrm{T}}^{\mathrm{miss}} < 140$ GeV with at least 3 signal jets (left) or at least 3 jets and $H_{\mathrm{T}} > 300$ GeV (right).

SR1	**ZCR1**	**ZSeed1**
Z preselection		
$E_{\mathrm{T}}^{\mathrm{miss}} > 220$ GeV	$E_{\mathrm{T}}^{\mathrm{miss}} < 140$ GeV	
$N_{\mathrm{jets}} > 2$, $p_{\mathrm{T}} > 80,\ 40,\ 40$ GeV		$N_{\mathrm{jets}} > 2$
-		$S < 1.5$
-		$f_{\mathrm{CellOut}} < 0.4$

(a) SR1, CR1, and ZSeed1 cut definitions.

SR2	**ZCR2**	**ZSeed2**
Z preselection		
$E_{\mathrm{T}}^{\mathrm{miss}} > 140$ GeV	$E_{\mathrm{T}}^{\mathrm{miss}} < 140$ GeV	
$H_{\mathrm{T}} > 300$ GeV		
-		$N_{\mathrm{jets}} > 2$
-		$S < 1.5$
-		$f_{\mathrm{CellOut}} < 0.4$

(b) SR2, CR2, and ZSeed2 cut definitions.

Table 7.19: The cuts defined for the SRs, ZCRs, and seed regions.

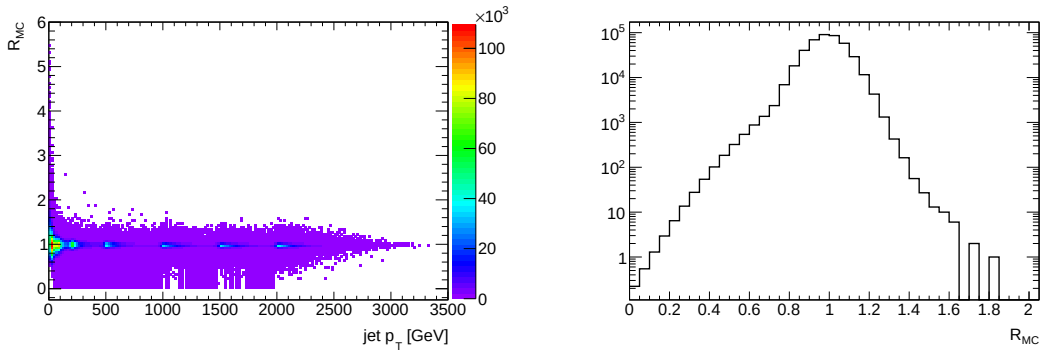

(a) The jet response R_{MC} as a function of jet p_{T}.

(b) The jet response for jets with $80 < p_{\mathrm{T}} < 100$ GeV.

Figure 7.22: Jet response distributions from `JetSmearing-00-01-12`, used for smearing jets in the seed regions.

response distribution, R_{MC}, as a function of jet p_{T}, and Figure 7.22b shows the jet response for jets having $80 < p_{\mathrm{T}} < 100$ GeV. As the seed selection is defined such that the jets are mostly well-measured, smearing the jets with these response functions will generate higher-$E_{\mathrm{T}}^{\mathrm{miss}}$ events, known as "pseudo-data", which should provide a shape for the $E_{\mathrm{T}}^{\mathrm{miss}}$ that accurately represents effects from jet mismeasurement and contributions from neutrinos in jets originating from heavy flavor decays. The smeared $E_{\mathrm{T}}^{\mathrm{miss}}$ is derived as:

$$\mathbf{E}_{\mathrm{T}}^{\mathrm{miss}\prime} = \mathbf{E}_{\mathrm{T}}^{\mathrm{miss}} - \sum_{i} \mathbf{p}_{\mathrm{T}}{}'(j_{\mathrm{i}}) + \sum_{i} \mathbf{p}_{\mathrm{T}}(j_{\mathrm{i}}) \tag{7.9}$$

where $\mathbf{E}_{\mathrm{T}}^{\mathrm{miss}}$ ($\mathbf{E}_{\mathrm{T}}^{\mathrm{miss}\prime}$) and $\mathbf{p}_{\mathrm{T}}$ and ($\mathbf{p}_{\mathrm{T}}{}'$) are the unsmeared (smeared) $E_{\mathrm{T}}^{\mathrm{miss}}$ and jet momenta, respectively. With the new values of jet momenta, all relevant quantities ($E_{\mathrm{T}}^{\mathrm{miss}}$, H_{T}, $\sum_{i}^{N_{\mathrm{jets}}} p_T^i$) were recomputed for each smeared event. Distributions of the $E_{\mathrm{T}}^{\mathrm{miss}}$ was then obtained for the control and signal regions used in this analysis. To minimize the statistical uncertainty associated with this method, an arbitrary number of pseudo-data events can be generated for each seed event, known as N_{smear}. For this analysis , $N_{\mathrm{smear}} = 5000$.

Uncertainties

The derivation of systematic and statistical uncertainties associated with the jet smearing method are described in detail in ATL-PHYS-INT-2012-008. The sources of the uncertainties are:

1. Statistical uncertainties due to the finite size of the seed and smeared event samples. N_{smear} is set to 5000 so that the smeared sample statistical uncertainty is minimal. Nonetheless, the statistical uncertainty due to both the seed and smeared samples is used, and is given by:

$$\sigma(j)_{\text{stat}} = \frac{1}{N_{\text{seed}} N_{\text{smear}}} \sqrt{\sum_{i}^{N_{\text{seed}}} n_{ij}(1 + n_{ij})} \tag{7.10}$$

   for the jth bin in the $E_{\text{T}}^{\text{miss}}$ distribution. The index i in the above expression represents the ith seed event. See [106] for a complete derivation of this uncertainty.

2. The uncertainties in the response function, due to fluctuations in the non-Gaussian tails of the response function. These uncertainties are described in detail in [106]. This region of the response function is responsible for large jet mis-measurement, and is thus the dominant factor in smearing to large $E_{\text{T}}^{\text{miss}}$ values. To account for these uncertainties, the jet smearing method is run with the nominal tail description, as well as for upward and downward-fluctuating tail widths, and the larger difference in the estimation in the SR is taken as a systematic uncertainty.

3. Uncertainty due to contributions from non-Z sources in the seed regions. The contamination due to these sources was found to be negligible ($< 1\%$).

Validation of the pseudo-data

Figure 7.23 shows the $E_{\text{T}}^{\text{miss}}$ of the data in the control regions, corrected for non-Z/γ^* + jets sources estimated from MC, and the pseudo-data for the ee and $\mu\mu$ channels. The pseudo-data is normalized to the data in the region $E_{\text{T}}^{\text{miss}} < 40$ GeV. In general, excellent agreement is observed between data and pseudo-data. However, there is a clear effect in the low $E_{\text{T}}^{\text{miss}}$ range, $E_{\text{T}}^{\text{miss}} < 10$ GeV, where the pseduo-data clearly underestimates the data. This effect can be explained by the cut on f_{CellOut} defined for the seed events, since events with low f_{CellOut} are known to be shifted to larger values of $E_{\text{T}}^{\text{miss}}$.

For completeness, Figure 7.24 shows the $E_{\text{T}}^{\text{miss}}$ in the control regions for data along with the data-driven estimates for Z/γ^* + jetsand top+WW+$\tau\tau$ and MC estimates for WZ and ZZ. The grey hatched band represents the uncertainties on

the $Z/\gamma^* +$ jets and diboson estimates.

Validation with an MC closure test

In addition to the validation above, a closure test was performed using only $Z/\gamma^* +$ jets MC. The MC events were run through the exact procedure outlined in 7.4.3, and the smeared MC events were compared with the nominal MC in the full range of $E_{\mathrm{T}}^{\mathrm{miss}}$. SHERPA MC was used for this comparison, and the response function used for smearing the jets was derived using the same generator. The same definitions for the seed and control region definitions were used. In both ZCR1 and ZCR2, good agreement is seen between nominal and smeared MC events, in the ee and $\mu\mu$ channels. Figure 7.25 shows these $E_{\mathrm{T}}^{\mathrm{miss}}$ distributions. Nominal Z MC, smeared Z MC, and smeared data are all shown for comparison.

To quantify the agreement between nominal and smeared MC in the signal regions, a looser selection analogous to SR1 was defined, known as SR1'. SR1' is identical to SR1 with two modifications: (1) the jets are required to pass $p_{\mathrm{T}} > 30$ GeV and (2) $E_{\mathrm{T}}^{\mathrm{miss}}$ is required to be above 100 GeV. This modified signal region definition reduces the problems of low statistics common to Z MC. After SR1' requirements, the expected number of events from nominal and smeared MC were compared, and the differences were found to be 8.3% (5.8%) in the ee ($\mu\mu$) channel. As these differences are negligible when compared to the uncertainties due to tail fluctuations in the nominal jet response function used in this method, no additional uncertainty is added due to the MC closure test.

Results

With the normalized $E_{\mathrm{T}}^{\mathrm{miss}}$ distributions from the pseudo-data, acquiring an estimate in the SRs is straightforward. For both ZCR1 and ZCR2, the only differences with respect to the SRs is the direction and magnitude of the $E_{\mathrm{T}}^{\mathrm{miss}}$ cut. The $E_{\mathrm{T}}^{\mathrm{miss}}$ requirement for SR1 (SR2) is $E_{\mathrm{T}}^{\mathrm{miss}} > 220$ (140) GeV.

The distributions in Figure 7.26 again show the pseudo-data compared to the data $E_{\mathrm{T}}^{\mathrm{miss}}$, but with an extended range. The number of expected events after the SR requirements are presented in Table 7.20.

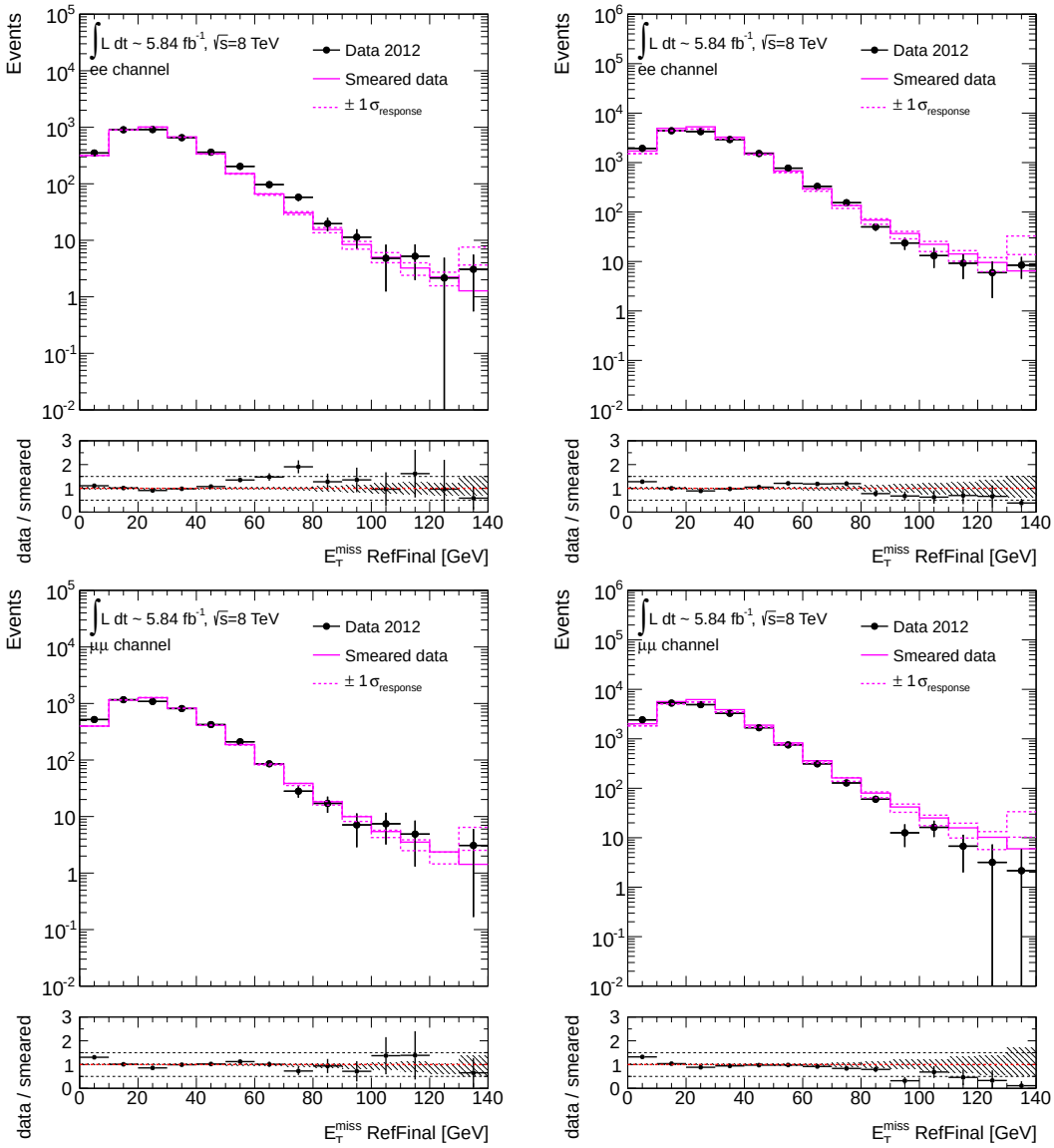

Figure 7.23: $E_{\mathrm{T}}^{\mathrm{miss}}$ distributions in ZCR1 (left) and ZCR2 (right), for ee (top) and $\mu\mu$ (bottom) events. The black points represent selected data, corrected for non-$Z/\gamma^* + \text{jets}$ sources. The magenta line is the $E_{\mathrm{T}}^{\mathrm{miss}}$ of the smeared events. The dotted lines represent the systematic variations due to the tail fluctuations in the jet response function. The hashed uncertainty in the ratio takes into account these systematic variations in addition to the statistical uncertainties.

	ee	$\mu\mu$
SR1	$0.46 \pm 0.05(\text{stat.}) \pm 0.32$ (syst.)	$0.30 \pm 0.04(\text{stat.}) \pm 0.24(\text{syst.})$
SR2	$16.95 \pm 0.55(\text{stat.}) \pm 8.07(\text{syst.})$	$14.84 \pm 0.51(\text{stat.}) \pm 10.01(\text{syst.})$

Table 7.20: Predictions for $Z/\gamma^* + \text{jets}$ in the signal regions, for both ee and $\mu\mu$ channels.

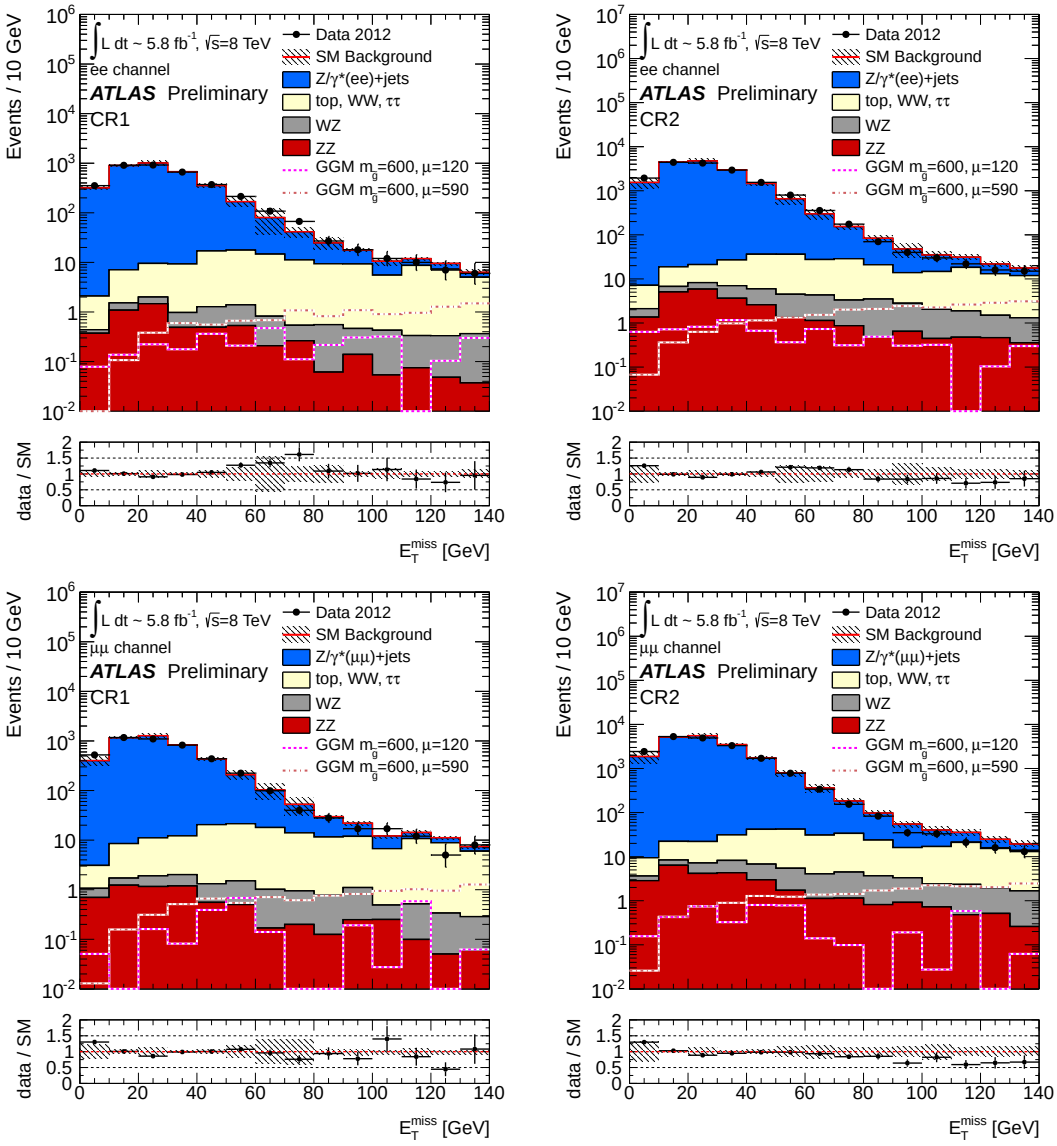

Figure 7.24: $E_{\mathrm{T}}^{\mathrm{miss}}$ distributions in CR1 (top) and CR2 (bottom), in the ee (left) and $\mu\mu$ (right) channels. The black points represent selected data. The Z/γ^*+jets contribution comes from the data-driven jet smearing method, the top+WW+$\tau\tau$ contribution comes from the data-driven $e\mu$ sample method, and the WZ and ZZ contributions come directly from MC. The hatched grey band represents the systematic uncertainties on the Z/γ^* + jets estimation and the MC expectations for WZ and ZZ.

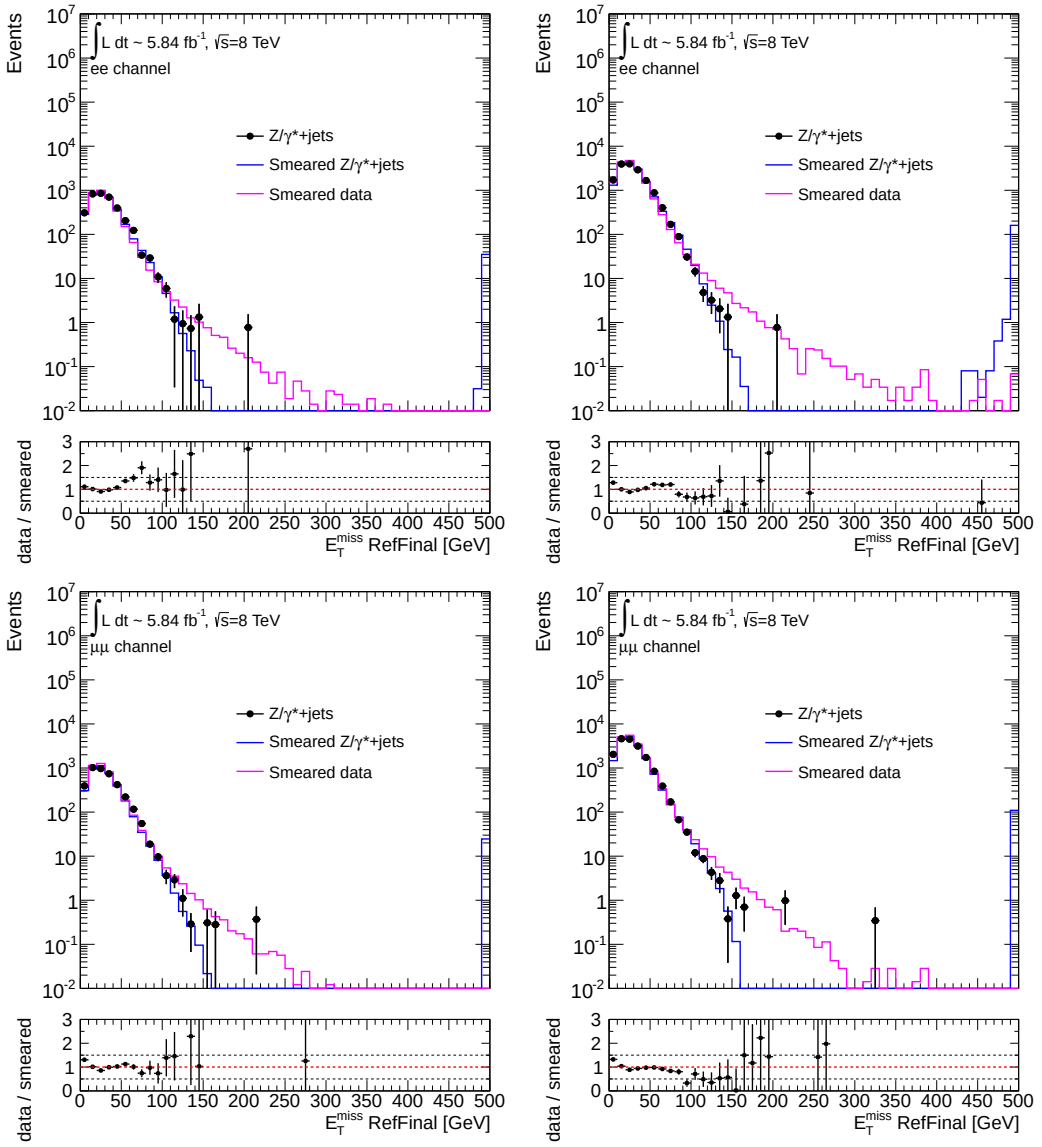

Figure 7.25: $E_{\mathrm{T}}^{\mathrm{miss}}$ distributions in ZCR1 (left) and ZCR2 (right), for ee (top) and $\mu\mu$ (bottom) events using $Z/\gamma^* + \mathrm{jets}$ MC samples.. The black points represent nominal selected events. The blue line is the $E_{\mathrm{T}}^{\mathrm{miss}}$ of the smeared MC events. The magenta line is the $E_{\mathrm{T}}^{\mathrm{miss}}$ of the pseudo-data used for the nominal estimate in this method.

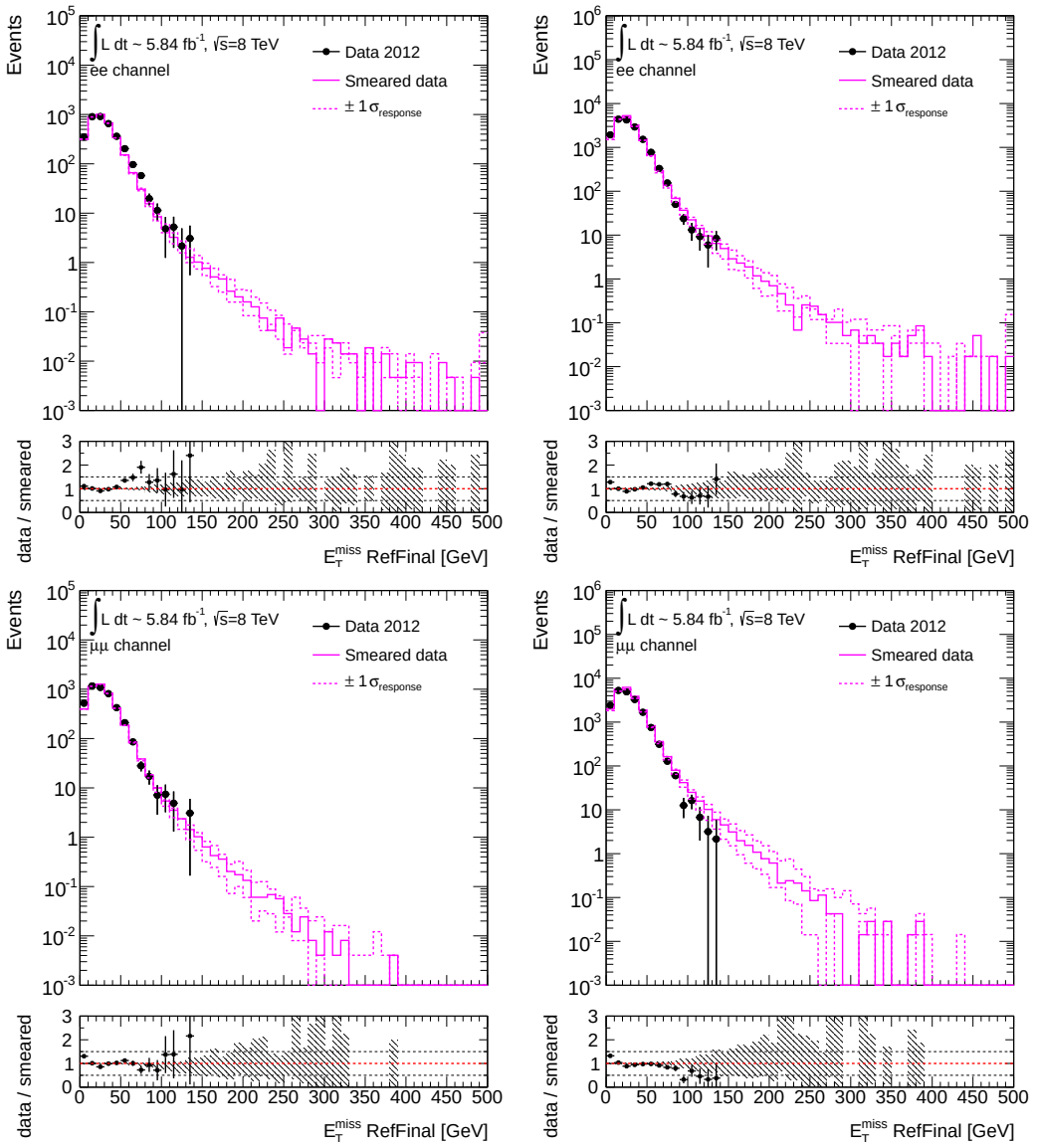

Figure 7.26: $E_{\mathrm{T}}^{\mathrm{miss}}$ distributions in SR1 (left) and SR2 (right), for ee (top) and $\mu\mu$ (bottom) events, before the cut on $E_{\mathrm{T}}^{\mathrm{miss}}$. The black points represent selected data, corrected for non-$Z/\gamma^{*}+\mathrm{jets}$ sources. The data are shown only in the control regions, which are used for validation. The magenta line is the $E_{\mathrm{T}}^{\mathrm{miss}}$ of the smeared events, shown for the entire $E_{\mathrm{T}}^{\mathrm{miss}}$ range. The dotted lines represent the systematic variations due to the tail fluctuations in the jet response function. The hashed uncertainty in the ratio takes into account these systematic variations in addition to the statistical uncertainties.

Signal Region	SR1		SR2	
	ee	$\mu\mu$	ee	$\mu\mu$
Z+jets	70%	80%	50%	67%
WW, $t\bar{t}$, Wt, $\tau\tau$	9%	9%	5%	5%
WZ	46%	45%	21%	24%
ZZ	26%	37%	10%	20%
Total	16%	13%	15%	17%

Table 7.21: Total systematic uncertainties on SM Z and non-Z events for the electron and muon channels in the two SRs.

7.5 Systematic Uncertainties

Systematic uncertainties affecting the background rate and SUSY signal yields in the signal regions have been evaluated. The systematics for the data-driven evaluation of WW, $t\bar{t}$, Wt, $\tau\tau$ background were discussed in the Section 7.4.1 and were found to be $\approx 8\%$ for SR1 and $\approx 6\%$ for SR2. The systematic uncertainties on the data-driven estimates of the $Z/\gamma^* + \text{jets}$ background are found to be 70% (80%) for SR1 and 50% (67%) for SR2 for the electron (muon) channel and summarized at Section 7.4.3. The backgrounds from WZ and ZZ are obtained using MC. The total uncertainty on WZ is estimated to be 46% (43%) for SR1 and 21% (24%) for SR2 for the electron (muon) channel. The uncertainty on ZZ is found to be 26% (37%) for SR1 and 10% (20%) for SR2 for the electron (muon) channel. The uncertainties are dominated by the uncertainty on the jet energy scale. Table 7.21 summarizes the total systematic uncertainties on the SM Z and non-Z backgrounds.

For the SUSY signal processes, various sources of uncertainties affect the theoretical cross sections. The following sources were considered in this analysis: PDF uncertainties, scale, and α_s uncertainties. The total theoretical uncertainties vary from 3% at the small values of μ to 34% (see Tables 7.22 and 7.23). The PDF uncertainties on the GGM cross sections were evaluated by using the CTEQ6.6M [107] and MSTW PDF error sets in the cross section calculation. The difference in the impact of the PDF and scale uncertainties on the various GGM points is related to the different production mechanisms in the GGM grid considered here. The systematic uncertainties due to experimental sources were also assessed for signal MC.

$m(\tilde{g})$[GeV]	μ[GeV]	Total theoretical uncertainties
400	120	0.12
	150	0.14
	200	0.15
	300	0.15
	390	0.15
500	120	0.08
	150	0.11
	200	0.14
	300	0.16
	400	0.17
	490	0.17
600	120	0.04
	150	0.07
	200	0.12
	300	0.17
	400	0.18
	500	0.19
	590	0.19
700	120	0.03
	150	0.04
	200	0.07
	300	0.16
	400	0.20
	500	0.21
	600	0.21
	690	0.21
800	120	0.03
	150	0.03
	200	0.04
	300	0.12
	400	0.19
	500	0.23
	600	0.24
	700	0.25
	790	0.25

Table 7.22: Total relative theoretical uncertainties on the GGM signal cross sections.

$m(\tilde{g})$[GeV]	μ[GeV]	Total theoretical uncertainties
900	120	0.03
	150	0.03
	200	0.03
	300	0.15
	400	0.19
	500	0.25
	600	0.28
	700	0.29
	800	0.29
	890	0.30
1000	120	0.03
	150	0.03
	200	0.03
	300	0.04
	400	0.11
	500	0.20
	600	0.28
	700	0.31
	800	0.33
	890	0.34

Table 7.23: Total relative theoretical uncertainties on the GGM signal cross sections.

	SR1	
	ee	$\mu\mu$
WW, $t\bar{t}$, Wt, $\tau\tau$	1.8±1.1±0.2	2.2±1.3±0.2
WZ	0.7±0.1±0.3	0.5±0.1±0.2
ZZ	0.2±0.03±0.1	0.2±0.03±0.1
$Z/\gamma^* + \text{jets}$	0.5±0.1±0.3	0.3±0.04±0.2
Total SM Background	3.1±1.1±0.5	3.2±1.3±0.4
Observed	5	5
GGM (600,120)	0.3±0.2±0.01	0.1±0.04±0.1
GGM (600,590)	52.9±0.9±11.0	47.3±0.9±9.8
$\sigma^{95\%}_{\text{BSM,max}} \cdot A \cdot \epsilon$ (exp) [fb]	1.3	
$\sigma^{95\%}_{\text{BSM,max}} \cdot A \cdot \epsilon$ (obs) [fb]	2.0	

Table 7.24: Expected SM background event yields and number of events observed in data for an integrated luminosity of 5.8 fb^{-1} after the SR1 requirements for the electron and muon channels. The first (second) uncertainty for each prediction represents the statistical (systematic) uncertainty. In addition, yields are given for the two representative $\tan\beta = 1.5$ GGM grid points (presented in previous figures). Finally, the observed and expected 95% CL upper limits on the visible cross section for SR1 selection are shown.

7.6 Results and Interpretation

Tables 7.24 and 7.25 show the number of expected events in the SRs for each background source together with the observed number of events. In both signal regions, the contribution from QCD and W+jets are negligible, and the dominant backgrounds are top, $Z/\gamma^* + \text{jets}$, and dibosons.

In the SRs, the expectation and observation agree within uncertainties. Given a lack of excess in the observed data, the results of the analysis are interpreted as 95% confidence level (CL) exclusion limits on $m(\tilde{g})$ and μ in the higgsino-like NLSP scenario defined for the GGM model grid. The expected and observed 95% CL upper limits are computed using the CL_s method combining the ee and $\mu\mu$ channels. Systematic uncertainties are treated as nuisance parameters, and their correlations are taken into account.

7.6.1 GGM $\tan\beta = 1.5$ grid interpretation

The observations in the SRs are first interpreted in the context of the low-$\tan\beta$ GGM grid, which, as seen in Figure 7.1, is characterized by a high $BR(\tilde{\chi}^0_1 \to Z\tilde{G})$. Figure 7.27 shows the final exclusion limit for this interpretation. This shows the SR1

	SR2	
	ee	$\mu\mu$
WW, $t\bar{t}$, Wt, $\tau\tau$	26.9±3.8±1.7	30.9±4.3±1.8
WZ	8.4±0.5±1.8	9.0±0.5±2.1
ZZ	3.7±0.1±0.4	4.8±0.2±0.9
$Z/\gamma^* + \text{jets}$	17.0±0.6±8.1	14.8±0.5±10.0
Total SM Background	55.9±3.9±8.4	59.5±4.4±10.4
Observed	66	61
GGM (600,120)	1.1±0.3±0.2	1.0±0.3±0.2
GGM (600,590)	151.8±1.6±28.9	133.8±1.5±25.8
$\sigma^{95\%}_{\text{BSM,max}} \cdot A \cdot \epsilon$ (exp) [fb]	6.3	
$\sigma^{95\%}_{\text{BSM,max}} \cdot A \cdot \epsilon$ (obs) [fb]	7.7	

Table 7.25: Expected SM background event yields and number of events observed in data for an integrated luminosity of 5.8 fb^{-1} after the SR2 requirements for the electron and muon channels. The first (second) uncertainty for each prediction represents the statistical (systematic) uncertainty. In addition, yields are given for the two representative $\tan\beta = 1.5$ GGM grid points (presented in previous figures). Finally, the observed and expected 95% CL upper limits on the visible cross section for SR2 selection are shown.

exclusion with a statistical combination of the ee and $\mu\mu$ channels. Because the upper expected limits computed at each point in the GGM grid are stronger in the case of SR1, SR2 results do not enter the final exclusion. For the range $180 < \mu < 800$ GeV, an upper limit of $680-880$ GeV is placed on the gluino mass. In addition to the results presented in this analysis, the excluded region from the 2011 $Z + E_{\text{T}}^{\text{miss}}$ analysis [105] is shown.

7.6.2 GGM $\tan\beta = 30$ grid interpretation

The results of the analysis are also interpreted in a large $\tan\beta$ grid. As discussed in Section 7.2.1, the $\tan\beta = 30$ grid differs from the $\tan\beta = 1.5$ grid because of the rise in $BR(\tilde{\chi}_1^0 \to h\tilde{G})$ with increasing μ. As a result of this feature, large μ events may give rise to hZ final states to which the analysis is also sensitive.

Figure 7.28 shows the final $ee + \mu\mu$ combined limit for SR1 using this high-$\tan\beta$ interpretation. Because the expected upper limits computed at each point in the GGM grid are stronger in the case of SR1, SR2 results do not enter the final exclusion. For the range $180 < \mu < 740$ GeV, an upper limit of $680 - 820$ GeV is placed on the gluino mass. Since this is the first interpretation of these models with ATLAS, no 2011 results were available with which to compare.

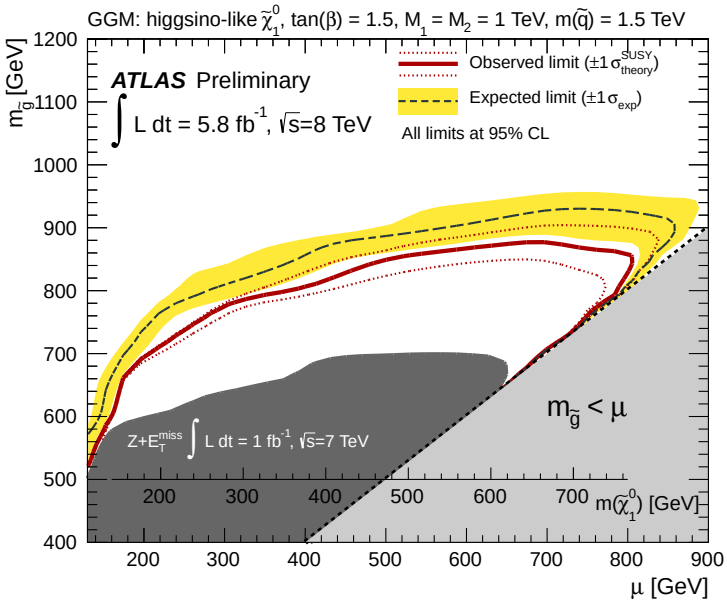

Figure 7.27: Expected and observed 95% CL exclusion limits for SR1 on the $m(\tilde{g})$ and μ parameters for GGM models with $\tan\beta = 1.5$, $M_1 = M_2 = 1$ TeV, $c\tau_{\mathrm{NLSP}} < 0.1\,\mathrm{mm}$, and $m(\tilde{q}) = 1.5$ TeV. An additional axis corresponding to $m(\tilde{\chi}_1^0)$ is provided. The dark grey area shows the observed exclusion based on the analysis in Ref. [105]. The light grey area indicates the region where the NLSP is the gluino, which is not considered in this analysis.

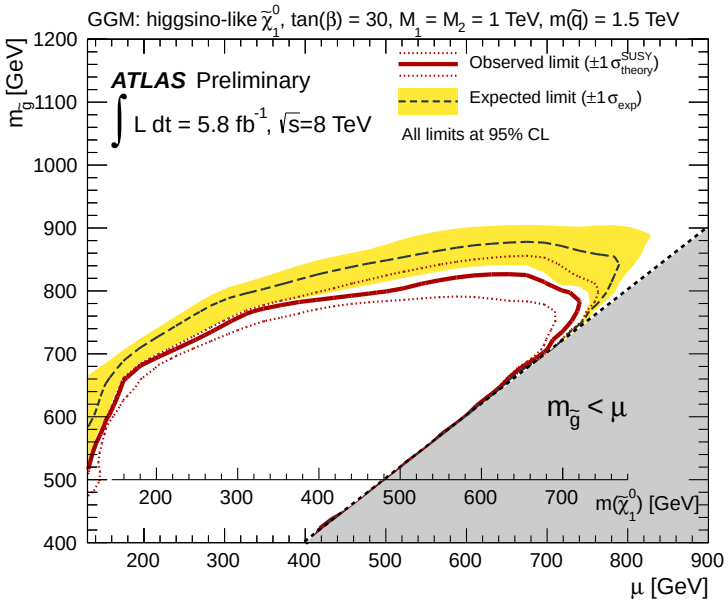

Figure 7.28: Expected and observed 95% CL exclusion limits for SR1 on the $m(\tilde{g})$ and μ parameters for GGM models with $\tan\beta = 30$, $M_1 = M_2 = 1$ TeV, $c\tau_{\mathrm{NLSP}} < 0.1\,\mathrm{mm}$, and $m(\tilde{q}) = 1.5$ TeV. An additional axis corresponding to $m(\tilde{\chi}_1^0)$ is provided. The grey area indicates the region where the NLSP is the gluino, which is not considered in this analysis.

Chapter 8

Summary and concluding remarks

The Large Hadron Collider has ushered particle physics into a new era. Particle collisions at the energies probed at the LHC have not occured since the very early universe. Data from these proton-proton collisions provide us with the opportunity to probe the known processes of the SM with unprecedented precision, as well as the chance to observe exotic physical processes beyond the Standard Model.

SUSY is an extension to the SM that predicts a spectrum of particles mirroring those in the SM. SUSY theories characterized by R-parity conservation can generally be associated with missing energy signatures experimentally, and thus allow for powerful discrimination against background processes. In certain regions of SUSY parameter space, having made various assumptions about the nature of SUSY breaking, processes involving Z bosons become important. Therefore, a healthy SUSY search program using the $Z + E_{\mathrm{T}}^{\mathrm{miss}}$ final state is essential for experiments on the LHC.

Along with a brief overview of the SM and SUSY, and summaries of the LHC and the ATLAS detector, this dissertation presents two searches for SUSY in collision data from the LHC, collected at center of mass energies $\sqrt{s} = 7$ and 8 TeV. In both analyses, the $Z + E_{\mathrm{T}}^{\mathrm{miss}}$ final state is motivated by GGM models with higgsino-like $\tilde{\chi}_1^0$'s. In the analysis of 1 fb^{-1} of 2011 data collected by the ATLAS detector, a data-driven estimation of the $Z/\gamma^* + \mathrm{jets}$ background is derived using a control sample of $\gamma + \mathrm{jets}$ events. Other backgrounds are evaluated with the use of simulated MC events. Three signal regions are defined. The observations from data align well with the SM predictions, and thus mass limits are placed on the gluino and NLSP for GGM models with low $\tan\beta$.

The 2012 analysis involving the same final state was carried out using 6 fb^{-1} of ATLAS data collected in 2012. This continuation of the 2011 analysis was marked by an improved measurement of the $Z/\gamma^* + \mathrm{jets}$ background using a method involving p_{T}-smeared jets, along with data-driven evaluation of flavor-symmetric backgrounds. Again, good agreement is observed between the SM predictions and observations in

data, and so further limits are placed on GGM SUSY models. In this case, two groups of GGM models were considered: one with low $\tan\beta$, as used in the 2011 results, and one with high $\tan\beta$, motivated by the Higgs boson observation in 2012.

Taking the results of these analyses into account, exclusion limits on the gluino mass and the higgsino mass parameter have been placed for GGM models with $\tan\beta = 1.5$ or 30, $M_1 = M_2 = 1$ TeV, and $c\tau_{\text{NLSP}} < 0.1$ mm. Assuming $\tan\beta = 1.5$, gluino masses up to $680 - 880$ GeV are excluded at 95% CL for higgsino masses in the range $180 - 800$ GeV. With $\tan\beta = 30$, gluino masses of $680 - 820$ GeV are excluded over the range $180 < m(\tilde{h}) < 740$ GeV.

The status of ATLAS SUSY searches as of December 2012 can be seen in Figure 8.1. This figure shows the breadth of the search program, and clearly demonstrates that no new heavy particles have been discovered up to a mass $M \sim 1$ TeV. Although this casts a shadow over the potential for discoveries in the immediate future, SUSY is a very extensive framework, and there is much parameter space to be explored. The reach of the LHC will be tested over the coming years, as more recorded luminosity will allow for further searches and refinements to the existing measurements. The prospect of new physics at the TeV scale is still exciting, and new particles may be lurking at masses just out of reach.

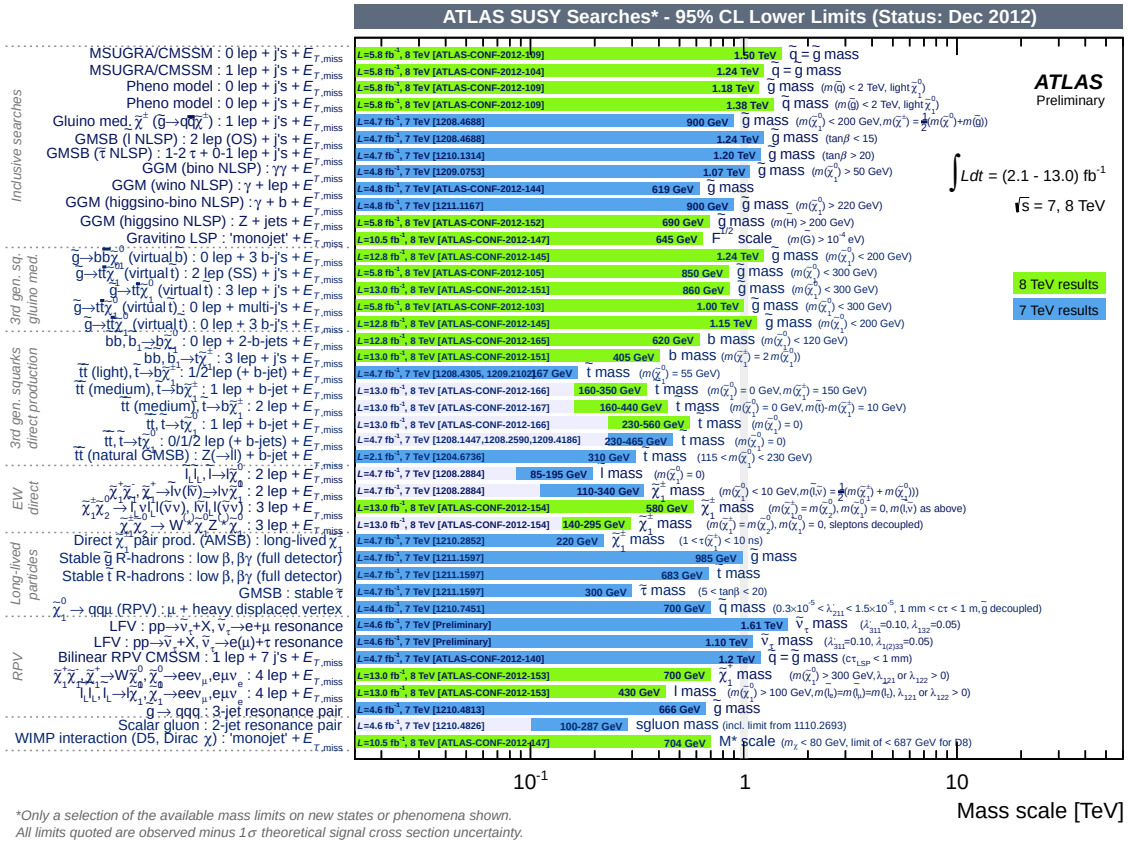

Figure 8.1: Mass reach of ATLAS searches for Supersymmetry. Only a representative selection of the available results is shown.

Appendix

Appendix A

Object definitions common to 2011 ATLAS SUSY dilepton analysis

The following definitions, used to select jets and leptons for the analysis, were derived for the purposes of an inclusive dilepton SUSY search [69]. As the analysis presented in Chapter 6 follows directly from the inclusive analysis, we apply the same selections for these objects.

A.1 Jets

Jets are reconstructed using the anti$-k_t$ jet algorithm [64] from topoclusters with four-momentum recombination and distance parameter $R = 0.4$ (in η - ϕ space). The jet transverse momentum is measured at the electromagnetic jet energy scale (EMJES). Jets are required to have $p_T > 20$ GeVand lie within $|\eta| < 2.8$. Jets must not lie within $\Delta R = \sqrt{(\eta)^2 + (\phi)^2} = 0.2$ of a selected electron.

Calorimeter effects may lead to high energy deposits which differ from the energy deposition of real jets. The event is rejected if such a "bad" jet has properties consistent with the following non-collision sources, to improve the $E_{\mathrm{T}}^{\mathrm{miss}}$resolution:

1. The electromagnetic energy fraction is larger than 0.95 ($EMf > 0.95$) and the absolute jet quality value is greater than 0.8 ($|LArQ| > 0.8$) for jets with $|\eta| < 2.8$. This source is known as EM coherent noise.

2. The fraction of energy in the hadronic endcap calorimeter is larger than 0.5 ($|HECf| > 0.5$) and the measured absolute value of quality of the jet is greater than 0.5 ($|HECQ| > 0.5$). The absolute value of the total energy in cells with a negative value is greater than 60 GeV. The signal from these sources is consistent with sporadic noise in the hadronic endcap calorimeters.

3. Jets with energy-squared-weighted time differing from the expected value by more than 25 ns. The EM energy fraction < 0.05 and the ratio of the sum $p_{\mathrm{T}}$of the tracks associated to the jets divided by the calibrated jet $p_{\mathrm{T}}$is less than 0.05 ($chf < 0.05$) for jets with $|\eta| < 2$, or EM energy fraction < 0.05 for jets with $|\eta| > 2$. A jet with $|\eta| < 2$ has 99% of its energy contained in a single layer in the calorimeter ($Fmax < 0.99$). These sources are consistent with the signal from either cosmic rays or beam halo.

A.2 Muons

In this analysis the muon candidates are required to be either *Combined*, where the muon track is reconstructed independently in the Muon Spectrometer and in the Inner Detector, or $Segment - tagged$, where the muon track is reconstructed only in the Inner Detector and associated with Muon Spectrometer segments. The muon candidates are required to pass the *Loose* quality criteria, as defined by the muon combined performance group. Muon candidates within $|\eta| < 2.4$ are considered, and their p_{T}must be greater than 10 GeV. These additional inner detector cuts are required for each muon candidate:

1. The Inner Detector track should have at least one B-layer hit (when such a hit is expected), at least 2 pixel hits and pixel dead sensors in total, at least 6 SCT hits and SCT dead sensors in total, at most 2 pixel holes and SCT holes in total.

2. If the η of track is less than 1.9 and the number of TRT outliers and TRT hits in total is less than 6, we reject the muon.

3. If the sum of the TRT outliers and the TRT hits is greater than 6, then the TRT outliers should not form more than 90% of the sum of the total TRT hits.

The muon is rejected if it falls within $\Delta R = 0.4$ of a selected jet (as defined above). All muons must satisfy d_0 and z_0 requirements (to reject against cosmics, $z_0 < 1.0$ mm and $d_0 < 0.2$ mm). A signal muon, if the leading lepton in the event, must have $p_T > 20$ GeV. The selected muons are required to be isolated, satisfying a track based isolation, $p_T cone20 < 1.8$ GeV. Here "$p_T cone20$" is the sum of the p_T of all the tracks in a cone of $\Delta R = 0.2$ surrounding the muon. Finally, muons in MC events are smeared with p_T- and η-dependent scale-factors, to improve the simulation's agreement with the data.

A.3 Electrons

Electrons are reconstructed by `Egamma` algorithms based on clusters reconstructed in the electromagnetic calorimeter, which then are associated to tracks of charged particles reconstructed in the inner detector. Information from both detectors is used to provide a good separation between isolated electrons and a fake signature from hadronic jets. The electron shower is required to be consistent with that expected of an electron. Cuts are applied on the fractional deposit in the hadronic calorimeter and on the shower width in η and ϕ in the first and second layers of the electromagnetic calorimeters. Furthermore, a reconstructed track containing at least 7 silicon hits, at least one of which having to be a pixel hit, is required to match the cluster by extrapolating them from their last measurement point to the second layer of the calorimeter. The specific quality requirement is referred as "medium". In addition, electrons must have $p_T > 20$ GeV and $|\eta^{\mathrm{cl}}| < 2.47$. Here η^{cl} refers to the η of the electron cluster. When calculating the $p_{\mathrm{T}}$of an electron, the energy is always taken to be from the calorimeter cluster, and the η is taken from either the cluster or the matched track, depending on the Inner Detector hit multiplicity. The electron energy scale is corrected for data and smeared for Monte Carlo, as specified in [87]. After passing these selections the electrons are subjected to an overlap removal requirement, which rejects an electron if it falls within $\Delta R = \sqrt{(\eta)^2 + (\phi)^2} = 0.4$ of a selected jet (as defined above). We exclude electrons if their cluster core, defined as the 3×4 cells in the second layer, or the cluster edge in the first or second sampling layer is read out by a dead calorimeter Front End Board (FEB). We also exclude electrons if the cluster core has any dead HV region or masked cells. These quality checks are made by using the object quality (OQ) flag "el_OQ & egammaPID::BADCLUSELECTRON != 0".

The selected electrons which pass the overlap removal and quality criteria are further required to be "tight" and isolated relative to their transverse momentum. The isolation requires the ratio of the transverse momentum in a cone $\Delta R \leq 0.2$ around the electron to the transverse momentum of the electron $p_T cone20/p_T$ be less than 0.1. The $p_{\mathrm{T}}$of the leading electron is required to be $p_T > 25$ GeV.

Bibliography

[1] A. Pich. The Standard model of electroweak interactions. 2007.

[2] S. P. Martin. A Supersymmetry primer. 1997.

[3] G. Aad et al. Observation of a new particle in the search for the Standard Model Higgs boson with the ATLAS detector at the LHC. *Phys.Lett.*, B716:1–29, 2012.

[4] S. Chatrchyan et al. Observation of a new boson at a mass of 125 GeV with the CMS experiment at the LHC. *Phys.Lett.*, B716:30–61, 2012.

[5] H. Miyazawa. *Prog. Theor. Phys.*, 36 (6):1266–1276, 1966.

[6] P. Ramond. *Phys. Rev.*, D3:2415–2418, 1971.

[7] Y. A. Golfand and E. P. Likhtman. *JETP Lett.*, 13:323–326, 1971.

[8] A. Neveu and J. H. Schwarz. *Nucl. Phys.*, B31:86–112, 1971.

[9] A. Neveu and J. H. Schwarz. *Phys. Rev.*, D4:1109–1111, 1971.

[10] J. Gervais and B. Sakita. *Nucl. Phys.*, B34:632–639, 1971.

[11] D. V. Volkov and V. P. Akulov. *Phys. Lett.*, B46:109–110, 1973.

[12] J. Wess and B. Zumino. *Phys. Lett.*, B49:52, 1974.

[13] J. Wess and B. Zumino. *Nucl. Phys.*, B70:39–50, 1974.

[14] G. Kane. *Modern Elementary Particle Physics: The Fundamental Particles and Forces?* Advanced book classics. Addison-Wesley Pub., 1993.

[15] F. Englert and R. Brout. Broken symmetry and the mass of gauge vector mesons. *Phys.Rev.Lett.*, 13:321–323, 1964.

[16] P. W. Higgs. Broken symmetries, massless particles and gauge fields. *Phys.Lett.*, 12:132–133, 1964.

[17] P. W. Higgs. Broken symmetries and the masses of gauge bosons. *Phys.Rev.Lett.*, 13:508–509, 1964.

[18] G. Guralnik, C. Hagen, and T. Kibble. Global conservation laws and massless particles. *Phys.Rev.Lett.*, 13:585–587, 1964.

[19] P. W. Higgs. Spontaneous symmetry breakdown without massless bosons. *Phys.Rev.*, 145:1156–1163, 1966.

[20] T. Kibble. Symmetry breaking in non-Abelian gauge theories. *Phys.Rev.*, 155:1554–1561, 1967.

[21] P. Fayet. *Phys. Lett.*, B64:159, 1976.

[22] P. Fayet. *Phys. Lett.*, B69:489, 1977.

[23] G. R. Farrar and P. Fayet. *Phys. Lett.*, B76:575–579, 1978.

[24] P. Fayet. *Phys. Lett.*, B84:416, 1979.

[25] S. Dimopoulos and H. Georgi. *Nucl. Phys.*, B193:150, 1981.

[26] J. Ellis, J. Hagelin, D. Nanopoulos, K. Olive, and M. Srednicki. Supersymmetric relics from the big bang. *Nuclear Physics B*, 238(2):453 – 476, 1984.

[27] H. Goldberg. Constraint on the Photino Mass from Cosmology. *Phys. Rev. Lett.*, 50:1419–1422, May 1983.

[28] G. F. Giudice and R. Rattazzi. Theories with gauge-mediated supersymmetry breaking. *Phys. Rept.*, 322:419–499, 1999.

[29] P. Meade, N. Seiberg, and D. Shih. General Gauge Mediation. *Prog. Theor. Phys. Suppl.*, 177:143–158, 2009.

[30] M. Buican et al. Exploring General Gauge Mediation. *JHEP*, 03:016, 2009.

[31] P. Meade, M. Reece, and D. Shih. Prompt Decays of General Neutralino NLSPs at the Tevatron. *JHEP*, 1005:105, 2010.

[32] J. T. Ruderman and D. Shih. General Neutralino NLSPs at the Early LHC. *JHEP*, 1208:159, 2012.

[33] L. Evans and P. Bryant. LHC Machine. *Journal of Instrumentation*, 3(08):S08001, 2008.

[34] M. Bajko et al. Report of the Task Force on the Incident of 19th September 2008 at the LHC. oai:cds.cern.ch:1168025. Technical Report LHC-PROJECT-Report-1168. CERN-LHC-PROJECT-Report-1168, CERN, Geneva, Mar 2009.

[35] J. P. Blewett. 200 GeV Intersecting Storage Accelerators. In *Proceedings of the 8th International Conference on High-Energy Accelerators*, Geneva, Switzerland, 1971.

[36] S. Holmes, R. S. Moore, and V. Shiltsev. Overview of the Tevatron collider complex: goals, operations and performance. *Journal of Instrumentation*, 6(08):T08001, 2011.

[37] G. Voss. Status of the HERA-project. *Nuclear Physics B - Proceedings Supplements*, 3(0):525 – 552, 1988.

[38] M. Harrison, T. Ludlam, and S. Ozaki. RHIC project overview. *Nuclear Instruments and Methods in Physics Research Section A: Accelerators, Spectrometers, Detectors and Associated Equipment*, 499(23):235 – 244, 2003. The Relativistic Heavy Ion Collider Project: RHIC and its Detectors.

[39] M. Benedikt et al. *LHC Design Report*. CERN, Geneva, 2004.

[40] C. Hill et al. Tests of the CERN Proton Linac Performance for LHC-Type Beams. In *Proceedings of the 2000 International Linac Conference*, Monterey, CA, USA, 2000.

[41] R. Bailey and P. Collier. Standard Filling Schemes for Various LHC Operation Modes. oai:cds.cern.ch:691782. Technical Report LHC-PROJECT-NOTE-323, CERN, Geneva, Sep 2003.

[42] The ATLAS Collaboration. The ATLAS Experiment at the CERN Large Hadron Collider. *Journal of Instrumentation*, 3(08):S08003, 2008.

[43] G. F. Knoll. *Radiation Detection and Measurement*. Wiley, New York, 2000.

[44] G. Aad et al. ATLAS pixel detector electronics and sensors. *Journal of Instrumentation*, 3(07):P07007, 2008.

[45] A. Ahmad et al. The silicon microstrip sensors of the ATLAS semiconductor tracker. *Nuclear Instruments and Methods in Physics Research Section A: Accelerators, Spectrometers, Detectors and Associated Equipment*, 578(1):98 – 118, 2007.

[46] Y. Unno et al. Application of Cu-polyimide flex circuit and Al-on-glass pitch adapter for the ATLAS SCT barrel hybrid. *Nuclear Instruments and Methods in Physics Research Section A: Accelerators, Spectrometers, Detectors and Associated Equipment*, 541:286 – 294, 2005.

[47] W. Blum, W. Riegler, and L. Rolandi. *Particle Detection with Drift Chambers*. Springer-Verlag, Berlin, 2008.

[48] B. Dolgoshein. Transition radiation detectors. *Nuclear Instruments and Methods in Physics Research Section A: Accelerators, Spectrometers, Detectors and Associated Equipment*, 326(3):434 – 469, 1993.

[49] J. Jackson. *Classical Electrodynamics*. Wiley, 1998.

[50] *ATLAS liquid-argon calorimeter: Technical Design Report*. Technical Design Report ATLAS. CERN, Geneva, 1996.

[51] *ATLAS tile calorimeter: Technical Design Report*. Technical Design Report ATLAS. CERN, Geneva, 1996.

[52] G. Charpak et al. The use of multiwire proportional counters to select and localize charged particles. *Nuclear Instruments and Methods*, 62(3):262 – 268, 1968.

[53] U. Amaldi et al. The real part of the forward proton proton scattering amplitude measured at the CERN intersecting storage rings. *Physics Letters B*, 66(4):390 – 394, 1977.

[54] G. Aad et al. Electron performance measurements with the ATLAS detector using the 2010 LHC proton-proton collision data. 2011. CERN-PH-EP-2011-117.

[55] W. Lampl et al. Calorimeter Clustering Algorithms: Description and Performance.

[56] H. Voss et al. TMVA: Toolkit for Multivariate Data Analysis with ROOT. TMVA, the Toolkit for Multivariate Data Analysis with ROOT. *PoS*, ACAT:040, 2007.

[57] https://twiki.cern.ch/twiki/bin/viewauth/AtlasProtected/IsEMIdentification.

[58] Expected photon performance in the ATLAS experiment. Technical Report ATL-PHYS-PUB-2011-007, CERN, Geneva, Apr 2011.

[59] Muon Reconstruction Performance. Technical Report ATLAS-CONF-2010-064, CERN, Geneva, Jul 2010.

[60] *ATLAS detector and physics performance: Technical Design Report, 1.* Technical Design Report ATLAS. CERN, Geneva, 1999.

[61] S. Hassani et al. A muon identification and combined reconstruction procedure for the ATLAS detector at the LHC using the (MUONBOY, STACO, MuTag) reconstruction packages. *Nuclear Instruments and Methods in Physics Research Section A: Accelerators, Spectrometers, Detectors and Associated Equipment*, 572(1):77 – 79, 2007.

[62] T. Lagouri et al. A muon identification and combined reconstruction procedure for the ATLAS detector at the LHC at CERN. *Nuclear Science, IEEE Transactions on Nuclear Science*, 51(6):3030–3033, 2004.

[63] https://twiki.cern.ch/twiki/bin/viewauth/AtlasProtected/MuTagDocumentation.

[64] M. Cacciari, G. P. Salam, and G. Soyez. The anti-k_t jet clustering algorithm. *JHEP*, 04:063, 2008.

[65] G. Aad et al. Jet energy measurement with the ATLAS detector in proton-proton collisions at $\sqrt{s} = 7$ TeV. 2011.

[66] Jet energy scale and its systematic uncertainty in proton-proton collisions at $\sqrt{s} = 7$ TeV with ATLAS 2011 data. Technical Report ATLAS-CONF-2013-004, CERN, Geneva, Jan 2013.

[67] G. Aad et al. *Expected performance of the ATLAS experiment: detector, trigger and physics.* CERN, Geneva, 2009.

[68] G. Aad et al. Performance of Missing Transverse Momentum Reconstruction in Proton-Proton Collisions at 7 TeV with ATLAS. *Eur.Phys.J.*, C72:1844, 2012.

[69] A. Alonso et al. Searching for Supersymmetry with two leptons and missing transverse momentum at sqrt(s)=7 TeV. Technical Report ATL-PHYS-INT-2011-091, CERN, Geneva, Nov 2011.

[70] S. Agostinelli et al. GEANT4: A simulation toolkit. *Nucl. Instrum. Meth.*, A506:250–303, 2003.

[71] G. Aad et al. Studies of the performance of the ATLAS detector using cosmic-ray muons. *Eur.Phys.J.*, C71:1593, 2011. * Temporary entry *.

[72] A. Djouadi, J.-L. Kneur, and G. Moultaka. SuSpect: A Fortran code for the supersymmetric and Higgs particle spectrum in the MSSM. *Comput. Phys. Commun.*, 176:426–455, 2007.

[73] M. Muhlleitner, A. Djouadi, and Y. Mambrini. SDECAY: A Fortran code for the decays of the supersymmetric particles in the MSSM. *Comput. Phys. Commun.*, 168:46–70, 2005.

[74] T. Sjostrand, S. Mrenna, and P. Z. Skands. PYTHIA 6.4 Physics and Manual. *JHEP*, 05:026, 2006.

[75] W. Beenakker et al. PROSPINO: A program for the PROduction of Supersymmetric Particles In Next-to-leading Order QCD. 1996.

[76] L. Carminati et al. Reconstruction and Identification Efficiency of Inclusive Isolated Photons. (ATL-PHYS-INT-2011-014), Mar 2011.

[77] J. Alasia et al. Search for a diphoton and E_T^{miss} final state in $\sqrt{s} = 7$ TeV pp collisions at the LHC using the ATLAS detector. Technical Report ATL-PHYS-INT-2011-095, CERN, Geneva, Nov 2011.

[78] https://twiki.cern.ch/twiki/bin/viewauth/AtlasProtected/SUSYCrosssections.

[79] S. Moch and P. Uwer. Theoretical status and prospects for top-quark pair production at hadron colliders. *Phys.Rev.*, D78:034003, 2008.

[80] U. Langenfeld, S. Moch, and P. Uwer. New results for $t\bar{t}$ production at hadron colliders. 2009.

[81] S. Frixione, P. Nason, and C. Oleari. *JHEP*, 11:070, 2007.

[82] B. P. Kersevan and E. Richter-Was. The Monte Carlo event generator AcerMC version 2.0 with interfaces to PYTHIA 6.2 and HERWIG 6.5. 2004.

[83] https://twiki.cern.ch/twiki/bin/view/AtlasProtected/JESUncertaintyProvider.

[84] Jet energy scale and its systematic uncertainty for jets produced in proton-proton collisions at sqrt(s) = 7 TeV and measured with the ATLAS detector. Technical Report ATLAS-CONF-2010-056, CERN, Geneva, Jul 2010.

[85] In-situ jet energy scale and jet shape corrections for multiple interactions in the first ATLAS data at the LHC. Technical Report ATLAS-CONF-2011-030, CERN, Geneva, Mar 2011.

[86] Jet energy resolution and selection efficiency relative to track jets from in-situ techniques with the ATLAS Detector Using Proton-Proton Collisions at a Center of Mass Energy *sqrts* = 7 TeV. Technical Report ATLAS-CONF-2010-054, CERN, Geneva, Jul 2010.

[87] https://twiki.cern.ch/twiki/bin/view/AtlasProtected/EnergyScaleResolutionRecommendations.

[88] Muon Momentum Resolution in First Pass Reconstruction of pp Collision Data Recorded by ATLAS in 2010. Technical Report ATLAS-CONF-2011-046, CERN, Geneva, Mar 2011.

[89] https://twiki.cern.ch/twiki/bin/view/AtlasProtected/MCPAnalysisGuidelinesPLHC2011.

[90] M. Antonelli et al. Performance of Missing Transverse Energy Reconstruction in Proton-Proton Collisions at 7 TeV with ATLAS. Technical Report ATL-COM-PHYS-2011-567, CERN, Geneva, May 2011.

[91] R. Bruneliere et al. Setting exclusion limits in ATLAS supersymmetry searches with a likelihood ratio based method. Technical Report ATL-COM-PHYS-2011-004, CERN, Geneva, Jan 2011.

[92] A. Sherstnev and R. Thorne. *Eur.Phys.J.*, C55:553–575, 2008.

[93] W. Beenakker et al. Squark and gluino production at hadron colliders. *Nucl.Phys.*, B492:51–103, 1997.

[94] A. Kulesza and L. Motyka. Threshold resummation for squark-antisquark and gluino-pair production at the LHC. *Phys.Rev.Lett.*, 102:111802, 2009.

[95] A. Kulesza and L. Motyka. Soft gluon resummation for the production of gluino-gluino and squark-antisquark pairs at the LHC. *Phys.Rev.*, D80:095004, 2009.

[96] W. Beenakker et al. Soft-gluon resummation for squark and gluino hadroproduction. *JHEP*, 0912:041, 2009.

[97] W. Beenakker et al. Squark and gluino hadroproduction. *Int.J.Mod.Phys.*, A26:2637–2664, 2011.

[98] M. Kramer et al. Supersymmetry production cross sections in pp collisions at $\sqrt{s} = 7$ TeV. 2012.

[99] S. Frixione and B. R. Webber. The MC@NLO 3.2 event generator. 2006.

[100] P. M. Nadolsky et al. Implications of CTEQ global analysis for collider observables. *Phys.Rev.*, D78:013004, 2008.

[101] T. Gleisberg et al. Event generation with SHERPA 1.1. *JHEP*, 0902:007, 2009.

[102] G. Aad et al. The ATLAS Simulation Infrastructure. *European Physical Journal C*, 70:823–874, Dec. 2010.

[103] G. Aad et al. Luminosity Determination in pp Collisions at $\sqrt{s} = 7$ TeV Using the ATLAS Detector at the LHC. *Eur.Phys.J.*, C71:1630, 2011.

[104] ATLAS Collaboration. Muon reconstruction efficiency in reprocessed 2010 LHC proton-proton collision data recorded with the ATLAS detector.

[105] ATLAS Collaboration. Search for physics beyond the Standard Model in events with a Z boson and large missing transverse momentum using $\sqrt{s} = 7$ TeV pp collisions from the LHC with the ATLAS detector. Technical Report ATLAS-COM-CONF-2012-046, CERN, Geneva, Feb 2012.

[106] G. Aad et al. Search for squarks and gluinos with the ATLAS detector in final states with jets and missing transverse momentum using 4.7 fb^{-1} of $\sqrt{s} = 7$ TeV proton-proton collision data. *Phys.Rev.*, D87:012008, 2013.

[107] D. Stump et al. Inclusive jet production, parton distributions, and the search for new physics. *JHEP*, 0310:046, 2003.